HEPARIN MICROPARTICLE-MEDIATED DELIVERY OF BMP-2 AND PLURIPOTENT STEM CELL MORPHOGENS FOR BONE REPAIR

A Dissertation
Presented to
The Academic Faculty

by

Marian Hirushika Hettiaratchi

In Partial Fulfillment
of the Requirements for the Degree
Doctor of Philosophy in the
Wallace H. Coulter Department of Biomedical Engineering

Georgia Institute of Technology & Emory University
December 2016

HEPARIN MICROPARTICLE-MEDIATED DELIVERY OF BMP-2 AND PLURIPOTENT STEM CELL MORPHOGENS FOR BONE REPAIR

Approved by:

Dr. Robert E. Guldberg, Advisor
School of Mechanical Engineering
Georgia Institute of Technology

Dr. Todd C. McDevitt, Advisor
Gladstone Institutes of Cardiovascular Disease
Gladstone Institutes

Dr. Scott D. Boden
Department of Orthopedic Surgery
Emory University

Dr. Edward A. Botchwey
Department of Biomedical Engineering
Georgia Institute of Technology

Dr. Andrés J. García
School of Mechanical Engineering
Georgia Institute of Technology

Dr. Johnna S. Temenoff
Department of Biomedical Engineering
Georgia Institute of Technology

Date Approved: September 16, 2016

To my family – grandparents Fabian and Sylvia, parents Patrick and Paula, sister Christine, and fiancé Matt – for their encouragement and support.

ACKNOWLEDGEMENTS

There are many people I need to thank for supporting me throughout my studies, without whom this work would not have been possible. Firstly, I would like to thank my advisors, Todd McDevitt and Robert Guldberg, who took me on as a co-advised student when I first arrived at Georgia Tech in 2011. Being co-advised, I had the opportunity to delve deeply into two different fields – stem cell engineering and bone tissue engineering – and attempt to become an expert at both; more importantly, I had the opportunity to learn from not one, but two great mentors and teachers. Todd and Bob provided me with the guidance I needed to become a better scientist and engineer and challenged me to continue to develop my Ph.D. project in the face of a number of unexpected results. Their optimism in meetings and belief in my abilities enabled me to chase down a number of interesting findings throughout my Ph.D., and I am incredibly grateful that they gave me the freedom and encouragement I needed to do that. Todd has been an attentive teacher, helping me improve my presentation and writing skills with his attention to detail and willingness to give feedback. I find myself having taken on a number of his writing quirks and can no longer see the verb "show" in a sentence without automatically changing it to "demonstrate," "exhibit," or one of the many other synonyms I've learned to avoid the word. Even after moving his lab to San Francisco, Todd continued to be a very active advisor, never failing to bring enthusiasm to our meetings, whether in person, over the phone, or via Skype. His passion for science is something I hope to emulate. Bob has been equally supportive throughout the last five years. Despite being very busy, he always found time to meet with me when I needed advice and go through papers and

presentations with me; his support has only increased over the years after Todd's lab moved, and he always takes the time to emphasize the things I'm doing well. His encouraging comments and ability to show me the big picture of my research when I was unsure of what to do next helped me move forward in my project. He would look at the results I showed him through a different lens, easily finding the broader impacts of my work. This is also a skill I'm happy to say I've started to learn from him.

I would also like to thank my thesis committee, who met with me a number of times over the last two years and provided me with unique perspectives and helpful advice. I know I may have sometimes left our meetings looking shell-shocked from the barrage of questions, but I can assure them I was happy to get the feedback. With a project that bridged multiple areas of research, their expertise in their respective fields was invaluable. Our meetings played a major role in shaping the overarching themes of this work. Throughout my Ph.D., I worked closely with Johnna Temenoff's lab and utilized their materials expertise in order to develop the heparin microparticles presented in this work. Johnna has been excellent to work with, providing insightful and practical feedback on many aspects of my project. Andrés García has similarly helped with developing the materials aspects of my project, giving me much needed advice on the capillary tube experiments in this work. He has been both challenging and encouraging during our meetings, and would be happy to know he has made me greatly improve my knowledge of statistics! Ed Botchwey has always been a friendly face during my committee meetings; I have appreciated how he always picked up on different parts of my project than my other committee members and found ways to help me make them better. Finally, Scott Boden has been great at providing a very different clinical

perspective on my project. I often met with him one-on-one because of his busy schedule, which gave me ample time to pick his brain for ideas on how to improve my experiments. He was willing to discuss both the big picture and minute details of my experiments, and he challenged me to keep the overall clinical goal of my project in mind.

Next, I'd like to thank the McDevitt and Guldberg labs for over five years of fun and hard work. As a co-advised student, I was also fortunate to become a part of two very collaborative, close-knit labs (and gain twice as many friends!). Both of these labs are filled with people who are passionate about the work they do, and more than willing to help others both inside and outside of the lab. When I first started graduate school, I spent the majority of my time working in the McDevitt lab. Ken Sutha, Barbara Nsiah, Andres Bratt-Leal, Alyssa Ngangan-Kitchel, and Priya Baraniak (the oldest and wisest lab members) only overlapped with me for a few months, but spent those few months teaching me and the other new students the ropes of lab work and (more importantly) lab traditions. I am especially grateful to Melissa Kinney for all the help she provided on papers, proposals, and experiments; I enjoyed talking with her about the path to becoming a professor (as I'm sure she'll make an excellent one!), and I continue to keep in touch and ask her advice. Jenna Wilson and Anh Nguyen have been great friends as well, introducing me to all kinds of fun Atlanta events and great Atlanta food. Doug White has always been a friendly face in the cell culture room and was the first person to help me get a grasp on the daunting idea of incorporating computational modeling into my work. Denise Sullivan, Alex McKinlay, and Olivia Burnsed brightened up the office with their antics, and it was great to have Denise's help when we first started troubleshooting the stem cell morphogen characterization. I enjoyed watching the newer

students, Chad Glen (fellow Canadian!) and Jessie Butts, start their projects over the last few years and can't wait to see the exciting results to come. I would also like to thank Yun Wang, Alex Ortiz, and Marissa Cooke, who helped me with countless things over the years – from paper writing to experiments to finding mysteriously misplaced objects in the lab – they made a number of difficult tasks less tedious. Finally, I would like to thank Tracy Hookway for the immense amount of work she put in to help the co-advised students at Georgia Tech during the lab transition to San Francisco; she was always available to help us with the logistics of staying behind and I'm very grateful for that.

Then, of course, there's the Guldberg lab. Despite having spent the majority of my first two years in grad school working in the McDevitt lab, the Guldberg lab also welcomed me with open arms. They provided me great feedback at all of my lab meeting presentations, which initially only involved chemistry; and, despite probably wondering when I was ever going to test something in an animal model, they always listened thoughtfully and still managed to provide me with great ideas for this project outside of their area of expertise. Despite being at the busy end of their grad school careers, Brent Uhrig and Chris Dosier taught me a lot about the animal models used by the lab. Nick Willet and Laxmi Krishnan both patiently took the time to teach me the segmental defect surgery and constantly cheered me on during the different phases of my project; Laxmi was a wealth of knowledge and new ideas during the *in vivo* phases of my research. Alice Li, Ashley Allen, and Tanu Thote were probably three of the main reasons I joined in the lab in the first place – their infectious enthusiasm and positive outlooks always made the lab a great place to be. Jason Wang and David Reece have also been great labmates and friends, always smiling and willing to help with surgeries – I look forward to hearing

about their own upcoming defenses. Lauren Priddy has also been a much-needed friend to share experiences and advice about working in academia; I'm excited to see what amazing things she'll do as a professor. Giuli, Albert, and Brennan make sure the Guldberg lab keeps having fun, while also being some of the most helpful people in the lab. I missed having Giuli as a desk mate while she was in Ireland! I've also really enjoyed working with the newer students – Brett Klosterhoff, Marissa Ruehle, Ryan Akman, and Lina Mancipe Castro. Their enthusiasm for learning new things makes me eager to pass on my knowledge, and it's been great to watch them get more comfortable with surgeries and see their research start to take off. They have also been a great help to me in the last few months of my Ph.D. with their willingness of help with my surgeries and even enduring evening/weekend alginate prep (Brett and Marissa!). I am also especially grateful to Hazel Stevens, Angela Lin, and Vivian Johnson for their continued support of the lab. Vivian usually has an entertaining story when I stop by her office and has repeatedly managed to find those magical times when both Bob and Todd are available for meetings. Angela has solved many of my micro-CT and mechanical testing crises, and I'm looking forward to her becoming the new heparin microparticle expert. Hazel Stevens has made everything run smoothly for me since I first started in the lab. In addition to being hilarious, she's given me so much help and advice over the years, that I cannot imagine my grad school experience without her. Finally, I would like to thank the PRL staff for taking care of our animals, guiding me through the ins and outs of post-surgery care, and dealing with all sorts of unexpected issues. Perhaps the most nerve-wracking part of my Ph.D. was discovering two of my rats had given birth to nine rat

babies before surgery (yikes!); even then the PRL staff managed to sort everything out and save the day.

During my time at Georgia Tech, I have also had the opportunity to work with a lot of amazing people outside of the grad students in my labs. Several undergraduate students, including Patrizia Grob, Camden Esancy, Nikhil Gupte, and Catherine Chou, all contributed in a big way to the work presented within this dissertation. Their excitement for learning new things made teaching them a great experience and one of the parts of grad school that I enjoyed the most. Catherine in particular worked with me for two years and learned countless new techniques to run every kind of experiment with me. I'm proud of the progress she made in the lab and know that her dedication and drive will allow her to continue to do great things. I was also lucky enough to work on a number of collaborative projects that broadened my area of expertise and exposed me to new areas of research. Johanna Smeekens from Ronghu Wu's lab performed all of the mass spectrometry analysis within this work and was eager to help and willing to troubleshoot techniques. Tel Rouse was instrumental in building the COMSOL framework for the computational model; together, we spent months developing this aspect of my project, and I'm grateful for his commitment and patience. I was also lucky to work with my good friend Alex Schudel on the capillary tube experiments; he was always enthusiastic to try new things and fun to work with – I've learned a lot from him in just a year! Working with Alex also meant spending a lot of quality time in the Thomas lab with Nate Rohner, Erin Edwards, and David Francis, and I know I'll miss their antics.

In addition to those I've worked with directly during the course of my Ph.D., there are others who have helped me along my career path in different ways. I would like

to thank Dr. Arin Sen at the University of Calgary for taking me on as an undergraduate student when I didn't know anything about stem cells at all, and giving me the personal attention I needed to first learn how to do research. His passion for teaching, science, and engineering is what motivated me to keep working in the lab and eventually apply to graduate school. Similarly, his graduate students Helen Hardiman and Imran Ratanshi provided me invaluable support and mentoring, and I feel very fortunate to have worked with them. I would also like to thank my funding sources, the Natural Sciences and Engineering Research Council of Canada (NSERC) and the Philanthropic Education Organization (P.E.O.). The women of Georgia's P.E.O. Chapter B in particular have been incredibly supportive over the past year when I needed it most. I have enjoyed working more closely with their organization, as they are always genuinely interested in hearing what I'm doing and let me know they are cheering me on as I finished my degree.

I've been lucky enough to make a lot of lasting friendships during my time here in Atlanta, but a few of them deserve special mention. Spencer Ng (another fellow Canadian!) has been my foodie best friend since I started grad school. I'm proud of everything he accomplished in grad school and will miss searching for the best poutine and ramen in Atlanta with him. Josh Zimmermann, also in the McDevitt lab, falls into the many categories of labmate, collaborator, and science friend. I've enjoyed working with him and laughing with him, and I know we'll continue to be friends despite living on opposite sides of the continent. With our shared lab space, Torri Rinker, Melissa Goude, and Liane Tellier became great friends of mine very quickly. Melissa was one of the first friends I made in Atlanta and helped make it feel like home. Torri, Liane, and Alex have turned me into a board game addict, and I will miss playing games with them every

weekend. Torri has also always been a thoughtful friend, and I hope we continue to message each other in capslock when we're far apart. Ariel Kniss-James remains my favourite person to drink tea with, and I'm sure the future will be filled with many trips between Toronto and Nashville. And finally, Reggie Tran has been an incredibly generous friend throughout the last five years, and has always been there for me, whether it was driving me around when I didn't have a car for the first 6 months of grad school, pet-sitting my feisty cat (whom he convinced me to get in the first place), or late night conversations at McDonald's. I am also grateful for the friendship of many other people I met over the last five years, including Jennifer Lei, Matthew Priddy, Pete James, Tom Bongiorno, Stefany Holguin, Phil Keegan, Shalini Saxena, and many others. I know grad school would not have been the same without my friends, and I can't thank them enough.

I would also like to thank my family – my mom and dad, grandparents, and sister. My family has always supported me throughout my academic career and never doubted that I could do whatever I put my mind to. They encouraged me to apply to Georgia Tech even though it was so far from home, and came to visit me as often as they could. My dad, who is a professor himself, reads all of my papers and proposals and tries to be my third advisor; it's been fun to share the experience of grad school with him. My mom is almost as attached to Atlanta as I am, and has come to visit me for my birthday (and cook delicious food for my friends!) every year since I've been here. She is always excited to hear about my work. My grandparents make sure to call me twice a week to see how I'm doing (and how my rats are doing) and always send me back to Atlanta with as much food as I can carry. Being teachers themselves, they have inspired me to be a teacher and mentor to others. Finally, my sister Christine has been responsible for buying me new

clothes and keeping me well dressed throughout all of grad school. More importantly, she is always there to talk when I need her, despite the distance. In the time that I've been away from home, she's accomplished a lot, and I'm proud of her.

Last but not least, I have to thank my fiancé Matt. After almost 11 years together (6 of which have been long distance!), he has an astonishing amount of patience. He encouraged me to apply to grad school in the United States despite knowing that it would mean years of long distance, and always made me feel like pursuing my passion was the right choice. He has not only supported me from afar, but has gotten to know my research almost as well as I know it myself. He has read every one of my papers and proposals (as well as the entirety of this thesis), has listened to me practice all of my conference presentations over Skype, and (much to my chagrin) is constantly critiquing my use of statistics. He is the smartest and kindest person I know, and I feel so lucky to have him by my side.

To everyone who has helped me get to this point in my career, thank you! Looking back on the last few years has reminded me how many people have been involved in my success, and for that, I am incredibly grateful.

TABLE OF CONTENTS

LIST OF FIGURES

LIST OF TABLES

LIST OF ABBREVIATIONS AND SYMBOLS

αCT	α-chymotrypsin
α-MEM	Minimum essential medium α
δ	Half of hydrogel thickness
AF647	Alexa Fluor 647
ALP	Alkaline phosphatase
APMAm	N-(3-aminopropyl)methacrylamide
APS	Ammonium persulfate
Ang 1	Angiopoietin 1
BDNF	Brain-derived neurotrophic factor
BSA	Bovine serum albumin
BMP	Bone morphogenetic protein
C_{BMP}	Concentration of free BMP-2
$C_{BMP, Alg}$	Concentration of free BMP-2 in alginate hydrogel
$C_{BMP, Tiss}$	Concentration of free BMP-2 in tissue
C_{BMP+MP}	Concentration of BMP-2 bound to microparticle sites
C_{MP}	Concentration of unbound microparticle sites
CM	Conditioned medium/media
D	Diameter
$D_{BMP, Alg}$	Effective diffusion coefficient of BMP-2 through alginate
$D_{BMP, Tiss}$	Effective diffusion coefficient of BMP-2 through tissue
D_{eff}	Effective diffusion coefficient
DMEM	Dulbecco's modified eagle medium
DMF	Dimethylformamide
EB	Embryoid body
ECM	Extracellular matrix
EDC	1-ethyl-3-(3-dimethylaminopropyl)carbodiimide
EdU	5-ethynyl-2'-deoxyuridine
erfc	Complementary error function

ELISA	Enzyme-linked immunosorbent assay
ESC	Embryonic stem cell
FBS	Fetal bovine serum
FGF	Fibroblast growth factor
GAG	Glycosaminoglycan
GDF	Growth differentiation factor
GDNF	Glial cell line-derived neurotrophic factor
H&E	Hematoxylin and eosin
HFP	Hexafluoro-2-propanol
HIF-1α	Hypoxia-inducible factor 1α
HMAm	Heparin methacrylamide
HSC	Hematopoietic stem cell
HUVEC	Human umbilical vein endothelial cell
IGF	Insulin-like growth factor
IgG	Immunoglobin
IL	Interleukin
IFN-γ	Interferon gamma γ
iPSC	Induced pluripotent stem cell
IGFBP	Insulin-like growth factor binding protein
IVIS®	In vivo imaging system
K_D	Dissociation constant
k_{off}	Dissociation rate constant
k_{on}	Association rate constant
L	Length
Lefty	Left-right determination factor
Micro-CT	Micro-computed tomography
M_t	Mass of BMP-2 in the release volume at time t
M_∞	Mass of BMP-2 in the release volume at time infinity
MP	Microparticle
MSC	Mesenchymal stem cell
NHS	N-hydroxysuccinimide

NGF	Nerve growth factor
NSC	Neural stem cell
NT-3	Neurotrophin 3
PBS	Phosphate buffered saline
PCL	Polycaprolactone
PDGF	Platelet-derived growth factor
PEG	Polyethylene glycol
PEG-MAL	Polyethylene glycol maleimide
PLGA	Poly-lactic-co-glycolic acid
pNIPAm	Poly-nisopropylacrylamide
PSC	Pluripotent stem cell
$R_{BMP,Alg}$	Rate of BMP-2 appearance/disappearance in alginate
ROI	Region of interest
RSA	Rat serum albumin
SCF	Stem cell factor
SDF-1	Stromal cell-derived factor 1
SDS-PAGE	Sodium dodecyl sulfate polyacrylamide gel electrophoresis
SEM	Scanning electron microscopy
Sulfo-NHS	N-hydroxysulfosuccinimide
t	Time
TEMED	*N,N,N',N'*-Tetramethylethylenediamine
TGF-β	Transforming growth factor β
TNF-α	Tumor necrosis factor α
TPO	Thrombopoietin
UCM	Unconditioned medium/media
VEGF	Vascular endothelial growth factor
VOI	Volume of interest
VS750	Vivotag 750
Wnt	Wingless type

SUMMARY

An astonishing number of patients are admitted to hospitals in the United States each year with musculoskeletal injuries. Of the 6.3 million fractures that occur annually in the U.S., approximately 1 million result in more complicated skeletal defects that require additional intervention to achieve normal healing [1]. Skeletal autografts and allografts remain the current gold standard for treating large bone defects, with over 500,000 being performed in the United States annually at a cost of $2.5 billion/year to the medical system [2]. However, bone grafting techniques suffer from a number of limitations, including low tissue availability, donor site morbidity, insufficient engraftment, and host immune rejection – all of which contribute to the need for multiple revision surgeries in as many as 15% of bone grafting procedures annually [1].

The discovery and pharmaceutical production of osteogenic proteins such as bone morphogenetic protein-2 (BMP-2) has revolutionized the treatment of large bone defects by providing a means to stimulate endogenous repair mechanisms to regenerate damaged bone [3-5]. Despite the promise of this approach, clinical approval for BMP-2 treatment using a collagen sponge delivery vehicle has thus far been limited to a few select applications. Furthermore, the widespread off-label use of BMP-2 coupled with poor dose control in the clinic has contributed to an increase in adverse events, eventually leading to a number of lawsuits being filed again Medtronic for its INFUSE® BMP-2 delivery vehicle between 2006-2012. The side effects associated with BMP-2 have been attributed to both the suprahysiological BMP-2 doses required to initiate healing (≥0.2 mg BMP-2/kg body weight) [6] and use of a collagen sponge delivery vehicle that

demonstrates low affinity for BMP-2. Thus, there is a clear need to develop biomaterials to improve the efficacy of BMP-2 delivery while minimizing the negative side effects associated with rapid growth factor release.

The goal of this work was to address the shortcomings of current growth factor treatment strategies for large bone defects by creating a versatile biomaterial delivery vehicle that could (1) improve current delivery strategies for clinical BMP-2 treatment, and (2) integrate novel approaches for the delivery of multiple growth factors for better targeting bone repair. We harnessed the high growth factor binding capacity of the glycosaminoglycan heparin to fabricate an affinity-based biomaterial delivery vehicle capable of accomplishing both aspects of this goal.

First, we developed a method to fabricate pure heparin microparticles from a modified cross-linkable heparin species and demonstrated the ability of these microparticles to retain bioactive BMP-2 (Chapter 3). Following *in vitro* success, we incorporated these microparticles into a previously characterized tissue engineering construct consisting of an RGD-functionalized alginate hydrogel and polycaprolactone nanofiber mesh tube for investigation of both ectopic mineralization and orthotopic bone healing at low BMP-2 doses (Chapter 4). We next developed a computational model to provide insight into the effect of heparin microparticles on BMP-2 release *in vivo* and help inform future experiments in the femoral defect model (Chapter 5). Taken together, this work revealed that the high affinity of heparin microparticles for BMP-2 resulted in attenuated BMP-2 release *in vivo*, resulting in reduced bone formation in the femoral defect when low BMP-2 doses were used.

Consequently, in Chapters 6 and 7, we shifted our focus to evaluating heparin microparticles for high dose BMP-2 delivery, as a method to improve spatial localization of bone formation at clinical BMP-2 doses. We demonstrated that, when high doses of BMP-2 were delivered *in vivo* using heparin microparticles mixed into the alginate hydrogel, bone formation could be better localized within the defect space and the incidence of heterotopic bone could be reduced (Chapter 6). However, when we incorporated empty heparin microparticles into the PCL nanofiber mesh as a barrier to BMP-2 diffusion, we found that this method was ineffective for reducing heterotopic bone formation (Chapter 7). This led to further *in vitro* investigation into the effects of competitive binding of serum components on BMP-2-heparin interactions.

Finally, we conducted a series of experiments to evaluate the efficacy of heparin microparticles as a biomaterial vehicle to sequester and deliver multiple proteins from a complex solution (Chapter 8). Since previous studies have demonstrated that embryonic stem cell conditioned media contain a variety of potent biomolecules capable of influencing cell fate [7, 8], we investigated the *in vitro* delivery of stem cell morphogens as a first step in developing morphogen-laden microparticles as a novel approach to tissue regeneration. The promising effects observed on cell growth and differentiation suggested that the delivery of stem cell morphogens could one day be explored as an alternative method for tissue regeneration. Overall, the studies completed within this thesis broadened current understanding of bone tissue engineering, affinity-based biomaterials, and stem cell-based therapeutics, and provided valuable information that could be used to develop heparin-based biomaterials for other tissue regeneration applications.

CHAPTER 1: INTRODUCTION

1.1 Motivation

Musculoskeletal injuries resulting in significant bone loss affect thousands of people each year. Given the limited success of current bone grafting treatments, the delivery of osteoinductive growth factors, such as bone morphogenetic protein-2 (BMP-2), offers a promising means of stimulating endogenous repair mechanisms to heal injured bone. However, clinical application of growth factor therapy is hindered by the lack of adequate biomaterial delivery vehicles to provide the sustained growth factor presentation necessary to induce repair. Current growth factor delivery approaches using a collagen sponge scaffold often rely on supraphysiological concentrations of BMP-2 (≥0.2 mg BMP-2/kg body weight) [6] to stimulate bone healing. Such high concentrations of a single growth factor do not recapitulate the natural bone healing cascade, and, when rapidly released from the defect site, can result in excessive inflammation and heterotopic ossification [9]. Thus, there is a clear need to develop biomaterials to improve the efficacy of growth factor delivery while minimizing the negative side effects associated with rapid growth factor release.

Affinity-based growth factor delivery systems have demonstrated promise in a number of tissue regeneration applications due to their tunable ability to noncovalently immobilize and present proteins of interest [1, 10, 11]. Glycosaminoglycans (GAGs), such as heparin, have a natural binding capacity for a number of growth factors influential in tissue development and repair and can be incorporated into a variety of

biomaterial scaffolds to create affinity-based delivery vehicles. Growth factor binding to heparin is mediated by reversible electrostatic interactions, resulting in promiscuous protein binding that can be harnessed for the delivery of single or multiple growth factors, including biological cues to initiate and resolve the stages of bone healing. Consequently, heparin-based delivery systems can be utilized for both (1) improving current delivery strategies for clinical BMP-2 treatment, and (2) developing novel approaches for the delivery of multiple growth factors for better targeting bone repair.

The therapeutic delivery of combinations of growth factors may improve tissue regeneration outcomes by providing several, specific biological cues to endogenous cell populations at different stages of repair. Therefore, the second major focus of this project was to evaluate the efficacy of pluripotent stem cell morphogens as a source of potent growth factors for tissue regeneration. Pluripotent stem cells (PSCs) secrete many heparin-binding growth factors during differentiation, which have been implicated in tissue regeneration following stem cell transplantation and may provide essential biological cues [11]. Thus, heparin-based delivery systems could also be used to concentrate and deliver PSC-derived morphogens to tissue injury sites, thereby overcoming challenges associated with stem cell transplantation, such as low cell engraftment, immune rejection, and tumorigenicity.

Ultimately, the ***long term goal*** of this work is to engineer affinity-based strategies to improve single and multiple growth factor delivery for bone repair. The ***overall objective*** of this project was to develop heparin-based microparticles for the enhanced delivery and presentation of growth factors to regenerate and spatially localize bone in a critically sized femoral defect. The ***central hypothesis*** of this project was that growth

factor-loaded heparin microparticles would increase retention of bioactive growth factors both *in vitro* and within the tissue injury site, leading to enhanced cellular responses and improved bone repair. This hypothesis was based upon the well-documented ability of heparin to bind and retain various growth factors without hindering bioactivity; it was tested through the following specific aims:

1.2 Specific Aims

Specific Aim 1: Engineer heparin-based microparticles for growth factor delivery. The *working hypothesis* of this aim was that heparin microparticles would enhance stable retention and controlled presentation of bioactive growth factors – specifically BMP-2. Heparin microparticles were fabricated via thermal cross-linking of methacrylamide-modified heparin. BMP-2 retention capacity was determined by loading heparin microparticles with increasing BMP-2 concentrations and measuring subsequent release. Bioactivity of microparticle-bound BMP-2 was evaluated via alkaline phosphatase (ALP) activity of skeletal myoblasts. The outcome of this aim was the establishment of a reproducible protocol for fabricating heparin-based microparticles with the ability to retain large amounts of bioactive BMP-2. These results are presented in Chapter 3.

Specific Aim 2: Evaluate the ability of heparin microparticles to deliver low and high doses of BMP-2 to a critically sized femoral defect to promote bone healing. The *working hypothesis* of this aim was that loading BMP-2 onto heparin microparticles prior to incorporation into a bulk tissue engineering construct (alginate hydrogel +

polycaprolactone nanofiber mesh) would increase growth factor retention within the defect site, resulting in higher volumes of spatially localized bone formation. Microparticle and BMP-2 retention in tissue engineering constructs were evaluated *in vivo* using fluorescently tagged heparin and BMP-2. BMP-2-mediated bone formation was investigated initially in an ectopic site, using 5 μg of BMP-2, followed by evaluation in an orthotopic bone defect site, using both a low dose (2.5 μg) and a high, clinically relevant dose (30 μg) of BMP-2. Through this aim, the enhanced *in vivo* presentation of BMP-2 achieved using heparin microparticles was determined to have utility in localizing bone formation at high BMP-2 doses, despite reducing bone formation at low BMP-2 doses in comparison to BMP-2 delivery without microparticles. These results are presented in Chapters 4 and 6. We also investigated the incorporation of unloaded microparticles into the PCL nanofiber mesh as an alternative method to spatially limit BMP-2 diffusion and localize bone formation. These results are presented in Chapter 7.

Specific Aim 3: Develop a computational model describing in vivo BMP-2 release from tissue engineering constructs containing heparin microparticles. The *working hypothesis* of this aim was that a computational model based on experimental and theoretical parameters for alginate diffusion and microparticle-BMP-2 interactions could predict BMP-2 release in experimental conditions and explain *in vivo* bone regeneration results observed. First, BMP-2 diffusion through alginate hydrogels was measured using a capillary tube diffusion method. A COMSOL computational model was then developed to simulate the delivery of various amounts of BMP-2 and heparin microparticles, as well as different heparin microparticle loading regimes. A sensitivity analysis was also

conducted to determine the impact of key parameters on BMP-2 diffusion in this model. The outcomes of this aim were the development of a novel method of analyzing protein diffusion through hydrogels and the creation of a computational model describing affinity-based BMP-2 release *in vivo*. These results are presented in Chapter 5.

Specific Aim 4: Evaluate the ability of heparin microparticles to sequester and concentrate PSC-derived morphogens for in vitro analysis and delivery to other cell populations. The *working hypothesis* of this aim was that the high growth factor loading capacity of heparin microparticles could also be used to concentrate and deliver a complex mixture of heparin binding proteins from PSC conditioned media, while minimizing the delivery of cellular metabolites and wastes. PSC aggregates were differentiated in suspension culture over 14 days, allowing for the collection of PSC conditioned media from various stages of differentiation. PSC conditioned media was then loaded onto heparin microparticles for proteomic analysis and delivered to other somatic cell populations *in vitro*, such as fibroblasts and skeletal myoblasts. PSC-derived proteins bound to heparin microparticles were found to differ based on stage of stem cell differentiation, and could influence fibroblast and myoblast growth, differentiation, and morphology. The outcome of this aim was the characterization of PSC conditioned media as a source of potent morphogens that could be harnessed and concentrated via heparin microparticles. These results are presented in Chapter 8.

1.3 Significance

This work presents significant contributions to bone tissue engineering, affinity-based biomaterial design, and the translation of stem cell-based therapeutics. The development of a heparin-based biomaterial delivery vehicle addresses current limitations in BMP-2 delivery strategies in an attempt to solve the clinical problem of bone regeneration in complex injury environments requiring surgical intervention. This innovative two-fold approach aimed to improve current growth factor delivery strategies by both creating a novel affinity-based biomaterial for clinically approved BMP-2 delivery and investigating PSC morphogens as a source of growth factors for the treatment of bone injuries. The heparin-based microparticles developed through this work have been studied herein as a BMP-2 delivery vehicle, but can also be used to facilitate the *in vitro* and *in vivo* delivery of a number of potent heparin-binding growth factors for alternative applications. Furthermore, the computational model developed to describe BMP-2 release from a tissue engineering construct, as well as the capillary tube method of determining protein diffusion through hydrogels, are both versatile tools that can benefit the design of numerous other affinity-based protein delivery vehicles, by simplifying the experimental space that must be investigated to develop a new material. Finally, the use of heparin microparticles to concentrate PSC-derived morphogens from conditioned media presents a novel approach to utilizing the paracrine effects of PSCs, while circumventing some of the typical challenges of stem cell-based therapies. This work provided new insight into the synergistic effects of PSC-derived proteins on somatic cell types *in vitro*, which may one day lead to use of this strategy for *in vivo*

tissue regeneration. Overall, this investigation of both single and multiple growth factor delivery from a single biomaterial delivery vehicle clearly demonstrates the versatility of this platform, which may be further developed for other applications in the future.

CHAPTER 2: BACKGROUND AND LITERATURE REVIEW[1]

2.1 Bone Tissue Engineering

2.1.1 Bone Structure and Function

Bone is a unique organ of the body that serves several functions, including the protection of soft organs, stabilization and load bearing capabilities of the musculoskeletal system, storage of minerals such as calcium and phosphate, and production of hematopoietic and mesenchymal stem cells from the bone marrow niche [12]. It is composed of an inorganic hydroxyapatite ($Ca_{10}(PO_4)_6(OH)_2$) fraction (70-90%) and organic collagen I fraction (10-30%) [13, 14]. Bone can be broadly categorized into two main groups based on its structure: cortical or compact bone, which forms the dense outer shell of many bones, and trabecular or cancellous bone, which has a lattice structure and is often found in the interior of many musculoskeletal structures, such as long bones and the vertebrae [15]. While the properties of these two types of bone can vary with age, disease, and mechanical environment, cortical bone is denser and ranges in porosity from 5-10%, while trabecular bone is typically more porous (75-95%) [16, 17].

The development and maintenance of bone is a dynamic process, which involves complex interplay between a variety of cell populations and soluble molecular cues. During development, long bones typically form via endochondral ossification, in which mesenchymal condensations gives way to chondrocyte-mediated cartilage formation and

[1] Modified from Hettiaratchi MH, Guldberg RE, McDevitt TC. (2016). Biomaterial strategies for controlling stem cell fate via morphogen sequestration. *Journal of Materials Chemistry B*. DOI: 10.1039/c5tb02575c

finally chondrocyte hypertrophy and bone formation [18, 19]. Alternatively, flat bones develop via intramembranous ossification, in which mesenchymal condensations differentiate directly into osteoblasts that produce mineral, bypassing the cartilage phase [18, 19]. In order to maintain established bone, mesenchymal stem cells (MSCs) from the bone marrow and osteoprogenitor cells from the endosteal and periosteal layers differentiate into mature osteoblasts and osteocytes, which secrete organic bone matrix that eventually undergoes mineralization [15]. Osteoblasts also regulate the differentiation of hematopoietic stem cells (HSCs) in the bone marrow compartment into osteoclasts, which are responsible for bone breakdown and resorption, resulting in release of minerals and bone remodeling [15, 20].

2.1.2 Bone Healing Cascade

Adult bone healing typically occurs via endochondral ossification and involves several key stages, which are broadly described as hematoma formation, inflammation, revascularization, cartilage formation and mineralization, woven bone formation, and remodeling (Figure 2.1) [1]. Immediately following a fracture, damage to the vasculature results in the formation of a blood clot (hematoma), triggering the onset of the inflammatory response and temporarily elevating levels of interleukins (ILs), tumor necrosis factor (TNF-α), and stromal cell-derived factor-1 (SDF-1) [21]. These cytokines recruit necessary mesenchymal stem cells (MSCs), inflammatory cells, and macrophages to the injury site from the periosteum, bone marrow, and circulating blood, and contribute to the revascularization of the bone defect, promoting secretion of angiogenic factors,

such as hypoxia-inducible factor 1-α (HIF-1α), angiopoietin 1 (Ang 1), and vascular endothelial growth factor (VEGF) [22-24]. During the intermediate stage of cartilage formation, the growth and calcification of cartilage within the defect site are mediated by differentiating and proliferating chondrocytes that become hypertrophic in response to VEGF and several growth factors of the transforming growth factor beta (TGF-β) family [25]. Finally, in the terminal stages of bone formation and remodeling, MSCs that have differentiated into osteoblasts deposit mineral in the presence of mitogenic and osteogenic factors, such as bone morphogenetic protein-2 (BMP-2), TGF-β3, and insulin-like growth factor-1 (IGF-1) [26, 27]. These osteoblasts also secrete cytokines such as a TNF-α, IL-1, IL-6, and IL-11, promoting the proliferation of osteoclasts, which organize the woven bone into mature, lamellar structures [27, 28]. Ultimately, the bone healing cascade is characterized by a dynamic profile of cell phenotypes and biomolecules within the bone injury site. Although the stages of bone healing are inherently different, there is significant overlap in the cellular and molecular profiles at the injury site between consecutive stages, with several growth factors being constitutively expressed at varying levels, including BMP-2, Ang 1, VEGF, TGF-β3, and IGF-1 [1, 26, 29].

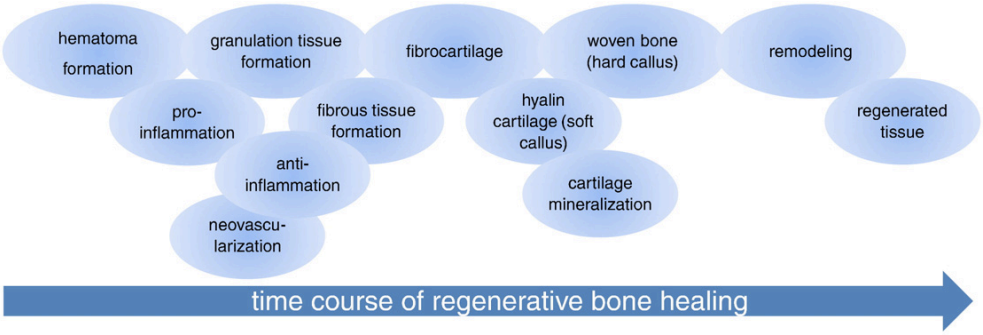

Figure 2.1. Stages of the Bone Healing Cascade. [1]

2.1.3 Incidence of Musculoskeletal Injuries and Current Treatments

Given that the bone healing cascade involves complex interplay between a variety of cell populations and signaling molecules, a mechanically challenged injury environment or imbalances in biological cues can easily disrupt the healing process and result in delayed healing and/or nonunion. Of the 6.3 million fractures that occur annually in the United States, approximately 1 million result in more complicated skeletal defects that require additional intervention to achieve normal healing [1]. Furthermore, large bone defects are not only the result of traumatic injury; they may also be caused by tumor resection, osteonecrosis, infection, and skeletal deformities – all of which result in significant loss of quality of life for the patient. Musculoskeletal injuries are also a leading cause of death and long term disability among military personnel, accounting for 50-60% of all combat injuries [30].

Despite the prevalence of severe bone loss, treatment methods to effectively regenerate damaged bone tissue and fully restore function to the affected limbs have not yet been developed. The current gold standard for treating large bone defects is the use of skeletal autografts and allografts, with over 500,000 being performed in the United States annually at a cost of $2.5 billion/year to the medical system [2]. Bone autografts are most commonly harvested from a patient's iliac crest, while allografts are often obtained from cadavers. However, these bone grafting techniques suffer from a number of limitations, including low tissue availability, donor site morbidity in the case of live bone grafts, insufficient engraftment of the tissue, and host immune rejection – all of which contribute to the need for multiple revision surgeries in as many as 15% of bone grafting procedures

annually [1]. Thus, there is a clear need to develop more effective bone repair strategies that can more reliably restore bone function and quality of life for injured individuals.

2.1.4 Clinical Recombinant Growth Factor Delivery Strategies

The identification of several key osteoinductive growth factors in the bone extracellular matrix has led to the investigation of recombinant growth factor delivery to stimulate endogenous repair mechanisms to heal injured bone [31-33]. Two recombinant human bone morphogenetic proteins (rhBMP-2 and rhBMP-7) are currently available for clinical use within absorbable collagen sponge delivery systems (Medtronic's INFUSE, Stryker's OP-1 Putty) [4]. Several successful clinical trials for anterior lumbar spinal fusions, open tibial fractures, and sinus augmentations have been completed using rhBMP-2 and have demonstrated comparable efficacy to bone grafting treatments, leading to FDA approval of BMP-2 delivery for these three specific applications [34-38].

The absorbable collagen sponge scaffold entraps rhBMP-2 through weak electrostatic interactions, resulting in a burst release of molecular cargo upon implantation in the tissue defect and low retention of BMP-2 at the site of interest [39-42]. This has led to the use of supraphysiological BMP-2 doses (≥0.2 mg/kg body weight) clinically [6] in order to ensure that an effective dose of BMP-2 remains bioactive at the site of interest. Rapid diffusion of high concentrations of BMP-2 away from the implantation site not only reduces the efficacy of orthopic bone formation within the defect site, but has also been associated with excessive vascular permeability, soft tissue inflammation, and heterotopic ossification when used "off-label" for other

bone regeneration applications, including cervical, posterior lumbar, and transforaminal lumbar spinal fusions [9, 43-45]. These detrimental effects are a combined result of both high BMP-2 concentrations and the use of biomaterial delivery vehicles that cannot effectively retain a sufficient local concentration of BMP-2 within the bone defect site. Consequently, biomaterials that provide better control over the spatiotemporal presentation of growth factors may enable the more widespread use of BMP-2 for other bone healing applications, while minimizing the negative side effects associated with rapid growth factor release.

2.2 Stem Cells and Stem Cell Morphogens

2.2.1 Pluripotent Stem Cells and PSC Secretomes

Stem cell potency defines the ability of a stem cell population to differentiate into other cell phenotypes, and ranges from pluripotent stem cells (PSCs), such as embryonic stem cells (ESCs) and induced pluripotent stem cells (iPSCs), which can differentiate into all cells of an organism, to multipotent stem cells, such as mesenchymal stem cells (MSCs), neural stem cells (NSCs), and hematopoietic stem cells (HSCs), which exhibit a more limited capacity for differentiation. ESCs are derived from the inner cell mass of a pre-implantation blastocyst and can differentiate into cells of all three germ layers, much like a developing embryo [46, 47]. Embryogenesis is a tightly regulated process, consisting of numerous cell-secreted biomolecular cues that orchestrate the complex and overlapping series of cell proliferation, differentiation, migration, and organization events

that ultimately give rise to the functioning tissues and organs of a complete organism. Considering the numerous cell fate decisions that ESCs undergo, directing ESC differentiation towards particular cell phenotypes requires the expression of many morphogens in concert and is highly dependent on cell state and the coordinated presence of other signals. As such, ESCs retain the potential to secrete a variety of potent morphogens responsible for maintaining pluripotency or promoting differentiation, and thus contribute to both embryonic and mature tissue development.

Mass spectrometry and/or antibody-based assays have been used to identify secreted proteins in ESC cultures, demonstrating the presence of many potent biomolecules, including fibroblast growth factors (FGFs), transforming growth factors (TGF-βs), insulin-like growth factors (IGFs), insulin-like growth factor binding proteins (IGFBPs), bone morphogenetic proteins (BMPs), vascular endothelial growth factor (VEGF), growth differentiation factors (GDFs), stromal cell-derived factor-1 (SDF-1), and stem cell factor (SCF) [48-52]. The signaling pathways in which these growth factors are involved play key roles in defining ESC fate, and can promote or inhibit numerous cell processes depending on stage of differentiation. For example, BMP is known to exert differential temporal effects on ESC differentiation. Early BMP signaling is required for specification towards the mesoderm germ layer and eventual mesenchymal morphogenesis [53-55]; conversely, the inhibition of BMP signaling promotes pluripotency [56, 57]. Later BMP signaling also influences the differentiation of primitive ESC-derived mesoderm towards cardiac phenotypes, as studies have demonstrated that both temporary inhibition and stage-specific activation of this pathway can promote cardiomyocyte generation [58-60]. FGF and IGF signaling pathways play

essential roles in supporting human ESC self-renewal and maintenance of pluripotency [56, 57, 61], while mouse ESCs undergo differentiation in the presence of FGFs [62]. Stable gradients of growth factors also serve important functions in ESC differentiation and embryogenesis. Gradients of VEGF in the developing embryo guide vessel development and promote endothelial cell differentiation [63], while spatially regulated FGF signaling is involved in gross embryonic patterning [64]. Taken together, these examples demonstrate the importance of ESC secreted morphogens in determining ESC fate, emphasize the conserved and divergent effects of individual morphogens on mouse and human ESC fate, and highlight the precise temporal and spatial control of morphogen presentation required to effectively maintain ESC pluripotency or activate differentiation and morphogenesis.

Similar to ESCs, iPSCs possess comparable abilities to self renew and differentiate into cells of the three embryonic germ layers and rely on many of the same signaling molecules to maintain pluripotency and direct differentiation [65, 66]. However, unlike ESCs, iPSCs are derived by reprogramming terminally differentiated, somatic cells with the overexpression of several key transcription factors [65, 66]. Although less information exists on the profiles of morphogens secreted by iPSCs in comparison to ESCs, recent studies that highlight potential benefits of iPSC secreted morphogens on other cell types may lead to further investigation in this area [67, 68].

2.2.2 Paracrine Effects of Stem Cell Morphogens

The diverse profiles of morphogens secreted by stem cell populations can influence the cell fate decisions of not only the stem cells that secrete the morphogens,

but often other cell populations within and outside of their respective stem cell niches. Morphogens such as FGFs, BMPs, IGFs, SCF, VEGF, SDF-1, and TGF-βs have far-reaching effects on basic cellular processes required by many cell types. Consequently, recent research has delved further into the use of stem cells as reservoirs of soluble factors that can act through paracrine mechanisms to influence other cell populations [69]. Delivery of ESC conditioned media containing secreted factors can stimulate the survival, proliferation, and/or migration of a variety of differentiated cell types, including muscle satellite cells, neural progenitor cells, fibroblasts, endothelial cells, and hematopoietic progenitor cells [7, 8, 51, 52]. Such effects on other cell types have been observed with conditioned media obtained from ESCs in various stages of differentiation, including undifferentiated ESCs, ESCs differentiated as adherent monolayer cells, and ESC differentiated as suspension aggregates (embryoid bodies) [7, 8, 51, 52]. Several studies have also demonstrated correlations between growth factor content and paracrine effects; for example, conditioned media collected from spontaneously differentiating embryoid bodies at later time points contained higher levels of IGF-2 and VEGF-A and induced greater endothelial cell proliferation and migration than conditioned media obtained from earlier time points [7].

Similar studies have also been conducted with MSC-conditioned media. Chen, et al. demonstrated that conditioned media collected from MSCs cultured under hypoxic conditions stimulated the proliferation of keratinocytes and endothelial cells and migration of keratinocytes, endothelial cells, and macrophages [70]. MSC conditioned media has also been used to successfully maintain the self renewal abilities and pluripotency of ESC cultures in the absence of feeder cells [71]. Furthermore, a number

of other studies have utilized MSC conditioned media or MSC co-cultures to expand and maintain the multipotency of HSC populations in vitro, hence mimicking the native MSC/HSC relationship of the bone marrow niche [72-74].

2.2.3 Stem Cell Approaches to Tissue Regeneration

Stem cells possess significant potential to cure degenerative diseases caused by cellular deficiencies and replace damaged tissues resulting from traumatic injuries. The promise of stem cell research has been further fueled by a large number of studies that have documented positive results following stem cell transplantation for various applications. However, the translation of stem cell research into viable cell transplantation technologies has been thwarted by the difficulty of obtaining large quantities of stem cells, low cell engraftment post-implantation, immune rejection, and, in the case of PSCs, the propensity to form teratomas [75]. Interestingly, despite the low persistence of transplanted stem cells within tissue injury sites, several studies have demonstrated improvements in tissue/organ function following stem cell transplantation in cardiac, neural, and bone defect environments [60, 76-78].

As such, researchers now believe that the beneficial effects of stem cell transplantation may be largely attributed to the presence of stem cell-secreted morphogens within the damaged tissue and the ability of stem cells to recruit and direct endogenous cell populations through the secretion of various soluble factors at the tissue defect site [79]. Transplanted stem cells may serve as reservoirs of secreted factors *in vivo* that can influence endogenous cell populations to repair and regenerate damaged

tissues through a variety of mechanisms. This is contrary to the traditional notion that transplanted stem cells directly contributed to tissue repair through stable engraftment and differentiation and represents a paradigm shift in the way researchers consider applying stem cells for regenerative medicine, placing emphasis on both the viability of the cells themselves and duration, amount, and efficacy of soluble factors they secrete.

Further investigation into the paracrine actions of transplanted stem cells *in vivo* has revealed improvements in heart function following myocardial infarction due to ESC-secreted VEGF, IGF-1, and IL-10 [80], axonal regeneration following spinal cord injury due to NSC-secreted NGF, BDNF, GDNF [81], and bone healing induced by the delivery of MSC conditioned media containing VEGF and IGF-1 [82]. Despite the plethora of musculoskeletal-related growth factors secreted by ESCs, such as BMPs, IGFs, TGF-βs, and VEGF, the tumorigenicity of ESCs has prevented their widespread use in animal models of bone injury without pre-differentiation into MSCs or osteoblasts [83, 84], further motivating the development of strategies employing stem cell paracrine factors. However, perhaps the most extensive research regarding stem cell paracrine effects has been conducted with MSCs transplanted for cardiac regeneration following myocardial infarction [85]. Numerous studies have demonstrated improvement in cardiac function following MSC transplantation, prompting investigation into whether these effects are paracrine-mediated. Although the mechanisms by which MSCs exert cardioprotective effects are still somewhat unknown, both *in vitro* and *in vivo* studies have revealed a role of pro-angiogenic and pro-survival MSC-secreted factors, such as VEGF, SDF-1, and IGF-1 [85-89].

2.3 Glycosaminoglycans

2.3.1 Structure and Function

The extracellular matrix (ECM) contains a variety of molecules responsible for providing structural integrity, mechanical cues, cell adhesion sites, and protein binding domains within the cellular microenvironment [90, 91]. Glycosaminoglycans (GAGs) are a class of ECM molecules composed of linear polysaccharide chains that exist both as free chains and covalently-linked components of glycosylated proteins known as proteoglycans [92, 93]. When attached to proteoglycan protein cores, the presence of multiple GAG chains in close proximity provides the dense negative charges that promote endogenous protein sequestration. Interactions between GAGs and various proteins have been extensively studied in the past, revealing that GAG–protein binding is primarily electrostatic and relies heavily on negatively charged sulfate groups within the disaccharide chains [91, 94]. Heparin, heparan sulfate, and chondroitin sulfate are all highly sulfated GAGs, and thus have a strong affinity for number of potent, positively charged morphogens, known collectively as ‘‘heparin binding proteins [93].’’ While heparan sulfate and chondroitin sulfate are somewhat less sulfated and almost exclusively found covalently attached to proteoglycans on cell membranes and in the ECM, heparin has the highest sulfation density of all naturally occurring GAGs and typically exists as free linear chains that are not bound to protein cores [91].

2.3.2 Affinity Interactions with Proteins

While many proteins interact with GAGs in a purely electrostatic manner, specific carbohydrate sequences have been identified within heparin and heparan sulfate that mediate binding with known domains on certain heparin binding proteins. Thus, the sulfation patterns displayed on different GAG species may play a significant role in determining protein binding affinity. For example, a specific pentasaccharide sequence is required for heparin binding to antithrombin III to inhibit coagulation, while a tetrasaccharide sequence is necessary for FGF-1 and FGF-2 binding [95, 96]. Likewise, specific protein sequences on FGF-1, FGF-2, and BMP-2 molecules have also been identified as being necessary for heparin binding [3, 97].

Although GAG interactions with FGFs and BMPs are the most extensively characterized, GAGs can also strongly and reversibly bind other morphogens influential in stem cell maintenance and developmental processes, including VEGF, Wnt3a, TGF-βs, IGFs, and IGFBPs [94, 98-100]. GAG binding to proteins can increase protein half-lives in *in vitro* cell cultures and *in vivo* tissues, by protecting them from enzymatic degradation and denaturing environmental agents [101-103]. Furthermore, interactions between GAGs and various growth factors have been previously shown to either enhance or inhibit a wide range of biological effects, depending on the relative concentrations of GAG and growth factor and context of interaction. This has been thoroughly investigated in the context of BMP-2-mediated osteogenesis, in which heparin has been specifically shown to extend BMP-2 half-life and enhance BMP-2/BMP receptor dimerization in some cases [101, 104], while interfering with BMP-2/BMP receptor binding and

downstream signaling pathway in others [105]. In general, higher concentrations of heparin over shorter periods of time tend to inhibit BMP-2 activity, while lower concentrations of heparin over longer periods of time promote BMP-2 signaling [105, 106]. Moreover, although soluble heparin can sequester BMP-2 away from cells to interfere with BMP-2-mediated alkaline phosphatase (ALP) activity, BMP-2 bound to similar amounts of heparin-based materials, such as microparticles, can directly interact with cell surface receptors to promote ALP activity [107].

2.4 Biomaterial Strategies for Protein Delivery and Sequestration

The natural capacity of the ECM to strongly and reversibly bind bioactive morphogens provides an attractive template for designing effective biomaterials. ECM-based, ECM-containing, and ECM-mimetic materials harness the protein sequestering qualities of the native ECM to provide biomimetic strategies for improving microenvironments for stem cell regulation and methods of morphogen delivery. Consequently, a variety of materials have been developed using this strategy and are summarized in Figure 2.2 and Table 2.1.

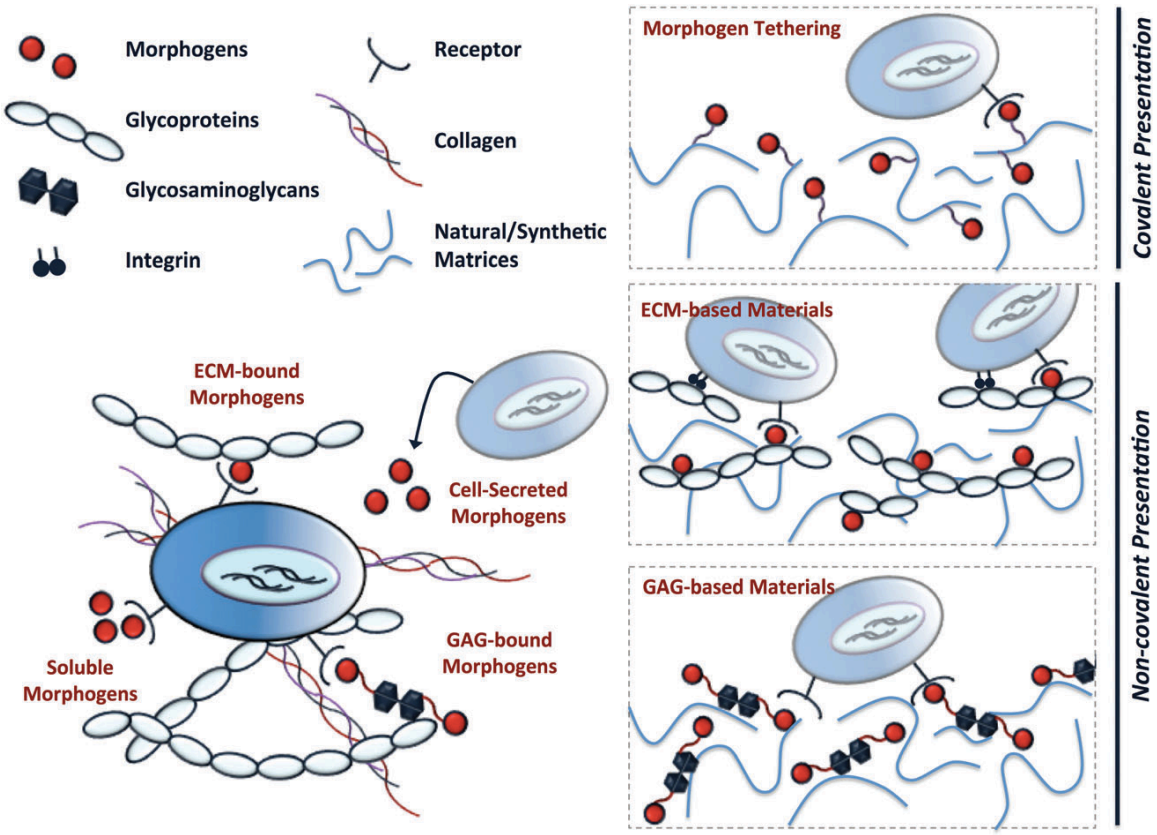

Figure 2.2. Methods of morphogen sequestration demonstrated in the cellular microenvironment (left) and employed in biomaterials for protein delivery (right). The cellular microenvironment displays soluble, ECM-bound, and GAG-bound morphogens that are typically secreted by other supporting cell types. Biomimetic materials make use of natural cell–material interactions, including both covalent morphogen presentation strategies (morphogen tethering to materials) and non-covalent presentation strategies (ECM-based and GAG-based materials).

Table 2.1. Summary of biomaterial strategies for growth factor delivery and sequestration.

Material	Growth Factor(s)	Purpose	Reference(s)
Collagen Scaffolds	BMP-2, BMP-7	*In vivo* delivery for bone regeneration	[40]
	VEGF	HUVEC proliferation	[108]
	TGF-β2	*In vivo* delivery for cell proliferation	[109]
	FGF-2, TGF-β1	MSC proliferation and chondrogenic differentiation	[110, 111]
Gelatin Microparticles	BMP-4, Noggin	Mesoderm differentiation of ESC aggregates	[112]
	BMP-4, TPO	Hematopoietic differentiation of ESC aggregates	[113]
	BMP-4, FGF-2		[114]
Heparinized Collagen/Gelatin Matrices	BMP-2	MSC osteogenic differentiation	[115]
	BMP-2	*In vivo* delivery for bone regeneration	[116]
	FGF-2	HUVEC proliferation	[117]
	BMP-4, TPO	Mesoderm/hematopoietic differentiation of ESCs	[112, 113]
	VEGF	Endothelial cell proliferation	[118]
Chondroitin Sulfate Sponges	PDGF-BB	Osteoblast migration and proliferation	[119]
Heparin-Containing Microparticles	BMP-2	C2C12 osteogenic differentiation	[107, 120]
	BMP-2, FGF-2, IGF, TGF- β3	MSC tri-lineage differentiation	[121]
Heparin-Containing Hydrogels	BMP-2	*In vivo* delivery for bone regeneration	[122]
	BMP-2	MSC osteogenic differentiation	[123]
	FGF-2	MSC proliferation	[124]
	TGF-β1	Cardiac progenitor cell proliferation, differentiation, and soluble factor secretion	[125, 126]
	No exogenous GF	MSC proliferation and osteogenic differentiation	[123, 124, 127, 128]
Heparin Mimetics	FGF-2	C2C12 proliferation and myogenic differentiation	[129]
	VEGF, FGF-2	HUVEC tube formation	[130, 131]
	NGF	Neurite extension from neural crest cells	[130]
	No exogenous GF	MSC proliferation, migration, and differentiation	[132]
	No exogenous GF	ESC pluripotency maintenance	[133]
Fibronectin Fragments	VEGF, PDGF-BB, FGFs	HUVEC, MSC, and smooth muscle cell migration, proliferation, and differentiation	[134, 135]
	BMP-2	MSC osteogenic differentiation	[135, 136]
	BMP-2, VEGF, PDGF-BB	*In vivo* delivery for bone regeneration and skin wound healing	[135, 136]
Sulfated Chitosan	No exogenous GF	ESC neural differentiation	[137]
Heparin-Binding Peptides	No exogenous GF	HUVEC proliferation	[138]
	No exogenous GF	MSC proliferation and osteogenic differentiation	[138]

2.4.1 Extracellular Matrix-based Materials

Both fibrillar ECM proteins, such as collagens, and glycoproteins, such as fibronectin, have been used to create biomimetic materials for growth factor delivery and cell culture. Collagens, with their self-assembling network structure, biodegradability, and ability to interact with cells and biomolecules, have frequently been used in a variety of applications. Perhaps the most common clinical application of collagens is as a delivery vehicle for BMP-2 and BMP-7 in the context of bone healing [40]. Porous sponges made of lyophilized Type I collagen networks are soaked in a concentrated BMP solution immediately prior to implantation, and growth factor loading occurs via electrostatic interactions between negatively charged residues on the collagen fibers and positively charged residues on BMP. When delivered *in vivo*, the porous network of the collagen sponge facilitates robust cell infiltration and degradation, while the sequestered BMP is rapidly released to promote osteogenesis. Collagen materials have also been used for protein delivery *in vitro*. The use of collagen I and collagen II hydrogels for delivery of TGF-β1 to MSC cultures has been shown to enhance chondrogenic differentiation [110]. Gelatin, which is simply denatured collagen, has been previously used as a delivery vehicle for BMP-4, thrombopoietin (TPO), and the BMP-4 antagonist noggin in ESC culture [112, 113]. Robust mesoderm differentiation was achieved with microparticle delivery of BMP-4 concentrations that were 12-fold lower than that required for soluble BMP-4 delivery, demonstrating the efficacy of this material-based protein delivery strategy [112].

As mentioned previously, collagens do not contain specific binding sites for

proteins; thus, protein binding is primarily achieved through relatively weak, electrostatic interactions that may easily be displaced by stronger, competing interactions with other biomolecules. As a result, two common approaches to improve the growth factor retention capacity of collagens have been to covalently tether biomolecules of interest to its fibers or physically incorporate other ECM molecules with specific protein binding sequences, such as glycoproteins or GAGs, into its matrix. High retention of FGF-2, VEGF, and TGF-βs within collagen matrices has been previously achieved through covalent conjugation methods, such as EDC/NHS and riboflavin/UV light-mediated cross-linking [108, 109, 111]. Despite promising outcomes observed with the use of covalently tethered growth factors, chemical modification of many proteins can attenuate their overall bioactivity by disrupting active sites for signaling, heparin binding domains, charges contributing to electrostatic interactions, and the ability of cells to internalize the molecule [139, 140]. Alternatively, many studies have investigated covalent or non-covalent addition of GAG chains to collagen matrices to enhance protein sequestration. ‘‘Heparinized’’ collagen substrates can be created by covalently tethering heparin chains to collagen films using EDC/NHS cross-linking; when loaded with FGF-2, heparinized substrates exhibited improved HUVEC proliferation compared to unmodified collagen substrates [117]. Heparinized gelatin microparticles, also fabricated using EDC/NHS chemistry, demonstrated reduced BMP-4 and TPO release compared to gelatin microparticles and stimulated greater differentiation of ESCs down the mesoderm lineage and into hematopoietic progenitors than soluble morphogen delivery [112, 113]. Heparin has also been non-covalently incorporated into collagen matrices through physical entanglement of GAG chains and collagen fibers [116, 118], leading to stable

incorporation of heparin within the scaffold, as well as attenuated VEGF release and prolonged bioactivity [118].

Aside from the presence of specific protein binding domains, other material properties can also influence the ability of ECM-based materials to deliver proteins *in vitro* and *in vivo*. For example, multiple studies have demonstrated that EDC/NHS cross-linking of collagen fibers can result in denser collagen matrices that are more resistant to collagenase-mediated degradation, and that this is also often accompanied by increased retention of molecular cargo within the collagen scaffold [111, 141]. We have previously demonstrated a similar effect of gelatin microparticles loaded with BMP-4 and FGF-2, in which increased methacrylate cross-linking density resulted in decreased morphogen release and reduced susceptibility to collagenase degradation [114].

2.4.2 Glycosaminoglycan-based Materials

The strong binding affinity of GAGs to a variety of proteins makes GAG-based materials a promising strategy for delivering morphogens with high spatial and temporal control. Numerous studies have investigated methods to fabricate biomaterials that immobilize GAG chains onto other materials or consist of modified GAG species that can be cross-linked to form pure GAG materials. The ability to maintain growth factor bioactivity and prolong growth factor half-life, while remaining biodegradable *in vivo*, provides GAGs with clear advantages as drug delivery systems. Heparin is most commonly used in GAG-based materials because of its high charge density, which confers its strong protein binding capacity, and well-studied interactions with potent

morphogens. Although chondroitin sulfate and heparan sulfate typically exhibit lower affinity for heparin binding proteins due to their decreased sulfation, biomaterials containing these GAG species have also been developed. Since chondroitin sulfate proteoglycans are abundant in cartilage ECM, chondroitin sulfate-containing materials have been frequently pursued for biomimetic cartilage tissue engineering applications [142, 143]. Moreover, given the natural anticoagulant ability of heparin, which stems from its strong affinity for antithrombin III, heparan sulfate presents an alternative GAG-based protein delivery strategy for situations in which heparin's anticoagulant activity may pose a risk [144].

Similar to methods for heparinizing collagen matrices as described above, heparin and other GAGs can be non-covalently or covalently incorporated into a number of other bulk materials, including polyethylene glycol (PEG), poly-lactic-co-glycolic acid (PLGA), chitosan, and fibrin. For example, heparin incorporation into PEG-based hydrogels can be accomplished by cross-linking methacrylamide or methacrylate-modified heparin with PEG dimethacrylate or diacrylate using free radical polymerization. Heparin incorporation into PEG hydrogels has been applied in bulk gels to enhance proliferation and osteogenic differentiation of MSCs either in the absence or presence of exogenous morphogens, such as FGF-2 and BMP-2 [123, 124, 128]. Importantly, methacrylamide and methacrylate-modified heparin species retain their ability to extend morphogen bioactivity and enhance morphogen presentation. Promising results have also been achieved with GAG incorporation into naturally derived materials such as chitosan and fibrin. Non-covalent incorporation of chondroitin sulfate into chitosan sponges has been used to modulate release of PDGF [119], while fibrin gels

containing covalently tethered heparin exhibit reduced BMP-2 release [122]. Finally, efforts have been made to fabricate pure GAG materials, such as methacrylated chondroitin sulfate nanoparticles and microparticles, in order to further maximize the growth factor holding capacity of biomaterials [145]. Low molecular weight heparin species (<8 kDa), such as fragmin, have been used in conjunction with the highly cationic peptide protamine to make GAG microparticles through stable ionic complexing, resulting in similar attenuation of FGF-2 release and enhancement of bioactivity [146]. The large number of GAG-modified materials that now exists to improve morphogen retention and enhance bioactivity highlights the broad utility of GAGs in biomaterial-based strategies for protein sequestration. Several studies undertaken by Anseth and colleagues elucidated the stimulatory effects of morphogen-laden heparin-PEG hydrogels on MSC proliferation and differentiation, showcasing dramatic increases in alkaline phosphate (ALP) activity and osteogenic gene expression in the presence of heparin-functionalized hydrogels compared to PEG hydrogels alone [124, 127]. PLGA microspheres coated with heparin-complexed FGF-2, BMP-7, IGF, and TGF-β3 have also been used as substrates for MSC culture, resulting in differential effects on MSC lineage commitment as evaluated by gene and protein expression, cell morphology, and biochemical assays [121]. Specifically, BMP-7 induced osteogenic differentiation, dual delivery of FGF-2 and IGF stimulated adipogenic differentiation, and TGF-β3 delivery resulted in chondrogenic differentiation, highlighting the versatility that heparin affords delivery systems by enhancing presentation of various morphogens contributing to tri-lineage MSC differentiation.

The sulfation patterns of GAG chains play a key role in the presentation of

morphogens, by modulating the electrostatic charges responsible for protein binding. Consequently, the ability to selectively desulfate GAG chains offers a means of manipulating morphogen binding and sequestration properties. Several studies have investigated chemical methods of desulfating GAG chains and its effects on protein binding. Fully sulfated heparin contains 2-O-sulfate, 6-O-sulfate, and N-sulfate groups, and common desulfation methods result in removal of one, two, or all of these sulfate groups [103, 115, 120]. Ratanavaraporn, et al. demonstrated that heparin chains desulfated at the 2-O-sulfate position retained more BMP-2 than native heparin and other desulfated species, and that MSCs cultured in gelatin hydrogels containing BMP-2 and non-covalently entangled 2-O desulfated heparin derivatives enhanced early osteogenic differentiation [115]. The sulfation patterns of heparin-containing microparticles can similarly modulate heparin-BMP-2 binding and subsequent BMP-2 bioactivity [120]. The importance of GAG sulfation patterns in ESC fate determination has also led to investigation into the effects of exogenous GAG addition in ESC cultures. For example, sulfating the 6-O positions of chitosan disaccharides can modulate their overall sulfate pattern and charge. When used as a substrate for ESC differentiation, sulfated chitosan can increase neural differentiation without the addition of exogenous morphogens [137].

2.4.3 Sequestration of Complex Cell-Secreted Mixtures of Proteins

The success of numerous recombinant protein binding systems for *in vitro* stem cell fate regulation and *in vivo* growth factor delivery has recently led to the development of new strategies to sequester and present soluble factors that are endogenously produced

during *in vitro* cell culture. The sequestration of endogenously secreted growth factors has long been considered a possible mechanism by which GAG-based biomaterials enhance morphogen effects on cell populations beyond the potency of the morphogens themselves; however, it is only recently that studies have attempted to more systematically test this hypothesis. The ability to capture and concentrate numerous cell-secreted and serum-borne morphogens using biomaterials may provide novel methods of more easily analyzing cell-secreted products and potentiating cell growth and differentiation through dynamic feedback between cells and biomolecules. Although this is an emerging concept in the field of stem cell engineering, several studies have begun to elucidate the effects of presenting complex mixtures of proteins on stem cell fate.

Because many morphogens are considered heparin binding growth factors, GAG-based biomaterials are prime candidates for sequestering cell-secreted proteins. Through the use of heparin-PEG hydrogels, Anseth and colleagues demonstrated the ability of GAG-based biomaterials to enhance the effects of exogenously added FGF-2 and BMP-2 on MSC proliferation and differentiation [124, 127]. Further investigation within this system next aimed to modulate the presentation and availability of both serum-borne and cell-secreted morphogens. By depleting heparin binding proteins from serum-containing media and selectively adding back in fibronectin and BMP-2, the necessity of serum-borne heparin binding proteins in inducing MSC osteogenesis as well as the role of exogenous heparin chains in concentrating fibronectin and BMP-2 was elucidated. A subsequent study investigated the role of heparin-PEG hydrogels in concentrating cell-secreted morphogens, by incorporating fluvastatin, a small molecule known to increase cellular BMP-2 secretion, into the gels [123]. The additional presence of heparin in

fluvastatin-containing hydrogels increased osteogenic gene expression, likely due to the sequestration and concentration of cell-secreted BMP-2.

Similar results have also been obtained using other strategies for GAG-mediated morphogen sequestration. Hudalla, et al. recently described the covalent tethering of a novel heparin binding peptide, derived from the heparin binding domain of FGF-2, at varying densities to oligoethylene glycol self-assembling monolayers using EDC/NHS chemistry; this peptide could sequester serum-borne heparin to subsequently modulate the presentation and availability of morphogens in culture [138, 147]. Sequestration of soluble heparin enhanced presentation of serum-borne FGF-2, resulting in increased HUVEC and MSC proliferation, and was hypothesized to similarly enhance presentation of endogenous, MSC-secreted FGFs [138, 147]. Investigation of this heparin binding peptide in osteogenic media also revealed a potential role of heparin sequestration in potentiating osteogenic differentiation mediated by MSC-secreted BMPs, corroborating results obtained by Anseth and colleagues.

Some of the latest work by Healy and colleagues further illustrates the benefits of GAG-based morphogen sequestration [125, 126]. In a recent study, hyaluronic acid hydrogels were fabricated with covalently cross-linked heparin using acrylated hyaluronic acid and cleavable peptide cross-linkers via Michael type addition. Cardiac progenitor cells (CPCs) seeded onto hydrogels containing heparin-bound TGF-β1 exhibited robust proliferation, differentiation, and formation of tubular structures. This was accompanied by dramatic increases in several matrix-bound morphogens, which contributed to endothelial cell mobilization (IGFBPs, VEGF, HGF) and vascular invasion (IL-10, endostatin), suggesting that heparin presentation both concentrated and amplified

cell-secreted signals to enhance CPC maturation. Moreover, heparin-mediated presentation of soluble signals also led to positive effects *in vivo*, where heparin-containing hydrogels enhanced CPC survival and differentiation following hindlimb implantation.

Heparin has also been used to concentrate cell-secreted morphogens in culture for delivery to primary myoblast and neural progenitor cells *in vitro*, as well as damaged tissues *in vivo* [8]. While whole ESC conditioned media induced proliferation and survival of both cell types, it was found that these mitogenic effects were mainly caused by the heparin binding fraction of the media. Heparin binding proteins were concentrated from conditioned media using heparin-agarose beads and eluted prior to *in vitro* delivery to primary myoblasts and *in vivo* delivery to sites of muscle injury. In both scenarios, heparin binding proteins enhanced proliferation, while conditioned media depleted of heparin binding proteins failed to induce proliferation of primary myoblasts in culture.

CHAPTER 3: DEVELOPMENT OF HEPARIN MICROPARTICLES FOR PRESENTATION OF BIOACTIVE BONE MORPHOGENETIC PROTEIN-2[2]

3.1 Introduction

Recombinant growth factor delivery has shown utility in a number of tissue engineering applications. In particular, bone morphogenetic proteins (BMPs), which are potent osteoinductive growth factors, have been used extensively to treat bone defects in both research and clinical settings [148-150]. However, current treatment strategies require supraphysiological levels of recombinant proteins, such as BMPs, in order to stimulate endogenous mechanisms of repair. This inefficient use of growth factor is largely due to the inability of biomaterial delivery vehicles to provide adequate sustained presentation of growth factors necessary to stimulate repair over long periods of time. Current biomaterial delivery vehicles have major limitations, such as the rapid release of molecular cargo upon deployment, causing low retention of soluble factors at the site of interest [151-153], or alternatively, covalent tethering of growth factors to delivery materials that can reduce growth factor bioactivity [154, 155]. Thus, materials with the ability to strongly, but reversibly, interact with their molecular payload are necessary, and may decrease the amount of growth factor required for such therapies, while improving physiological response.

Recently, glycosaminoglycan-containing biomaterials have become an attractive delivery method for recombinant growth factors, due to their ability to strongly bind a

[2] Modified from Hettiaratchi MH, Miller, T, Temenoff, JS, Guldberg RE, McDevitt TC. (2014). Heparin microparticle effects on presentation and bioactivity of bone morphogenetic protein-2. *Biomaterials*. 35(25): 7228-7238. DOI: 10.1016/j.biomaterials.2015.05.011

variety of growth factors in a reversible manner. Glycosaminoglycans (GAGs) are linear polysaccharide chains that bind positively charged growth factors primarily through their negatively charged sulfate groups and exist both as free chains and covalently-linked components of glycosylated proteins known as proteoglycans [91, 92]. GAGs such as heparin, heparan sulfate, and chondroitin sulfate are ubiquitous components of natural extracellular matrices (ECM) and are involved in sequestering and immobilizing growth factors within the cellular microenvironment [156-158]. Thus, GAG-based materials present the opportunity to harness the natural growth factor binding capacity of the ECM and deliver growth factors in a biomimetic manner with spatiotemporal control. Heparin, in particular, is highly negatively charged and has a strong affinity for a class of positively charged growth factors known as "heparin binding growth factors," for which specific growth factor binding sequences on heparin chains have been identified [3, 159, 160]. The non-covalent, reversible interactions between heparin and heparin-binding growth factors ensure that binding occurs with minimal impact on growth factor structure. Heparin-binding growth factors such as transforming growth factor β (TGF-β), vascular endothelial growth factor (VEGF), fibroblast growth factors (FGFs), insulin-like growth factors (IGFs), and bone morphogenetic proteins (BMPs), are especially influential in many developmental and regeneration processes, and it is thought that heparin itself may play a role in the preservation and presentation of such molecules through electrostatic interactions [161, 162].

The use of heparin and heparin-containing biomaterials for BMP-2 delivery, as well as the delivery of several other growth factors, including FGF-2, VEGF, and TGF-β2, has been widely explored in both *in vitro* and *in vivo* test beds [163-168]. Although

several studies have investigated heparin-BMP-2 interactions, the effects of heparin-BMP-2 binding on BMP-2 bioactivity have been inconsistent and depend largely on the amount of heparin and method of heparin immobilization. Previous studies have demonstrated that co-delivery of soluble heparin with BMP-2 can enhance BMP-2-mediated osteogenesis or, contrastingly, interfere with BMP-2 and BMP receptor binding to inhibit osteogenesis, depending on the cell type and culture conditions [101, 104-106, 169-171]. Nevertheless, the addition of heparin to biomaterials, including microparticles and bulk gels, has previously resulted in an improvement in growth factor retention and BMP-2-induced osteogenesis [122, 172-175]. Heparin-mediated delivery of BMP-2 has also resulted in a wide range of effects *in vivo,* with studies demonstrating variable amounts of mineralization in both ectopic and orthotopic sites [101, 115, 116, 144, 176], reflecting an inconsistent ability to form functional bone. Furthermore, the majority of these materials consist of relatively small amounts of heparin immobilized within a larger bulk material [167, 168, 177-180], which may attenuate heparin's ability to effectively bind and present growth factors. As a result, previous reports on heparin-containing biomaterials may significantly underestimate the amount of BMP-2 that can be delivered via heparin binding. Thus, improving the growth factor binding ability of heparin-containing biomaterials may enable consistent delivery of highly localized BMP-2 concentrations necessary to stimulate effective bone formation.

Herein, we present a method of fabricating pure heparin microparticles from a modified heparin methacrylamide species that can be thermally cross-linked. Physical and chemical characterization of heparin microparticles was performed, and growth factor loading and release were quantified with different BMP-2 loading concentrations.

Additionally, growth factor bioactivity was confirmed by introducing BMP-2-laden heparin microparticles to cultures of C2C12 cells and evaluating BMP-2-induced alkaline phosphatase activity, as well as changes in DNA content. Overall, this study marks a crucial first step in developing heparin microparticles as a versatile delivery vehicle and therapeutic platform for growth factor-stimulated *in vivo* tissue engineering, by demonstrating their capacity to efficiently capture and present BMP-2 to induce a potent functional cell response.

3.2 Materials and Methods

3.2.1 Heparin Methacrylamide Modification

Heparin ammonium salt from porcine intestinal mucosa (17-19 kDa; Sigma-Aldrich, St. Louis, MO) was conjugated with N-(3-aminopropyl)methacrylamide (APMAm; Polysciences, Warrington, PA) using 1-ethyl-3-(3-dimethylaminopropyl) carbodiimide (EDC; Thermo Fisher Scientific, Waltham, MA) and N-hydroxysulfosuccinimide (Sulfo-NHS; Thermo Fisher Scientific) as described in previous protocols [128, 181] (Figure 3.1A). EDC/Sulfo-NHS chemistry activates carboxyl groups on heparin for subsequent methacrylamide substitution via covalent bonds created with the primary amines on APMAm. Briefly, 325 mg of heparin ammonium salt was mixed with 10-fold molar excess of sulfo-NHS, EDC, and APMAm, in relation to heparin's carboxyl groups, in a reaction volume of 200 mL at room temperature and pH 6.5. The total reaction time was 5 hours, with a second set of 10-fold molar excess of EDC and

APMAm being added after the first 2.5 hours, to replace reactants that had undergone hydrolysis. The reaction volume was then dialyzed against 2 L of water using dialysis tubing with a molecular weight cutoff of 3500 Da (Spectrum Laboratories, Rancho Dominguez, CA) for at least 48 hours to remove excess reactants; dialysis water was replaced every 12 hours. The remaining volume in the dialysis tubing (~200 mL) was lyophilized (Labconco, Kansas City, MO) for four days.

5 mg of modified and unmodified heparin was dissolved in 750 µL deuterium oxide (Cambridge Isotope Laboratories, Tewksbury, MA) and analyzed using a Bruker Avance III 400 MHz spectrometer (Bruker Biospin Corp, Billerica, MA) for proton nuclear magnetic resonance (^{1}H-NMR) spectra analysis. ^{1}H-NMR spectra were phase corrected, baseline subtracted, and integrated using ACD/NMR processor 12.0 software. For the determination of methacrylamide modification degree, protons located at the C_1 position of heparin's disaccharide units were integrated between the chemical shifts of δ=5.0 ppm and δ=5.75 ppm and assigned a reference value of 1. However, in modified heparin, the protons of the methacrylamide groups (δ=5.41 ppm and δ=5.66 ppm) have a similar chemical shift within the aforementioned heparin integration region. Therefore, an alternate region in the heparin spectra (δ=4.0 ppm and δ=4.33 ppm) that was not affected by the presence of methacrylamide signals was selected, set to an integral of 1, and compared to the integral of the methacrylamide protons at δ=5.41 ppm and δ=5.66 ppm. By taking the ratio of the integration regions of the methacrylamide protons (δ=5.41 ppm and δ=5.66 ppm) and heparin (δ=4.0 ppm and δ=4.33 ppm), the number of methacrylamide groups per heparin disaccharide unit was determined.

3.2.2 Heparin Microparticle Fabrication

Heparin methacrylamide microparticles were fabricated using a water-in-oil emulsion followed by thermal cross-linking of the methacrylamide groups, similar to a previously developed protocol [145]. Briefly, 55.6 mg of heparin methacrylamide was dissolved in 440 μL of phosphate buffered saline (PBS; Corning Mediatech, Manassas, VA) and mixed with equimolar amounts (30 μL of a 0.3 M solution) of the free radical initiators ammonium persulfate (APS; Sigma Aldrich) and tetramethylethylenediamine (TEMED; Sigma Aldrich). Immediately after mixing, the solution was added dropwise to 60 mL of corn oil and 1 mL of polysorbate 20 (Promega, Madison, WI), and the entire mixture was homogenized on ice at 3000 rpm for 5 minutes using a Polytron PT3100 homogenizer (Kinematica, Switzerland) to create a water-in-oil emulsion. The emulsion was then submerged in a hot water bath (55ºC) and stirred to activate free radical polymerization and thermal cross-linking of the methacrylamide groups; the reaction proceeded for 30 minutes under nitrogen purging to prevent depletion of free radicals by the presence of oxygen. The solution was centrifuged at 3000 rpm for at least 10 minutes and the corn oil phase was removed. The resulting pellet of microparticles was washed once in acetone and centrifuged again (3000 rpm, 10 minutes), before undergoing several water washes to remove any excess oil or loosely cross-linked microparticles that did not settle with centrifugation. Prior to cell culture studies, microparticles were disinfected in a 70% ethanol solution for 30 minutes followed by three additional sterile water washes. The microparticles were then lyophilized for 24 hours and stored at 4ºC until use.

3.2.3 Heparin Microparticle Characterization

To visualize the microparticles, samples were incubated with 0.0016% (w/v) 1,9-dimethylmethylene blue (DMMB; Sigma Aldrich), which specifically stains sulfated GAGs, for 30 minutes at room temperature, and then washed several times with water before being imaged on a Nikon Eclipse TE2000-U inverted microscope (Nikon Instruments, Melville, NY). Microparticle size distribution was determined by using CellProfiler image analysis software [182] to evaluate images of microparticle samples. For size analysis, microparticles were stained with 0.1% (w/v) Safranin O for 30 minutes for enhanced contrast prior to imaging on a Nikon Eclipse TE2000-U inverted microscope. Images were then analyzed using a custom script on CellProfiler to quantify individual microparticle sizes. Briefly, images were loaded into CellProfiler and converted to grayscale. Microparticles were identified using the Otsu Adaptive thresholding method and the cross-sectional area of each microparticle was measured in order to estimate microparticle diameter. The number of microparticles per mg of polymer was determined using a Z2 Coulter Particle Counter with a 100 μm aperture (Beckman Coulter, Fullerton, CA). A known weight of lyophilized microparticles was resuspended in 5 mL of Isoton II diluent (Beckman Coulter) for counting. For scanning electron microscopy (SEM), 0.1 mg of lyophilized microparticles were resuspended in 70% ethanol and placed on an SEM mounting stud covered in copper tape. The samples were left at room temperature overnight to allow the ethanol to evaporate. The studs were sputter coated with gold using a Hummer 5 Gold/Palladium Sputterer (Anatech, Union

City, CA) at 140-160 mTorr and 25-30 mA. Images were taken on a FEI Nova Nanolab 200 Focused Ion Beam/Scanning Electron Microscope (FEI, Hillsboro, OR).

3.2.4 Growth Factor Loading and Release

The loading capacity of the microparticles for human VEGF (pI = 8.5), human FGF-2 (pI = 9.6), and human tumor necrosis factor alpha (TNF-α, pI = 5.3) [183-185] were investigated at a fixed growth factor concentration (10 ng/mL) and fixed microparticle amount (0.1 mg), while loading capacity for human BMP-2 (pI = 9.0) [42] was investigated over a broad range of growth factor concentrations (0.1–5000 μg/mg of microparticles) and microparticle amounts (0.02–200 μg). For comparison with gelatin methacrylate microparticles, 0.1 mg of both heparin microparticles and gelatin microparticles were incubated with a single fixed concentration of BMP-2 (10 ng/mL). All growth factors were purchased from R&D Systems. Microparticles were incubated with a single growth factor in 1 mL of 0.1% (w/v) bovine serum albumin (BSA; Millipore Corporation, Billerica, MA) in PBS, and rotated at 4ºC for 16 hours. The microparticles were then centrifuged, and the supernatant was removed and analyzed for growth factor content via ELISA (R&D Systems, Minneapolis, MN). Growth factor loading on the material was determined by subtracting the amount of growth factor remaining in solution for microparticle-containing samples from growth factor solutions rotated at 4ºC for 16 hours that lacked microparticles.

Passive release of BMP-2 into 0.1% (w/v) BSA in PBS was monitored over a period of 28 days at both 4ºC and 37ºC. Heparin microparticles (0.1 mg) were incubated

with a range of BMP-2 concentrations to obtain growth factor loading between 25 and 1000 ng BMP-2 per mg of microparticles. For comparison with gelatin methacrylate microparticles, heparin microparticles and gelatin microparticles (0.1 mg) were incubated with 25 and 50 ng/mL of BMP-2 respectively, to obtain an equal loading of 200 ng BMP-2 per mg of microparticles. At various time points over 28 days, the microparticles were centrifuged at 3000 rpm for 5 minutes, and 300 μL samples of the supernatant were removed and replaced with an equivalent volume of fresh 0.1% (w/v) BSA in PBS. Release samples were then analyzed for growth factor content via ELISA.

For investigating dual growth factor loading and release using BMP-2 and VEGF, 0.1 mg of microparticles were either (1) incubated in 100 ng of BMP-2 for 16 hours first, followed for 16 hours of incubation in 100 ng of VEGF, (2) incubated in 100 ng of VEGF first, followed by incubation in 100 ng of BMP-2, or (3) incubated in 100 ng of BMP-2 and 100 ng of VEGF simultaneously. BMP-2 and VEGF loading efficiencies, as well as displacement after loading with the second growth factor, were evaluated via ELISA of respective growth factor depleted solutions. Passive release of BMP-2 and VEGF into 0.1% (w/v) BSA in PBS was monitored over a period of 7 days at 37ºC; samples were collected and analyzed similarly to BMP-2 release experiments.

3.2.5 C2C12 Alkaline Phosphatase Activity Assay

Skeletal myoblasts (C2C12; ATCC, Manassas, VA) were cultured in growth media consisting of DMEM (Corning Mediatech, Manassas, VA) supplemented with 16% fetal bovine serum (FBS; Thermo Fisher Scientific – Hyclone, Logan, UT) and

maintained at 37ºC in a 5% CO_2 humidified incubator. For the alkaline phosphatase (ALP) activity assay, C2C12 cells were seeded in 96-well plates at an initial density of 20,000 cells per well and allowed to attach for 6 hours under growth conditions (16% FBS in DMEM). Cells were then switched to low serum media (1% FBS in DMEM), and the following treatments were added: soluble BMP-2 (5-1500 ng/mL), loaded and unloaded heparin microparticles (0.02-0.5 mg), and soluble unmodified heparin (0.1 mg). For transwell experiments, cells were cultured on the bottom compartment of a 96-well transwell plate (Corning), and microparticles were added above the polycarbonate membrane (0.2 μm pore diameter) placed on top. After 72 hours of treatment, cells were washed twice with PBS and lysed using 100 μL of CelLytic M (Sigma Aldrich). Cell lysate was stored at -80ºC prior to analysis.

ALP activity of C2C12 cultures was measured by incubating 50 μL of cell lysate with 50 μL of CelLytic M and 100 μL of a substrate solution consisting of 3.33 mM $MgCl_2$ (VWR, West Chester, PA), 500 mM 2-amino-2-methyl-1-propanol (Sigma Aldrich), and 6.67 mM p-nitrophenyl phosphate (pNPP; Sigma Aldrich). The reaction was terminated with 0.2 M NaOH after 5 minutes, and absorbance measured at 405 nm on a Synergy H4 microplate reader (Biotek, Winooski, VT). A standard curve for total ALP activity was generated using graded concentrations of the ALP product, 4-nitrophenol (0-1 nmol/μL; Sigma Aldrich).

3.2.6 C2C12 DNA Assay and Staining

DNA content of C2C12 cultures was measured using the QuantiFluor dsDNA kit (Promega, Madison, WI). Briefly, 20 µL of cell lysate were incubated with 80 µL of the assay buffer and 100 µL of the fluorescent DNA-binding dye for five minutes, protected from light. Fluorescence was measured on a Synergy H4 microplate reader (Bioteck, Winooski, VT), using an excitation wavelength of 504 nm and emission wavelength of 519 nm. Total DNA content was correlated to fluorescence by comparison to a DNA standard curve (48.5 kb). DNA fold change was determined by dividing the final DNA content after 72 hours by DNA content after 6 hours of initial cell attachment (Day 0).

C2C12 cultures were also fixed and stained with Hoechst for visualization of cell nuclei. Cells were washed twice with PBS and fixed with 4% paraformaldehyde in PBS (Alfa Aesar, Ward Hill, MA) for 15 minutes. Hoechst 33258 (50 mg/mL; Sigma Aldrich) was diluted 1:100 in 2% BSA and 0.1% polysorbate 20 in PBS and added to the cells for 15 minutes, followed by two additional PBS washes. Fixed cultures were imaged with a laser scanning confocal microscope (Zeiss LSM 700-405; Carl Zeiss Inc., Oberkochen, Germany).

3.2.7 Statistical Analysis

All data are reported as mean ± standard error of the mean. Experiments were run with three or more replicates for each experimental group. Statistical significance was determined using one-way or two-way ANOVA as appropriate, followed by Tukey's post hoc test (Systat Software, Version 12). $P < 0.05$ was considered statistically significant.

3.3 Results

3.3.1 Heparin Methacrylamide and Heparin Microparticle Characterization

^{1}H NMR indicated that approximately 50% of the carboxyl groups of heparin were conjugated with methacrylamide groups (Figure 3.1B). Heparin microparticle fabrication produced microparticles with an average diameter of 5.6 ± 4.0 µm (Figure 3.2), and approximately 1.9 x 10^{7} microparticles per mg of heparin methacrylamide polymer. SEM images of the microparticles depicted a smooth, spherical morphology (Figure 3.1C), while brightfield images revealed that the microparticles stained positively with DMMB, confirming the presence of sulfated GAGs (Figure 3.1D).

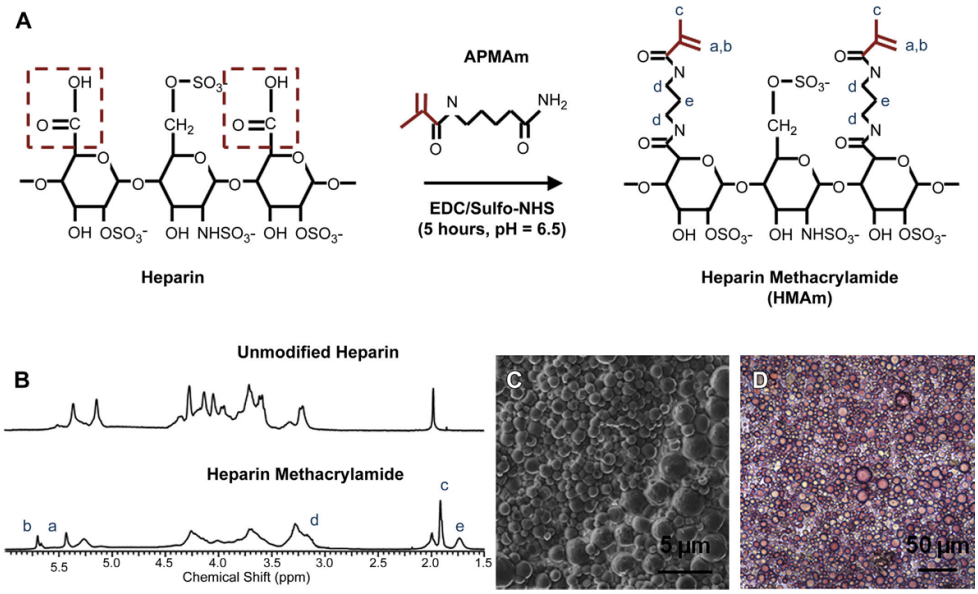

Figure 3.1. Characterization of Heparin Microparticles. A) Heparin ammonium salt was combined with excess APMAm, sulfo-NHS, and EDC to produce heparin methacrylamide (HMAm). B) ^{1}H-NMR results indicated that ~50% of carboxyl groups on heparin were substituted with methacrylamide groups. Degree of substitution was determined by comparing the integration regions of modified and unmodified heparin. C) Scanning electron microscopy image of heparin microparticles demonstrating the polydisperse and spherical nature of the microparticles. D) Image of heparin microparticles stained with 1,9-dimethylmethylene blue (DMMB), confirming the presence of heparin. Scale bars are as indicated.

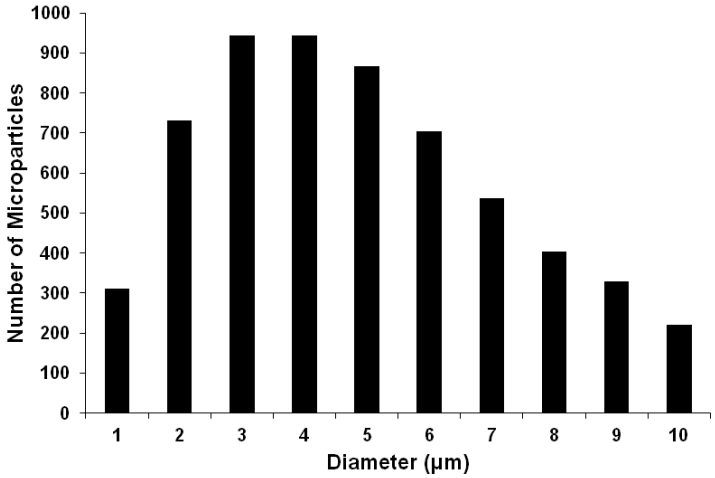

Figure 3.2. Heparin Microparticle Size Distribution. Microscope images of heparin microparticles were analyzed using a custom CellProfiler script. Microparticles exhibited a polydisperse, unimodal size distribution with an average diameter of 5.6 ± 4.0 μm.

3.3.2 Growth Factor Loading on Microparticles

Growth factors that had a net positive charge at pH = 7.5, such as FGF-2 (pI = 9.6), VEGF (pI = 8.5), and BMP-2 (pI = 9.0), were depleted from solution, and exhibited high loading (~85%) on the negatively charged heparin microparticles (Figure 3.3A). In contrast, TNF-α (pI = 5.3), which is negatively charged at pH = 7.5, was not significantly depleted from solution, with only 1.9% ± 1.1% of the added growth factor loaded onto the microparticles (Figure 3.3A), revealing that growth factor loading on heparin microparticles was dependent on electrostatic charge interaction. Additionally, when compared to gelatin microparticles, heparin microparticles loaded ~44% more BMP-2 than similarly cross-linked gelatin methacrylate microparticles (Figure 3.4A).

To further investigate the growth factor loading capacity of heparin microparticles, BMP-2 loading was measured with different amounts of microparticles (0.02-200 μg) and a fixed loading concentration of BMP-2 (20 ng/mL in 1 mL; Figure

3.3B). As expected, the percentage of BMP-2 loaded onto the microparticles increased in a dose-dependent manner with the addition of more microparticles, and nearly all of the BMP-2 was captured with >20 μg of microparticles, which loaded >95% of the added BMP-2. Conversely, the amount of BMP-2 loaded per milligram of microparticles decreased with increasing numbers of microparticles, indicating a reduced amount of BMP-2 bound per microparticle.

The relationship between microparticle loading capacity and BMP-2 solution concentration was evaluated using a fixed amount of microparticles (0.2 μg) and range of BMP-2 concentrations (0.1–5000 μg/mg of microparticles) (Figure 3.3C, D). Heparin microparticles depleted more BMP-2 from solution as the loading mass of BMP-2 was increased. At BMP-2 loading concentrations between 0.1-10 μg/mg of microparticles, the relationship between loading mass and BMP-2 bound was relatively linear, with approximately 80% of the added BMP-2 loaded onto the microparticles, regardless of loading concentration; however, as the BMP-2 loading mass increased beyond 10 μg/mg of microparticles, the percentage of BMP-2 loaded onto the microparticles decreased to <55% of the loading mass. Maximum BMP-2 loading was observed at approximately 300 μg BMP-2/mg microparticles.

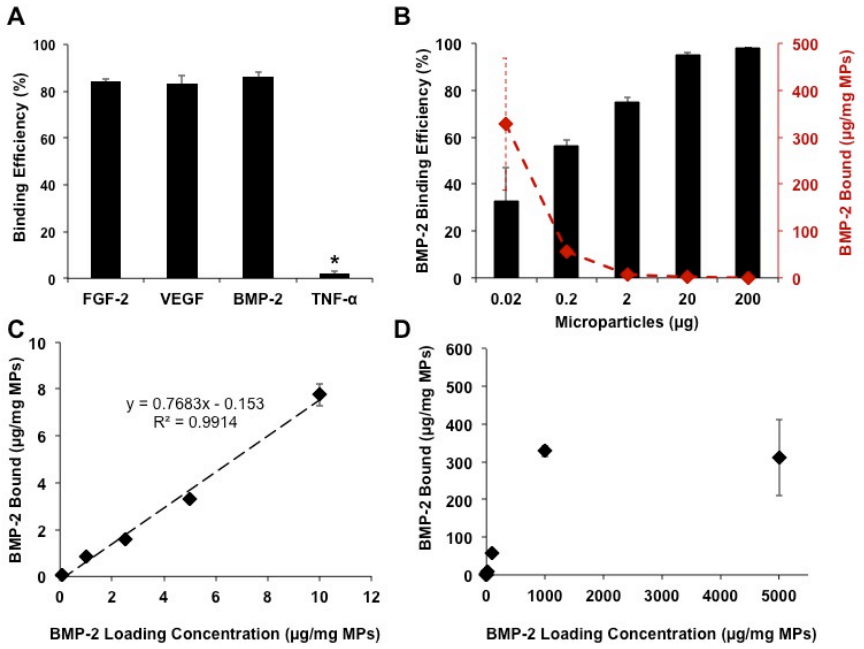

Figure 3.3. Growth Factor Loading Capacity of Heparin Microparticles. A) 0.1 mg of microparticles were incubated with 10 ng of FGF-2, VEGF, BMP-2, and TNF-α. Heparin microparticles depleted the majority of positively charged growth factors (FGF-2, VEGF, BMP-2), while negatively charged TNF-α was not depleted. (* = $p < 0.05$ compared to all other conditions.) B) Heparin microparticles were incubated with 20 ng of BMP-2. Percentage of BMP-2 depleted increased with the addition of more microparticles. Conversely, the amount of BMP-2 depleted on a per mg of microparticles basis increased with decreasing microparticle amounts. C, D) 0.2 µg of microparticles were incubated with increasing amounts of BMP-2. Heparin microparticles deplete more BMP-2 from solution as the loading mass of BMP-2 is increased. Microparticles become saturated with BMP-2 at ~300 µg BMP-2/mg microparticles.

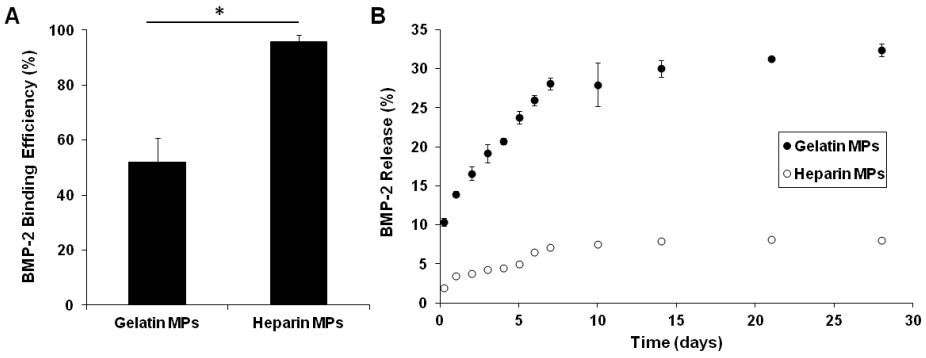

Figure 3.4. Comparison of Growth Factor Loading and Release of Heparin and Gelatin Microparticles. A) 0.1 mg of heparin methacrylamide and gelatin methacrylate microparticles were incubated with 10 ng of BMP-2. Heparin microparticles depleted more BMP-2 than gelatin microparticles. (* = $p < 0.05$ as indicated.) B) Heparin and gelatin microparticles loaded with 200 ng of BMP-2/mg of microparticles were allowed to passively release BMP-2 into at 37°C. Heparin microparticles retained more BMP-2 than gelatin microparticles over 28 days. ($p < 0.05$ between gelatin and heparin microparticles at each time point.)

3.3.3 Growth Factor Release from Microparticles

Release profiles of BMP-2 from heparin microparticles were investigated at different growth factor loading densities (25-1000 ng BMP-2/mg of microparticles) and temperatures (4ºC, 37ºC) (Figure 3.5). At both temperatures, microparticles exhibited low initial release within the first 6 hours (<10%), followed by additional sustained release over the next 4 weeks. Heparin microparticles loaded with higher concentrations of BMP-2 exhibited a greater initial release and overall cumulative release over the 28-day period than microparticles loaded at lower BMP-2 concentrations; the differences in final cumulative release were significant for release profiles at both temperatures, while the differences in initial release were significant at 37ºC. Despite drastically different BMP-2 loading (ng BMP-2/mg microparticles), the cumulative percentage of BMP-2 released was independent of loading mass and similar for all growth factor loading concentrations at 4ºC (Figure 3.5D). Total release of BMP-2 after 28 days was <20% of the loaded growth factor at 37ºC, and <25% at 4ºC, indicating that the majority of growth factor was retained by the microparticles at both temperatures. Release profiles of BMP-2 from heparin microparticles were also compared to BMP-2 release from gelatin methacrylate microparticles. When both types of microparticles were loaded with the same amount of BMP-2 (200 ng BMP-2/mg microparticles), the BMP-2 release from the gelatin microparticles at 37ºC was greater at each time point, with ~30% of the growth factor being released from the gelatin microparticles within the first seven days (Figure 3.4B).

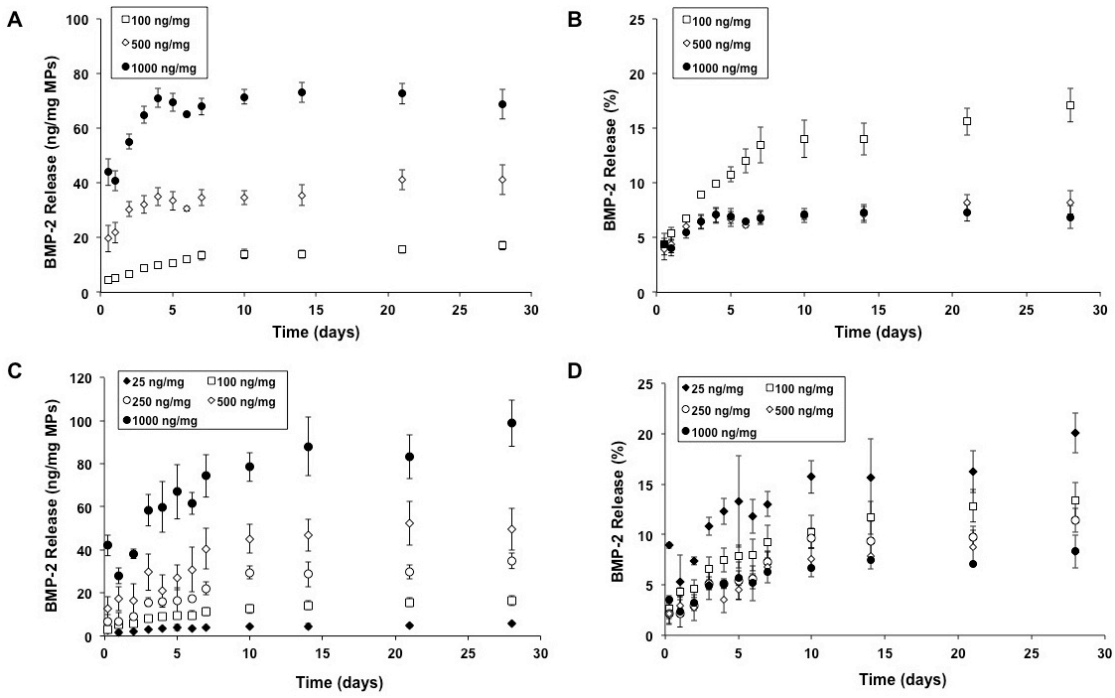

Figure 3.5. BMP-2 Release from Heparin Microparticles. Heparin microparticles were incubated with different amounts of BMP-2 to obtain loading between 25-1000 ng BMP-2/mg of microparticles. Microparticles were allowed to passively release BMP-2 into a PBS solution over 28 days. A) Release curves at 37^{o}C presented as cumulative mass of BMP-2 released per mg of microparticles show that microparticles loaded with more BMP-2 exhibit greater release over 28 days. B) Release curves at 37^{o}C presented as cumulative percent of loaded BMP-2 show that percentage of BMP-2 released highest for the lowest loading amount investigated. C) Release curves at 4^{o}C presented as cumulative mass of BMP-2 released per mg of microparticles also show that microparticles loaded with more BMP-2 exhibit greater release over 28 days. D) Release curves at 4^{o}C presented as cumulative percent of loaded BMP-2 show that percentage of BMP-2 released was independent of loading mass and similar for all BMP-2 loading densities.

3.3.4 Dual Growth Factor Loading and Release from Heparin Microparticles

The ability of heparin microparticles to deplete multiple growth factors from solution was evaluated using stepwise and simultaneous loading with BMP-2 and VEGF. Microparticles depleted more BMP-2 from solution (~95% vs. ~55%), regardless of whether microparticles were incubated in BMP-2 first, VEGF-2 first, or both simultaneously (Figure 3.6A). Furthermore, when microparticles were first incubated in BMP-2, followed by VEGF, only 3.1% ± 0.3% of the BMP-2 was displaced; however,

when microparticles were incubated in VEGF, followed by BMP-2, 15.4% ± 0.8% of the VEGF was displaced (Figure 3.6B). Finally, release profiles of dual loaded microparticles demonstrated that VEGF release from the microparticles was greater than BMP-2 release. Although there were some differences in the cumulative amount of growth factor released when BMP-2 was loaded first (Figure 3.6C), VEGF was loaded first (Figure 3.6D), or both were loaded together (Figure 3.6E), VEGF release was consistently greater than BMP-2 release at all time points and in all conditions, at ~40% overall compared to ~20% overall. This was likely due to the lower affinity of VEGF for heparin compared to BMP-2, as the dissociation constant of VEGF-heparin interactions (K_D = 40-80 nM) [94] is higher than that of BMP-2-heparin interactions (K_D = 20 nM) [3].

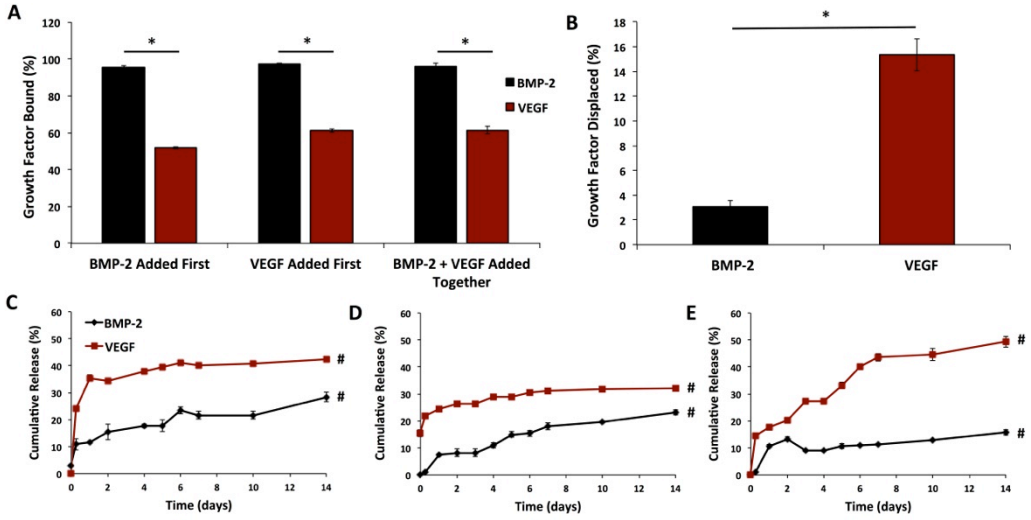

Figure 3.6. BMP-2 and VEGF Loading and Release from Heparin Microparticles. A) Both stepwise and simultaneous loading of microparticles with BMP-2 and VEGF resulted in greater BMP-2 depletion than VEGF depletion. (* = $p < 0.05$ as indicated) B) Loading with VEGF followed by loading with BMP-2 resulted in higher VEGF displacement than the BMP-2 displacement observed when BMP-2 was loaded prior to VEGF loading. (* = $p < 0.05$) Cumulative release of VEGF was higher than that of BMP-2 when A) BMP-2 was added first and VEGF was added second, B) VEGF was added first and BMP-2 was added second, and C) when both growth factors were added together. (# = $p < 0.05$ between groups at all time points.)

3.3.5 Microparticle-mediated Effects on C2C12 Alkaline Phosphatase Activity

The bioactivity of BMP-2 bound to heparin microparticles was examined using an ALP activity assay on skeletal myoblasts (C2C12). C2C12 cells were chosen as a platform to evaluate BMP-2 bioactivity, since the addition of BMP-2 to low serum culture conditions can robustly inhibit C2C12 myogenesis and enhance expression of osteogenic markers, such as ALP [186]. A fixed amount of microparticles (0.1 mg) was loaded with several BMP-2 amounts (10, 30, 100 ng) that stimulate ALP activity within the dynamic range of the cells (Figure 3.7). When normalized to DNA content, resulting ALP activity was comparable between soluble BMP-2 and loaded microparticle groups at 10 and 30 ng, and lower for the loaded microparticle group at 100 ng (Figure 3.8A). Interestingly, unloaded heparin microparticles (without BMP-2) induced a 6-fold increase in ALP activity compared to no treatment, resulting in ALP activity that was comparable to that of 10 ng of soluble BMP-2 treatment (~1 nmol pNP/ng DNA).

The effect of microparticle dose on ALP activity was also determined by culturing C2C12 cells with different amounts of microparticles (0.02, 0.1, 0.5 mg) loaded with a fixed BMP-2 dose (30 ng total; Figure 3.8B). Representative images of Safranin O-stained microparticles cultured with cells after 6 hours of attachment demonstrate differences in microparticle coverage area on a 96-well plate (Surface Area = 0.32 cm^2) (Figure 3.8C). As expected, C2C12 cells cultured with 0.02 mg and 0.1 mg of BMP-2-loaded microparticles stimulated higher ALP activity than no treatment and cells cultured with unloaded microparticles. However, 0.5 mg of loaded microparticles induced lower ALP activity that equivalent amounts of BMP-2 delivered solubly and with 0.02 and 0.1

mg of microparticles, with no difference in ALP expression between cultures containing 0.5 mg of unloaded and loaded microparticles. Interestingly, increasing the amount of unloaded microparticles dose-dependently increased ALP, and 0.1 and 0.5 mg of unloaded microparticles induced higher ALP activity than no treatment.

In order to determine whether the stimulation of C2C12 ALP activity could simply be attributed to the presence of heparin in the cultures, C2C12 cells were treated with 0.1 mg of soluble modified heparin, with and without BMP-2 (Figure 3.8D). The presence of soluble heparin alone did not stimulate an increase in ALP activity compared to unloaded heparin microparticles. Additionally, when soluble heparin was incubated with 30 ng of BMP-2 beforehand and cultured with the cells, ALP activity was attenuated compared to soluble BMP-2 and an equivalent amount of loaded microparticles (1.07 ± 0.08 nmol pNP/ng DNA compared to 1.45 ± 0.09 nmol pNP/ng DNA and 2.84 ± 0.09 nmol pNP/ng DNA, respectively).

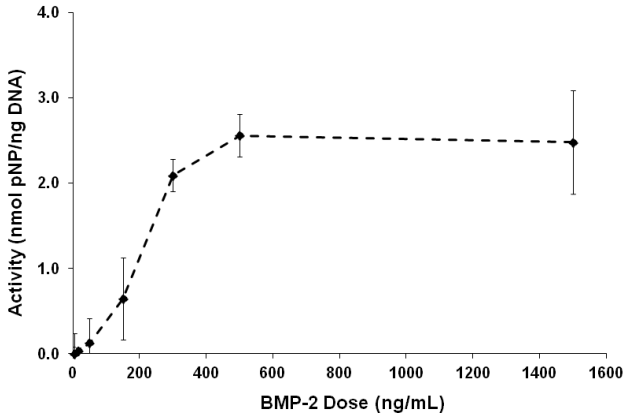

Figure 3.7. Effect of Soluble BMP-2 on Alkaline Phosphatase Activity in C2C12 Cultures. C2C12 cells were cultured for 72 hours with 0-1500 ng/mL of soluble BMP-2. Cell lysate was incubated with p-nitrophenyl phosphate substrate to determine ALP activity. C2C12 cells demonstrated a dose-dependent increase in ALP activity that plateaued at 500 ng/mL of BMP-2.

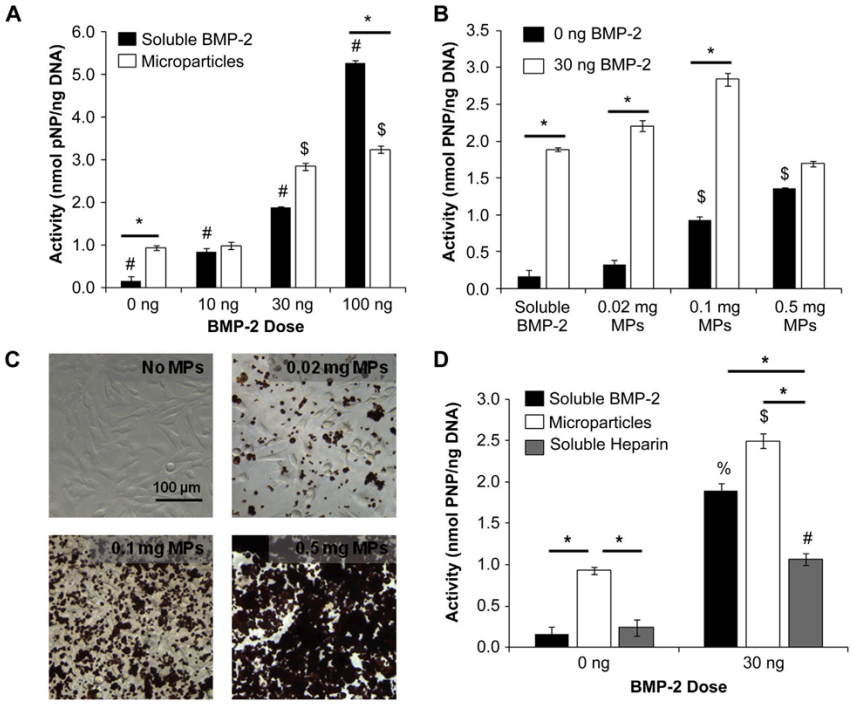

Figure 3.8. Effect of Heparin Microparticles Loaded with BMP-2 on Alkaline Phosphatase Activity in C2C12 Cultures. C2C12 cells were cultured for 72 h with each treatment. Cell lysate was incubated with p-nitrophenyl phosphate substrate to determine ALP activity and normalized to DNA content. A) 0.1 mg of microparticles pre-loaded with BMP-2 induced ALP activity in a dose-dependent manner comparable to that of soluble BMP-2 at 10 and 30 ng, and lower than soluble BMP-2 at 100 ng. 0.1 mg of unloaded MPs also induced greater ALP activity than cells without treatment. (* = $p < 0.05$ as indicated; # = $p < 0.05$ for all conditions in group; $ = $p < 0.05$ compared to unloaded MPs (0 ng)) B) C2C12 cells were cultured with different doses of microparticles (0.02 mg, 0.1 mg, 0.5 mg) that were either unloaded or loaded with 30 ng of BMP-2. Loaded microparticles induced higher ALP activity than unloaded microparticles in all cases except for 0.5 mg of microparticles. (* = $p < 0.05$ as indicated; $ = $p < 0.05$ compared to no treatment and 0.02 mg of unloaded MPs (0 ng)) C) Representative images of C2C12 cells cultured without microparticles and with 0.02 mg, 0.1 mg, and 0.5 mg of microparticles in a 96-well plate. Microparticles were stained with Safranin O for enhanced contrast. D) 0.1 mg of soluble heparin did not induce the same increase in ALP activity as 0.1 mg of unloaded microparticles. Soluble heparin in the presence of BMP-2 inhibited ALP activity compared to BMP-2 delivered solubly and via microparticles. (* = $p < 0.05$ as indicated; % = $p < 0.05$ compared to no treatment; $ = $p < 0.05$ compared to unloaded MPs (0 ng); # = $p < 0.05$ compared to soluble heparin (0 ng))

3.3.6 Microparticle-mediated Effects on C2C12 DNA Content

The DNA content of C2C12 cultures treated with a fixed number of BMP-2-loaded microparticles (0.1 mg) increased 3-4 fold over the three day culture period, while

cultures treated with equivalent amounts of soluble BMP-2 did not display any appreciable change in DNA content (Figure 3.9A), suggesting that the presence of loaded microparticles increased cell number. At a fixed BMP-2 dose (30 ng), C2C12 cells cultured with fewer loaded microparticles (0.02 and 0.1 mg) at a higher BMP-2 loading density exhibited a ~3.5-fold increase in DNA content compared to unloaded microparticle controls, whereas cells cultured with 0.5 mg of microparticles exhibited no change in DNA content (Figure 3.9B). Comparable differences in cell number were observed with Hoechst staining of C2C12 cells cultured without microparticles and with various doses of microparticles in the presence of 30 ng of BMP-2 (Figure 3.9C). This result demonstrated that BMP-2 loading density of the microparticles may determine effects on DNA content, with higher loading densities stimulating larger DNA increases.

C2C12 cells cultured with 0.1 mg of soluble heparin and 0.1 mg of unloaded microparticles both exhibited similar decreases in DNA content over the culture period, indicating that the presence of heparin alone in the system reduced cell number (Figure 3.9D). Although BMP-2-loaded microparticles induced an increase in DNA content compared to no treatment, cells cultured with soluble heparin in the presence of BMP-2 (30 ng) did not exhibit any increase in DNA content.

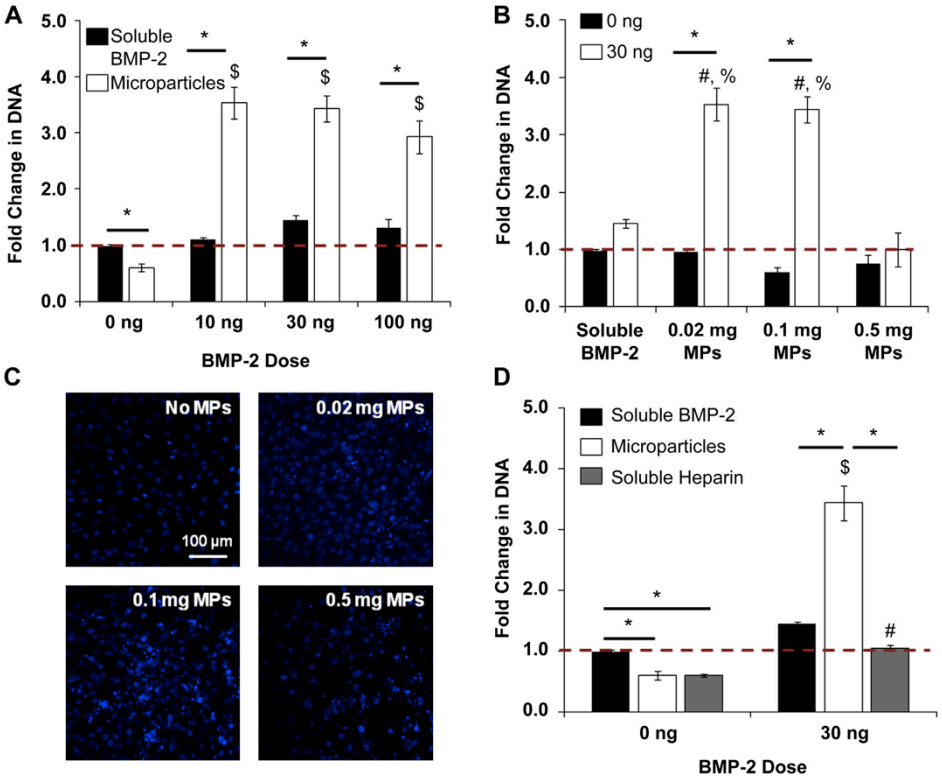

Figure 3.9. Effect of Heparin Microparticles Loaded with BMP-2 on DNA Content in C2C12 Cultures. C2C12 cells were cultured for 72 h with each treatment. Cell lysate was incubated with a fluorescent dsDNA-binding dye to determine DNA content. Fold change in DNA is presented as final Day 3 DNA content compared to initial Day 0 DNA content. A) Microparticles loaded with BMP-2 increased DNA content compared to soluble BMP-2 controls. Unloaded microparticles did not increase DNA content. (* = $p < 0.05$ as indicated; $ = $p < 0.05$ compared to unloaded MPs.) B) Cells cultured with 0.02 mg and 0.1 mg of microparticles in the presence of BMP-2 both exhibited an increase in DNA content compared to unloaded microparticle controls, while cells cultured with 0.5 mg of microparticles did not. (* = $p < 0.05$ as indicated; # = $p < 0.05$ compared to soluble BMP-2 (30 ng); % = $p < 0.05$ compared to 0.5 mg MP (30 ng)) C) Representative images of cells cultured without microparticles and with 0.02 mg, 0.1 mg, and 0.5 mg of microparticles in the presence of 30 ng of BMP-2 for three days. Cell nuclei were stained with Hoechst. D) Cells cultured with soluble heparin without BMP-2 displayed similar DNA content compared to cells cultured without treatment and with unloaded microparticles. Cells cultured with soluble heparin in the presence of BMP-2 did not exhibit an increase in DNA content. (* = $p < 0.05$ as indicated; $ = $p < 0.05$ compared to unloaded MPs; # = $p < 0.05$ compared to soluble heparin (0 ng))

3.3.7 Contact-mediated Effects of Microparticles on C2C12 Cultures

In order to determine whether the observed effects of heparin microparticles on C2C12 ALP activity and DNA content were contact-dependent, heparin microparticles were physically separated from the cells by a transwell membrane and added without BMP-2 or with 30 ng of BMP-2 (soluble or pre-loaded; Figure 3.10A). The presence of unloaded microparticles in direct contact with the cells increased normalized and total ALP activity compared to both no treatment and physically separated unloaded microparticles (Figure 3.10B, D). In BMP-2 treatment groups, ALP activity normalized to DNA content was similar between cells in direct contact with the microparticles and physically separated from the microparticles, regardless of whether the BMP-2 was added solubly or loaded onto the microparticles (Figure 3.10B). However, total ALP activity of C2C12 cultures physically separated from the microparticles was lower than that of direct contact cultures (Figure 3.10D). This was due to the fact that transwell separation of cells and microparticles in the presence of soluble or loaded BMP-2 did not affect DNA content over the culture period, while cultures in which the cells and microparticles were in direct contact exhibited significant DNA increases (3-4 fold; Figure 3.10C). This indicated that the changes in DNA content were contact-mediated. Similarly, while cells cultured in direct contact with unloaded microparticles exhibited a decrease in DNA content over three days, there was no change in DNA content when the cells and unloaded microparticles were physically separated from each other.

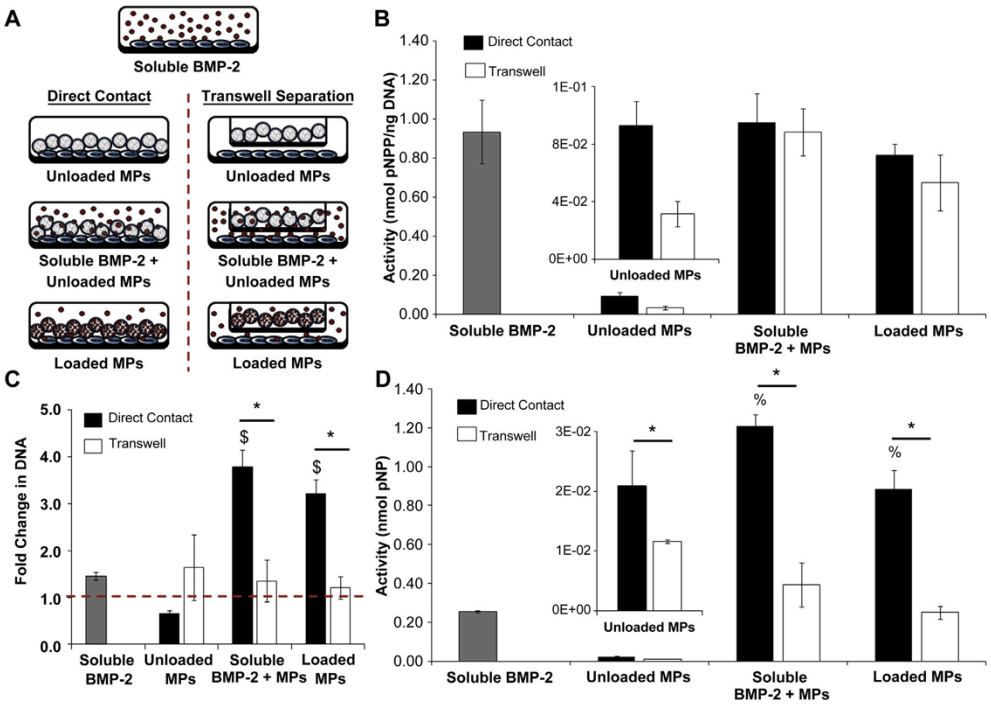

Figure 3.10. Contact-mediated Effect of Heparin Microparticles on Alkaline Phosphatase Activity and DNA Content in C2C12 Cultures. C2C12 cells were cultured for 72 h with each treatment. Cell lysate was incubated with p-nitrophenyl phosphate substrate to determine ALP activity and incubated with a fluorescent dsDNA-binding dye to determine DNA content. Fold change in DNA is presented as final Day 3 DNA content compared to initial Day 0 DNA content. A) Schematic indicating the conditions investigated with cells and microparticles in direct contact and physically separated. B) Normalized ALP activity of cells incubated with microparticles in direct contact and physically separated were comparable to each other and soluble BMP-2 treatment, regardless of whether the BMP-2 in the culture was added solubly or pre-loaded onto the microparticles. Normalized ALP activity of cells in direct contact with unloaded microparticles was higher than that of cells separated from unloaded microparticles. C) Cells cultured in the presence of both BMP-2 and microparticles physically separated from the cells by a transwell demonstrated lower DNA content than cells cultured in direct contact with microparticles and in the presence of BMP-2. (* = $p < 0.05$ as indicated; $ = $p < 0.05$ compared to unloaded MPs) D) Total ALP activity of cells in direct contact with the microparticles was higher than that of cells that were separated from the microparticles via transwell insert and soluble BMP-2 treatment alone. Total ALP activity of cells in direct contact with unloaded microparticles was also higher than that of cells separated from unloaded microparticles. (* = $p < 0.05$ as indicated; % = $p < 0.05$ compared to soluble BMP-2)

3.3.8 Long-term Bioactivity of Microparticle-bound Growth Factors

Since previous studies have demonstrated the ability of heparin to prolong the half-life of BMP-2 and maintain its bioactivity in culture [101, 172], we also evaluated whether complexing BMP-2 with heparin microparticles would result in a similar effect on BMP-2 bioactivity. We pre-incubated 30 ng of soluble BMP-2, 0.1 mg of unloaded microparticles, and 0.1 mg of microparticles loaded with 30 ng of BMP-2 in low serum media for 2 weeks at 37°C, and compared the ability of pre-incubated treatments to induce C2C12 ALP activity and cell proliferation with that of fresh soluble BMP-2, unloaded microparticles, and BMP-2-loaded microparticles. BMP-2-loaded heparin microparticles induced higher total ALP activity than unloaded heparin microparticles and soluble BMP-2 at both 0 and 2 weeks (Figure 3.11A). While the ALP activity induced by both BMP-2-loaded microparticles and soluble BMP-2 dropped significantly over the two week period of pre-incubation, there was no difference between the ALP activity induced by pre-incubated loaded microparticles and fresh soluble BMP-2; this result indicates that heparin microparticles were able to maintain BMP-2 bioactivity at a similar level as the fresh soluble protein even after a 2 week period of pre-incubation in the presence of low serum containing media. Moreover, BMP-2-loaded heparin microparticles retained their ability to increase cell proliferation in C2C12 cultures after both 0 and 2 weeks of pre-incubation (Figure 3.11B).

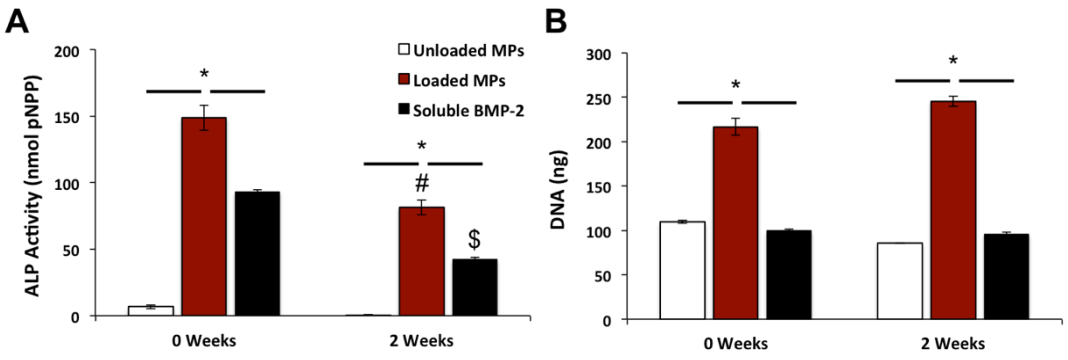

Figure 3.11 Effect of Heparin Microparticles on Long Term Bioactivity of BMP-2 in C2C12 Cultures. C2C12 cells were cultured for 72 h with each treatment. Cell lysate was incubated with p-nitrophenyl phosphate substrate to determine ALP activity and incubated with a fluorescent dsDNA-binding dye to determine DNA content. A) BMP-2-loaded microparticles induced higher total ALP activity than unloaded microparticles and soluble BMP-2 at both time points. ALP activity induced by both BMP-2-loaded microparticles and soluble BMP-2 dropped over the 2-week period of pre-incubation. (* = $p < 0.05$ as indicated; # = $p < 0.05$ compared to loaded MPs (0 weeks); $ = $p < 0.05$ compared to soluble BMP-2 (0 weeks)) B) Treatment with BMP-2-loaded microparticles resulted in higher DNA content after three days compared to unloaded microparticles and soluble BMP-2 treatment at both 0 and 2 weeks. (* = $p < 0.05$ as indicated)

3.3.9 Reproducibility of Heparin Microparticle Fabrication Method

In order to investigate the reproducibility of heparin microparticle fabrication, ten independent batches of microparticles made from six independent batches of heparin methacrylamide were evaluated for their ability to deplete BMP-2 (50 ng) and induce ALP activity and cell proliferation in C2C12 cultures. Phase images of microparticles cultured with C2C12 cells depict similar microparticle morphology between batches (Figure 3.12A), although microparticle clumping was more apparent in some batches than in others (MP #1, #2, #6, #9). Ultimately, microparticle clumping did not result in differences in BMP-2 loading ability, and each batch of microparticles depleted ~70-85% of the added BMP-2 (Figure 3.12B), as expected. BMP-2-loaded microparticles from each batch induced more ALP activity than unloaded microparticles (Figure 3.12C).

Although the degree of ALP activity induced was variable, all but one of the microparticle batches stimulated similar or greater ALP activity (Average ALP: 120.6 ± 6.5 nmol pNPP) compared to soluble BMP-2 treatment (110.8 ± 10.6 nmol pNPP). Furthermore, ALP activity did not appear to be influenced by microparticle clumping. BMP-2-loaded microparticles also induced significant increases in C2C12 DNA content compared to soluble BMP-2 treatment (Figure 3.12D). Overall, these results demonstrate the reproducibility and robust functionality of the heparin microparticles.

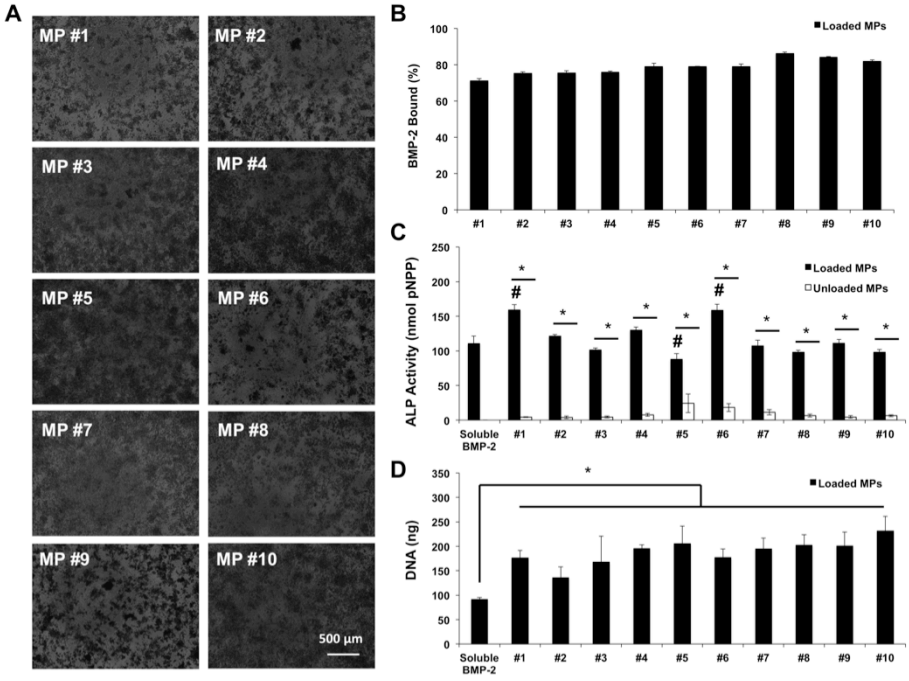

Figure 3.12. Reproducibility of Microparticle Loading and BMP-2 Bioactivity. Ten batches of microparticles made from six batches of heparin methacrylamide were evaluated for their ability to deplete BMP-2 and induce ALP activity and DNA increases in C2C12 cells. A) Phase images of 0.1 mg of microparticles cultured with 20,000 cells in 96-well plates. B) 0.1 mg of microparticles were loaded with 50 ng of BMP-2. All batches of microparticles depleted a similar amount of BMP-2 (~70-85%). C) C2C12 cells were cultured for 72 h with soluble BMP-2, unloaded microparticles, or BMP-2-loaded microparticles. Cell lysate was incubated with p-nitrophenyl phosphate to determine ALP activity. Each batch of loaded microparticles induced higher ALP activity than unloaded microparticles. (* = $p < 0.05$ as indicated; # = $p < 0.05$ compared to soluble BMP-2) D) Cell lysate was incubated with a fluorescent dsDNA-binding dye to determine DNA content. Treatment with loaded microparticles resulted in higher C2C12 DNA content after 72 h compared to soluble BMP-2. (* = $p < 0.05$ as indicated)

3.3.10 Effect of Lyophilization on BMP-2-Loaded Microparticles

Another practical consideration in developing heparin microparticles as a BMP-2 delivery system for clinical applications is the stability of both unloaded and loaded microparticles prior to use by a surgeon. Lyophilized heparin microparticles can be stored at 4°C for extended periods of time and maintain their ability to load functional BMP-2 for at least two years (Figure 3.12, Batch #1). Furthermore, heparin microparticles can be loaded with BMP-2 and lyophilized for future use. 0.1 mg of microparticles were either loaded with 30 ng of BMP-2 overnight at 4°C and lyophilized for 24 hours or freshly loaded with 30 ng of BMP-2 overnight at 4°C. Lyophilized BMP-2-loaded microparticles demonstrated a similar cumulative BMP-2 release profile to freshly loaded microparticles (Figure 3.13A), releasing slightly more BMP-2 over 7 days (24.7% ± 1.0% vs. 21.3% ± 0.3%). Moreover, lyophilized BMP-2-loaded microparticles induced robust ALP activity in C2C12 cells that was comparable to that of both soluble BMP-2 and freshly loaded BMP-2-loaded microparticles (Figure 3.13B). Lyophilized unloaded microparticles did not have an effect on ALP activity. Overall, these results demonstrate that lyophilization does not impact the bioactivity and release kinetics of microparticle-bound BMP-2, and thus BMP-2-loaded microparticles may be easily transported and stored in a lyophilized state prior to use in the clinic.

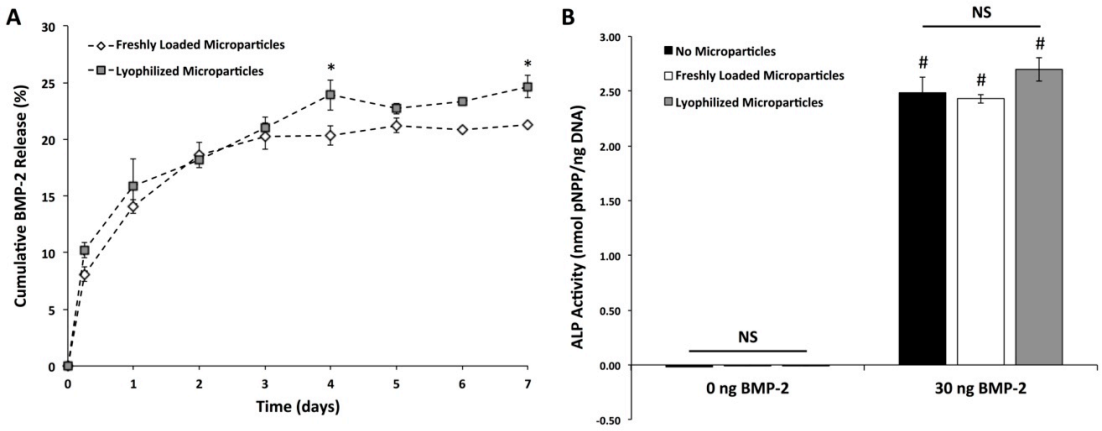

Figure 3.13. BMP-2 Release and Bioactivity from Lyophilized Loaded Heparin Microparticles. 0.1 mg of microparticles were either loaded with 30 ng of BMP-2 overnight and lyophilized for 24 hours or freshly loaded with 30 ng of BMP-2 overnight. A) Lyophilized loaded microparticles and freshly loaded microparticles demonstrated similar cumulative BMP-2 release profiles over 7 days with differences at 4 and 7 days. (* = $p < 0.05$ between groups at time point) B) Both lyophilized loaded microparticles and freshly loaded microparticles induced comparable normalized ALP activity to soluble BMP-2 treatment. Low serum media without BMP-2 or with unloaded microparticles did not induce ALP activity. (# = $p < 0.05$ compared to 0 ng of BMP-2, NS = not statistically different)

3.4 Discussion

In this study, the ability of heparin methacrylamide microparticles to bind, retain, and present bioactive growth factors *in vitro* was investigated. Heparin microparticles depleted considerable amounts of several positively charged heparin-binding growth factors (BMP-2, VEGF, FGF-2) from solution, including a high quantity of BMP-2 that exceeded the maximum reported growth factor loading capacity of other heparin-containing biomaterials by >1000-fold [115, 167, 168, 175, 187, 188] and surpassed the BMP-2 loading of gelatin methacrylate microparticles by nearly 50%. The majority of BMP-2 loaded onto heparin microparticles at various concentrations (25-1000 ng BMP-2/mg microparticles) was retained within the hydrogel matrix, with <25% of the growth factor being released over 28 days. Heparin microparticles could also simultaneously

bind and release different amounts of multiple growth factors (BMP-2 and VEGF), in a manner related to their relative affinities for heparin.

BMP-2-loaded microparticles stimulated ALP activity in C2C12 cells comparable to soluble BMP-2 treatment at multiple BMP-2 and microparticle doses, demonstrating that microparticle-bound BMP-2 maintained its bioactivity under conditions of low release. Moreover, in addition to inducing ALP activity, BMP-2-loaded microparticles also stimulated a striking contact-mediated increase in DNA content over the three day culture period, which was inhibited when cells and microparticles were physically separated and absent when cells were cultured with an equivalent amount of heparin instead. The ability of heparin microparticles to maintain BMP-2 bioactivity and elicit increases in C2C12 ALP activity and DNA content was also preserved after a 2-week period of pre-incubation at 37°C, as well as after lyophilization of BMP-2-loaded microparticles. Overall, this study illustrates that heparin microparticles can reproducibly retain and present high amounts of BMP-2 that elicit functional cell responses and can therefore serve as a potent vehicle for the sustained delivery of bioactive growth factors.

Conventional heparin delivery strategies typically involve immobilization of soluble heparin onto other bulk biomaterials, such as collagen, PLGA, fibrin, or Sepharose [101, 115, 116, 122, 173, 174, 189]. However, the methacrylamide-mediated cross-linking reaction used here allows for the generation of hydrogel microparticles that consist purely of heparin, facilitating the delivery of highly concentrated molecular cargo. Heparin microparticles exhibit high BMP-2 retention (>75%), which may make them better suited for localized growth factor presentation than conventional delivery vehicles that exhibit much lower growth factor retention (<20%), such as polyethylene glycol

(PEG) and gelatin biomaterials [152, 190-192]. The gelatin methacrylate microparticles used in this study were thermally cross-linked with free radical polymerization in a manner similar to heparin methacrylamide [114]. Although gelatin also primarily interacts with positively charged growth factors electrostatically, heparin microparticles captured and retained more BMP-2 than gelatin microparticles, likely due to their higher charge density [91, 156].

Furthermore, we have also demonstrated that heparin microparticles can be used to simultaneously deliver multiple growth factors (BMP-2 and VEGF), exhibiting a temporal offset in release profiles created by differences in heparin binding affinity. This ability of heparin microparticles to provide differential release profiles of co-delivered biomolecules may have utility in tissue regeneration strategies in which delivery of multiple growth factors is required; for example, bone defects in which revascularization is severely impeded may benefit from an initial fast release of VEGF followed by long term sustained presentation of BMP-2 [193-195]. However, since growth factor release from heparin microparticles is dependent upon a protein's relative affinity for heparin, tuning the growth factor loading capacity and sequence/extent of growth factor release from a naturally derived biomaterial may pose a challenge, and some studies have demonstrated that the combinatorial delivery of growth factors may inhibit osteogenesis and bone regeneration if not suitably tuned [196, 197].

Previous studies investigating the co-delivery of heparin and BMP-2 have demonstrated both stimulatory and inhibitory effects on BMP-2-mediated osteogenesis [101, 104-106, 169-171]. In this study, ALP activity induced in C2C12 cells by soluble BMP-2 and microparticle-bound BMP-2 was comparable. Interestingly, since release

curves of BMP-2 from heparin microparticles at 37ºC indicated that the majority of BMP-2 was retained within the microparticles, ALP activity results suggested that the heparin-BMP-2 interaction formed by the microparticles effectively presented BMP-2 to cells and induced a functional cellular response without complete release of the growth factor. This finding agrees with several studies that have shown that co-delivery of heparin and BMP-2 promotes ALP secretion in several cell types, including C2C12 skeletal myoblasts, MC3T3 pre-osteoblasts, and mesenchymal stem cells (MSCs) [101, 106, 115]. Although the specific mechanism by which heparin enhances BMP-2 signaling remains unclear, co-delivery of BMP-2 and heparin may enhance BMP-2 cell signaling by facilitating formation of growth factor-receptor complexes on the cell surface [3, 198] or by prolonging the half life of BMP-2 in culture [101, 104, 144]. Furthermore, this mechanism could also explain the fact that unloaded heparin microparticles dose-dependently elicited an increase in ALP activity without the addition of exogenous BMP-2. Heparin microparticles could potentially sequester cell-secreted heparin-binding proteins, such as BMPs and other growth factors, thereby prolonging growth factor presentation and subsequently enhancing ALP activity [199].

Unlike microparticle delivery of BMP-2, co-delivery of soluble heparin and BMP-2 resulted in ALP activity that was lower than that of soluble BMP-2 alone. This may suggest that soluble heparin binds to BMP-2 in solution, preventing its interaction with cell surface receptors and subsequently inhibiting further cell signaling [105, 106, 171]. Since BMP-2-loaded heparin microparticles induced higher ALP activity than co-delivery of soluble heparin and BMP-2, microparticle delivery of heparin may be a more efficient method of concentrating and presenting BMP-2 to cells. Heparin microparticles

may improve growth factor delivery by concentrating BMP-2 locally in the immediate proximity of the cells, where high densities of BMP-2 bound to the microparticles result in an effective increased local growth factor concentration. Similar effects have been observed in other systems containing surface-immobilized growth factors through direct growth factor tethering or indirect affinity-based growth factor-ECM interactions, in which the sustained presentation of immobilized growth factor stimulates enhanced cell signaling compared to similar concentrations of soluble growth factors [138, 200, 201]. Concentrated BMP-2 effects may be stronger when fewer microparticles are loaded with higher BMP-2 densities, as evidenced by the increased ALP activity observed with fewer microparticles loaded with the same total amount of BMP-2 (0.02 and 0.1 mg) while decreased ALP activity was observed with more microparticles (0.5 mg). Furthermore, total ALP activity decreased when cells and BMP-2-loaded microparticles were physically separated from each other, indicating that contact between cells and heparin materials are critical to efficient BMP-2 signaling. Ultimately, the ability to spatially concentrate growth factors using heparin microparticles may provide an advantage for numerous growth factor delivery applications, such as the regeneration of tissue defects, in which the local presentation of high concentrations of growth factor is often necessary to stimulate repair. This is similar to the native role played by cell membrane-bound GAG species during wound healing, in which signaling pathways involved in cell proliferation and migration, such as FGF signaling, are potentiated by direct GAG-growth factor contact [202].

In addition to inducing ALP activity, BMP-2-loaded microparticles also stimulated a striking increase in DNA content in C2C12 cultures. Both heparin and

heparan sulfate have been shown to increase cell proliferation by binding to endogenous mitogens in the system, such as basic fibroblast growth factor (FGF-2), and facilitating their interactions with cell surface receptors [203, 204]. In studies with MSCs, delivering soluble BMP-2 with selectively desulfated heparin increased the number of MSCs in *in vitro* cultures, while native heparin did not [115]. This is similar to the effects observed herein, in which the combined presence of both heparin microparticles and BMP-2 (soluble or pre-loaded) increased DNA content. Since changes in DNA content were not observed when soluble heparin was delivered or when C2C12 cells were physically separated from the microparticles, the effects of heparin microparticles on DNA content appear to be both contact-mediated and specific to the microparticle delivery platform. Taken together, these results indicate that BMP-2 laden heparin microparticles may simultaneously initiate cell signaling events related to both cell proliferation and ALP production, and that these effects may involve multiple pathways, such as Smad 1/5/8-dependent and Smad 1/5/8-independent pathways, which have both previously been observed in BMP-2-stimulated C2C12 cells [101, 205, 206].

The ability of heparin to prolong the bioactivity and functional cellular effects of co-delivered BMP-2 by protecting it from degradation and cell endocytosis has also been well documented *in vitro* [101, 104, 172]. Our results demonstrate that heparin microparticles can similarly extend BMP-2 bioactivity, as microparticle-bound BMP-2 pre-incubated in cell culture media for 2 weeks at 37°C induced comparable C2C12 ALP activity to fresh soluble BMP-2 treatment. Conversely, the equivalent amount of soluble BMP-2 pre-incubated in cell culture media exhibited a significant loss of bioactivity, which we hypothesized was due to degradation of the protein. This protective aspect of

heparin-BMP-2 interactions has been further investigated by Seto, et al. in a recent paper that demonstrates the ability of soluble heparin to protect BMP-2 from heat denaturation [103]. Heat-treated BMP-2 maintained its ability to induce C2C12 ALP activity in the presence of native heparin, but not in the presence of selectively desulfated heparin species, suggesting that both the overall charge of the molecule and presence of individual sulfate groups may contribute to heparin-mediated BMP-2 preservation.

Finally, because batch-to-batch variability and biomaterial stability are important considerations in the fabrication of any growth factor delivery vehicle, the reproducibility of the heparin microparticle fabrication method and effects of lyophilization on BMP-2-loaded microparticles were also evaluated. Although individual batches of microparticles demonstrated slight differences in appearance (i.e. microparticle clumping), this did not affect the ability of the microparticles to load BMP-2 and induce ALP activity and cell proliferation in C2C12 cultures, with only one microparticle batch demonstrating lower ALP induction than soluble BMP-2 treatment. Furthermore, the method of methacrylamide functionalization used in this protocol consistently resulted in 50-60% methacrylamide substitution of heparin. Since the density of reactive groups on the heparin polymer is one factor that dictates the degree of cross-linking, it is expected that the cross-linking density and size distribution of each batch of microparticles fabricated using this protocol will be similar. Studies using gelatin methacrylate microparticles have demonstrated an effect of cross-linking density on microparticle size, elastic modulus, and growth factor loading and release [114]; thus, controlling the methacrylamide functionalization and cross-linking density of heparin microparticles will aid in maintaining reproducible biomaterial properties.

In terms of biomaterial stability, our results demonstrate that lyophilized microparticles maintain their BMP-2 loading and presentation capacity for at least two years, suggesting a long shelf life that will be amendable to clinical use. Furthermore, the ability to lyophilize BMP-2-loaded microparticles without disrupting BMP-2-heparin interactions and changing the release profile and bioactivity of the growth factor may mean that heparin microparticles can be stored in loaded form until use, making both transportation and clinical application of this biomaterial easier in the future.

3.5 Conclusions

The results of this study demonstrate that heparin microparticles can be used to reproducibly sequester and retain large amounts of bioactive BMP-2, and that enhanced presentation of BMP-2 via heparin microparticles can elicit a comparable cellular response to soluble BMP-2 treatment. Heparin microparticles offer a versatile platform for growth factor delivery, as loaded microparticles can be directly injected and retained in a tissue defect site, providing a much higher surface area for efficient growth factor presentation and contact with infiltrating cells. Consequently, heparin microparticles may be an effective method of delivering and spatially retaining growth factors for a variety of applications, including both *in vitro* growth factor-mediated induction of cell fates and *in vivo* tissue regeneration therapies.

CHAPTER 4: HEPARIN MICROPARTICLES FACILITATE HEALING OF A CRITICALLY SIZED FEMORAL DEFECT USING LOW DOSE BMP-2

4.1 Introduction

Large tissue defects of the extremities resulting in significant bone loss are a particularly challenging problem for orthopedic surgeons; these injuries often lead to inadequate healing and subsequent non-union due to the complexity of the injury environment and lack of robust biological cues that can initiate and resolve the bone healing cascade [2, 21, 30]. The discovery and pharmaceutical production of bone morphogenetic proteins (BMPs), particularly BMP-2 and BMP-7, have resulted in effective strategies to overcome the injury environment and stimulate bone growth following injury [4, 32, 33]. However, limitations in the ability of current BMP delivery vehicles, such as the clinically used collagen sponge, to provide adequate growth factor retention within bone defects hinder these therapies from widespread use [40-42, 153]. Consequently, biomaterials that can provide more sustained presentation of BMPs within bone defects are necessary to improve bone regeneration strategies in the clinic.

Animal models of bone repair provide valuable test beds for evaluating novel biomaterial strategies for the delivery of BMPs, and include a variety of fracture models, segmental defects, and non-unions [207]. Segmental defect models of the femur, tibia, mandible, and calvaria are most commonly used to explore methods of BMP-induced bone regeneration across large gaps in the tissue and are typically investigated as critically sized defects, which are characterized by their inability to achieve bony

bridging without intervention [208-210]. Furthermore, segmental defects created in load-bearing bones such as the femur and tibia present additional challenges for repair, since the bone that regenerates must be able to withstand the normal mechanical loading environment in order to be functional, and are thus more representative of musculoskeletal injuries of the extremities.

Since segmental bone defects are inherently difficult to heal, models of ectopic bone formation can serve as valuable intermediate platforms to more easily screen the osteoinductive abilities of therapeutics. Biomaterials implanted in muscle and the kidney capsule can induce ectopic mineralization due to the presence of skeletal progenitor cells and a highly vascular environment, respectively [211]. Subcutaneous implantation of materials enables the evaluation of large tissue engineering scaffolds [212] and allows for longitudinal tracking of exogenous cells and biomolecules within materials via *in vivo* imaging of luminescence or fluorescence that cannot easily be visualized in deeper tissues [212]. However, subcutaneous implantation of osteoinductive materials typically results in lower ectopic bone formation than materials implanted in the muscle and kidney capsule [213, 214], due to the lack of appropriate progenitor cells and reduced vascularity.

Many BMP delivery vehicles that have demonstrated promise *in vivo* thus far have been tested in ectopic mineralization models [215]. Calcium phosphate ceramics, which mimic the inorganic mineral component of bone, can readily adsorb BMPs and possess attractive mechanical properties as bone graft substitutes [216-220]. Conversely, a number of soft hydrogels have also been developed for BMP delivery due to their tunable protein release profiles, biodegradability, and injectability. Ectopic bone

formation has been previously demonstrated using BMP-2-loaded hydrogels fabricated from hyaluronic acid [172, 221], fibrin [222, 223], alginate [224], polyethylene glycol (PEG) [225, 226], poly(lactic-co-glycolic acid) (PLGA) [227, 228], and numerous composite materials. Fewer materials have demonstrated promise in critically sized defect models; however, several studies have documented robust bone healing in defects treated with BMP-2 delivered from many of the aforementioned material strategies, including ceramics and both natural and synthetic hydrogels [229-232].

In our laboratory, we have developed a novel BMP-2 delivery system consisting of a degradable RGD-functionalized alginate gel injected into the lumen of a perforated polycaprolactone (PCL) nanofiber mesh tube [233, 234]. This BMP-2 delivery vehicle can induce robust bone healing in a rat model of a critically sized femoral defect and restore the mechanical properties of the regenerated femurs to ~75% of intact bone [234]. Furthermore, when compared to BMP-2 delivery using the clinical collagen sponge, our alginate/PCL mesh delivery system prolonged BMP-2 retention and increased remineralization of the defect space [233].

Despite these promising results, the half-life of BMP-2 delivered to the bone defect using the alginate/PCL mesh system is still relatively short, with >40% of the growth factor leaving the thigh within the first three days after delivery [233]. Since regeneration of the damaged bone tissue is a dynamic process involving several weeks of coordinated cellular responses and biomolecule presentation, the ability to maintain a substantial depot of bioactive BMP-2 within the bone defect over longer periods of time may help to improve the healing response.

One strategy to prolong BMP-2 retention *in vivo* involves the presentation of affinity molecules to specifically bind BMP-2 through electrostatic interactions. Since heparin has been shown to strongly and reversibly bind growth factors, biomaterials are often "heparinized" to increase their growth factor loading capacity [235]. Several studies have demonstrated that incorporating heparin chains into biomaterial scaffolds, such as collagen, calcium phosphate, and various hydrogels, can improve BMP-2 retention both *in vitro* and *in vivo* [116, 223, 227, 236-238]. Chapter 3 described the development of pure heparin microparticles that retain large amounts of bioactive BMP-2 *in vitro* [107]. These microparticles can be easily mixed into the hydrogel component of the alginate/PCL mesh delivery system for *in vivo* delivery, providing a simple method of adding heparin into the tissue engineering construct and subsequently increasing the growth factor loading capacity of the system in a dose dependent manner.

Herein, we investigated the incorporation of heparin microparticles into the alginate/PCL mesh delivery vehicle and its effect on BMP-2 retention both *in vitro* and *in vivo*, as well as its eventual impact on bone formation in ectopic and orthotopic sites in a rat model. This study served as the initial *in vivo* evaluation of heparin microparticles as a BMP-2 delivery vehicle using a low dose of BMP-2 (10 μg BMP-2/kg body weight) compared to clinical standards; it revealed that the delivery of heparin microparticles to a segmental bone injury contributes to significant changes in BMP-2 retention and presentation in the tissue that influences overall bone healing.

4.2 Materials and Methods

4.2.1 Fabrication of Alginate/Polycaprolactone Constructs

Hybrid alginate/polycaprolactone tissue engineering constructs for *in vivo* delivery were fabricated as previously described [234]. Briefly, irradiated, RGD-functionalized alginate (FMC Biopolymer, Philadelphia, PA) was first slowly dissolved in α-MEM (Corning Mediatech, Manassas, VA) at room temperature to achieve a 3% (w/v) alginate solution. Equal volumes of α-MEM and 0.1% rat serum albumin (RSA; Sigma, Aldrich) in 4 mM HCl were then added to dilute the alginate to 2% (w/v) prior to cross-linking. At this stage, the requisite amounts of BMP-2 (0-5 μg) and/or heparin microparticles (0-5 mg) per 150 μL of alginate hydrogel were added into the solution in 0.1% RSA in HCl. Heparin microparticles were fabricated as previously described [107]. The 2% alginate solution was then cross-linked with excess calcium sulfate (8.4 mg/mL; Sigma Aldrich) by rapid mixing between two 1 mL syringes (Becton-Dickinson, Franklin Lakes, NJ) connected through a Luer-Lok style connector (Cole-Parmer, Vernon Hills, IL). After several minutes of mixing, the alginate was allowed to solidify at room temperature for 30 minutes before being transferred to 4°C for storage overnight.

Polycaprolactone (PCL) nanofiber mesh tubes were also fabricated as previously described [234]. Briefly, PCL (Sigma Aldrich) was dissolved overnight with gentle stirring in a 90:10 solution of hexafluoro-2-propanol (HFP; Sigma Aldrich) and dimethylformamide (DMF; Sigma Aldrich) to obtain a 12% (w/v) PCL solution. 5 mL of solution was loaded into a 5 mL syringe (Becton Dickinson) with a 20-gauge blunt-tip

needle (Howard Electronic Instruments, El Dorado, KS), bubbles were removed, and the syringe was mounted onto a PHD2000 Infusion syringe pump (Harvard Apparatus, Holliston, MA). For the electrospinning setup, the syringe pump was placed so that the needle tip was ~20 cm away from a rectangular copper collection plate covered with aluminum foil for PCL nanofiber deposition. The syringe pump was set to a constant infuse rate of 0.75 mL/hr and infuse diameter of 12.060 mm, and a high voltage supply (HV Power Supply, Gamma High Voltage Research, Ormond Beach, FL) was connected to the syringe needle and collection plate to provide a voltage difference of ~15-20 kV. The voltage was periodically adjusted to maintain a Taylor cone at the needle tip during electrospinning. 4.5 mL of PCL solution were infused through the syringe pump for each mesh, creating circular meshes with an area of ~100 cm^2 and thickness of ~500 μm.

12 mm by 19 mm rectangles with twenty-three, evenly spaced 0.9 mm diameter perforations were laser-cut into the meshes to prepare nanofiber mesh tubes for tissue engineering constructs. Each rectangular sheet was rolled into a tube with an inner diameter of 5 mm and length of 12 mm and glued using UV cure adhesive (1187-M MD Medical Device Adhesives & Coatings, DYMAX, Torrington, CT; BlueWave LED Prime UVA Spot Curing System, DYMAX, Torrington, CT). Mesh tubes were sterilized by 100% ethanol evaporation overnight, followed by immersion in 70% ethanol for 4 hours, immersion in PBS for 30 minutes, and finally immersion in α-MEM up until use.

For all assays, 150 μL of alginate gel were injected through a 22-gauge, blunt-tip needle (Howard Electrical Instruments) into the center of each nanofiber mesh tube immediately prior to use. For *in vitro* assays, alginate was allowed to set in the mesh tube for at least 10 minutes prior to immersion in any solution. For *in vivo* assays, alginate was

injected into the mesh tube after it had been placed in the femoral defect.

4.2.2 BMP-2 Release from Alginate/Polycaprolactone Constructs

Passive release of BMP-2 from alginate/PCL constructs into 0.1% (w/v) BSA in PBS was monitored over a period of 21 days at 37°C. Alginate/PCL constructs were fabricated with or without 1 mg of heparin microparticles and 0.5-2.5 μg of BMP-2. Microparticles were loaded with BMP-2 in a small volume of 0.1% BSA in 4 mM HCl (25 μL/mg MPs) for 16 hours at 4°C the day before construct assembly. BMP-2 was added into the construct one of three ways: (1) solubly into the alginate solution, (2) solubly into the alginate solution with 1 mg of heparin microparticles added separately, or (3) loaded onto the microparticles and then added into the alginate solution; in all cases, BMP-2 and microparticles were added prior to alginate cross-linking. After alginate/PCL constructs were assembled and allowed to set for at least 10 minutes, the constructs were transferred to individual wells in an ultra-low attachment 24-well plate (Corning) and 1 mL of 0.1% BSA in PBS was added. At various time points over 21 days, the solution was completely removed and centrifuged at 3000 rpm for 5 minutes to separate the supernatant from any alginate or microparticle debris. The supernatant was removed and replaced with 1 mL of fresh 0.1% BSA in PBS before the solution was added back to the wells. This step was included to ensure minimal loss of alginate and microparticles from the system at each time point. Release samples were analyzed for BMP-2 content via ELISA.

4.2.3 Fluorescent Labeling of BMP-2 and Heparin Microparticles

BMP-2 was fluorescently labeled using Vivotag-S 750 Flurochrome (VS750; Perkin Elmer, Waltham, MA; Ex: 750 nm, Em: 780 nm), which contains an NHS ester reactive group for coupling to primary amines on proteins. BMP-2 was reconstituted at 250 μg/mL in 100 mM $NaPO_4$ (pH = 7.4), and VS750 was reconstituted at 50 μg/mL in 100 mM $NaPO_4$ (pH = 7.4). 40 μL of BMP-2 was mixed with 60 μL of VS750 to achieve a final BMP-2 concentration of 100 μg/mL in a solution containing 10 times molar excess of label. The reaction was allowed to proceed at room temperature in the dark for 4 hours. Following this, the solution was transferred to a Slide-A-Lyzer MINI dialysis device (MWCO = 3.5 kDa; Thermo Fisher Scientific) to dialyze out hydrolyzed NHS and unreacted label. Dialysis into 100 mM $NaPO_4$ (pH = 7.4) proceeded for 24 hours, with complete buffer changes after 1 and 4 hours. BMP-2 labeling and removal of excess dye was confirmed by taking samples of the solution for gel electrophoresis, followed by near infrared imaging on an Odyssey gel scanner (Li-cor Biotechnology, Lincoln, NE), as well as fractionation through a PD-10 desalting column (GE Healthcare Bio-Sciences, Pittsburgh, PA), followed by quantification of fluorescence of each molecular weight fraction of the BMP-2 solution using a Synergy H4 microplate reader (Biotek). Fluorescently labeled BMP-2 was stored at -20°C until use.

Fluorescently labeled heparin microparticles were fabricated by conjugation of Alexa Fluor 647 hydrazide (AF647; Thermo Fisher Scientific; Ex: 650 nm, Em: 670 nm) to heparin methacrylamide prior to microparticle formation. A hydrazide-functionalized label was used to allow conjugation of the label to the remaining unmodified carboxyl

groups on the heparin methacrylamide chains. Heparin methacrylamide was reconstituted at 10 mg/mL in 100 mM $NaPO_4$ (pH = 7.4) and combined with 0.1 M EDC and 1 mM AF647 hydrazide; the reaction was allowed to proceed at room temperature in the dark for 2 hours. The reaction volume was then dialyzed against water (MWCO = 3.5 kDa; Spectrum Laboratories) for 24 hours to remove excess reactants; dialysis buffer was replaced after 1 and 4 hours. The remaining volume in the dialysis tubing (~50 mL) was lyophilized for two days and then stored in the fridge, protected by light, until heparin microparticle fabrication using the aforementioned protocol. Heparin microparticle labeling was confirmed through confocal microscopy and macroscopic imaging on an IVIS® Spectrum platform (Ex: 640, Em: 720; Perkin Elmer).

4.2.4 Subcutaneous Implant Surgical Procedure

Subcutaneous implant studies were undertaken to (1) determine the persistence of heparin microparticles within the alginate/PCL constructs, (2) evaluate the ability of constructs with or without BMP-2 and heparin microparticles to form ectopic mineral, and (3) track retention of BMP-2 in constructs with or without heparin microparticles. All subcutaneous implant surgical procedures were conducted according to the Georgia Institute of Technology Institutional Animal Care and Use Committee (IACUC) protocol A16043. 13-week-old female Sprague Dawley rats (Charles River Labs, Wilmington, MA) were anesthetized using isoflurane prior to surgery. Two lateral incisions were made on the back of each animal and a tunneling device was used to create four individual subcutaneous pockets for construct insertion, as previously described [212]. A metal rod

and cannula were used to insert two constructs near the forelimbs and two near the hindlimbs. Constructs from each group were randomly distributed according to location.

For microparticle retention and ectopic mineralization studies, constructs consisted of PCL meshes containing (1) 150 μL alginate only (n=6), (2) 1 mg of labeled microparticles in 150 μL alginate (n=6), (3) 5 μg of BMP-2 in 150 μL alginate (n=6), and (4) 5 μg of BMP-2 loaded onto 1 mg of labeled microparticles in 150 μL alginate (n=6). Animals for these studies were euthanized using carbon dioxide asphyxiation after 6 weeks post-surgery. For BMP-2 tracking studies, constructs consisted of PCL meshes containing (1) 2.5 μg of labeled BMP-2 in alginate (n=8) and (2) 2.5 μg of labeled BMP-2 loaded onto 1 mg of microparticles in alginate (n=8). These animals were euthanized after 3 weeks.

4.2.5 In Vivo/Ex Vivo Fluorescence Imaging

In vivo and *ex vivo* fluorescent imaging was performed using an IVIS® Spectrum platform (Perkin Elmer). For evaluation of AF647-labeled microparticle retention, alginate/PCL constructs were imaged *ex vivo* (Ex: 640, Em: 720) prior to subcutaneous implantation and immediately after explanting at 6 weeks. For VS750-labeled BMP-2 tracking, longitudinal *in vivo* imaging (Ex: 745, Em: 800) was performed immediately following subcutaneous implantation on Day 0, as well as on Day 1, 4, 7, 10, 14, and 21, as previous studies have demonstrated loss of detectable fluorescent signal after 21 days [233]. Alginate gels contained either (1) 2.5 μg of labeled BMP-2 (n=8) or (2) 2.5 μg of labeled BMP-2 loaded onto 1 mg of microparticles (n=8). Animals were placed on their

sides for imaging of two constructs at once. Total fluorescent counts and radiant efficiency were evaluated for each construct at each time point, both *in vivo* and *ex vivo*, using a ~7 cm^2 elliptical region of interest (ROI) in the Living Image Software (Perkin Elmer). Background fluorescence from the animal's skin was subtracted from each measurement, and fluorescent signal at each time point was normalized to the initial fluorescent signal measured at Day 0. BMP-2 retention data was fit to a one-phase exponential decay equation ($y=a\exp(-\lambda x)$) in MATLAB to obtain the decay constant, λ. IVIS® imaging was also used for *in vitro* experiments to confirm fluorescent labeling of BMP-2 and heparin microparticles and to determine the distribution of labeled microparticles in alginate, before and after syringe injection.

4.2.6 Femoral Defect Surgical Procedure

Femoral defect studies were undertaken to determine the ability of constructs with and without heparin microparticles and BMP-2 to promote bone healing in a critically sized defect. All surgical procedures were conducted according to the Georgia Institute of Technology IACUC protocol A14037. 13-week-old female Sprague Dawley rats (Charles River Labs) were anesthetized using isoflurane prior to surgery, and bilateral surgeries were performed as previously described [233, 239]. Briefly, after opening up the leg using an anterior approach, a radiolucent fixation plate (polysulfone) and two stainless steel risers were screwed directly onto the femur of the rat for limb stabilization, and an oscillating saw was used to create an 8-mm wide, full thickness diaphyseal defect. A PCL nanofiber mesh tube was inserted into the defect to cover the bone ends, and 150 μL of

alginate were injected through the perforations into the center of the tube. Each alginate gel contained one of the following: (1) 1 mg of unloaded microparticles (n =4), (2) 2.5 μg of BMP-2 (n=5), or (3) 2.5 μg of BMP-2 loaded onto 1 mg of microparticles (n=5). Animals were euthanized after 2 or 12 weeks post-surgery.

4.2.7 Faxitron and Micro-computed Tomography

Construct mineralization was evaluated 6 weeks post-surgery, after constructs were harvested and fixed in 10% neutral buffered formalin for 48 hours. *Ex vivo* micro-computed tomography (CT) was performed using a microCT42 scanner (Scanco, Switzerland) as previously described [213, 214], with a voxel size of 16 μm, voltage of 55 kVp, and current of 145 μA. A threshold of 80 was set for new mineral formation, and a Gaussian filter (sigma = 1.2, support = 1) was applied to suppress noise.

Longitudinal *in vivo* radiographs of femurs were obtained at 2, 4, 8, and 12 weeks post-surgery, using a Faxitron MX-20 Digital machine at a voltage of 23 kV and exposure time of 15 seconds; radiographs were used to qualitatively access bony bridging across the defect space. *In vivo* micro-CT of femurs was performed at 4, 8, and 12 weeks post-surgery to quantify total bone volume and overall mineral density. Animals were anesthetized and scanned at a medium resolution using a VivaCT40 live animal scanner (Scanco) with a voxel size of 38.5 μm, voltage of 55 kVp, and current of 109 μA [234]. Mineral was quantified within the central 6 mm (160 scan slices) of each 8 mm defect. A global threshold for new mineral was set at 50% of the average mineral density of native cortical bone, and a Gaussian filter (sigma = 1.2, support = 1) was used to suppress noise.

4.2.8 Biomechanical Testing

Femurs removed from rats at 12 weeks underwent torsion testing using a uniaxial torsion testing system (Bose EnduraTEC ELF200; Bose Electroforce Systems Group, Eden Prairie, MN), in order to compare the strength of the regenerated bone in the defect to that of native bone (age-matched historical data). Briefly, fixation plates and soft tissue were removed from isolated femora, before the bone ends were placed in hot Wood's metal (Alfa Aesar, Haverhill, MA), allowed to solidify, and mounted into the machine. Torsion was applied at a rate of 3º per second until failure, allowing for the determination of maximum torque and calculation of torsional stiffness, using the slope of the linear segment of the torque-rotation curve.

4.2.9 Histological Sectioning and Staining

To determine the distribution of heparin microparticles within alginate gels, alginate/PCL constructs with or without 1-5 mg of microparticles (n=3) were fabricated and processed for cryosectioning. Constructs were incubated in successively more concentrated solutions of sucrose and optimal cutting temperature (OCT) compound (Sakura Finetek USA Inc., Torrance, CA) at room temperature under vacuum in order to promote complete infiltration of OCT compound into the hydrogel matrix. Constructs were then transferred to 100% OCT compound and frozen in a bath of 100% ethanol and dry ice. 5 μm sections were obtained and stained with Safranin O to visualize alginate and heparin microparticles.

For *in vivo* subcutaneous implant studies, all constructs were collected for histology after 6 weeks post-surgery. For *in vivo* femoral defect studies, femurs from each treatment group demonstrating representative bone formation (as evaluated by radiography) were isolated for histology at 2 and 12 weeks post-surgery. After harvesting, the constructs and femurs were fixed in 10% neutral buffered formalin at 4°C for 24 and 48 hours, respectively, followed by decalcification at room temperature using a formic acid decalcifier (Cal Ex-II, Thermo Fisher Scientific) with gentle agitation and complete replacement of the solution every 2-3 days for up to two weeks. Complete decalcification of constructs and femurs was verified using vivaCT scoutview. Samples were then dehydrated through submersion in a series of alcohol and xylene solutions and vacuum-embedded in paraffin wax (Paraplast, Sigma Aldrich) at 60°C. 5 μm midsagittal sections of the defects were obtained for histological analysis using Safranin O/Fast Green staining in order to characterize microparticle and alginate persistence, mineral formation, and gross tissue morphology.

Immunohistochemistry for Ki67 antigens was performed using a rat/mouse MIB-5 antibody (1:50, Dako, Carpinteria, CA), followed by a horseradish peroxidase secondary antibody (Vector Labs, Burlingame, CA), to evaluate cell proliferation within the defect space. Gill's hematoxylin served as a counterstain to visualize cell nuclei, and Safranin O was used to visualize heparin microparticles. Histological sections of rat small intestine were also processed for immunohistochemistry and treated with mouse serum, followed by the horseradish peroxidase secondary antibody, as a control for nonspecific antibody binding, and MIB-5 antibody followed by the horseradish peroxidase secondary antibody as a Ki67 positive control.

4.2.10 Statistical Analysis

All data are reported as mean ± standard error of the mean. *In vitro* experiments were run with a minimum of three replicates for each experimental group. For *in vivo* subcutaneous implant experiments, 6-8 constructs per group were implanted. For *in vivo* bone defect experiments, longitudinal micro-CT was conducted on 4-5 femurs per group, and biomechanical testing was conducted on 3-4 femurs per group. Statistical significance was determined using one-way or two-way ANOVA as appropriate, followed by Bonferroni's post hoc analysis (Graphpad Prism, Version 5.0, La Jolla, CA). For data that did not satisfy the assumptions of equal variances and Gaussian distributions, the nonparametric Kruskal-Wallis test was used. $P < 0.05$ was considered statistically significant.

4.3 Results

4.3.1 Distribution of Heparin Microparticles in Alginate Gel

Two different methods were used to establish whether heparin microparticles could be evenly distributed throughout the alginate hydrogels without disrupting calcium-mediated cross-linking. First, alginate hydrogels were fabricated with Alexa Fluor 647-labeled heparin microparticles at a density of 1 mg of microparticles per 150 μL of alginate and imaged on an IVIS® platform to evaluate the distribution of fluorescence. Addition of heparin microparticles prior to alginate cross-linking using the dual syringe

method resulted in even distribution of fluorescent signal throughout the alginate hydrogel in the syringe (Figure 4.1A(i)). Furthermore, when the alginate gel was injected through a blunt-tip needle in 150 μL aliquots, similar to injection during surgery, the fluorescence in each of the three aliquots was similar (Figure 4.1B). This was the case for alginate gels injected into PCL mesh tubes (Figure 4.1A(ii), B; $3.87x10^7 \pm 0.04x10^7$) or directly onto a glass slide (Figure 4.1A(iii), B; $5.64x10^7 \pm 0.09x10^7$). The presence of the PCL mesh tube around the alginate hydrogel attenuated the fluorescent signal detected by the IVIS® platform, but did not affect the variability of the signal between similarly treated hydrogels.

Alginate hydrogels were also fabricated for histological processing using 0, 1, and 5 mg of heparin microparticles per 150 μL alginate construct. In Safranin O stained cryosections from hydrogel constructs, microparticles appeared as dark red, punctate circles, while alginate stained lighter orange-red (Figure 4.1C). Heparin microparticles (indicated by black arrows) were well distributed in constructs containing either 1 mg or 5 mg of microparticles; however, the higher concentration of microparticles appeared to interfere with alginate cross-linking and resulted in a poorly formed gel. Consequently, all further studies were completed using a microparticle density of 1 mg per 150 μL alginate construct.

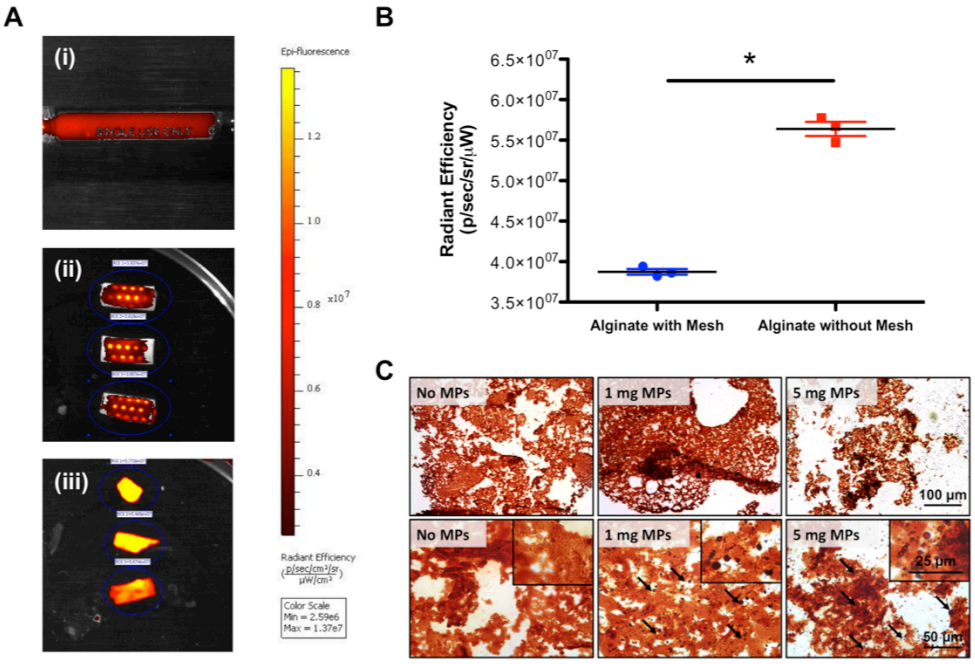

Figure 4.1. Quantitative and Qualitative Evaluation of Heparin Microparticle Distribution in Alginate/PCL Constructs. A) AF647-labeled heparin microparticles were mixed into 2% RGD-alginate at a density of 1 mg of MPs per 150 μL of alginate and imaged on an IVIS® imaging platform (Ex: 640, Em: 720) before and after syringe injection. IVIS® images depict (i) homogeneous fluorescence throughout the syringe prior to injection, (ii) alginate/PCL constructs (1 mg of MPs in 150 μL of alginate) that exhibit comparable fluorescence, and (iii) alginate hydrogels without PCL meshes (1 mg of MPs in 150 μL of alginate) that exhibit comparable fluorescence. B) Quantification of radiant efficiency detected in images (ii) and (iii) revealed differences in fluorescent signal due to the presence of the PCL mesh, but low variability between individual constructs or hydrogels. (* = $p < 0.001$ as indicated) C) Representative images of Safranin O-stained sections of constructs containing 0, 1, or 5 mg of microparticles per 150 μL of 2% alginate. Black arrows indicate microparticles.

4.3.2 BMP-2 Release from Alginate/Polycaprolactone Constructs

In order to determine whether heparin microparticles could improve BMP-2 retention in alginate/PCL constructs, 150 μL alginate constructs fabricated with or without 1 mg of heparin microparticles were loaded with 0.5 or 2.5 μg of BMP-2 and allowed to passively release BMP-2 into a 0.1% (w/v) BSA in PBS solution over 21 days. At the lower BMP-2 dose (Figure 4.2A), constructs containing BMP-2 solubly entrapped

within the alginate ("BMP-2") exhibited higher BMP-2 release at each time point compared to constructs containing BMP-2 loaded onto heparin microparticles within the alginate ("Loaded MPs"). At the higher BMP-2 dose (Figure 4.2B), differences in cumulative BMP-2 release between solubly entrapped BMP-2 and BMP-2 loaded onto the microparticles were only observed after 14 days. Interestingly, alginate/PCL constructs containing 1 mg of unloaded microparticles and 2.5 μg of solubly entrapped BMP-2 ("Unloaded MPs + BMP-2") demonstrated cumulative BMP-2 release that fell between that of the other two groups. Finally, when constructs loaded with 2.5 μg of BMP-2 were washed with BSA/PBS at the end of the 21-day period, the amount of BMP-2 retrieved from the constructs was higher in constructs lacking microparticles (Figure 4.2C), likely due to the inability to detect BMP-2 that remained bound to the microparticles via ELISA. Overall, only a small fraction of the BMP-2 initially incorporated into the constructs could be retrieved through BSA/PBS washes after 21 days (3-7%); this could be due to a number of reasons, including protein degradation and protein adsorption onto plastic surfaces.

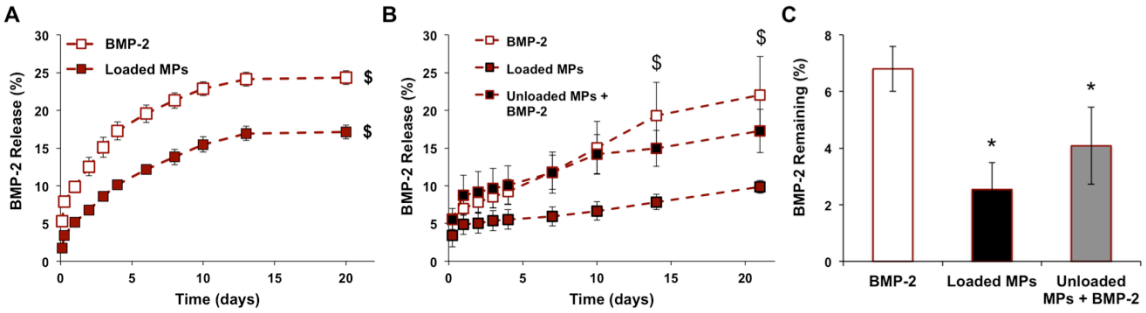

Figure 4.2. BMP-2 Release from Alginate/PCL Constructs with or without Heparin Microparticles. BMP-2 was mixed directly into the alginate solution (BMP-2), loaded onto 1 mg of microparticles prior to being mixed into the alginate solution (Loaded MPs), or mixed into the alginate solution along with 1 mg of empty microparticles (Unloaded MPs). Assembled alginate/PCL constructs were immersed in 1 mL of 0.1% BSA in PBS, which was sampled over 21 days. A) When 0.5 µg of BMP-2 was used, constructs containing BMP-2-loaded microparticles retained more BMP-2 overall. ($ = $p < 0.05$ at each time point) B) When 2.5 µg of BMP-2 was used, BMP-2 release from constructs without microparticles was greater than BMP-2 release from loaded microparticle-containing constructs after 2 weeks. ($ = $p < 0.05$ between BMP-2 and Loaded MPs) C) After 21 days, all constructs originally loaded with 2.5 µg of BMP-2 were thoroughly rinsed in PBS to remove remaining BMP-2. Constructs containing microparticles yielded less detectable BMP-2. (* = $p < 0.05$ compared to BMP-2)

4.3.3 Microparticle Retention in Subcutaneous Implants

Alginate/PCL constructs containing 1 mg of Alexa Fluor 647-labeled heparin microparticles with or without 5 µg of BMP-2 were implanted subcutaneously in the backs of rats for 6 weeks in order to determine whether heparin microparticles could be retained in the constructs following *in vivo* implantation. Fluorescence imaging of constructs was performed using an IVIS® platform prior to implantation and immediately following explanting; constructs were placed on glass slides for imaging as depicted and oriented such that the same number of perforations were visible in each PCL mesh (Figure 4.3A). IVIS® imaging revealed retention of ~55% of the initial fluorescent signal from heparin microparticles after 6 weeks *in vivo* (Figure 4.3B); there were no differences in fluorescence retention between unloaded ("MP") and BMP-2-loaded

microparticles ("MP + BMP-2"). After constructs were explanted and imaged, they were fixed and processed for histological analysis. Safranin O/Fast Green staining of constructs revealed the presence of intact heparin microparticles (yellow arrows) in all microparticle-containing constructs after 6 weeks *in vivo* (Figure 4.3C, D). Constructs containing BMP-2-loaded microparticles also contained areas of mineralized bone formation (dark green staining) (Figure 4.3C), while constructs containing unloaded microparticles were primarily filled with fibrous tissue (Figure 4.3D).

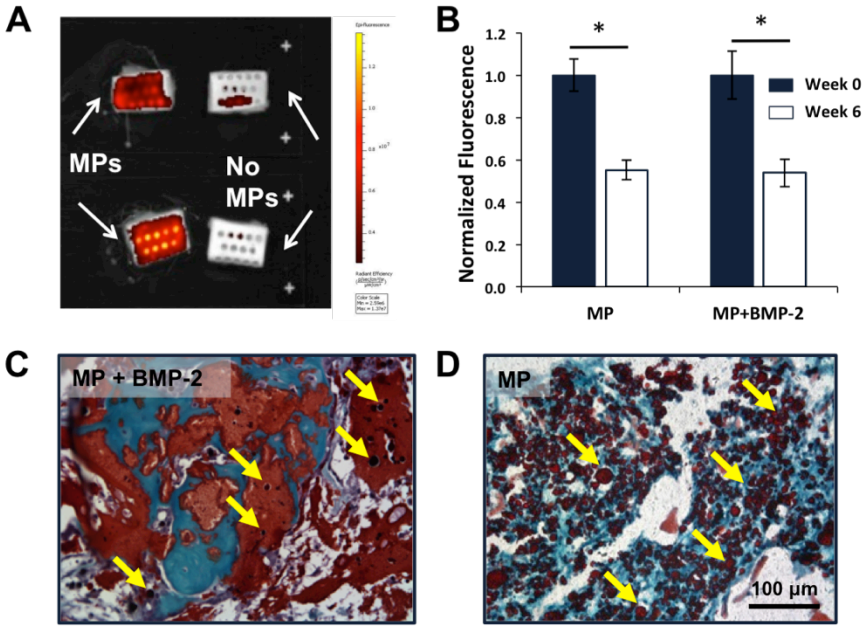

Figure 4.3. Retention of Heparin Microparticles in Subcutaneously Implanted Alginate/PCL Constructs. AF647-labeled microparticles (unloaded or loaded with 5 µg of BMP-2) were mixed into 2% RGD-alginate at a density of 1 mg of MPs per 150 µL of alginate; alginate/PCL constructs were implanted subcutaneously in the backs of rats for 6 weeks (n=6). A) Representative IVIS® image (Ex: 640, Em: 720) depicting explanted alginate/PCL constructs with and without labeled microparticles after 6 weeks. B) Quantification of radiant efficiency detected in IVIS® images of constructs immediately prior to implantation (Week 0) and following explanting (Week 6). Radiant efficiency was normalized to Week 0 values. AF647 signal decreased over 6 weeks in both unloaded and loaded microparticle-containing constructs. (* = $p < 0.05$ as indicated) Safranin O/Fast Green staining of alginate/PCL constructs containing C) BMP-2-loaded microparticles and D) unloaded microparticles demonstrates the persistence of intact microparticles after 6 weeks *in vivo*, as indicated by yellow arrows.

4.3.4 BMP-2 Retention in Subcutaneous Implants

Alginate/PCL constructs containing fluorescently labeled BMP-2 were also implanted subcutaneously to track *in vivo* retention of BMP-2 over time. Constructs containing either 2.5 μg of BMP-2 or 2.5 μg of BMP-2 loaded onto 1 mg of heparin microparticles were implanted and imaged periodically for three weeks using an IVIS® platform. Representative fluorescence images demonstrate a decrease in fluorescent signal from subcutaneously implanted constructs over time (Figure 4.4A-D). Quantification of fluorescent signal using a 7 cm^2 region of interest and normalized to Day 0 values confirmed this decrease in signal (Figure 4.4E). Although no differences in BMP-2 retention were observed between constructs with and without heparin microparticles at individual time points, constructs containing microparticles exhibited a lower average decay constant when this data was fit to an exponential decay curve, indicating prolonged BMP-2 retention (Figure 4.4F). When constructs were explanted after 21 days and imaged, the remaining radiant efficiency and number of fluorescent counts were higher in constructs containing heparin microparticles, indicating a greater amount of BMP-2 was retained overall (Figure 4.4G).

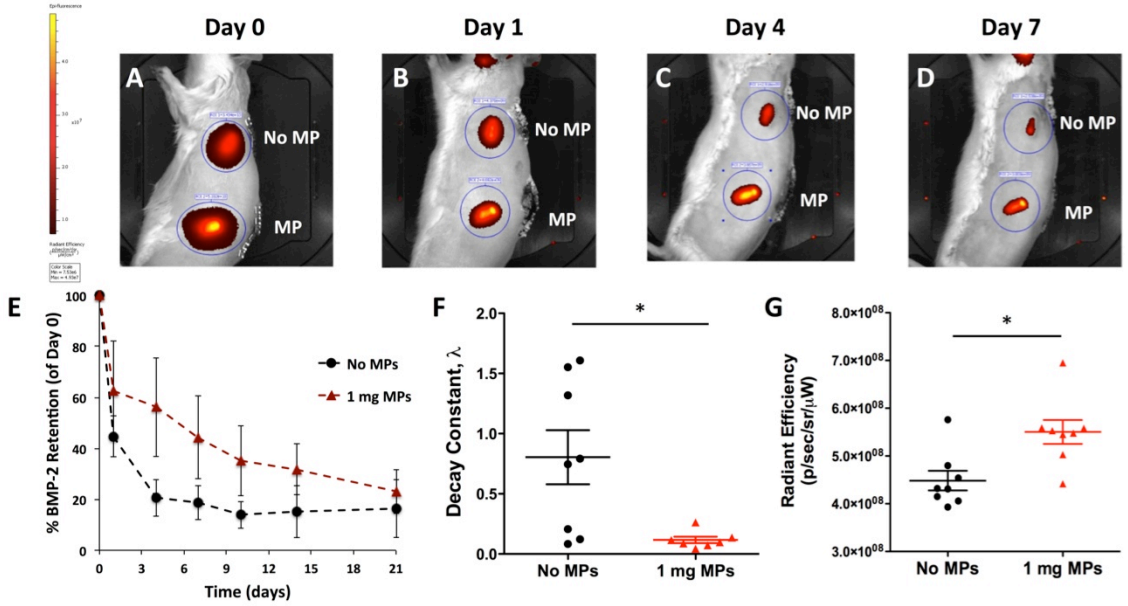

Figure 4.4. Longitudinal BMP-2 Tracking of Subcutaneously Implanted Alginate/PCL Constructs. 2.5 μg of VS750-labeled BMP-2 (alone or loaded onto 1 mg of heparin microparticles) were mixed into 150 μL of 2% RGD-alginate. Alginate/PCL constructs were implanted subcutaneously in the backs of rats for 3 weeks (n=8) and imaged on an IVIS® platform at Day 0, 1, 4, 7, 10, 14, and 21 after surgery. A-D) Representative fluorescence IVIS® images of subcutaneous implants at indicated time points. E) Quantification of *in vivo* VS750 fluorescence over time (normalized to Day 0 fluorescence) revealed somewhat faster loss of BMP-2 signal from constructs lacking microparticles; however, these data were not significantly different. F) Decay constants from BMP-2 retention data fit to a one-phase exponential decay curve revealed differences in average decay constants of constructs treated with No MPs and 1 mg MPs. (* = $p < 0.05$ as indicated) G) Quantification of *ex vivo* VS750 fluorescence from explanted constructs 21 days post-surgery. (* = $p < 0.01$ as indicated)

4.3.5 Ectopic Mineralization in Subcutaneous Implants

To evaluate their ability to induce ectopic mineralization, subcutaneously implanted alginate/PCL constructs that had been loaded with heparin microparticles and BMP-2 were also scanned using micro-CT after 6 weeks *in vivo*. Constructs containing alginate only, 1 mg of unloaded microparticles, 5 μg of BMP-2, and 5 μg of BMP-2 loaded onto 1 mg of microparticles were evaluated. Quantification of micro-CT scans demonstrated low mineral volume in constructs containing alginate only and unloaded

microparticles; on the other hand, constructs containing BMP-2 only and BMP-2 loaded onto heparin microparticles demonstrated variable amounts of ectopic mineral formation (Figure 4.5A). Due to the variability in mineral formation, there were no significant differences in average mineral volumes. Safranin O/Fast Green staining of constructs revealed ectopic mineral in both BMP-2 and BMP-2-loaded microparticle-containing constructs (white arrows; Figure 4.5B, C). This ectopic mineralization study confirmed that both BMP-2 alone and BMP-2-loaded microparticles within alginate/PCL constructs could induce mineralization *in vivo*; however, due to the variability exhibited in this model, future studies were undertaken in the segmental defect model.

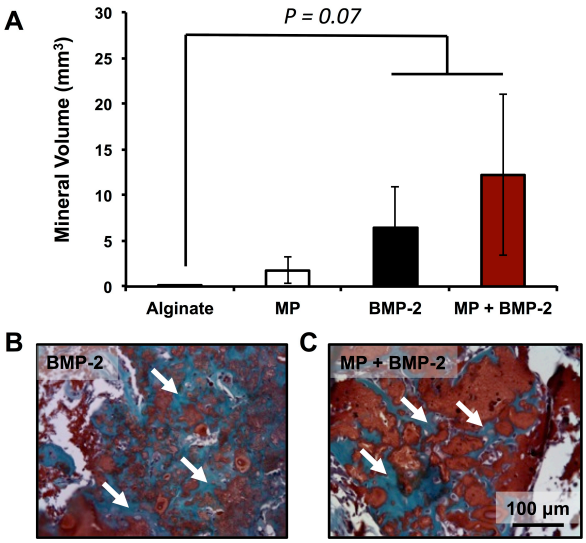

Figure 4.5. BMP-2-Mediated Ectopic Mineralization of Subcutaneously Implanted Alginate/PCL Constructs. Alginate/PCL constructs were assembled and implanted subcutaneously in the backs of rats for 6 weeks (n=6). One of each of the following groups was implanted into each rat: 150 µL of 2% RGD-alginate, 1 mg unloaded microparticles in 150 µL of alginate, 5 µg of BMP-2 in 150 µL of alginate, or 5 µg of BMP-2 loaded onto 1 mg of microparticles in 150 µL of alginate. A) Quantification of mineral volume in alginate PCL/constructs. Safranin O/Fast Green staining of constructs containing B) BMP-2 only and C) BMP-2-loaded microparticles demonstrates the formation of ectopic mineral after 6 weeks *in vivo*, as indicated by white arrows.

4.3.6 Orthotopic Mineralization in Femoral Defects

After alginate/PCL constructs containing BMP-2-loaded heparin microparticles were confirmed to induce mineralization in an ectopic site, the ability of loaded microparticles to stimulate bone healing in a femoral defect model was investigated. Femoral defects were treated with 2.5 μg of BMP-2, 2.5 μg of BMP-2 loaded onto 1 mg of heparin microparticles, or 1 mg of unloaded heparin microparticles. After twelve weeks, bony bridging was observed in all defects treated with BMP-2 alone ("BMP-2") (5/5), 60% of defects treated with BMP-2-loaded microparticles ("MP + BMP-2") (3/5), and none of the defects treated with unloaded microparticles ("MP") (0/4). Representative radiographs at 2, 4, 8, and 12 weeks demonstrate the progression of bone formation in defects treated with BMP-2 and BMP-2-loaded microparticles (Figure 4.6A). Of defects treated with loaded microparticles, three bridged completely (top row), while two exhibited bone formation throughout the bone defect but did not bridge (bottom row).

Longitudinal *in vivo* micro-CT scans at 4, 8, and 12 weeks provided bone volume (Figure 4.6B) and bone mineral density (Figure 4.6C) quantification of the regenerated femurs. As expected, minimal bone regeneration was observed in the defect following treatment with unloaded microparticles, although the mineral that did form had a similar density to that of BMP-2-regenerated femurs at 8 and 12 weeks. Both BMP-2-containing groups induced higher mineral formation than unloaded microparticles. Overall, BMP-2-loaded microparticles induced less mineral volume than BMP-2 treatment; however, these differences were not significant at each individual time point. Mineral density of the

regenerated bone increased after 4 weeks in both BMP-2 and BMP-2-loaded microparticle treated femurs; there were no differences between the mineral densities of the bone regenerated by BMP-2 and loaded microparticle treatment at any time point.

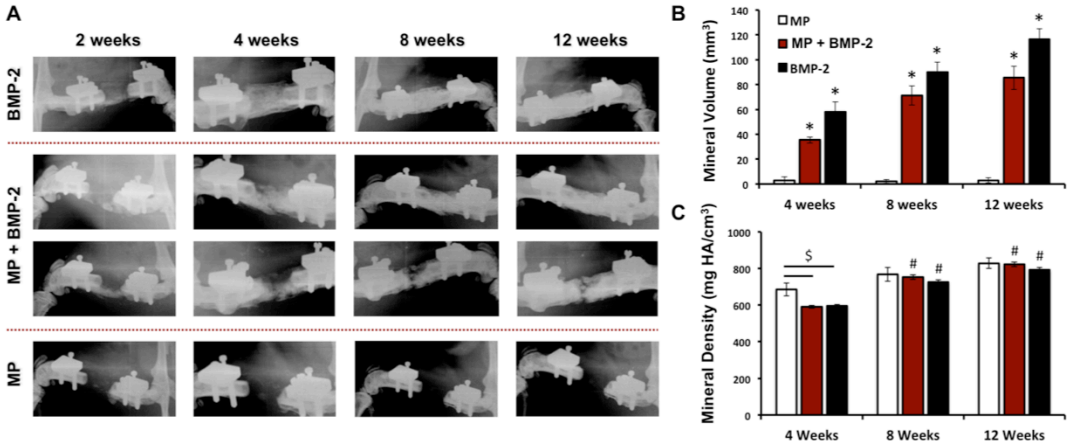

Figure 4.6. Qualitative and Quantitative Assessment of Orthotopic Mineralization in Femoral Defects. Bilateral femoral defects were treated with alginate/PCL constructs containing 1 mg of unloaded heparin microparticles, 1 mg of microparticles loaded with 2.5 μg of BMP-2, or 2.5 μg of BMP-2 (n=4-5). A) Representative radiographs of femurs at 2, 4, 8, and 12 weeks post-surgery. All defects (5/5) containing BMP-2 bridged, while only 3/5 defects containing BMP-2-loaded microparticles bridged. Radiographs of femurs treated with BMP-2-loaded microparticles are representative images of both bridging and non-bridging cases. No defects containing unloaded microparticles bridged. B) Quantification of mineral volume in bone defects using micro-CT at 4, 8, and 12 weeks post-surgery. Both BMP-2 and BMP-2-loaded microparticle treated femurs demonstrated higher bone formation than unloaded microparticles at each time point (* = $p < 0.05$ compared to unloaded microparticles). BMP-2 treatment induced higher bone formation than loaded microparticles overall ($p < 0.001$), although these differences were not significant at individual time points. C) Mineral density of regenerated bone in defects containing unloaded microparticles was higher than that of the other treatments at 4 weeks ($ = $p < 0.05$ as indicated). Mineral densities of loaded microparticles and BMP-2 treated defects increased over 12 weeks. (# = $p < 0.05$ compared to 4 weeks.)

4.3.7 *Biomechanical Properties of Regenerated Femurs*

After 12 weeks, all animals were euthanized, and femurs were removed for torsion testing to evaluate the mechanical properties of the regenerated bone. Both

bridged and non-bridged samples were tested. Femurs regenerated by BMP-2 and BMP-2-loaded microparticles exhibited maximum torque and torsional stiffness that were not statistically different from each other or from the properties of intact femurs (Figure 4.7).

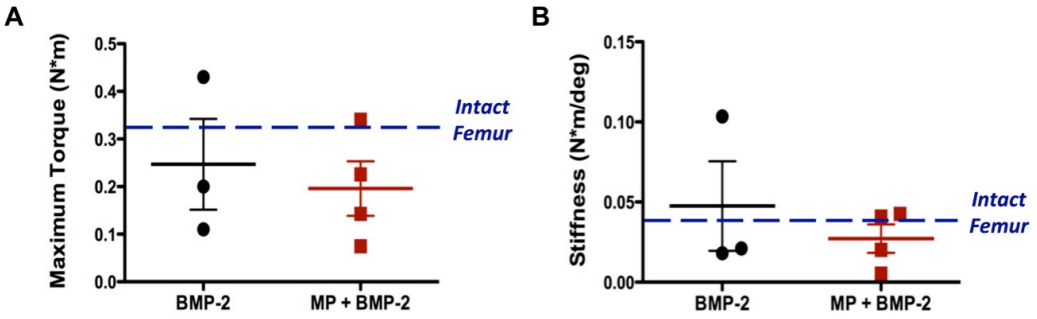

Figure 4.7. Biomechanical Testing of Regenerated Femurs. Femurs were isolated and mechanically tested via torsion to failure (n=3-4). Mechanical properties were compared against that of intact femurs of age-matched rats (historical data [234]). A) Maximum torque withstood by femurs treated with BMP-2 and BMP-2-loaded microparticles. B) Stiffness demonstrated by femurs treated with BMP-2 and BMP-2-loaded microparticles. No differences were observed between groups or compared to intact bone.

4.3.8 *Histological Analysis of Femoral Defects*

Sections from representative femurs 12 weeks post surgery were stained with Safranin O/Fast Green to visualize tissue morphology within the bone defect site. Sections of femurs treated with BMP-2 alone revealed areas of residual alginate (shown in red) surrounded by areas of new mineral formation (white arrows; Figure 4.8A). On the other hand, sections of femurs treated with unloaded heparin microparticles did not show any bone formation, and only fibrous tissue could be observed, interspersed between alginate and remaining microparticles (yellow arrows; Figure 4.8B). Femurs treated with BMP-2-loaded microparticles demonstrated similar areas of mineral

formation to femurs treated with BMP-2 alone, in close proximity to both residual alginate and intact microparticles (Figure 4.8C). Immunohistochemistry for the cell proliferation marker Ki67 on femurs explanted after 2 weeks post-surgery revealed minimal positive staining in femurs treated with BMP-2 alone (Figure 4.8D). However, both femurs treated with unloaded microparticles and BMP-2-loaded microparticles exhibited $Ki67^{+}$ cell nuclei throughout the defect, with some cells in close proximity to regions of microparticles (Figure 4.8E, F), suggesting that cells infiltrating the defect site were proliferating in response to heparin microparticles but not in response to BMP-2 alone. As an additional control, sections of rat small intestine were incubated with Ki67 antibody or mouse serum, followed by the horseradish peroxidase secondary antibody; horseradish peroxidase staining was only observed in the presence of Ki67 (Figure 4.9).

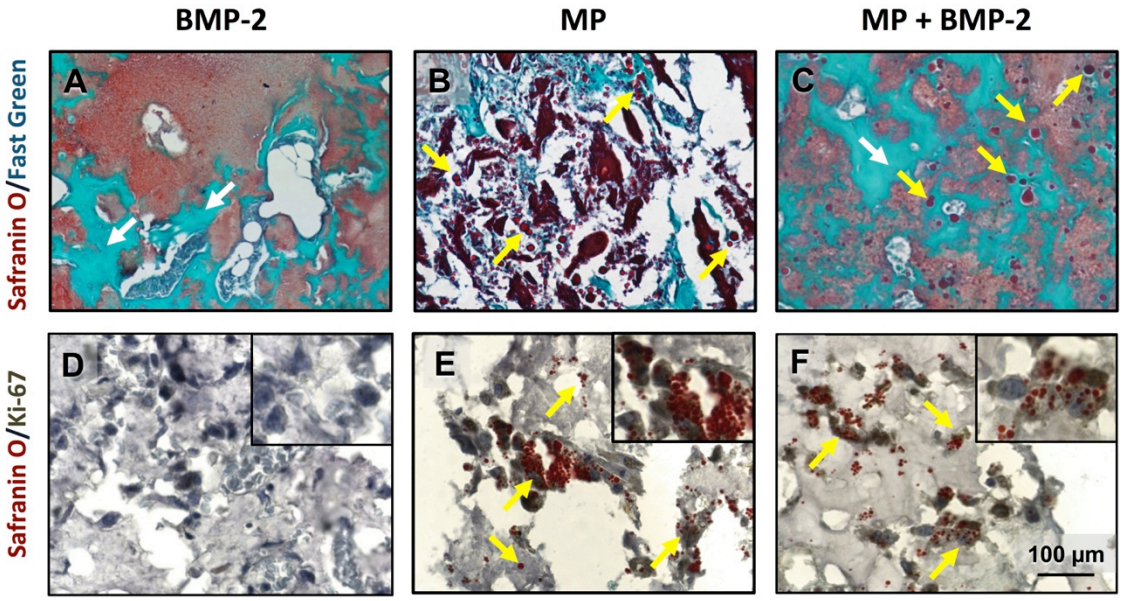

Figure 4.8. Histological Analysis of Regenerated Femurs. Representative femurs were fixed, decalcified, and embedded in paraffin for sectioning and staining. Safranin O/Fast Green staining of femurs treated for 12 weeks with A) 2.5 µg of BMP-2, B) 1 mg of unloaded heparin microparticles, and C) 2.5 µg of BMP-2 loaded onto 1 mg of heparin microparticles. Ki67 antibody staining of femurs treated for 2 weeks with D) 2.5 µg of BMP-2, E) 1 mg of unloaded heparin microparticles, and F) 2.5 µg of BMP-2 loaded onto 1 mg of heparin microparticles. Yellow arrows indicate heparin microparticles, and white arrows indicate new mineral formation.

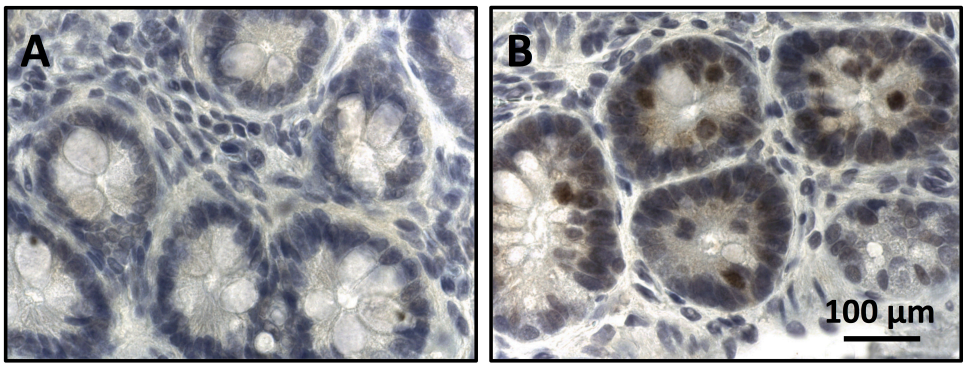

Figure 4.9. Negative and Positive Controls for Ki67 Staining. A) Sections of rat small intestine incubated in mouse serum, followed by secondary horseradish peroxidase antibody, did not display positive staining. B) Small intestine incubated with Ki67 antibody, followed by secondary horseradish peroxidase antibody, displayed positive staining for Ki67.

4.4 Discussion

Heparin, with its known affinity for a number of potent growth factors, has been frequently added to biomaterial delivery vehicles to slow the release of biomolecules from a site of interest. In this study, we investigated the incorporation of heparin microparticles into an alginate/PCL tissue engineering construct that has been previously used in our laboratory for *in vivo* delivery of BMP-2. We demonstrated that heparin microparticles could be evenly dispersed throughout the alginate hydrogel network, to reduce the total amount of BMP-2 released *in vitro* and attenuate the overall rate of BMP-2 loss from subcutaneous implants. Furthermore, BMP-2-loaded heparin microparticles could be retained *in vivo* within alginate/PCL constructs implanted both subcutaneously and in the femoral bone defect, inducing mineral formation in both ectopic and orthopic sites and leading to bony bridging of 60% of the defects treated. Despite lower mineral volumes observed in defects treated with BMP-2-loaded microparticles compared to BMP-2 alone, both treatments lead to comparable restoration of biomechanical

properties. Histological analysis of defects after 2 and 12 weeks revealed persistence of intact microparticles throughout the entire period of bone healing, as well as an early increase in the number of proliferating Ki-67^{+} cells within the defect site in the presence of both unloaded and BMP-2-loaded heparin microparticles.

Of the heparinized materials that have been developed for BMP-2 delivery, a number have demonstrated improved BMP-2 retention and sustained release profiles *in vitro* compared to non-heparinized controls. For example, the covalent addition of heparin into PLGA scaffolds extended the time required for total BMP-2 release from under four hours to three weeks [173], while the incorporation of 1-10% heparin into hyaluronan microgels dose-dependently increased BMP-2 loading and decreased BMP-2 release [167]. We observed similar results in our experiments, in which the addition of 1 mg of heparin microparticles into alginate/PCL constructs reduced *in vitro* BMP-2 release by 50% compared to constructs containing BMP-2 alone, at two different doses of BMP-2 (0.5 and 2.5 μg). Interestingly, when BMP-2 was mixed into alginate hydrogels in the presence of 1 mg of empty microparticles, we also observed a slight attenuation in BMP-2 release *in vitro*, suggesting that free BMP-2 within the hydrogel may associate with microparticles over time. Similar results have been observed in other composite hydrogels, including methylcellulose and hyaluronan-methylcellulose hydrogels containing empty PLGA nanoparticles and soluble SDF-1, NT-3, and BDNF [240].

We next evaluated BMP-2 retention in alginate/PCL constructs *in vivo* with longitudinal fluorescence imaging techniques. Few studies have attempted to assess differences in the *in vivo* release profiles of growth factors from implanted biomaterials due to the difficulty of consistently and accurately imaging through deeper tissue;

however, the evaluation of *in vivo* release profiles may provide more accurate information for developing *in vivo* applications. For example, Shah, et al. performed *in vivo* imaging of fluorescently tagged PDGF-BB and BMP-2 in a calvarial defect for 14 and 21 days, respectively [241], and in our previous studies, we demonstrated the ability to detect fluorescently tagged BMP-2 within a femoral defect for 21 days [233]. In our current study, in order to enhance the signal of the delivered BMP-2 while minimizing background fluorescence, we chose to implant alginate/PCL constructs in superficial locations along the backs of the rats. Fluorescent signal was detected for 21 days in this location, with constructs containing BMP-2-loaded microparticles displaying a lower decay constant ($\lambda = 0.12$) indicative of slower overall release compared to constructs containing BMP-2 alone ($\lambda = 0.80$). The differences observed between *in vitro* and *in vivo* BMP-2 release may be due to several causes, including fluorophore degradation, discrepancies due to different measurement methods (BMP-2 release *in vitro* vs. BMP-2 retention *in vivo*), altered interactions of BMP-2 with alginate and heparin microparticles following fluorophore addition, and the presence of numerous proteases and cells in the subcutaneous environment that could accelerate BMP-2 release and degradation. While the ideal environment to investigate BMP-2 release would be the bone defect itself, in which many different cell types and biomolecules reside, there are significant technical challenges in imaging fluorescent molecules implanted deeper within tissues; additionally, previous studies have reported consistent BMP-2 release profiles from subcutaneous and bone defect sites [194].

Given that the molecular cargo of this tissue engineering construct was loaded directly onto the heparin microparticles, microparticle retention *in vivo* likely dictated

BMP-2 retention and distribution throughout the subcutaneous space and bone defect. *Ex vivo* IVIS® imaging and Safranin O/Fast Green staining of ectopically implanted constructs revealed the persistence of microparticles throughout the 6-week period of implantation, with retention of ~55% of the original fluorescent signal from AF647-labeled microparticles. Furthermore, when constructs containing microparticles were implanted into the bone defect, Safranin O/Fast Green staining after 12 weeks similarly depicted the remaining microparticles throughout areas of residual alginate and regenerated bone. Unlike alginate, heparin microparticles were not hydrolytically degradable; thus, the loss of fluorescent signal observed following ectopic construct implantation may be due to several other reasons, including cell-mediated microparticle degradation and clearance via the bloodstream following alginate degradation [242, 243].

Ultimately, while subcutaneous implantation of alginate/PCL constructs provided valuable information regarding BMP-2 and microparticle retention, ectopic mineralization induced by BMP-2-loaded microparticles demonstrated promising but highly variable results. Consequently, further investigation was conducted in an orthotopic bone defect model, in which BMP-2-loaded heparin microparticles induced robust mineralization within the defect space, resulting in bridging of 60% of the treated defects and restoration of mechanical properties similar to that of intact femurs. Despite these encouraging results, defects treated with alginate/PCL constructs containing BMP-2 alone out-performed BMP-2-loaded microparticles, with increased mineral volumes and complete bridging in all defects.

The reduction in overall bone healing displayed in defects treated with BMP-2-loaded microparticles may be attributed to the differences in BMP-2 retention and

presentation caused by the presence of microparticles in the constructs. Both *in vitro* and *in vivo* results suggested that heparin microparticles increased BMP-2 retention within the constructs. Although we have demonstrated that heparin microparticles provide the sustained BMP-2 presentation necessary to induce cellular differentiation *in vitro* upon contact [107], an initial burst release of BMP-2 from the construct may also be required to promote chemotaxis and initial cell infiltration into the alginate hydrogel [153, 244]. Furthermore, in our previous publication, we also highlighted the importance of BMP-2 presentation, demonstrating that barriers to cell-microparticle contact, such as transwell separation and inadequate numbers of BMP molecules per microparticle, decreased the efficiency of C2C12 alkaline phosphatase induction and, potentially, BMP signaling. The dosing of BMP-2 and microparticles in this study resulted in a theoretical concentration of ~5 million BMP-2 molecules per microparticle. Since heparin microparticles are on a similar size scale as cells (5 μm compared to 10 μm) and are expected to retain the majority of loaded BMP-2 based on *in vitro* results, this high density of spatially confined BMP-2 molecules may have reduced the probability of infiltrating cells contacting BMP-2 molecules and increased steric hindrance of BMP-receptor interactions on cell surfaces.

Interestingly, both unloaded and BMP-2-loaded microparticles also induced proliferation of infiltrating cells after 2 weeks *in vivo* as evidenced by $Ki67^{+}$ staining in proximity to microparticles. We have previously addressed this phenomenon in regards to *in vitro* C2C12 proliferation in the presence of BMP-2-loaded microparticles, speculating that other mitogenic proteins may have bound to heparin microparticles and interacted with cells. We expect that similar events may be occurring *in vivo* in the bone defect, and that the concentration of serum borne proteins with high affinity for heparin, such as

fibronectin, apolipoproteins, and thrombospondins, may modulate cell proliferation [245-247]. Binding and adsorption of serum components to heparin microparticles and their subsequent effects on growth factor loading and release is an important consideration in the design of *in vivo* protein delivery vehicles, and is described further in Chapter 7.

4.5 Conclusions

In summary, delivery of BMP-2 using heparin microparticles incorporated into an alginate/PCL tissue engineering construct resulted in increased BMP-2 retention *in vivo* and robust mineralization within an orthotopic bone defect site, but did not perform as well as alginate/PCL constructs containing BMP-2 alone. Since the results observed in this study may be due to microparticle-mediated differences in BMP-2 retention and presentation, future BMP-2 delivery strategies using heparin microparticles will aim to mitigate this by further tuning the kinetics of BMP-2 release. This may be accomplished using a number of approaches, including changing the number of microparticles to alter BMP-2 distribution in the defect, introducing a combination of alginate-bound and microparticle-bound BMP-2 to provide a burst release of growth factor followed by sustained presentation, or incorporating more recently developed degradable heparin microparticles to prolong the timeframe of BMP-2 release into the surrounding tissue [120]. Ultimately, this study demonstrated the utility of heparin microparticles for BMP-2 delivery in a segmental bone defect model and provided valuable information about *in vivo* BMP-2 retention and presentation that informed additional experiments using this hybrid biomaterial system.

CHAPTER 5: DEVELOPMENT OF A MATHEMATICAL MODEL FOR BMP-2 DIFFUSION FROM AN ALGINATE TISSUE ENGINEERING CONSTRUCT

5.1 Introduction

In Chapter 4, we demonstrated that the addition of BMP-2-loaded heparin microparticles into alginate/PCL tissue engineering constructs resulted in attenuated mineralization within a rat femoral bone defect. It was hypothesized that this was partly due to the increased retention of BMP-2 by the microparticles (and, by extension, within the alginate construct), resulting in a low chemotactic effect and reduced cell infiltration from surrounding tissues. The ability to easily "dose in" specific amounts of heparin microparticles into this system provides us with the unique opportunity to further investigate the effect of BMP-2-microparticle interactions on BMP-2 release kinetics and retention in a tissue engineering construct. Given the vast number of combinations available in choosing both BMP-2 and microparticle doses, a computational model was created to explore the factors that influence BMP-2 release kinetics in the alginate/PCL construct *in silico* prior to conducting further *in vivo* experiments. Moreover, since the diffusion of BMP-2 through alginate hydrogel was expected to play an important role in BMP-2 release from the construct, a robust method to experimentally determine BMP-2 diffusion through hydrogels was also developed.

Both natural and synthetically engineered affinity-based growth factor delivery systems rely on specific protein-material interactions that can be defined by a characteristic association/binding rate constant (k_{on}) and dissociation/unbinding rate

constant (k_{off}). In the case of synthetic materials, these interactions can often be tuned by varying the density and strength of protein binding partners presented on a material [10, 134, 135, 248], as well as the relative amounts of free and bound protein [249, 250]. Natural affinity-based interactions, such as antibody-protein interactions and heparin-protein interactions, have provided the basis for designing many engineered protein delivery systems. Heparin's reversible interactions with a number of potent growth factors (BMPs, FGFs, VEGF, NT-3) have been well-documented and exploited for biomaterial development [235, 251, 252]; however, heparin itself lacks the tunability of growth factor binding affinities that many synthetic materials offer. Thus, biomaterials that allow incorporation of graded amounts of heparin, such as hybrid hydrogels containing heparin chains [120, 168] and the heparin microparticle-containing alginate/PCL construct described herein, present the opportunity to more specifically select the degree of protein affinity that a material exhibits.

Computational modeling can aid in designing and characterizing biomaterials for affinity-based growth factor delivery. Models have been previously developed to describe protein release from a number of affinity-based biomaterials [139, 253-256], including, most notably, FGF-2 and NGF release from a heparin-containing fibrin hydrogel [248, 257, 258], proteolysis-mediated VEGF release from a fibrin network [259], and the release of therapeutic fusion proteins (FGF-2 and chondroitinase ABC) from affinity peptide-modified hydrogels [260]. However, the majority of models developed thus far have focused primarily on specific interactions between proteins and affinity ligands, with minimal investigation into the additional role of protein diffusion through ligand-containing hydrogels. Moreover, even fewer models have attempted to combine diffusion

through a biomaterial with diffusion into surrounding tissue to gain a better understanding of how a released protein will penetrate an *in vivo* tissue defect over time, since the biological complexity of tissue injury environments renders such scenarios difficult to model over long time periods.

Consequently, we aimed to both create a computational model of *in vivo* BMP-2 delivery to a bone defect site and develop a facile method to experimentally determine the diffusion of therapeutic proteins, such as BMP-2, through commonly used biomaterial delivery vehicles. The model we developed employed both theoretical and experimentally determined values for BMP-2-microparticle affinities, BMP-2 diffusion through the alginate hydrogel, and BMP-2 diffusion through tissue surrounding the bone defect site. BMP-2 release was modeled over period of 14 days, because this time frame encompasses the majority of BMP-2 release *in vivo*, while minimizing the amount of biomaterial degradation and tissue remodeling that can occur, and simplifying the parameters required for the model.

Since the development of this model required an accurate measure of BMP-2 diffusion through the alginate hydrogel that makes up the bulk of the biomaterial delivery vehicle, we also developed a method to easily determine protein diffusion through hydrogels. By tracking the one-dimensional diffusion of a fluorescently labeled protein through a capillary tube over time, we were able to measure protein diffusion as accurately as standard well plate release assays, which can be subject to variability and require larger amounts of proteins and materials. This method was tested using several model proteins of various molecular weights, as well as BMP-2. Diffusion was

investigated in three commonly used hydrogels for BMP-2 delivery, including alginate [233], collagen [41, 153, 261], and poly-ethylene glycol (PEG) [262, 263].

Overall, these studies aimed to broaden the current understanding of affinity-based protein delivery systems, by providing a more comprehensive mathematical model of *in vivo* BMP-2 delivery and demonstrating the tunability of the alginate/PCL construct when affinity ligands, such as heparin microparticles, are included. Since heparin microparticles can be easily and dose-dependently added into the alginate/PCL delivery system, this tissue engineering construct provides the opportunity to investigate tunable BMP-2 release kinetics. Finally, by developing a robust method to measure protein diffusion through hydrogels, we also aimed to improve evaluation of protein release from biomaterial delivery vehicles, by providing tailored diffusion coefficients that are more accurate than those determined from theoretical calculations and easier to obtain than using other methods.

5.2 Materials and Methods

5.2.1 Fluorescent Labeling of Proteins

Proteins were fluorescently labeled for microscopy using NHS-fluorescein (5/6-carboxyfluorescein succinimidyl ester; Thermo Fisher Scientific; Ex: 494 nm, Em: 518 nm). Human immunoglobin G (IgG, MW = 150 kDa; Sigma Aldrich), bovine serum albumin (BSA, MW = 63 kDa; Sigma Aldrich), and bovine α-chymotrypsin (αCT, MW = 25 kDa; Sigma Aldrich) were reconstituted at 50 nM in 100 mM $NaPO_4$ (pH = 8.5),

while human recombinant BMP-2 (MW = 25 kDa; R&D Systems) was reconstituted in the same buffer at 10 nM due to its reduced solubility at basic pH. NHS-fluorescein was reconstituted in DMSO at 2 mM and diluted in sodium phosphate buffer to 750 nM for labeling IgG, BSA, and αCT, and 150 nM for labeling BMP-2 in order to achieve 15 times molar excess of label to protein. The reaction was allowed to proceed at room temperature in the dark for 4 hours in a total reaction volume of 100 μL. Following this, excess label was removed via gel filtration through Zeba Spin Desalting Columns with a 7 kDa molecular weight cut-off (Thermo Fisher Scientific). Protein labeling and removal of excess dye was confirmed by fractionation through a PD-10 desalting column (GE Healthcare Bio-Sciences), followed by quantification of fluorescence of each molecular weight fraction of the protein solution using a Synergy H4 microplate reader (Biotek). Proteins were stored at 4°C until use.

5.2.2 Preparation of Hydrogels

RGD-functionalized alginate (FMC Biopolymer, Philadephia, PA), which has previously been used for BMP-2 delivery in a rat femoral bone defect [233, 234], was reconstituted at 2% (w/v) in a 5:1 solution of Minimal Essential Media – Alpha Modification (αMEM; Thermo Fisher Scientific) and 4 mM hydrochloric acid (Sigma Aldrich). For alginate cross-linking via calcium sulfate, 2% alginate solution was mixed with excess $CaSO_4$ (61.7 mM final concentration) using the dual syringe method described previously [234] and in Chapter 4. Following gelation, alginate was injected in microcentrifuge tubes through a 22-gauge, blunt-tip needle to mimic injection in the bone

defect during surgery. Hollow borosilicate tubes (L: 100 mm, ID: 600 μm; VitroCom, Mountain Lakes, NJ) were immersed in a microcentrifuge tube containing ~100 μL of alginate hydrogel and tapped against the bottom of the microcentrifuge tube to fill ~3-4 cm of each capillary tube.

For alginate cross-linking via calcium chloride, hollow borosilicate tubes (L: 100 mm, ID: 600 μm; VitroCom, Mountain Lakes, NJ) were directly immersed in ~100 μL of uncross-linked 2% alginate solution such that liquid was drawn up via capillary action to fill ~3-4 cm of each tube. An insulin syringe with a 15-mm, 27-gauge needle (BD, Franklin Lakes, NJ) was used to inject a solution of 100 mM calcium chloride into the tubes in direct contact with the alginate solution. Calcium chloride was allowed to diffuse into the alginate solution overnight at 4°C to promote calcium-mediated cross-linking.

Collagen Type I from rat tail (Corning) in 0.02 N acetic acid at 8-11% (w/v) was mixed with 1 N sodium hydroxide and ethylenediaminetetraacetic acid (EDTA) on ice to obtain a final collagen solution of 6% (w/v) at a neutral pH (~7.4), as previously described [264]. Hollow borosilicate tubes (L: 100 mm, ID: 600 μm) were immersed in ~100 μL of collagen solution such that liquid was drawn up via capillary action to fill ~3-4 cm of each tube. Tubes were incubated in a humidified incubator at 37°C with 5% CO_2 overnight to promote collagen gelation.

Four-arm polyethylene glycol maleimide (PEG-MAL, 20 kDa; Laysan Bio, Arab, AL) was reconstituted in 20 mM HEPES (pH = 7.4) at 8% (w/v) and mixed with an equal volume of VPM cross-linker peptide (GCRDVPMSMRGGDRCG; AAPTEC, Louisville, KY) in 20 mM HEPES (pH = 7.4) at 1.2% (w/v) to get a final PEG-MAL solution of 4% (w/v), which has been previously used for BMP-2 and VEGF delivery in a mouse radial

bone defect model [262, 263]. Hollow borosilicate tubes (L: 100 mm, ID: 600 μm) were immersed in ~100 μL of PEG-MAL solution such that liquid was drawn up via capillary action to fill ~3-4 cm of each tube. The cysteine groups on the VPM peptide were allowed to react with the maleimide groups on the PEG macromer at room temperature at an acidic pH for at least 15 minutes until gelation had occurred.

5.2.3 Protein Diffusion through Hydrogels in Capillary Tubes

Fluorescently labeled proteins were diluted to 50 μg/mL for capillary tube diffusion experiments. After tubes were filled with collagen, alginate, or PEG hydrogels, an insulin syringe with a 15-mm, 27-gauge needle was used to inject the protein solutions into the tubes in direct contact with the hydrogels. Tubes were tapped gently to remove air bubbles from the interface. Three tubes were then placed on a glass microscope slide approximately 0.5 mm apart and with the protein-hydrogel interfaces aligned. The ends of the tubes were affixed to the glass slide and sealed using Silly Putty™ (Crayola, Easton, PA) to avoid evaporation of the protein solution or water loss from the hydrogels. This set-up is depicted in Figure 5.1.

Slides were imaged using a Zeiss AxioObserver XLmulti S1 inverted microscope (Carl Zeiss, Jena, Germany) with Zeiss MTB2004 64 bit software and an incubated stage. Images were taken at 37°C using a 2.5x objective lens, 0.5x camera, and GFP channel (Ex: 488 nm). A fluorescence image was taken every 4 minutes over a period of 2 hours to yield a total of 31 images. Hydrogels were visually inspected under the 2.5x objective lens at the end of the experiment to ensure no macroscopic structural changes had

occurred during imaging [262, 263]. Experiments with each protein and hydrogel were conducted in triplicate. Diffusion of free fluorescein dye (MW = 0.33 kDa; Thermo Fisher Scientific) was also evaluated as a small molecule control.

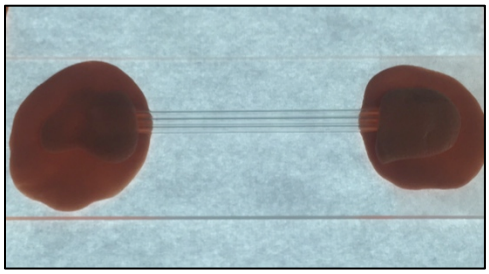

Figure 5.1. Capillary Tube Diffusion Set Up. For microscope imaging, three capillary tubes filled with hydrogel and protein solution were affixed to a glass slide (approximately 0.5 mm apart) using Silly Putty™.

5.2.4 Calculation of Effective Diffusion Coefficients in Capillary Tubes

Images from the capillary tube diffusion experiments were analyzed using ImageJ Software (NIH, Bethesda, MD). Images were opened as a stack and converted to gray scale; next, a line was drawn through the long axis of each tube to define a region of interest for fluorescence intensity measurements. The fluorescence intensity across each tube was measured within the microscope field of view (3.6 mm) and recorded for all 31 images, yielding a matrix of fluorescence intensity values at each time and distance. Fluorescence intensity throughout the hydrogel was normalized to the average fluorescence intensity displayed in the protein reservoir.

Diffusion of proteins through hydrogels in capillary tubes was approximated as one-dimensional diffusion from an infinite protein reservoir, since the length of the hydrogels (~3-4 cm) was much greater than their diameter (~600 μm), and the

fluorescence intensity of the protein reservoirs did not change significantly over the course of the experiments. Thus, diffusion through capillary tubes could be described using the following equation [264, 265]:

$$F(x,t) \propto erfc\left(\frac{x}{2\sqrt{D_{eff}t}}\right) \qquad (1)$$

in which *erfc* is the complementary error function, F = fluorescence normalized to the initial time point (dimensionless), x = distance from the protein reservoir (cm), t = time since protein-hydrogel contact (s), and D_{eff} = effective diffusion coefficient (cm^2/s). Normalized fluorescence intensity values were inputted into a custom MATLAB code (Appendix A), in which the *fmincon* function was used to perform non-linear curve fitting, evaluate the complementary error function, and determine D_{eff}.

5.2.5 Protein Release from Hydrogels in Well Plates

In order to compare typical protein release methods to the capillary tube diffusion method, 2% (w/v) alginate hydrogels containing 2.5 μg of BMP-2 were cross-linked using calcium sulfate and the dual syringe method mentioned above, and injected through a blunt-tip needle to form discs with a diameter of ~10 mm and thickness of ~2 mm (Total Volume = ~150 μL). The discs were then transferred to a 6-well plate (CoStar® Ultra-low Attachment Plate; Corning) and immersed in 10 mL of 0.1% (w/v) BSA in PBS for protein release in a 37°C humidified incubator with 5% CO_2. Small volume

samples (500 μL) were collected after 0.5, 1, 2, 4, 6, 9.5, and 24 hours and analyzed for BMP-2 content via ELISA; 500 μL of fresh solution was added after sample collection.

5.2.6 Calculation of Effective Diffusion Coefficients in Well Plates

The alginate discs made for well plate diffusion experiments satisfied both the infinite slab condition (disc diameter at least 4 times larger than thickness) and near-zero concentration boundary condition (fluid volume at least 20 times greater than hydrogel volume); thus, diffusion from the protein-filled hydrogel could be described using the following equation [266, 267]:

$$\frac{M_t}{M_\infty} \cong 2\sqrt{\frac{D_{eff}t}{\pi\delta^2}} \qquad (2)$$

in which t = time (s), δ = half of the disc thickness (cm), M_t = mass of BMP-2 in the release volume at time t (ng), M_∞ = final mass of BMP-2 in the release volume after equilibrium is reached at time infinity (ng), and D_{eff} = effective diffusion coefficient (cm^2/s). Using BMP-2 masses obtained via ELISA, M_t/M_∞ was plotted against $t^{1/2}$ and linear regression was used to determine the effective diffusion coefficient.

5.2.7 COMSOL Model Development

COMSOL Multiphysics software (Version 5.1.0.180; Burlington, MA) was used to develop a mathematical model to describe diffusion of BMP-2 from alginate and

heparin microparticle-containing alginate constructs within a femoral bone defect *in vivo*. The three-dimensional geometry of the construct (cylinder, D = 4.5 mm, L = 10 mm) and thigh (cylinder, D = 15 mm, L = 18 mm) (Figure 5.2A) was reduced to a two-dimensional modeling domain consisting of two nested rectangles with axial symmetry (Figure 5.2B).

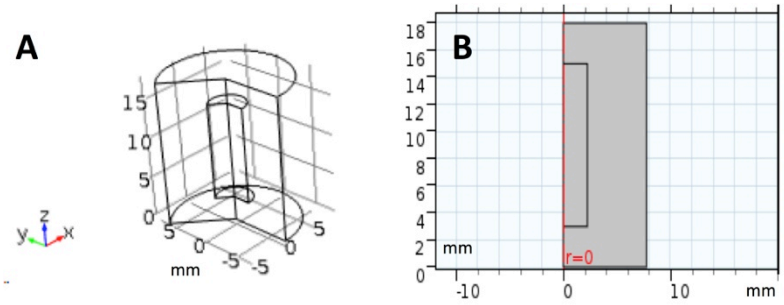

Figure 5.2. 3D and Reduced 2D Geometry of Alginate Construct in Rat Thigh. A) Three-dimensional geometry of alginate construct in bone defect in which construct is modeled as inner cylinder and surrounding thigh tissue is modeled as outer cylinder. B) Reduced two-dimensional geometry of alginate construct in bone defect consisting of two nested rectangles with axial symmetry, such that rotation around r=0 (red line) results in an inner and outer cylinder.

The reaction engineering interface was used to describe BMP-2 release from heparin microparticles (reaction), BMP-2 diffusion through alginate hydrogel (transport of dilute species), and BMP-2 diffusion through tissue (transport of dilute species). These processes can be described by the following equations:

$$\frac{\partial c_{BMP,Alg}}{\partial t} = \nabla \cdot \left(\mathrm{D}_{BMP,Alg} \nabla c_{BMP,Alg}\right) + R_{BMP,Alg} \qquad (3)$$

which describes the change in BMP-2 concentration in the alginate hydrogel over time ($\frac{\partial c_{BMP,Alg}}{\partial t}$) as a function of $D_{BMP,Alg}$ = diffusion coefficient of BMP-2 through alginate (m^2/s), $C_{BMP,Alg}$ = BMP-2 concentration in alginate (mol/m^3), and $R_{BMP,Alg}$ = rate of BMP-2 appearance/disappearance through microparticle association/dissociation ($mol/ m^3 \cdot s$);

$$\frac{\partial c_{BMP,Tiss}}{\partial t} = \nabla \cdot \left(D_{BMP,Tiss} \nabla c_{BMP,Tiss}\right) \qquad (4)$$

which describes the change in BMP-2 concentration in the thigh tissue over time ($\frac{\partial c_{BMP,Tiss}}{\partial t}$) as a function of $D_{BMP,Tiss}$ = diffusion coefficient of BMP-2 through thigh tissue (m^2/s) and $C_{BMP,Tiss}$ = BMP-2 concentration in thigh tissue (mol/m^3);

$$R_{BMP,Alg} = k_{off} C_{BMP+MP} - k_{on} C_{BMP} C_{MP} \qquad (5)$$

which describes the rate of BMP-2 appearance/disappearance in the alginate ($R_{BMP,Alg}$) based on binding with free sites on heparin microparticles to form the microparticle-BMP-2 complex (C_{BMP+MP}) at the association rate constant, k_{on}, and dissociation from occupied sites on heparin microparticles to form free BMP-2 (C_{BMP}) and free microparticle binding sites (C_{MP}) at the dissociation rate constant, k_{off}.

Several assumptions were made in order to model this complex biological system. First, it was assumed that the alginate hydrogel did not appreciably degrade in the time frame investigated (21 days); thus $D_{BMP,Alg}$ was not time-dependent, and heparin microparticles did not diffuse from their locations in the alginate construct or leave the construct boundary ($D_{MP,Alg} = 0$). Heparin microparticles were also assumed to be evenly distributed throughout the hydrogel, since this was demonstrated via histology and fluorescence imaging in Chapter 4. Furthermore, since the alginate hydrogel and thigh were semi-solid materials that allowed transport of BMP-2, which was somewhat spatially constrained, both materials were modeled as liquids in a batch reactor that was

not well mixed. At the boundary between the alginate hydrogel and the thigh, it was assumed that the BMP-2 concentrations were equal ($C_{BMP,Alg} = C_{BMP,Tiss}$). Finally, interstitial fluid flow and advection in the bone defect were considered negligible.

The parameters necessary for the equations above were defined and inputted into the COMSOL reaction engineering interface to compute solutions for alginate constructs (1) with and without heparin microparticles and (2) with BMP-2 either initially loaded into the alginate or loaded onto the microparticles; a time-dependent, direct solver (PARDISO) and an extra fine, user-defined mesh were used. All parameters are defined in Table 5.1 below for a low dose of BMP-2 (2.5 μg) delivered using 1 mg of heparin microparticles. The effective diffusion coefficient of BMP-2 through alginate ($D_{BMP,Alg}$) was calculated based on experimental data collected in capillary tube and well plate diffusion experiments, while the effective diffusion coefficient of BMP-2 through the surrounding nanofiber mesh and thigh tissue ($D_{BMP,Tiss}$) was approximated using previous BMP-2 retention data obtained through fluorescent BMP-2 tracking in the segmental bone defect [233]. The total number of BMP-2 binding sites on heparin microparticles was calculated on a per molecule basis using previous data that revealed the maximum binding capacity of heparin microparticles to be ~300 μg BMP-2/mg microparticles [107]. Previous data on the release of BMP-2 from heparin microparticles in PBS was also used to verify that the association and dissociation rate constants chosen accurately described the system. Rate constants were initially chosen based on literature values for BMP-2 binding to linear heparin (K_D = 20 nM, k_{on} = 5.1e-04 1/nM•s, k_{off} = 0.01 1/s) [3] and subsequently adjusted for heparin microparticles using a COMSOL model of *in vitro* BMP-2 and heparin microparticle interactions, which revealed that a slightly higher

dissociation constant than that of linear heparin was necessary to accurately model the experimental results (K_D = 50 nM, k_{on} = 5.1e-04 1/nM•s, k_{off} = 0.025 1/s).

Table 5.1. Parameters Used in COMSOL Model of BMP-2 Diffusion in Bone Defect

Category	Parameter	Value	Reference
Dimensions	Diameter of Alginate Cylinder	4.5 mm	
	Length of Alginate Cylinder	10 mm	
	Diameter of Thigh Cylinder	15 mm	
	Length of Thigh Cylinder	18 mm	
BMP-2 Diffusion Through Alginate	Effective Diffusion Coefficient ($D_{BMP,Alg}$)	1.7E-06 cm^2/s	
BMP-2 Diffusion Through Thigh	Effective Diffusion Coefficient ($D_{BMP,Tiss}$)	2.0E-08 cm^2/s	[233]
BMP-2 Interactions with Heparin Microparticles	Number of Heparin Microparticles	2.0E07	
	Number of Binding Sites	7.0E15	
(2.5 µg BMP-2 with 1 mg of microparticles)	Number of BMP-2 Molecules	5.8E13	
	Dissociation Constant (K_D)	50 nM	Adapted from [3]
	Dissociation Rate Constant (k_{on})	5.1E-04 1/nM•s	Adapted from [3]
	Association Rate Constant (k_{off})	0.025 1/s	Adapted from [3]

5.2.8 Statistical Analysis

All data are reported as mean ± standard error of the mean. Diffusion experiments were run with a minimum of three replicates for each experimental group. Statistical significance was determined using one-way or two-way ANOVA as appropriate, followed by Bonferroni's post hoc analysis (Graphpad Prism, Version 5.0, La Jolla, CA). $P < 0.05$ was considered statistically significant.

5.3 Results

5.3.1 Determination of Diffusion Coefficients Using Capillary Tube Method

In order to test the capillary tube method of evaluating hydrogel diffusivities, effective diffusion coefficients of proteins through 2% alginate ($CaCl_2$ cross-linked) and 6% collagen hydrogels were calculated for free fluorescein, BMP-2, and several model proteins of various molecular weights (α-chymotrypsin, bovine serum albumin, immunoglobin) by fitting the time- and space-dependent changes in fluorescence intensity throughout the hydrogel to a one-dimensional model of diffusion (Equation 1) [264, 265]. Samples images of BSA diffusion through 2% alginate hydrogels at 0 and 3 hours, can be seen in Figure 5.3 below. As expected, free fluorescein, which is a small molecule with a molecular weight of 0.3 kDa, displayed a higher effective diffusion coefficient than all model proteins diffusing through either alginate or collagen hydrogels (Figure 5.4A). There was no effect of the hydrogel used on the diffusivity of model proteins overall.

When the diffusion coefficients of model proteins were compared, it was found that α-chymotrypsin exhibited higher diffusion in collagen hydrogels compared to higher molecular weight proteins (bovine serum albumin, immunoglobin), while the diffusion coefficients of all of these proteins were similar in alginate (Figure 5.4B). This was likely due to the increased weight percent of collagen hydrogels compared to alginate hydrogels, which could further hinder diffusion. Despite the fact that few differences were observed, a linear correlation was identified when effective diffusion coefficients

were plotted against the molecular weights of model proteins (Figure 5.5), suggesting that the effective diffusion coefficient was, as expected and previously demonstrated [268-270], negatively correlated with protein molecular weight (R^2 = 0.96 for alginate, R^2 = 0.84 for collagen).

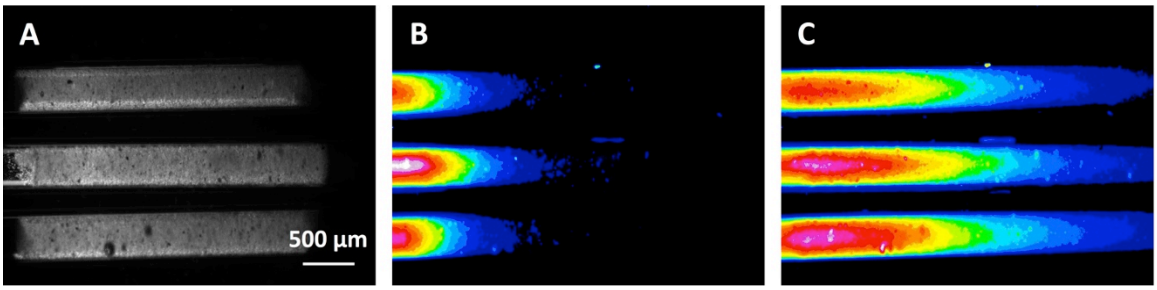

Figure 5.3. Images of Capillary Tube Diffusion Experiment. A) Bright field image of capillary tubes filled with 2% (w/v) alginate ($CaSO_4$ cross-linked) hydrogels. Fluorescence (GFP) images of fluorescein-labeled BSA diffusing through alginate hydrogels at B) 0 hours and C) 3 hours. Protein reservoirs are on the left side of the images.

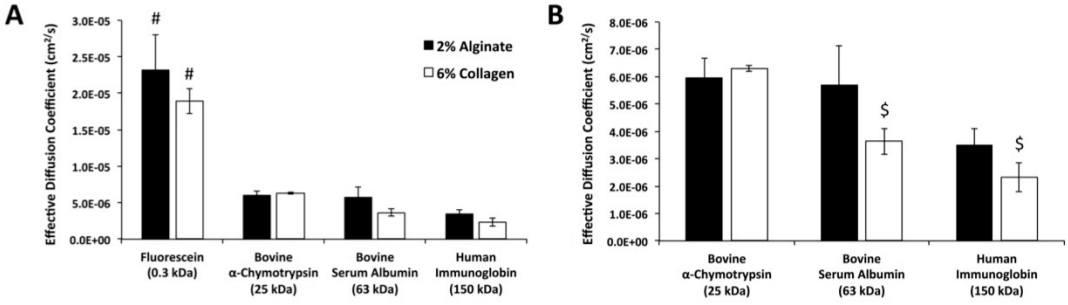

Figure 5.4. Effective Diffusion Coefficients of Free Fluorescein and Model Proteins in Hydrogels. A) Effective diffusion coefficients of fluorescein and model proteins (bovine α-chymotrypsin, bovine serum albumin, and human immunoglobin) in 2% (w/v) alginate ($CaCl_2$ cross-linked) and 6% (w/v) collagen hydrogels. Diffusion coefficients were determined using image analysis of fluorescently labeled biomolecules diffusing through capillary tubes filled with hydrogels. (# = $p < 0.05$ compared to all other proteins) B) Effective diffusion coefficients of only model proteins in 2% (w/v) alginate ($CaCl_2$ cross-linked) and 6% (w/v) collagen hydrogels. ($ = $p < 0.05$ compared to bovine α-chymotrypsin)

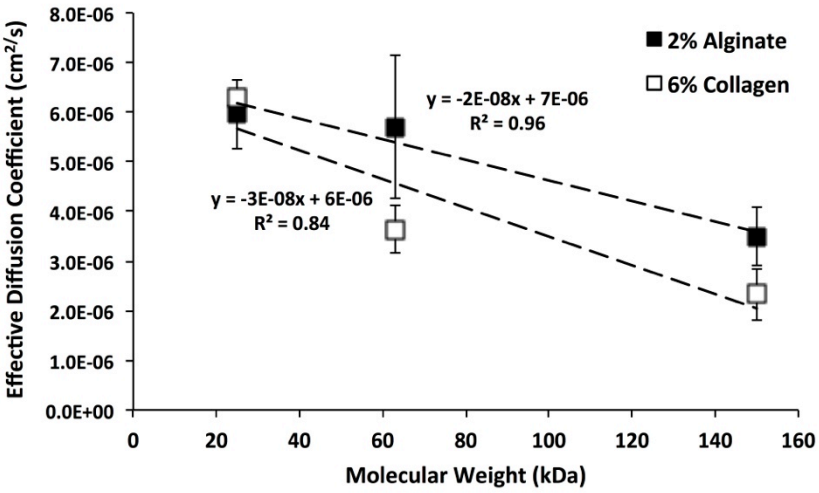

Figure 5.5. Effective Diffusion Coefficients of Model Proteins in Hydrogels. Effective diffusion coefficients of model proteins (bovine α-chymotrypsin, bovine serum albumin, and human immunoglobin) in 2% (w/v) alginate ($CaCl_2$ cross-linked) and 6% (w/v) collagen hydrogels plotted as a function of molecular weight. Trend lines represent linear fit of data for each hydrogel.

Effective diffusion coefficients of the therapeutic protein of interest, BMP-2, were determined for diffusion through 2% alginate ($CaCl_2$ cross-linked), 2% alginate ($CaSO_4$ cross-linked), 6% collagen, and 4% PEG hydrogels in capillary tubes. BMP-2 diffusion coefficients through 2% alginate ($CaCl_2$) and 6% collagen were comparable to diffusion coefficients of bovine α-chymotrypsin, which has a similar molecular weight and isoelectric point to BMP-2 (α-chymotrypsin: MW=25 kDa, pI=8.75; BMP-2: MW=26 kDa, pI=9.15). Interestingly, diffusion of BMP-2 through 2% alginate gels that were $CaSO_4$ cross-linked prior to filling capillary tubes and 4% PEG hydrogels was significantly slower (Figure 5.6). For $CaSO_4$ cross-linked alginate gels, slower BMP-2 diffusion may have been caused by entrapped air bubbles created during syringe cross-linking (as opposed to cross-linking after capillary tube loading). For PEG gels, slower BMP-2 diffusion may be attributed a smaller mesh size and structural differences caused

by the branched nature of the smaller PEG chains (~5 kDa) compared to the larger, more fibrillar collagen and alginate monomers (130-200 kDa).

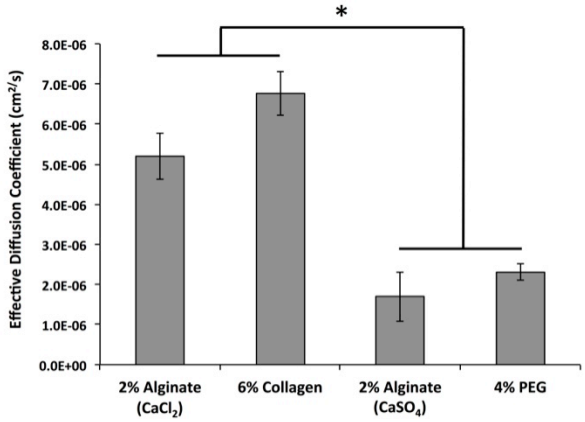

Figure 5.6. Effective Diffusion Coefficients of BMP-2 Through Various Hydrogels. Effective diffusion coefficients of BMP-2 diffusing through 2% (w/v) alginate ($CaCl_2$ cross-linked), 6% (w/v) collagen, 2% (w/v) alginate ($CaSO_4$ cross-linked), and 4% (w/v) PEG hydrogels. Diffusion coefficients were determined using image analysis of fluorescently labeled BMP-2 diffusing through capillary tubes filled with hydrogel. (* = $p < 0.05$ as indicated)

5.3.2 Determination of Diffusion Coefficients Using Well Plate Method

In order to verify the accuracy of the capillary tube method for determining diffusion coefficients through hydrogels, BMP-2 diffusion from a $CaSO_4$ cross-linked 2% alginate hydrogel in a 6-well plate was also monitored and used to calculate an effective diffusion coefficient with Equation 2. BMP-2 release from the alginate discs was monitored over 24 hours and reached a plateau after 9.5 hours (M_∞) (Figure 5.7B); the linear portion of the release curve was plotted as M_t/M_∞ vs. $t^{1/2}$ (Figure 5.7C), and the slope was evaluated to determine the effective diffusion coefficient. Of the 2.5 μg of BMP-2 loaded into the hydrogel disc, only ~200 ng total (8%) were released, despite considerable hydrogel degradation after only 6 hours in 0.1% BSA in PBS (Figure 5.7A); this may have been due to a number of reasons, including protein adsorption on plastic

surfaces and difficulty detecting BMP-2 via ELISA due to presence of alginate chains. Nevertheless, the portion of BMP-2 released and detected revealed an approximate effective diffusion coefficient of 1.2E-06 cm^2/s, which was similar to the diffusion coefficient of 1.7E-06 cm^2/s determined using the capillary tube method. The differences in the diffusion coefficients obtained may have been due to the aforementioned sources of protein loss or structural differences in hydrogels formed in glass capillary tubes versus plastic well plates.

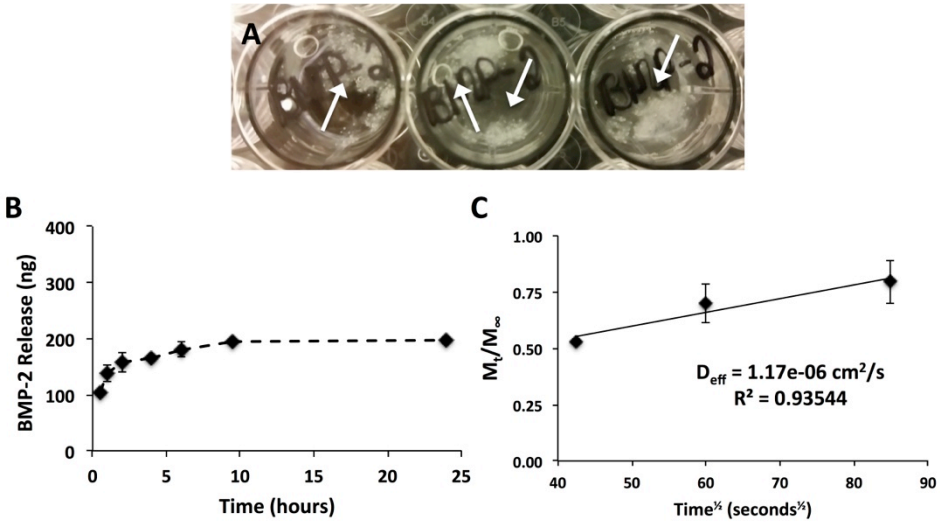

Figure 5.7. Effective Diffusion Coefficient of BMP-2 Through Alginate Hydrogel Disc. 2% (w/v) alginate containing 2.5 µg BMP-2 was $CaSO_4$ cross-linked in syringes and injected into ~150 µL discs. Discs were placed in 10 mL of 0.1% BSA in PBS, and 500 µL samples of release media were taken periodically over 24 hours. A) Alginate discs began breaking apart and degrading after 6 hours in 0.1% BSA in PBS. B) BMP-2 release from alginate discs was measured via ELISA over 24 hours. C) Using the linear portion of the BMP-2 release curve, M_t/M_∞ was plotted against the square root of time, and the slope was used to determine the effective diffusion coefficient of BMP-2 (D_{eff}) through 2% alginate gel.

5.3.3 COMSOL Simulations with Low Dose BMP-2

COMSOL simulations were run to model BMP-2 release from alginate/PCL constructs under the conditions investigated *in vivo* in Chapter 4, as well as a number of additional conditions. Simulations were run with and without microparticles, with partially loaded and unloaded microparticles (0% and 50% of total BMP-2), and with varying amounts of microparticles (0.001, 0.01, 0.1, 1 mg of microparticles). Table 5.2 below lists the simulations run using a low dose of BMP-2 (2.5 μg).

Table 5.2. COMSOL Simulations with Low Dose (2.5 μg) BMP-2.

Simulation	Description
1	2.5 μg of BMP-2 loaded in Alginate
2	2.5 μg of BMP-2 loaded in 1 mg of Microparticles in Alginate (100% Loaded)
3	2.5 μg of BMP-2 loaded in Alginate with 1 mg of Unloaded Microparticles (0% Loaded)
4	1.25 μg of BMP-2 loaded in Alginate and 1.25 μg of BMP-2 loaded 1 mg of Microparticles (50% Loaded)
5	2.5 μg of BMP-2 loaded in 0.1 mg of Microparticles in Alginate
6	2.5 μg of BMP-2 loaded in 0.01 mg of Microparticles in Alginate
7	2.5 μg of BMP-2 loaded in 0.001 mg of Microparticles in Alginate

COMSOL simulations of the conditions investigated *in vivo* in Chapter 4 (2.5 μg of BMP-2 in alginate and 2.5 μg of BMP-2 loaded onto 1 mg of heparin microparticles) revealed drastically different BMP-2 release profiles. Figure 5.8 displays heat maps of BMP-2 spatial distribution in the alginate construct and thigh after 1 and 14 days, as well as plots of the percentage of BMP-2 in the alginate and thigh over time. When BMP-2 was delivered in the alginate hydrogel (Figure 5.8A), 86% of the BMP-2 delivered was

released from the alginate construct into the surrounding tissue. Conversely, when the same amount of BMP-2 was delivered via 1 mg of heparin microparticles (Figure 5.8B), the model predicted that only 0.2% of the BMP-2 delivered was released into the surrounding tissue and 0.1% remained soluble within the alginate, while >99% of the BMP-2 delivered remained entrapped within the microparticles. This low release of BMP-2 was likely due to the large excess of BMP-2 binding sites (~6.9E15) available within constructs containing this number of microparticles, which could have resulted in re-association of BMP-2 that had previously dissociated from microparticles.

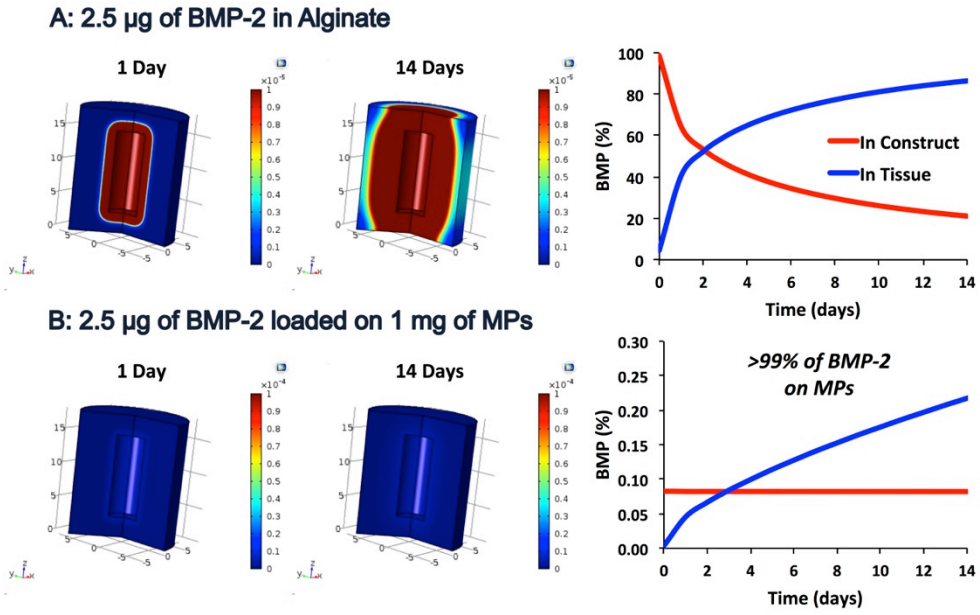

Figure 5.8. COMSOL Simulations of Low Dose BMP-2 Delivered in Alginate and on 1 mg of Heparin Microparticles. COMSOL simulations were run with A) 2.5 µg of BMP-2 in alginate and B) 2.5 µg of BMP-2 loaded onto 1 mg of microparticles in alginate. Heat maps display spatial distribution of BMP-2 concentration at 1 and 14 days. Graphs depict percentage of BMP-2 distributed between alginate hydrogel and thigh tissue between 0 and 14 days. In simulations of the microparticle-containing constructs, >99% of the delivered BMP-2 remains bound to the microparticles over the entire 14-day period.

Based on the above COMSOL simulations, it was hypothesized that the initial microparticle-containing alginate constructs investigated *in vivo* led to inadequate BMP-2

release and limited chemotactic stimulus for infiltrating cells, eventually resulting in a reduction in bone volume formed. Thus, further simulations were run to determine which parameters could be modified to increase BMP-2 release into the surrounding thigh tissue, while ensuring that a sufficient amount of BMP-2 remained within the construct to provide an osteogenic stimulus for infiltrating cells. Simulations were run to determine whether delivering a split dose of BMP-2 within the alginate and microparticles or delivering unloaded microparticles in a construct with alginate-bound BMP-2 would increase the amount of BMP-2 leaving the construct. Figure 5.9 depicts results from simulations run for (A) unloaded microparticles (all BMP-2 in alginate), (B) 50% loaded microparticles (split BMP-2 dose), and (C) 100% loaded microparticles (no BMP-2 in alginate); the total amount of BMP-2 delivered in all of these simulations was 2.5 μg. The model predicted that changing the loading regime of the microparticles would not drastically change the amount of BMP-2 leaving the alginate construct and entering the tissue, with the total amount of BMP-2 released into the tissue ranging from 0.2-0.4% after 14 days. Introducing unloaded heparin microparticles into an alginate construct loaded with BMP-2 was predicted to result in almost all of the BMP-2 in the construct associating with the empty microparticles in the delivery syringe before being injected into the bone defect for surgery; again, this model prediction may be attributed to the large excess of BMP-2 binding sites presented by this amount of heparin microparticles.

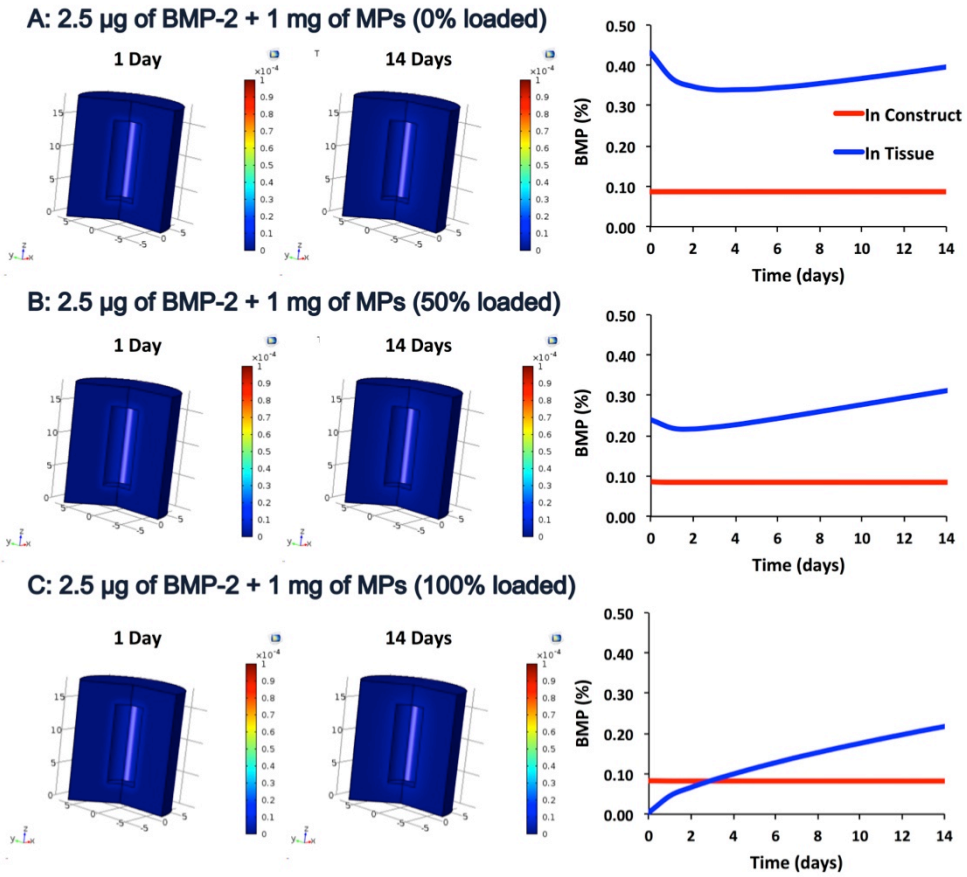

Figure 5.9. COMSOL Simulations of Low Dose BMP-2 Split Between Alginate and 1 mg of Heparin Microparticles. COMSOL simulations were run with A) 2.5 µg of BMP-2 in alginate with 1 mg of unloaded heparin microparticles (0% loaded), B) 2.5 µg of BMP-2 with 50% loaded onto 1 mg of microparticles and 50% alginate-bound (50% loaded), and C) 2.5 µg of BMP-2 loaded entirely on 1 mg of microparticles (100% loaded). Heat maps display spatial distribution of BMP-2 concentration at 1 and 14 days. Graphs depict percentage of BMP-2 distributed between alginate hydrogel and thigh tissue between 0 and 14 days. Regardless of loading regime, the majority of BMP-2 delivered re-associates with the microparticles, and >99% of the BMP-2 remains microparticle-bound over 14 days; only 0.2-0.4% of the BMP-2 enters the thigh tissue.

Thus, we next took advantage of the ability to dose-dependently alter the number of BMP-2 binding sites in the alginate construct by varying the number of microparticles delivered from 0.001-1 mg, with the goal of reducing the probability of BMP-2 molecules re-associating with microparticles after dissociation. Reducing the number of microparticles by 10-fold (0.1 mg or 2.0E06 microparticles) resulted in a 10-fold increase

in the amount of BMP-2 leaving the alginate construct (2.7% compared to 0.2%); the number of binding sites on 0.1 mg of microparticles was still in an excess of the number of BMP-2 molecules by an order of magnitude, promoting re-association of >95% of BMP-2 to microparticles (Figure 5.10B). However, when the number of microparticles was reduced by 100-fold (0.01 mg or 2.0E05 microparticles), and the total number of binding sites was of a similar magnitude to the number of BMP-2 molecules (7.0E13 sites and 5.8E13 BMP-2 molecules), BMP-2 dissociation from the microparticles and release into the surrounding tissue increased drastically, with predicted values of ~30% of the delivered BMP-2 entering the tissue, ~60% remaining bound to the microparticles, and ~10% free in the alginate hydrogel after 14 days (Figure 5.10C). Reducing the number of microparticles further, by 1000-fold (0.001 mg or 2.0E04 microparticles), resulted in far fewer binding sites than BMP-2 molecules (7.0E12 sites and 5.8E13 BMP-2 molecules), and a similar release profile to constructs without microparticles, with the majority of BMP-2 leaving the alginate hydrogel (79%) and only 8% of the BMP-2 remaining on the microparticles (Figure 5.10D). Thus, using a similar number of microparticle binding sites (0.01 mg microparticles) and BMP-2 molecules resulted in the most evenly distributed combination of both BMP-2 release and retention and better distribution of BMP-2 throughout the bone defect and surrounding tissue.

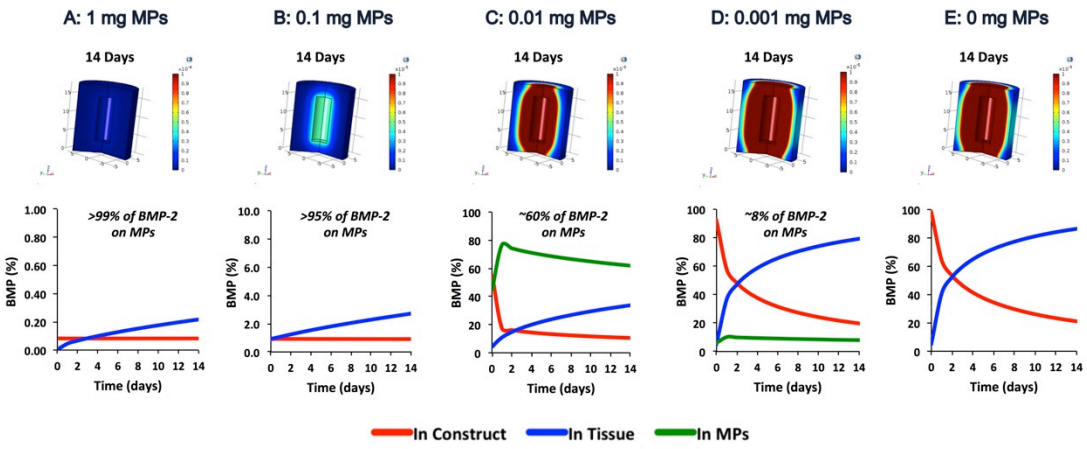

Figure 5.10. COMSOL Simulations of Low Dose BMP-2 Delivered Using Varying Amounts of Microparticles. COMSOL simulations were run with A) 2.5 µg of BMP-2 loaded onto 1 mg of heparin microparticles, B) 2.5 µg of BMP-2 loaded onto 0.1 mg of microparticles (10-fold reduction), C) 2.5 µg of BMP-2 loaded onto 0.01 mg of microparticles (100-fold reduction), D) 2.5 µg of BMP-2 loaded onto 0.001 mg of microparticles (1000-fold reduction), and E) 2.5 µg of BMP-2 loaded into alginate without microparticles. Heat maps display spatial distribution of BMP-2 concentration at 14 days. Graphs depict percentage of BMP-2 distributed between alginate hydrogel and thigh tissue between 0 and 14 days. Decreasing the number of microparticles in the system resulted in an increased amount of BMP-2 leaving the tissue engineering construct and entering the surrounding tissue.

5.3.4 COMSOL Simulations with High Dose BMP-2

Given the high affinity of heparin microparticles for BMP-2, resulting in low release of bound BMP-2 overall, it was hypothesized that heparin microparticles could also improve the spatial distribution of bone formation following treatment with high doses of BMP-2 (30 µg). Such BMP-2 doses typically result in the formation of heterotopic bone outside of the bone defect site when delivered in alginate hydrogel (Chapter 6) or collagen sponge (Chapter 7; Krishnan and Priddy, et al. *In review.*). Thus, heparin microparticles could be used to better localize BMP-2 release and subsequent bone formation within the bone defect. Since varying the number of microparticles

delivered was predicted to be the best way to alter the release kinetics of BMP-2 from the system, COMSOL simulations were run using a 30 μg BMP-2 dose in alginate or loaded onto 0.01-1 mg of heparin microparticles.

When 30 μg of BMP-2 were delivered using 1 mg of microparticles, >99% of the BMP-2 remained bound to the microparticles and only 0.2% of the BMP-2 entered the surrounding tissue after 14 days (Figure 5.11A); this was comparable to what was predicted for delivery of low dose BMP-2 with heparin microparticles, and was similarly due to the large excess of microparticle binding sites compared to BMP-2 molecules (7.0E15 sites and 3.5E14 BMP-2 molecules). When the number of microparticles in the system was reduced 10-fold to 0.1 mg (2.0E06 microparticles), the predicted amount of BMP-2 leaving the construct increased to 13%, with 83% of the BMP-2 bound to the microparticles and the residual 4% remaining free in the alginate hydrogel after 14 days (Figure 5.11B). However, a further reduction in the amount of microparticles (100-fold, 0.01 mg or 2.0E5 microparticles) resulted in fewer microparticle binding sites than BMP-2 molecules (7.0E13 sites and 3.5E14 BMP-2 molecules), and subsequently, the majority of the BMP-2 delivered was predicted to exit the construct (78%), with only 9% remaining bound to the microparticles (Figure 5.11C). This release profile was similar to that of alginate constructs lacking microparticles (Figure 5.11D), which has previously resulted in poor BMP-2 localization and heterotopic bone formation (Krishnan and Priddy, et al. *In review*.). Thus, delivering 30 μg of BMP-2 using 0.1-1 mg of heparin microparticles was expected to improve BMP-2 localization within the bone defect site. Furthermore, delivery of 30 μg of BMP-2 using 0.1 mg of microparticles was predicted to result in similar BMP-2 release into the surrounding tissue compared to delivery of 5 μg

of BMP-2 in alginate after 14 days (~4 µg; Figure 5.12); delivery of 5 µg of BMP-2 in alginate has previously exhibited robust bone formation in this animal model [233, 234], suggesting that its BMP-2 release profile promotes mineralization.

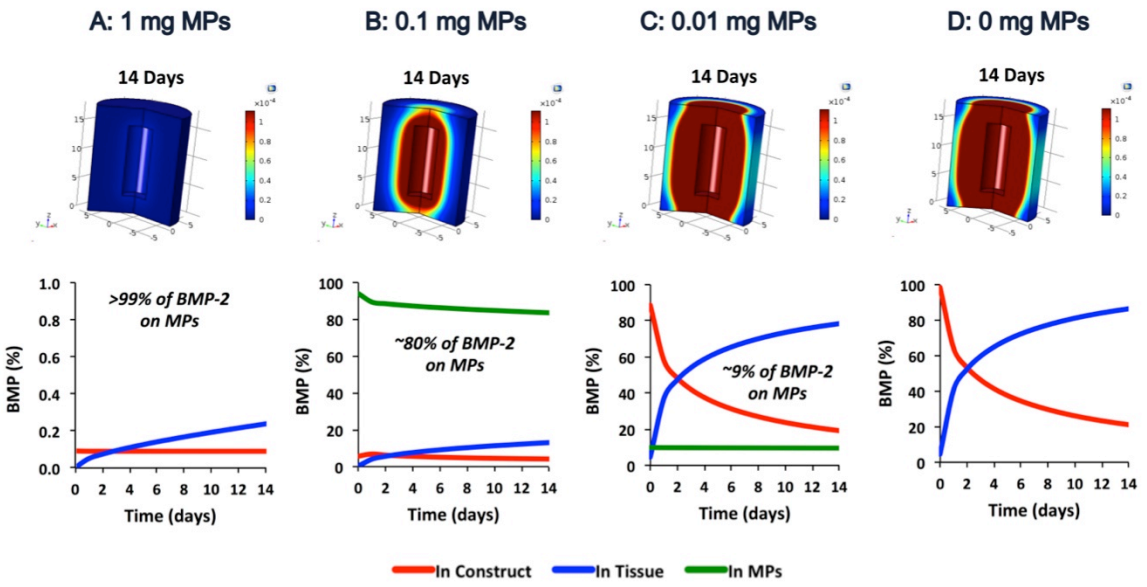

Figure 5.11. COMSOL Simulations of High Dose BMP-2 Delivered Using Varying Amounts of Microparticles. COMSOL simulations were run with A) 30 µg of BMP-2 loaded onto 1 mg of heparin microparticles, B) 30 µg of BMP-2 loaded onto 0.1 mg of microparticles (10-fold reduction), C) 30 µg of BMP-2 loaded onto 0.01 mg of microparticles (100-fold reduction), and D) 30 µg of BMP-2 loaded into alginate without microparticles. Heat maps display spatial distribution of BMP-2 concentration at 14 days. Graphs depict percentage of BMP-2 distributed between alginate hydrogel and thigh tissue between 0 and 14 days. Decreasing the number of microparticles in the system resulted in an increased amount of BMP-2 leaving the tissue engineering construct and entering the surrounding tissue.

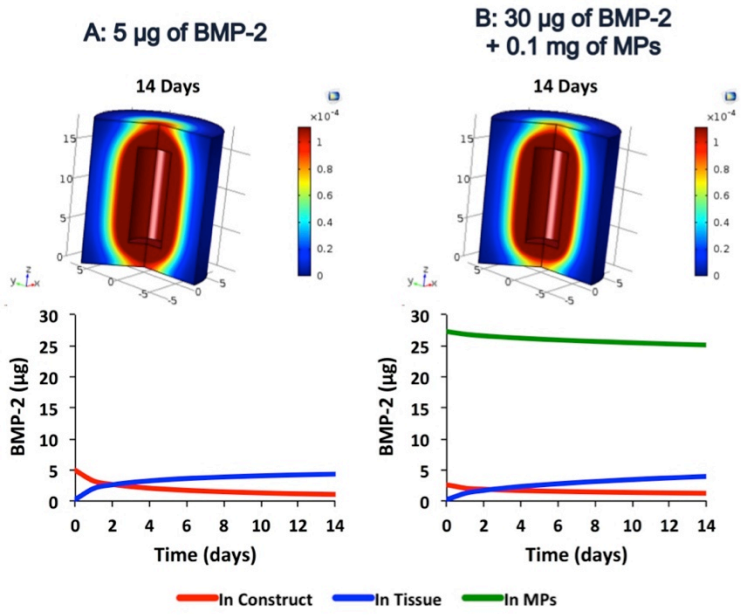

Figure 5.12. Comparison of COMSOL Simulations Using 5 µg of BMP-2 and 30 µg of BMP-2 Loaded onto 0.1 mg of Microparticles. COMSOL simulations were run with A) 5 µg of BMP-2 in alginate and B) 30 µg of BMP-2 loaded onto 0.1 mg of microparticles. Heat maps display spatial distribution of BMP-2 concentration at 14 days. Graphs depict amount of BMP-2 distributed between alginate hydrogel and thigh tissue between 0 and 14 days. Both conditions result in similar release of BMP-2 into tissue over 14 days.

5.3.5 COMSOL Model Sensitivity Analysis

Finally, a sensitivity analysis was run on several key parameters used in the COMSOL model to determine which parameters had the greatest effects on BMP-2 release kinetics and could potentially result in changes to the overall BMP-2 distribution if they deviated from the expected values. The sensitivity analysis was run using 0.1 mg of heparin microparticles and 2.5 µg of BMP-2, since the large excess of binding sites present on 1 mg of microparticles made it difficult to detect differences caused by changes in BMP-2-microparticle interactions.

Under the standard parameters used, 97% of the BMP-2 delivered was predicted to remain on the microparticles after 14 days, while 0.3% and 2.7% were released into the alginate and surrounding tissue, respectively. When the dissociation kinetics of BMP-2 from microparticles were increased 10-fold (k_{off} = 0.25 1/s), the amount of BMP-2 released from the microparticles increased substantially, with 18% of the delivered BMP-2 being released into the tissue and 76% remaining on the microparticles. Conversely, when the dissociation constant was decreased 10-fold (k_{off} = 0.0025 1/s), the majority of BMP-2 remained bound to the microparticles (>99%). Interestingly, increasing and decreasing the effective diffusion coefficient of BMP-2 through alginate did not have a effect on BMP-2 release from the construct. On the other hand, when the diffusion coefficient of BMP-2 through the surrounding tissue was increased 10-fold ($D_{BMP,Tiss}$ = 2.0E-07 cm^2/s), BMP-2 release into the tissue increased to 9%, and the amount remaining of the microparticles dropped to 90%. When $D_{BMP,Tiss}$ was decreased 10-fold (2.0E-09 cm^2/s), BMP-2 retention of the microparticles was increased to 99%.

Overall, the sensitivity analysis suggested that the results of the COMSOL model are governed primarily by the dissociation kinetics of BMP-2 from heparin microparticles (i.e. the affinity of heparin microparticles for BMP-2) and the diffusion coefficient of BMP-2 through the surrounding tissue, whereas the diffusion coefficient of BMP-2 through alginate does not play an important role. Deviations from the expected values for k_{off} and $D_{BMP,Tiss}$ are more likely to result in changes to the overall BMP-2 distribution, and thus, the heparin-BMP-2 dissociation constant and BMP-2 diffusion through surrounding tissue deserve additional consideration.

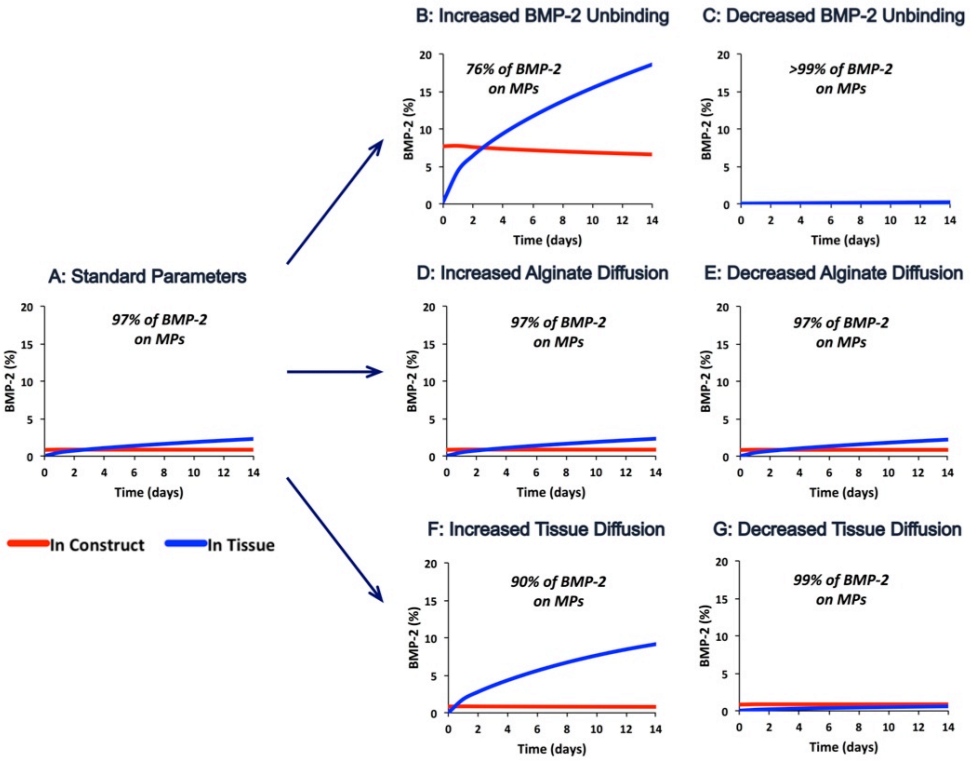

Figure 5.13. Sensitivity Analysis of Key Parameters in COMSOL Model. COMSOL simulations were run with 2.5 μg of BMP-2 loaded onto 0.1 mg of microparticles, and several key parameters were increased and decreased by 10-fold to determine the model's sensitivity to deviations in these values. A) Graph of BMP-2 distribution in microparticles, alginate, and tissue based on the standard modeling parameters. Graphs of BMP-2 distribution if dissociation constant of BMP-2 from heparin microparticles was B) increased 10-fold (k_{off} = 0.25 1/s) or C) decreased 10-fold (k_{off} = 0.0025 1/s). Graphs of BMP-2 distribution if BMP-2 diffusion through alginate was D) increased 10-fold ($D_{BMP,Alg}$ = 1.7E-05 cm^2/s) or E) decreased 10-fold ($D_{BMP,Alg}$ = 1.7E-07 cm^2/s). Graphs of BMP-2 distribution if BMP-2 diffusion through tissue was F) increased 10-fold ($D_{BMP,Tiss}$ = 2.0E-07 cm^2/s) or G) decreased 10-fold ($D_{BMP,Alg}$ = 2.0E-09 cm^2/s).

5.4 Discussion

In order to improve heparin microparticle-based BMP-2 delivery *in vivo*, an *in silico* investigation of BMP-2 delivery strategies was conducted following the initial *in vivo* segmental defect study using heparin microparticles described in Chapter 4. A COMSOL model was created to determine how the relative amounts of BMP-2 and microparticles in the system, as well as different microparticle loading regimes, could

impact overall BMP-2 release from alginate/PCL constructs implanted in the femoral defect site. Interestingly, constructs containing the dose of heparin microparticles used in the initial *in vivo* study (1 mg) were predicted to exhibit low BMP-2 release (<0.4%), regardless of the proportion of the BMP-2 loaded onto the microparticles vs. entrapped within the alginate. These results were supported by *in vitro* BMP-2 release profiles, which, despite demonstrating a higher magnitude of BMP-2 release overall, revealed that alginate/PCL constructs containing loaded microparticles exhibited BMP-2 release that was not statistically different from that of constructs containing unloaded microparticles co-delivered with the same amount of BMP-2 (Figure 4.2B). The high quantity of theoretical unoccupied BMP-2 binding sites on 1 mg of heparin microparticles compared to the number of BMP-2 molecules delivered may be the most significant factor contributing to the low BMP-2 release predicted in this scenario, since the likelihood of BMP-2 molecules rebinding to heparin microparticles and impeding release from the construct is increased.

Attenuated BMP-2 release demonstrated in the presence of heparin microparticles in the alginate/PCL construct may explain the lower bone volumes observed following heparin microparticle-mediated BMP-2 delivery *in vivo*; however, considering that 60% of the defects treated with heparin microparticles exhibited mineralized bridging (Figure 4.6), it is unlikely that only 0.2% of delivered BMP-2 entered the surrounding tissue. This possible discrepancy between *in vivo* experimental data and *in silico* model simulations may be due to a variety of biological factors that could not be accurately recapitulated in this model, including early alginate degradation, microparticle movement, and changes in the diffusivity of the construct following cell infiltration and material degradation.

Although we chose to ignore the effects of interstitial fluid flow on advective transport in order to simplify the parameters of the model, literature values for typical interstitial flow velocities observed within tissues suggest that advection may indeed play a role in BMP-2 transport in the bone defect. The Peclet number of the system, which is a indication of the relative contributions of advection and convection to transport of a biomolecule, could be calculated based on our approximated BMP-2 diffusion coefficient through tissue (2.00E-8 cm^2/s) and theoretical interstitial fluid velocity (6.00E-7 cm/s) [271]; the Peclet number was found to be on the order of ~1600, indicating a potentially significant contribution of advection; this parameter could be incorporated into future models.

Furthermore, numerous cytokines, ECM proteins, and growth factors present in the tissue injury site with affinity for heparin may displace BMP-2 from heparin microparticles upon contact and accelerate its release [1]. The role of serum proteins in BMP-2-heparin microparticle interactions is an important consideration, which will be explored further in Chapter 7. Although the current model does not take into account competitive protein binding as a factor affecting BMP-2 dissociation from microparticles, future iterations could include this aspect to increase model accuracy. Additionally, a COMSOL model of *in vitro* BMP-2 release from alginate/PCL constructs in well plates could also be developed to validate the some of the parameters chosen for the *in vivo* COMSOL model.

Despite these shortcomings, the computational model developed provides valuable information that informed the design of the *in vivo* experiments described in Chapter 6 and will contribute to future experiments that employ a heparin microparticle-based protein delivery vehicle. The drastic changes in BMP-2 release caused by changing

the number of microparticles delivered revealed that microparticle dosing could provide the alginate/PCL construct with a substantial degree of BMP-2 affinity tunability. The sensitivity analysis of key model parameters, such as the kinetics of BMP-2-microparticle association/dissociation and BMP-2 diffusion through alginate and surrounding tissue, further confirmed that the interactions between BMP-2 and heparin microparticles played the most significant role in determining BMP-2 release from the construct, and thus changing the number of available BMP-2 binding sites (i.e. microparticles) could present a simple strategy for altering these interactions. Other researchers have created delivery systems that tailor affinity interactions by selectively desulfating heparin to change its affinity for growth factors [103, 115, 120] and isolating ECM and protein fragments to serve as more specific affinity ligands [134, 272, 273]. The computational model developed in this work can also be applied to these systems in the future by simply changing the kinetics of protein association/dissociation (k_{on}, k_{off}) to suit these specific affinity ligands.

In addition to the mathematical model developed, a simple and robust method for determining protein diffusion through hydrogels was also established to fulfill the need for an accurate effective diffusion coefficient for BMP-2 through 2% (w/v) alginate. Since alginate is a naturally derived material that exhibits high natural and post-processing variability [274-276], the ability to experimentally determine a diffusion coefficient for the specific alginate used in our studies was imperative. The equation describing one-dimensional diffusion that was chosen for our analysis has typically been applied to diffusion of proteins through *in vivo* capillary beds and has been widely used to investigate interstitial transport in normal and neoplastic tissues [265]. Previously,

diffusion of gelatin nanoparticles through collagen hydrogels in capillary tubes has been investigated as an *in vitro* model of nanoparticle penetration through collagen-rich tumor tissues. We sought to adapt this *in vitro* model of tumor transport so that it could be more broadly applied as a method of determining diffusion through various hydrogels.

The capillary tube diffusion method was successfully used to evaluate the effective diffusion coefficients of several model proteins in addition to our protein of interest (BMP-2) in alginate, collagen, and PEG hydrogels, since all of these hydrogels have previously shown utility as BMP-2 delivery vehicles [42, 234, 263]. Diffusion of model proteins through hydrogels decreased with increasing molecular weight, as previously observed [268-270], and no differences were detected between diffusion in 2% (w/v) alginate ($CaCl_2$ cross-linked) and 6% (w/v) collagen hydrogels. In fact, the effective diffusion coefficients for BMP-2 through these hydrogels were similar to that of BMP-2 diffusion through water, as calculated using the Stokes-Einstein equation (1.3E-06 cm^2/s) [269], suggesting that the low weight percentages of the gels and density of crosslinks were not high enough to cause hindered diffusion.

Interestingly, BMP-2 diffusion was decreased through 2% (w/v) alginate hydrogels that were cross-linked with $CaSO_4$ prior to filling capillary tubes and also 4% (w/v) PEG hydrogels. Cross-linking alginate hydrogels using $CaSO_4$ and the dual syringe method introduced numerous air bubbles into the gel, similar to air bubbles introduced into gels using during surgical injection; these air bubbles may have impeded protein diffusion. Since the dual syringe method has typically been used for alginate preparation for the segmental defect model [234], we were able to use our diffusion characterization method to obtain an effective diffusion coefficient unique to our system, while

demonstrating that distinct differences in diffusion through alginate hydrogels can occur simply due to cross-linking method. As mentioned previously, for PEG hydrogels, slower BMP-2 diffusion may be attributed to a smaller hydrogel mesh size due to the branched nature of the PEG chains. The four-arm PEG-MAL used within this study contained uniformly spaced cross-linking sites at the end of each ~5 kDa branch. On the other hand, individual collagen fibers (~130 kDa) and alginate chains (150-200 kDa) are more fibrillar in nature; larger, non-uniform meshes are typically formed by these natural materials that rely heavily on physical entanglement as well as electrostatic interactions for cross-linking, and the spacing between cross-links can vary. Overall, the capillary tube method of determining diffusion coefficients provides comparable results to standard protein release assays, but over a shorter period of time and without variability introduced by hydrogel and protein degradation. While other fluorescence-based diffusion analyses often require microfluidic platforms [277] or confocal microscopes to perform fluorescence recovery after photo-bleaching (FRAP) [278], this method can be easily performed with a standard laboratory microscope with a low power objective and temperature controlled stage.

5.5 Conclusions

Herein, we described the development of a mathematical model to predict BMP-2 release from an alginate/PCL tissue engineering construct within a segmental bone defect, as well as a novel method for evaluating protein diffusion in hydrogels commonly used for BMP-2 delivery. Together, these new developments provide insight into *in vitro*

protein diffusion through hydrogel biomaterials and may help to design better biomaterial delivery vehicles that can effectively modulate protein release *in vivo*. The ability to model varying numbers of heparin microparticles in the alginate/PCL construct helped to both reveal the tunable nature of this system and inform future *in vivo* experiments using heparin microparticles. Furthermore, these versatile platforms can be more broadly applied to other tissue engineering constructs in the future, providing valuable information on protein release profiles that will aid in the design of other *in vivo* studies.

CHAPTER 6: HEPARIN MICROPARTICLES REDUCE HETEROTOPIC BONE IN A FEMORAL DEFECT MODEL USING HIGH DOSE BMP-2

6.1 Introduction

In Chapter 5, we developed a mathematical model, which predicted that the presence of heparin microparticles in alginate/PCL constructs would attenuate BMP-2 release *in vivo*; furthermore, the *in vivo* bone healing results in a femoral bone defect model that were presented in Chapter 4 demonstrated that the delivery of a low dose of BMP-2 using heparin microparticles resulted in decreased mineral formation. Together, these data led to the hypothesis that heparin microparticles reduced BMP-2 release from the alginate/PCL construct, resulting in decreased BMP-2 availability and suboptimal bone healing. Since heparin microparticles have exhibited a strong affinity for BMP-2 both *in vitro* and *in vivo* thus far, they may be better suited for use in bone healing applications in which highly localized delivery of BMP-2 is required.

BMP-2 use in the clinic is typified by supraphysiological growth factor doses ranging from 0.1-0.5 mg BMP-2/kg body weight, although off-label use of doses as high as 1 mg BMP-2/kg body weight have also been reported [6, 9, 36, 279, 280]; high BMP-2 doses are required in order to ensure stimulation of endogenous repair mechanisms despite rapid growth factor release from the site of interest. In comparison, the rat femoral defect model described herein exhibits consistent bony bridging using BMP-2 doses of 0.01-0.02 mg BMP-2/kg body weight [233, 234]. The significantly higher doses of BMP-2 required for bone healing in humans compared to pre-clinical rodent models

may be attributed to a lower capacity for bone regrowth following traumatic injury [281], and thus biomaterial strategies developed with lower doses of BMP-2 in rats may be required to effectively deliver higher BMP-2 doses when ultimately used in humans.

The absorbable collagen sponge, most commonly used in the clinic as a BMP-2 delivery scaffold, has also contributed to the use of supraphysiological BMP-2 doses in humans. Collagen sponges entrap BMP-2 through weak electrostatic interactions, resulting in a burst release of molecular cargo upon implantation in the tissue defect; thus, low retention of BMP-2 at the site of interest has necessitated the use of high BMP-2 doses in order to ensure adequate stimulation of bone healing. The lack of definitive dose response data for BMP-2 treatment in humans due to differences in surgical approaches used between studies has also made lowering standard doses while maintaining similar efficacy difficult [9, 279, 280].

Due to the collagen sponge's limited ability to control BMP-2 diffusion following implantation *in vivo*, a number of side effects associated with rapid growth factor loss have been documented in patients. Excessive soft tissue inflammation or seroma [9, 44, 282], hematoma [9, 283], and heterotopic ossification [43, 45, 283] adjacent to the bone defect site have been observed following delivery of higher doses of BMP-2 using the clinical collagen sponge. In patients undergoing off-label BMP-2 treatment for spinal fusion, adverse events have been documented to occur in as many as 23-28% of patients [9, 44]. Heterotopic ossification in particular has been reported in both on- and off-label use of BMP-2-loaded collagen sponges in the clinic, as well as a number of pre-clinical animal studies in which relatively high doses of BMP-2 have been delivered in canine and rat segmental defect models [284, 285]. Overall, these studies highlight the

limitations of current BMP-2 delivery strategies and motivate further investigation into methods of spatially limiting BMP-2 diffusion *in vivo* when high dose BMP-2 is used.

Our laboratory has recently investigated high, clinically relevant doses of BMP-2 (0.12 mg BMP-2/kg body weight) in a rat femoral defect model, and recapitulated the incidence of heterotopic bone observed using a collagen sponge delivery vehicle (Krishnan and Priddy, et al. *In review*.). In comparison, the use of our alginate/PCL tissue engineering construct reduced heterotopic ossification from >50% to <30% of the total bone volume, but could not completely eliminate bone formation outside of the defect space, suggesting that an appreciable amount of BMP-2 was still released into the surrounding tissue. Alternatively, the high growth factor loading capacity of heparin microparticles (~300 μg BMP-2/mg microparticles) and low *in vitro* release of loaded BMP-2 (<20%) [107] make heparin-based materials a prime candidate for improving high dose BMP-2 delivery and reducing the incidence of heterotopic ossification. The *in vivo* results presented in Chapter 4, which use heparin microparticles in an alginate/PCL construct as a carrier of low dose BMP-2, suggested that increased BMP-2 retention within the tissue engineering constructs (Figure 4.4) may have been responsible for the decreased mineral volumes observed within the defect (Figure 4.6).

Thus, in this study, we chose to deliver 30 μg of BMP-2 (0.12 mg BMP-2/kg body weight) in a rat femoral defect model using alginate/PCL constructs with and without 0.1-1 mg of heparin microparticles. The ability to cross-link alginate hydrogels with varying amounts of BMP-2-laden microparticles gave us the opportunity to tune the density of BMP-2 presentation and effective BMP-2 release profiles of the alginate/PCL constructs used. Since the results of our computational model predicted that loading 30

μg of BMP-2 onto 0.1 or 1 mg of heparin microparticles would result in release of ~13% (4 μg) or ~0.2% (0.06 μg) of the total BMP-2 dose, respectively, we could compare these release profiles with that of a construct containing no heparin microparticles, which has been shown to induce some heterotopic bone formation with a predicted release of ~86% (25.8 μg) of the delivered BMP-2 over 14 days. Herein, we present both *in vitro* and *in vivo* BMP-2 release profiles from alginate/PCL constructs with or without heparin microparticles, followed by the results of the *in vivo* study investigating bone healing in an orthotopic model in response to BMP-2 delivery vehicles of varying effective BMP-2 affinities.

6.2 Materials and Methods

6.2.1 Fabrication of Alginate/Polycaprolactone Constructs

Alginate/PCL constructs for *in vitro* testing and *in vivo* delivery were fabricated as described previously [233, 234] and in Chapter 4. Heparin microparticles were fabricated as previously described [107]. Briefly, irradiated, RGD-functionalized alginate (FMC Biopolymer) was first slowly dissolved in α-MEM (Corning Mediatech) for 4 hours at room temperature to achieve a 3% (w/v) alginate solution. Equal volumes of α-MEM and 0.1% rat serum albumin (RSA; Sigma, Aldrich) in 4 mM HCl were then added to dilute the alginate to 2% (w/v) prior to cross-linking. At this stage, the requisite amounts of BMP-2 (2.5-30 μg) and/or heparin microparticles (0-1 mg) per 150 μL of alginate hydrogel were added into the solution in 0.1% RSA in HCl. The 2% alginate

solution was then cross-linked with excess calcium sulfate (8.4 mg/mL; Sigma Aldrich) by rapid mixing between two 1 mL syringes (Becton-Dickinson) connected through a Luer-Lok style connector (Cole-Parmer, Vernon Hills, IL). After several minutes of mixing, the alginate was allowed to solidify at room temperature for approximately 30 minutes before being transferred to 4°C for storage overnight.

Polycaprolactone (PCL) nanofiber mesh tubes were also fabricated as previously described [234]. Briefly, PCL (Sigma Aldrich) was dissolved overnight with gentle stirring in a 90:10 solution of hexafluoro-2-propanol (HFP; Sigma Aldrich) and dimethylformamide (DMF; Sigma Aldrich) to obtain a 12% (w/v) PCL solution. 5 mL of solution was loaded into a 5 mL syringe (Becton Dickinson) with a 20-gauge blunt-tip needle (Howard Electronic Instruments), bubbles were removed, and the syringe was mounted onto a PHD2000 Infusion syringe pump (Harvard Apparatus). For the electrospinning setup, the syringe pump was placed so that the needle tip was ~20 cm away from a rectangular copper collection plate covered with aluminum foil for PCL nanofiber deposition. The syringe pump was set to a constant infuse rate of 0.75 mL/hr and infuse diameter of 12.060 mm, and a high voltage supply (HV Power Supply, Gamma High Voltage Research, Ormond Beach, FL) was connected to the syringe needle and copper collection plate to provide a voltage difference of ~15-20 kV. The voltage was periodically adjusted to maintain a Taylor cone at the needle tip during electrospinning [286]. A total of 4.5 mL of PCL solution was infused for each mesh, creating a circular mesh with an area of ~100 cm^2 and thickness of ~500 μm.

12 mm by 19 mm rectangles with twenty-three, evenly spaced 0.9 mm diameter perforations were laser-cut into the meshes to prepare nanofiber mesh tubes for tissue

engineering constructs. Each rectangular sheet was rolled into a tube with an inner diameter of 5 mm and length of 12 mm and glued using UV cure adhesive (1187-M MD Medical Device Adhesives & Coatings, DYMAX, Torrington, CT; BlueWave LED Prime UVA Spot Curing System, DYMAX, Torrington, CT). Mesh tubes were sterilized by 100% ethanol evaporation overnight, followed by immersion in 70% ethanol for 4 hours, immersion in PBS for 30 minutes, and finally immersion in α-MEM up until use.

For both *in vitro* and *in vivo* assays, 150 μL of alginate gel was injected through a 22-gauge, blunt-tip needle (Howard Electrical Instruments) into the center of each nanofiber mesh tube immediately prior to use. For *in vitro* assays, alginate was allowed to set in the mesh tube for at least 10 minutes prior to immersion in any solution. For *in vivo* assays, alginate was injected into the mesh tube after it was placed in the bone defect.

6.2.2 BMP-2 Release from Alginate/Polycaprolactone Constructs

Passive release of BMP-2 from alginate/PCL constructs into 0.1% (w/v) BSA in PBS was monitored over a period of 7 days at 37°C. Alginate/PCL constructs were fabricated with 2.5 μg of BMP-2 mixed into alginate alone or loaded onto 0.1 or 1 mg of heparin microparticles prior to mixing into alginate. Microparticles were loaded with BMP-2 in a small volume of 0.1% BSA in 4 mM HCl (25 μL/mg MPs) for 16 hours at 4°C the day before construct assembly. After alginate/PCL constructs were assembled and allowed to set for at least 10 minutes, the constructs were transferred to individual wells in an ultra-low attachment 24-well plate (Corning) and 1 mL of 0.1% BSA in PBS was added. At various time points, the solution was removed and centrifuged at 3000 rpm

for 5 minutes to separate the supernatant from any alginate or microparticle debris. The supernatant was removed and replaced with 1 mL of fresh 0.1% BSA in PBS before the entire solution was added back to the wells. This step was included to ensure minimal loss of alginate and microparticles from the system at each time point. Release samples were then analyzed for BMP-2 content via ELISA.

6.2.3 Subcutaneous Implant Surgical Procedure

Subcutaneous implant studies were undertaken to track *in vivo* retention of BMP-2 in constructs with or without heparin microparticles. BMP-2 was fluorescently labeled for tracking using the near-infrared dye Vivotag-750 (Perkin Elmer), according to the protocol reported in Chapter 4. All subcutaneous implant surgical procedures were conducted according to the Georgia Institute of Technology Institutional Animal Care and Use Committee (IACUC) protocol A16043. Briefly, 13-week-old female Sprague Dawley rats (Charles River Labs, Wilmington, MA) were anesthetized using isoflurane prior to surgery. Two lateral incisions were made on the back of each animal and a tunneling device was used to create four individual subcutaneous pockets for construct insertion, as previously described [212]. A metal rod and cannula were used to insert two constructs near the forelimbs and two near the hindlimbs. Constructs from each group were randomly distributed according to location (proximity to left forelimb, right forelimb, left hindlimb, and right hindlimb).

Constructs consisted of PCL meshes surrounding 150 μL alginate hydrogels containing (1) 2.5 μg of labeled BMP-2 in alginate (n=8), (2) 2.5 μg of labeled BMP-2

loaded onto 0.1 mg of microparticles in alginate (n=8), and (3) 2.5 μg of labeled BMP-2 loaded onto 1 mg of microparticles in alginate (n=8). Animals for these studies were euthanized using carbon dioxide asphyxiation after three weeks post-surgery.

6.2.4 In Vivo and Ex Vivo Fluorescence Imaging

In vivo and *ex vivo* fluorescent imaging was performed using an IVIS® Spectrum platform (Perkin Elmer). For VS750-labeled BMP-2 tracking, longitudinal *in vivo* imaging (Ex: 745, Em: 800, 5 second exposure) was performed immediately following subcutaneous implantation on Day 0, as well as on Day 1, 4, 7, 10, 14, and 21, as previous studies have demonstrated loss of detectable fluorescent signal after 21 days [233]. Alginate gels contained (1) 2.5 μg of labeled BMP-2 (n=8), (2) 2.5 μg of labeled BMP-2 loaded onto 0.1 mg of microparticles (n=8), or (3) 2.5 μg of labeled BMP-2 loaded onto 1 mg of microparticles (n=8). Animals were placed on their sides for imaging of two constructs at once. Total fluorescent counts and radiant efficiency were evaluated for each construct at each time point, both *in vivo* and *ex vivo*, using a ~7 cm^2 elliptical region of interest (ROI) in the Living Image Software (Perkin Elmer). Background fluorescence from the animal's skin was subtracted from each measurement, and fluorescent signal at each time point was normalized to the initial fluorescent signal measured at Day 0. BMP-2 retention data was fit to a one-phase exponential decay equation ($y=a\exp(-\lambda x)$) in MATLAB to obtain the decay constant, λ. Constructs were explanted after 21 days and also imaged *ex vivo* using the IVIS® Spectrum platform to examine residual BMP-2 fluorescence.

6.2.5 Femoral Defect Surgical Procedure

Femoral defect studies were undertaken to determine the ability of constructs with and without heparin microparticles and BMP-2 to promote bone healing and reduce heterotopic ossification in a critically sized defect. All surgical procedures were conducted according to the Georgia Institute of Technology IACUC protocol A14037. 13-week-old female Sprague Dawley rats (Charles River Labs) were anesthetized using isoflurane prior to surgery, and unilateral surgeries were performed as previously described [233, 239]. Briefly, after opening up the leg using an anterior approach, a radiolucent fixation plate (polysulfone) and two stainless steel risers were screwed directly onto the femur of the rat for limb stabilization, and an oscillating saw was used to create an 8-mm wide, full thickness diaphyseal defect. A PCL nanofiber mesh tube was inserted into the defect to cover the bone ends, and 150 μL of alginate was injected through the perforations into the center of the tube. Each alginate gel contained one of the following: (1) 30 μg of BMP-2 (n=14), (2) 30 μg of BMP-2 loaded onto 0.1 mg of microparticles (n=13), or (3) 30 μg of BMP-2 loaded onto 1 mg of microparticles (n=14). Animals for these studies were euthanized using carbon dioxide asphyxiation after twelve weeks post-surgery.

6.2.6 Faxitron and Micro-computed Tomography

Longitudinal *in vivo* radiographs of femurs were obtained at 2, 4, 8, and 12 weeks post-surgery, using a Faxitron MX-20 Digital machine at a voltage of 23 kV and

exposure time of 15 seconds; radiographs were used to qualitatively assess bony bridging across the defect space. *In vivo* micro-computed tomography (CT) of femurs was performed at 4, 8, and 12 weeks post-surgery to quantify total bone volume and overall mineral density, as well as the spatial distribution of bone formation and mineral density inside and outside of the defect space. Animals were anesthetized and scanned at a medium resolution using a VivaCT40 live animal scanner (Scanco, Switzerland) with a voxel size of 38.5 μm, voltage of 55 kVp, and current of 109 μA. Mineral was quantified within the central 5.85 mm (152 scan slices) of each 8 mm defect, and three different volumes of interest (VOIs) were identified: (1) total mineral volume of the thigh within the central region of interest, (2) mineral volume within the defect space, as defined by 6 mm diameter circular contours corresponding to the diameter of the nanofiber mesh, and (3) heterotopic mineral volume, which fell outside of the 6 mm diameter circular contours. A global threshold for new bone formation was set at 50% of the average mineral density of native cortical bone, and a Gaussian filter (sigma = 1.2, support = 1) was applied to suppress noise.

6.2.7 Statistical Analysis

All data are reported as mean ± standard error of the mean. *In vitro* experiments were run with a minimum of three replicates for each experimental group. For *in vivo* BMP-2 retention experiments, 8 constructs from each group were implanted. For *in vivo* bone defect experiments, longitudinal micro-CT was conducted on 13-14 femurs per group. Statistical significance was determined using one-way or two-way ANOVA as

appropriate, followed by Bonferroni's post hoc analysis (Graphpad Prism, Version 5.0, La Jolla, CA). For data that did not satisfy the assumptions of equal variances and Gaussian distributions, the nonparametric Kruskal-Wallis test was used. $P < 0.05$ was considered statistically significant.

6.3 Results

6.3.1 In Vitro BMP-2 Release from Alginate/Polycaprolactone Constructs

BMP-2 release from alginate/PCL constructs containing 0.1 mg of BMP-2-loaded heparin microparticles was evaluated similarly to BMP-2 release from constructs containing 1 mg of heparin microparticles presented in Chapter 4. 150 μL alginate constructs fabricated with 0, 0.1, or 1 mg of heparin microparticles were loaded with 2.5 μg of BMP-2 and allowed to passively release BMP-2 into a 0.1% (w/v) BSA in PBS solution over 7 days (Figure 6.1). Constructs containing 1 mg of BMP-2-loaded heparin microparticles released less BMP-2 than constructs containing 0.1 mg of microparticles or constructs lacking microparticles at all time points examined, with a total cumulative release of 55.1 ± 3.9 ng of BMP-2. Constructs containing BMP-2 alone and 0.1 mg of BMP-2-loaded microparticles exhibited similar release profiles, releasing nearly double the amount of BMP-2 as constructs containing 1 mg of microparticles, with a total release of 111.1 ± 1.7 ng and 102.2 ± 11.2 ng of BMP-2, respectively. Overall, only a small fraction of the BMP-2 initially incorporated into the constructs was released into the surrounding solution over one week (2-5%), indicating the need to evaluate BMP-2

release over a longer period of time *in vitro*. The relatively low BMP-2 amounts observed may have also been due to protein degradation and protein loss on plastic surfaces.

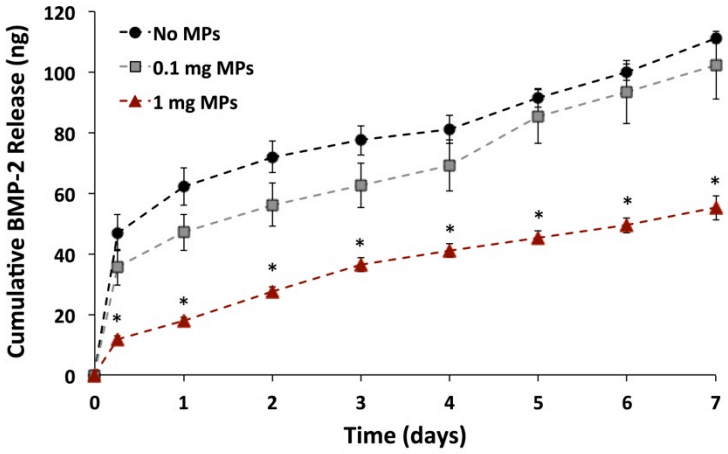

Figure 6.1. BMP-2 Release from Alginate/PCL Constructs Containing 0, 0.1, or 1 mg of Heparin Microparticles. 2.5 µg of BMP-2 per 150 µL construct was either mixed directly into the 2% alginate solution (No MPs), loaded onto 0.1 mg of microparticles overnight prior to being mixed into the alginate solution (0.1 mg MPs), or loaded onto 1 mg of microparticles overnight prior to being mixed into the alginate solution (1 mg MPs). 150 µL of alginate was injected into each PCL mesh tube and allowed to set for 10 minutes prior to addition of 1 mL of 0.1% BSA in PBS. The entire volume of PBS was removed and replaced at each time point over a period of 7 days. Constructs containing 1 mg of BMP-2-loaded microparticles retained more BMP-2 at each time point than constructs lacking microparticles or containing 0.1 mg of microparticles. (* = $p < 0.05$ compared to No MPs and 0.1 mg MPs at each time point)

6.3.2 BMP-2 Retention in Subcutaneous Implants

BMP-2 retention in alginate/PCL constructs was also evaluated *in vivo* to complement *in vitro* BMP-2 release data. 150 µL alginate hydrogels were fabricated with 2.5 µg of fluorescently labeled (VS750) BMP-2 alone or with 0.1 or 1 mg of heparin microparticles that were pre-loaded with 2.5 µg of fluorescently labeled BMP-2. Constructs were assembled immediately prior to subcutaneous implantation in the backs of rats and imaged *in vivo* using an IVIS® platform on Day 0, 1, 4, 7, 14, and 21, and *ex*

vivo at 21 days after explanting. Representative fluorescence images taken between Day 0-7 demonstrated somewhat higher retention of fluorescence signal in constructs containing 1 mg of heparin microparticles compared to constructs containing 0.1 mg of heparin microparticles (Figure 6.2A-D); however, all constructs exhibited a decrease in fluorescent signal over time. All groups displayed an overall decrease in fluorescent signal over time, when fluorescence from the constructs was quantified within 7 cm^2 regions of interest and normalized to Day 0 values (Figure 6.2E). Although no differences were observed between groups at each time point due to animal-to-animal and construct position variability, BMP-2 retention profiles appeared to be similar between constructs lacking microparticles and containing 0.1 mg of microparticles, while constructs containing 1 mg of microparticles exhibited more gradual BMP-2 release at early time points (Day 1-7). When this data was fit to an exponential decay curve, constructs containing 1 mg of microparticles exhibited a lower average decay constant than constructs without microparticles and with 0.1 mg of microparticles, indicating prolonged BMP-2 retention (Figure 6.2F). These results corresponded with BMP-2 release results obtained *in vitro*, which also demonstrated similar BMP-2 release profiles between constructs without microparticles and with 0.1 mg of microparticles, while BMP-2 release from constructs containing 1 mg of microparticles was lower than that of other groups. However, unlike *in vitro* BMP-2 release results, all constructs exhibited similar amounts of BMP-2 retention after 21 days *in vivo* (16-23%). Interestingly, when these constructs were explanted and imaged *ex vivo*, the final radiant efficiency measured in constructs containing 1 mg of microparticles was ~15% higher than that of constructs containing 0.1 mg of microparticles and ~20% higher than that of constructs lacking

microparticles (Figure 6.2G). These data suggest that the higher dose of microparticles altered the release profile of BMP-2 from the construct implantation site compared to constructs lacking microparticles, while the lower dose of microparticles did not.

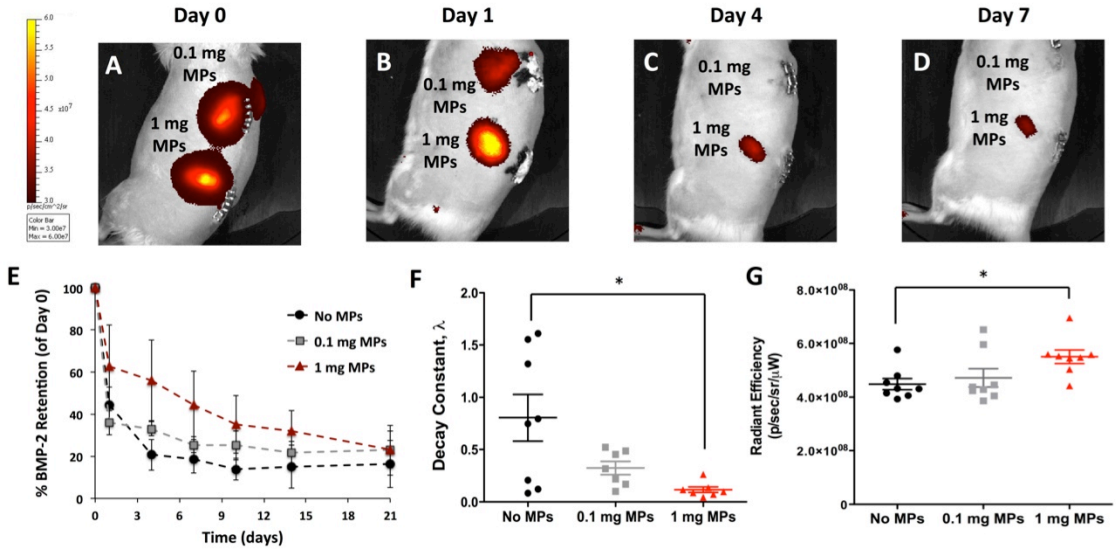

Figure 6.2. Longitudinal BMP-2 Tracking in Subcutaneously Implanted Alginate/PCL Constructs Containing 0, 0.1, or 1 mg of Heparin Microparticles. 2.5 μg of VS750-labeled BMP-2 (alone or loaded onto 0.1 or 1 mg of microparticles) were mixed into 150 μL of 2% RGD-alginate. Alginate/PCL constructs were implanted subcutaneously in the backs of rats for 3 weeks (n=8) and imaged on an IVIS® platform periodically after surgery. A-D) Representative fluorescence IVIS® images of subcutaneous implants at Day 0, 1, 4, and 7. E) Quantification of *in vivo* VS750 fluorescence over time (normalized to Day 0 fluorescence) revealed somewhat faster loss of BMP-2 signal from constructs lacking microparticles and containing 0.1 mg of microparticles; however, these data were not statistically different. F) BMP-2 retention data fit to an exponential decay curve revealed differences in average decay constants of constructs treated with No MPs and 1 mg MPs. (* = $p < 0.05$) G) Quantification of *ex vivo* VS750 fluorescence from explanted constructs 21 days post-surgery. (* = $p < 0.01$ between No MPs and 1 mg MPs)

6.3.3 Spatial Distribution of Mineralization in Femoral Defects

We next attempted to alter the spatial distribution of bone formation and reduce heterotopic ossification by including BMP-2-loaded heparin microparticles in alginate/PCL constructs used to treat femoral defects with high dose BMP-2. Femoral

defects were treated with constructs containing 30 μg of BMP-2, 30 μg of BMP-2 loaded onto 0.1 mg of heparin microparticles, or 30 μg of BMP-2 loaded onto 1 mg of heparin microparticles. Longitudinal radiographs revealed progressive mineralization in and around the bone defect site in all groups over time (Figure 6.3), resulting in robust bony bridging in almost all samples after 12 weeks (12/14 defects treated with BMP-2 alone, 12/13 defects treated with 0.1 mg of BMP-2-loaded microparticles, and 13/14 defects treated with 1 mg of BMP-2-loaded microparticles). Some degree of heterotopic ossification outside of the defect area was observed in all groups as early as 2 weeks post-surgery and persisted through 12 weeks; however, the amount of heterotopic ossification apparent in constructs containing microparticles was visibly decreased in comparison to constructs without microparticles. Constructs without microparticles also induced a more variable distribution of mineralization in and around the defect space, and thus two sets of representative radiographs demonstrating relatively lower and higher amounts of heterotopic bone were chosen.

Longitudinal *in vivo* micro-CT scans provided quantification of total bone volume and bone mineral density over time; furthermore, contouring around the entire thigh and within the 6 mm diameter of the PCL mesh allowed for determination of heterotopic and defect bone volumes (Figure 6.4A). Total bone volume increased in all groups over 12 weeks post-surgery. Although no differences were observed in total bone volume (Figure 6.4B) or overall mineral density (Figure 6.4C) between groups, when total bone volume was divided into heterotopic (Figure 6.4D) and defect bone volumes (Figure 6.4E), constructs containing 0.1 mg or 1 mg of heparin microparticles reduced the percentage of bone formed outside the defect space and increased the percentage formed within the

defect. In femurs treated with BMP-2 alone, 65.8 ± 5.3% of the total bone volume was located outside of the defect space after 4 weeks post-surgery, whereas this amount was decreased to 39.4 ± 5.9% and 44.8 ± 7.9% with treatment with 0.1 mg and 1 mg of heparin microparticles, respectively. While heterotopic bone volume decreased in all groups over time, femurs treated with BMP-2 alone still displayed almost twice as much heterotopic bone than femurs treated with BMP-2-loaded microparticles at the end of the study (40.3 ± 6.8% compared to 21.9 ± 2.8% and 21.0 ± 3.4%). The percentage of bone formed within the defect increased in all groups over time; however, defect bone volumes were highest in femurs treated with loaded microparticles.

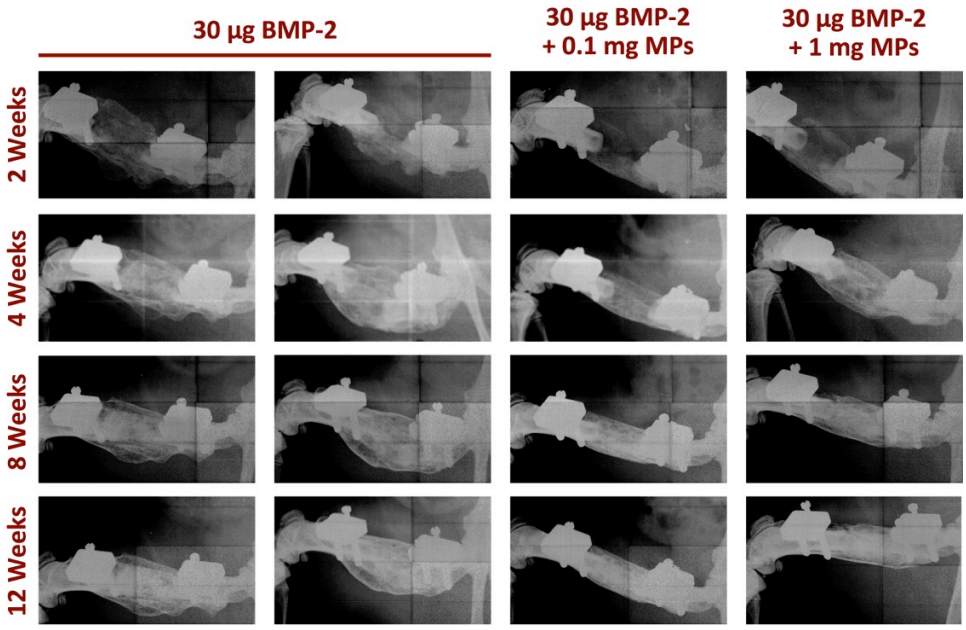

Figure 6.3. Representative Radiographs of Femoral Defects Treated with BMP-2 and BMP-2-Loaded Microparticles. Femoral defects were treated with alginate/PCL constructs containing 30 µg of BMP-2, 0.1 mg of microparticles loaded with 30 µg of BMP-2, or 1 mg of microparticles loaded with 30 µg of BMP-2 (n=13-14). Representative radiographs of femurs at 2, 4, 8, and 12 weeks post-surgery depicted variable amounts of heterotopic ossification in defects treated with BMP-2 alone, while femurs treated with BMP-2-loaded microparticles exhibited less heterotopic bone. Complete bony bridging was achieved in 12/14 defects treated with BMP-2 alone, 12/13 defects treated with 0.1 mg of BMP-2-loaded microparticles, and 13/14 defects treated with 1 mg of BMP-2-loaded microparticles.

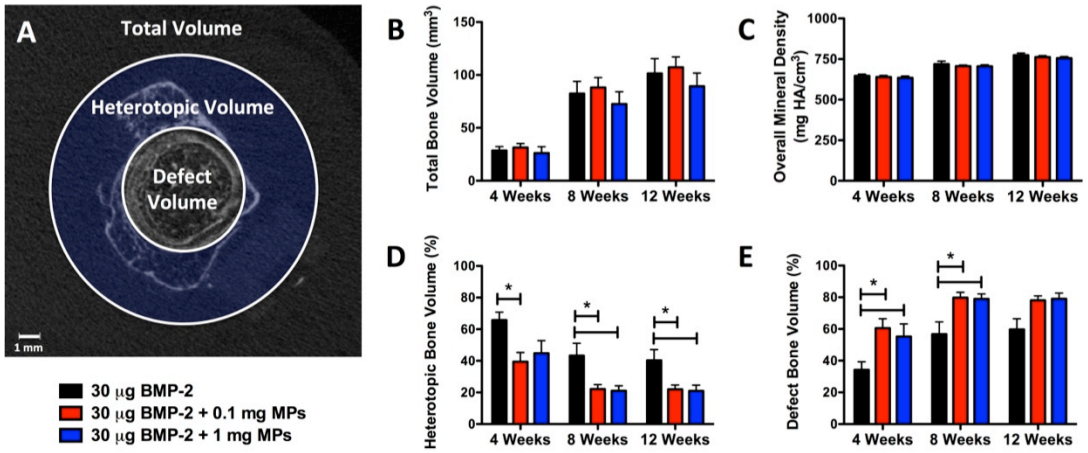

Figure 6.4. Quantitative Assessment of Bone Regeneration and Distribution in Femoral Defects Treated with BMP-2 and BMP-2-Loaded Microparticles. Femoral defects were treated with alginate/PCL constructs containing 30 μg of BMP-2, 0.1 mg of microparticles loaded with 30 μg of BMP-2, or 1 mg of microparticles loaded with 30 μg of BMP-2 (n=13-14). A) Representative micro-CT slice depicting 6 mm contours chosen to separate heterotopic mineral volume from defect mineral volume. Micro-CT quantification of B) total bone volume, C) mineral density, D) heterotopic bone volume as a percentage of total bone volume, and E) defect bone volume as a percentage of total bone volume in bone defects at 4, 8, and 12 weeks post-surgery. (* $p = < 0.05$ as indicated)

6.4 Discussion

Affinity-based growth factor delivery systems aim to improve growth factor retention *in vivo* in order to localize the healing response. In this study, we demonstrated that the addition of ≥0.1 mg of BMP-2-laden heparin microparticles in alginate/PCL constructs used for high dose BMP-2 delivery in a bone defect could effectively alter the spatial distribution of bone formed in and around the defect site and reduce the amount of heterotopic ossification observed. *In vitro* BMP-2 release profiles and *in vivo* BMP-2 retention profiles from alginate/PCL constructs revealed differences in BMP-2 localization within the construct with the addition of a higher dose of microparticles (1 mg), whereas the addition of a lower dose of microparticles (0.1 mg) had a minimal

effect on BMP-2 retention. Despite this, both doses of microparticles reduced the incidence of heterotopic ossification around the femoral defect and increased the volume of bone formed within the boundary of the PCL nanofiber mesh, suggesting that heparin microparticles may improve localized delivery of clinically relevant doses of BMP-2.

Previous studies that have investigated the delivery of high doses of BMP-2 in preclinical animal models have reported varying results. In studies employing collagen sponge and PLGA delivery vehicles, cyst-like bone voids and soft tissue swelling were observed at higher BMP-2 doses [284, 285]; conversely, BMP-2 delivery using a 40-fold range of BMP-2 doses (0.005-0.25 mg BMP-2/kg body weight) in a poly-lactic acid scaffold in a canine spinal fusion model did not demonstrate any dose-dependent changes in bone distribution or adverse events [287]. Thus far, the majority of studies that have investigated high dose BMP-2 delivery have aimed to characterize dose responses in animal models in an attempt to better understand BMP-2 dose effects in humans. However, this study and our recent study comparing the efficacy of the alginate/PCL delivery vehicle to the clinical collagen sponge (Krishnan and Priddy, et al. *In review*.) represent some of the first investigations into improving BMP-2 localization at higher, clinically relevant doses.

As expected based on release profiles presented in Chapters 3 and 4 and predicted by the computational model presented in Chapter 5, *in vitro* and *in vivo* BMP-2 release from alginate/PCL constructs was attenuated in the presence of 1 mg of heparin microparticles, likely due to the excess of unoccupied BMP-2 binding sites available. Interestingly, although the computational model also predicted a reduction of BMP-2 release in alginate/PCL constructs containing 0.1 mg of microparticles, experimental data

revealed similar release/retention profiles between constructs lacking microparticles and constructs containing 0.1 mg of microparticles. The idealized *in vivo* environment simulated by the model did not capture all of the elements of the system that could influence BMP-2 release kinetics, including degradation of the alginate hydrogel, interstitial fluid flow, and competitive binding of numerous other proteins and soluble factors to heparin microparticles in the *in vivo* injury environment. Furthermore, since individual heparin microparticles contained a large number of concentrated BMP-2 binding sites, reducing the number of microparticles by 10-fold (from 7.0E15 to 7.0E14 sites) may have also decreased the probability of BMP-2 molecules (3.5E14 total molecules) rebinding to other heparin microparticles while diffusing through the alginate hydrogel. Finally, the conditions under which BMP-2 release from constructs was evaluated differed drastically from the femoral bone defect environment. BMP-2 release from alginate/PCL constructs was measured in PBS *in vitro*, which may have accelerated dissociation of the ionically cross-linked alginate [274, 288], while BMP-2 release *in vivo* was observed subcutaneously, which may have led to hydrogel leaking out of the flexible, open-ended PCL mesh cylinder [212-214]. While both of these experiments provided valuable information, it is important to note that the distinct cellular and molecular makeup of the tissue injury site likely contributed to an altered BMP-2 release profile. Further model development could attempt to account for competitive protein binding and BMP-2 diffusion through degrading alginate and alginate cross-linked with microparticles, in order to more accurately predict BMP-2 release in the bone defect.

Despite the limitations of the computational model used, it provided a theoretical basis for the microparticle concentrations chosen for the *in vivo* study; the BMP-2 release

profiles generated *in silico* correctly suggested that order of magnitude changes in the number of microparticles used could change BMP-2 localization within the bone defect, allowing for much fewer conditions to be tested *in vivo*. We observed considerable heterotopic bone formation in femoral defects treated with alginate/PCL constructs containing high dose BMP-2 without microparticles, similar to what had been reported previously in this model (Krishnan and Priddy, et al. *In review*.). The inclusion of heparin microparticles in this tissue engineering construct reduced heterotopic ossification; however, the outer boundary of bone formation, characterized by a densely mineralized shell, still largely formed outside of the PCL mesh boundary, resulting in this mineral being considered heterotopic and calling into question the chosen segmentation of defect and heterotopic cross-sectional areas. As a result, the average polar moment of inertia of each sample could also be calculated from micro-CT scans of explanted 12-week femurs, as previously described [289], in order to complement current bone volume data with an unbiased evaluation of the spatial distribution of mineralization.

Another goal of incorporating varying amounts of heparin microparticles into alginate/PCL constructs was the investigation of tissue engineering constructs with tunable growth factor affinity [240]. BMP-2 release could be tuned both *in vitro* and *in vivo* using heparin microparticles, although the range of release profiles observed was not as wide as what was predicted *in silico*. Surprisingly, we found that, while incorporating different amounts of microparticles could alter the BMP-2 release profiles of these constructs, the spatial distribution of regenerated bone was ultimately the same between both microparticle-containing groups. This could be due to a variety of reasons that warrant future investigation, including the fact that different amounts of microparticles

could influence the cross-linking of the alginate gel and that the density of BMP-2 per microparticle may effect its presentation to cells, which has been previously observed *in vitro* [107]. Histological analysis of alginate gels formed *ex vivo* and femurs treated with alginate/PCL constructs for 2 and 12 weeks will reveal the structure of microparticle-containing gels before and after implantation and provide valuable information about the interactions of infiltrating cells with microparticles *in vivo*. In the future, in order to control for differences in alginate cross-linking, microparticles with different heparin content, such as 1% and 10% heparin-PEG microparticles [120], could be incorporated into alginate/PCL constructs, so that equivalent numbers of microparticles with varying degrees of heparin content could be investigated.

6.5 Conclusions

In this study, we investigated the incorporation of different doses of heparin microparticles (0.1 mg, 1 mg) into alginate/PCL constructs to examine the effects on localization of high dose BMP-2 delivery to a critically sized rate femoral defect. We demonstrated that BMP-2 release from the alginate/PCL constructs could be tuned using varying amounts of microparticles based on *in vitro* BMP-2 release and *in vivo* retention of BMP-2 fluorescent signal. Alginate/PCL constructs containing both doses of BMP-2-loaded microparticles reduced heterotopic ossification and increased defect bone volume compared to alginate/PCL constructs containing BMP-2 alone, suggesting that, above a certain threshold concentration, heparin microparticles may have utility in localizing growth factor delivery in systems containing higher, clinically relevant doses of BMP-2.

CHAPTER 7: COMPETITIVE PROTEIN BINDING INFLUENCES HEPARIN-BASED MODULATION OF SPATIAL BMP-2 DELIVERY[3]

7.1 Introduction

In Chapter 6, we demonstrated that heparin microparticles could be used as an effective delivery vehicle for high doses of BMP-2 in a rat femoral defect, resulting in the majority of bone regeneration occurring within the defect site. The positive results of this study suggested that the affinity of heparin microparticles for BMP-2 may be better suited to controlling the spatial distribution of higher, clinically relevant doses of BMP-2 (30 μg/defect), rather than prolonging the effect of low doses of BMP-2 (2.5 μg/defect).

Despite the prevalence of BMP-2-associated side effects in the clinic, such as inflammation, seroma, and heterotopic ossification, the majority of animal models thus far have focused on lowering BMP-2 doses instead of mitigating the negative effects of clinical doses, which are most likely due to the inability of the collagen sponge delivery vehicle to retain high local concentrations of BMP-2. Although a number of clinical studies have reported appreciable rates of heterotopic ossification in patients [43, 45, 283], few studies have attempted to replicate and alleviate heterotopic ossification in preclinical animal models. Studies undertaken to systematically investigate the effects of high doses of BMP-2 in animal models have yielded mixed results. Delivery of BMP-2 doses ranging between 58-2300 μg (0.005-0.25 mg BMP-2/kg body weight) in a poly-lactic acid scaffold resulted in no differences in bone volume in a canine spinal fusion

[3] Modified from Hettiaratchi MH, et al. Competitive protein binding influences heparin-based modulation of BMP-2 delivery for bone regeneration. *Submitted to J Tissue Eng Regen Med.*

model with a noted lack of adverse events [287], while delivery of 150-2500 μg of BMP-2 in collagen sponges resulted in improved mineralization at lower doses (150-600 μg) and the occurrence of large heterotopic bone cysts at higher doses (>600 μg) [290]. Evaluation of an apatite-coated poly(lactic-co-glycolic) acid (PLGA) scaffold in a rat femoral defect model revealed that a lower BMP-2 dose (2.25 μg) induced bony bridging over 8 weeks, but higher BMP-2 doses (11.25-45 μg) resulted in the formation of abnormal bone and soft tissue swelling [291].

As mentioned previously, our laboratory has recently investigated high, clinically relevant doses of BMP-2 (0.12 mg BMP-2/kg body weight) in a rat femoral defect model, and recapitulated the incidence of heterotopic bone observed using a collagen sponge delivery vehicle (Krishnan and Priddy, et al. *In review*.); delivery of 0.12 mg BMP-2/kg body weight resulted in >50% of total bone regenerate forming outside of the intended defect space. Herein, we examined an alternative method of reducing heterotopic ossification in the rat femoral defect model using the high BMP-2 loading capacity of heparin microparticles. Instead of delivering BMP-2 within heparin microparticles, we physically entrapped heparin microparticles within an electrospun polycaprolactone nanofiber mesh tube in an attempt to create a barrier to rapid BMP-2 diffusion from the clinical collagen sponge. Unlike the studies in Chapters 4 and 6, which utilize an alginate hydrogel for BMP-2 delivery, this design could allow clinicians the choice of current delivery methods (i.e. collagen sponge), thus lowering perceived adoption barriers, while harnessing the high affinity of heparin microparticles for BMP-2 to improve patient safety in BMP-2 therapeutics.

Histology was used to ascertain the distribution of heparin microparticles deposited in the nanofiber meshes at two densities (0.05 mg MP/cm^2 and 0.10 mg MP/cm^2), followed by *in vitro* evaluation of BMP-2 loading and release. Our hybrid mesh barrier system was then evaluated *in vivo* in a critically sized rat femoral defect model using a supraphysiological dose of BMP-2 (30 μg) delivered within the clinically used collagen sponge; remineralization of the defect space and the extent of heterotopic ossification were evaluated. We hypothesized that heparin microparticles incorporated into the polycaprolactone mesh tube would act as a growth factor sink, rapidly capturing BMP-2 dissociating from the collagen sponge after implantation. This approach could potentially limit the exposure of surrounding tissues to high BMP-2 doses, thereby reducing heterotopic ossification, while maximizing presentation of BMP-2 within the defect site to promote effective bone repair.

7.2 Materials and Methods

7.2.1 Polycaprolactone Mesh Fabrication

Polycaprolactone (PCL; Sigma Aldrich) was dissolved overnight in a 90:10 solution of hexafluoro-2-propanol (HFP; Sigma Aldrich) and dimethylformamide (DMF; Sigma Aldrich) with gentle stirring, and a clear polymer solution of 12% (w/v) PCL in organic solvent was obtained. 5 mL of solution was loaded into a 5 mL syringe (Becton Dickinson, Franklin Lakes, NJ) with a 22-gauge 1” blunt tip needle (Howard Electronic Instruments, El Dorado, KS), bubbles were removed, and the syringe was mounted onto a

PHD2000 Infusion syringe pump (Harvard Apparatus, Holliston, MA). For the electrospinning setup, the syringe pump was placed so that the needle tip was ~19 cm away from a rectangular copper collection plate covered with aluminum foil for PCL nanofiber deposition. The syringe pump was set to a constant infusion rate of 0.75 mL/hr, and a high voltage supply (HV Power Supply, Gamma High Voltage Research, Ormond Beach, FL) provided a voltage difference of ~15-20 kV between the needle and copper collection plate. The voltage was periodically adjusted to maintain a Taylor cone at the needle tip during electrospinning [292]. A total of 3.6 mL of PCL solution was infused through the syringe pump, creating a circular mesh with an area of ~100 cm^2 and thickness of ~500 μm, as measured with digital calipers.

Heparin microparticles were sprayed onto the meshes in two batches, after 1.2 mL and 2.4 mL of PCL had been electrospun (Figure 7.1A) and physically entrapped into the meshes. 2.5 or 5 mg of microparticles suspended in ethanol were sprayed evenly across the mesh using an airbrush (Iwata Medea Inc., Portland, OR) driven by an air pump (Master Airbush, TCP Global Co., San Diego, CA). The ethanol was allowed to evaporate briefly before continuing the electrospinning process. Spraying each suspension twice entrapped microparticles in two layers between polymer fibers and created 0.05 mg MP/cm^2 and 0.10 mg MP/cm^2 meshes. 0.05 mg MP/cm^2 meshes containing 4-μm diameter polystyrene microparticles (Polysciences Inc., Warrington, PA) were also fabricated similarly to serve as an uncharged microparticle control. Meshes without microparticles received two empty ethanol sprays after 1.2 and 2.4 mL of PCL had been electrospun. 12 mm by 19 mm sheets with or without twenty-three 0.9 mm diameter perforations were laser cut from the circular meshes (Universal Laser Systems,

Scottsdale, AZ), rolled into tubes (diameter 5 mm, length of 12 mm), and glued using UV cure adhesive (1187-M MD Medical Device Adhesives & Coatings, BlueWave LED Prime UVA Spot Curing System, DYMAX, Torrington, CT). Mesh tubes underwent 100% ethanol evaporation overnight, followed by disinfection in 70% ethanol for 4 hours, and finally immersion in sterile PBS until surgery.

7.2.2 Microparticle-containing Polycaprolactone Mesh Characterization

6-mm diameter discs from representative meshes were embedded in cryomedium, and 5 μm cross-sections were taken along the disc diameter for histological analysis. Sections were stained with Safranin O and Fast Green to visualize heparin microparticle distribution within each mesh. Images of meshes were taken on a Zeiss Axio Observer Z.1 inverted microscope with Zeiss AxioVision software (Zeiss, Oberkochen, Germany).

7.2.3 In Vitro BMP-2 Loading and Release from Meshes

To evaluate *in vitro* BMP-2 loading and release, 6-mm diameter discs from each mesh were incubated in a solution of 100 ng of BMP-2 (Pfizer, New York, NY) in 1 mL of 0.1% (w/v) bovine serum albumin (BSA, Sigma Aldrich) in PBS with gentle mixing (Tube Revolver/Rotator, Thermo Fisher Scientific) for 16 hours at 4°C. Meshes were then removed and the remaining solution was evaluated for BMP-2 content using an enzyme-linked immunosorbent assay (ELISA; R&D Systems, Minneapolis, MN). The mass of BMP-2 entrapped within the meshes was determined by normalizing unbound

BMP-2 to a solution of 100 ng of BMP-2 incubated for 16 hours at 4°C without microparticles. BMP-2-loaded meshes were then placed in 1 mL of fresh solution and incubated at 37°C for a period of 21 days to measure passive BMP-2 release from the meshes. After 0.25, 1, 4, 7, 10, 14, and 21 days, the entire solution was removed and replaced with 1 mL of fresh 0.1% BSA in PBS.

7.2.4 Rat Femoral Defect Surgical Procedure

Surgeries were performed on 13-week-old female SASCO Sprague Dawley rats (~250 g) as previously described [293], using procedures approved by the Georgia Institute of Technology Institutional Animal Care and Use Committee. Briefly, using an anterior approach and blunt dissection of the overlaying muscles, a radiolucent fixation plate (polysulfone) with two stainless steel risers at the ends was attached directly onto the femur for stabilization. An oscillating saw was used to create an 8-mm long, full thickness mid-diaphyseal defect. Each defect was treated with a collagen sponge (L = 10 mm, D = 5 mm; Kensey Nash, Exton, PA) soaked with 30 μg of BMP-2 in 150 μL of 0.1% (w/v) rat serum albumin (RSA) in 4 mM hydrochloric acid, inserted into a PCL nanofiber mesh tube (L = 12 mm, D = 5 mm), and gently fit into the defect. The following PCL mesh formulations were tested *in vivo*: (1) no heparin microparticles, (2) meshes with 0.05 mg MP/cm^2 (0.11 mg heparin microparticles total), (3) meshes with 0.10 mg MP/cm^2 (0.23 mg microparticles total), (4) meshes with 0.9 mm perforations without heparin microparticles, and (5) meshes with 0.9 mm perforations and 0.10 mg MP/cm^2 (0.23 mg heparin microparticles total, prior to perforation).

7.2.5 In Vivo Faxitron and Micro-computed Tomography

Longitudinal *in vivo* radiographs were obtained at 2, 4, 8, and 12 weeks post-surgery (Faxitron MX-20, Faxitron Bioptics LLC, Tucson, AZ) at a voltage of 23 kV and exposure time of 15 seconds; radiographs were used to qualitatively assess mineralized bridging across the defect space and the presence of heterotopic bone outside of the defect. *In vivo* micro-CT was conducted at 4, 8, and 12 weeks post-surgery (Viva CT, Scanco, Brüttisellen, Switzerland) to quantify total bone volume, bone mineral density, and spatial distribution of mineral inside and outside of the defect space. Animals were scanned at a voxel size of 38.5 μm, voltage of 55 kVp, current of 109 μA, and medium resolution. Mineral was quantified within the central ~6 mm (160 scan slices) of each 8 mm defect, and three different volumes of interest (VOIs) were identified: (1) total mineral volume of the thigh within the region of interest, (2) mineral volume within the defect space, as defined by 5 mm diameter circular contours corresponding to the diameter of the nanofiber mesh, and (3) heterotopic mineral volume, which fell outside of the 5 mm diameter circular contours. A global threshold for newly regenerated bone was set at 50% of the mineral density of native cortical bone.

7.2.6 Biomechanical Testing

Femurs harvested from animals at 12 weeks were wrapped in saline-soaked gauze and stored at -20^{o}C. For mechanical testing, samples were thawed to room temperature, and soft tissue and polysulfone fixation plates were removed, leaving the metal risers

attached to the bone. The bone ends (including part of the metal risers) were potted in molten Wood's metal (Alfa Aesar, Haverhill, MA) in custom metal holders, allowed to solidify, and mounted in the test clamps. Torsion was applied at a rate of 3º per second until failure on a uniaxial torsion testing system (Bose EnduraTEC ELF200; Bose Electroforce Systems Group, Eden Prairie, MN), allowing for the determination of maximum torque and calculation of torsional stiffness, using the slope of the linear segment of the torque-rotation curve. 7-8 samples from each treatment group and 5 contralateral intact femurs were tested.

7.2.7 Histological Analysis of Microparticle Retention and Bone Regeneration

One femur from each treatment group demonstrating representative bone formation (as evaluated by radiography) was isolated for histology at 12 weeks post-surgery. After harvesting, the femurs were fixed in 10% neutral buffered formalin at 4°C for 48 hours, followed by decalcification at room temperature (Cal Ex-II, Fisher Scientific, Pittsburgh, PA) with gentle agitation for 14 days. Samples were then dehydrated through submersion in a series of alcohol and xylene solutions and vacuum-embedded in paraffin wax at 60°C; 5-7 μm mid-sagittal sections of the defects were obtained for histological analysis using Safranin O/Fast Green staining, primarily for identification of heparin microparticles within the mesh. Images of sections were taken on a Zeiss Axio Observer Z.1 inverted microscope with Zeiss AxioVision software (Zeiss, Oberkochen, Germany).

7.2.8 In Vitro BMP-2 Loading and Release from Heparin Microparticles

a) Contact time required for BMP-2 loading onto heparin microparticles: *In vitro* evaluation of BMP-2 loading and release from heparin microparticles was performed as previously described [107]. 0.1 mg of microparticles were incubated with 100 ng of BMP-2 in 0.1% BSA in PBS at 4°C for various periods of time between 0-16 hours, to establish the minimum contact time required for BMP-2 loading onto microparticles.

b) Competitive binding/adsorption of serum components to heparin microparticles: To determine whether the presence of serum borne biomolecules interfered with BMP-2 loading onto microparticles, 10 μg samples of heparin microparticles were incubated with a range of BMP-2 concentrations (3-3000 ng/mL) in 1 mL of fetal bovine serum (FBS; Hyclone – GE Healthcare Life Sciences, Logan, UT) or 0.1% BSA in PBS for 16 hours at 37°C. BMP-2 content of microparticle-containing samples were normalized to samples containing BMP-2 alone in 0.1% BSA in PBS or FBS and incubated for 16 hours at 37°C. BMP-2 release (100 ng) from heparin microparticles (0.1 mg) was also evaluated in both 0.1% BSA/PBS and FBS at 37°C over 21 days. At each time point, the entire solution was removed and replaced with 1 mL of fresh solution. All samples were evaluated for BMP-2 content via ELISA.

7.2.9 Polyacrylamide Gel Electrophoresis (PAGE) Analysis

Binding and adsorption of serum proteins to heparin microparticles was confirmed by sodium dodecyl sulfate polyacrylamide gel electrophoresis (SDS-PAGE)

followed by silver staining for all protein bands. 0.1 mg of heparin microparticles were incubated in PBS, 30 ng of BMP-2 in 0.1% BSA in PBS, FBS, or 30 ng of BMP-2 in FBS at 4°C for 16 hours. Heparin microparticles were then centrifuged, washed once with PBS, and resuspended in SDS-PAGE loading buffer. 30 ng of soluble BMP-2 in 0.1% BSA in PBS and diluted FBS (1:25, 1:50) were also resuspended in loading buffer as additional controls. All solutions were heated to 95°C for 10 minutes prior to loading onto a 12% Mini-PROTEAN TGX gel (Bio-Rad Laboratories, Hercules, CA). Gel electrophoresis was performed in SDS/PAGE running buffer under reducing and denaturing conditions using a Mini-PROTEAN Tetra Cell system (Bio-Rad) set at a constant voltage (200 V) for 40 minutes. A 10-250 kDa protein ladder (Precision Plus Kaleidoscope, Bio-Rad) was used as a molecular weight reference. Silver staining of SDS-PAGE gels was performed using the Silver Staining Plus Kit (Bio-Rad) as per the manufacturer's instructions, rinsed, and imaged using a CanoScan LiDE 220 Flatbed Scanner (Canon USA, Melville, NY).

7.2.10 Mass Spectrometry of Heparin Microparticle Samples

In order to identify serum proteins bound to heparin microparticles, mass spectrometry analysis was conducted on 1 mg of microparticles loaded with 5 mL of FBS or 5 mL of FBS and 8 μg BMP-2 together using aforementioned techniques. The microparticles were centrifuged, washed with PBS, and proteins bound to microparticles were digested with 2 units of Glu-C (EMD Millipore, Darmstadt, Germany) for 16 hours and 10 units of Lys-C (Wako Chemicals USA, Richmond, VA) for 3.5 hours in 50 mM

HEPES (pH=7.9). Digestion was quenched with formic acid (FA) until samples reached a final pH of 2. Samples were then purified using the stage tip method [294], dried and resuspended in 10 µL solvent containing 5% acetonitrile (ACN) and 4% formic acid.

For mass spectrometry (MS) analysis, an WPS-3000(T)PLRS autosampler (Thermostatted Pulled Loop Rapid Separation Nano/Capillary Autosampler; Dionex, Sunnyvale, CA) loaded 4 µL of each sample onto a microcapillary column packed with C18 beads (Magic C18AQ, 5 µm, 200 Å, 100 µm x 16 cm). Peptides were separated by reversed-phase chromatography using an UltiMate 3000 binary pump with a 15 minute gradient of 5-60% ACN and detected in a hybrid dual-cell quadrupole linear ion trap – Orbitrap mass spectrometer (LTQ Orbitrap Elite, Thermo Scientific, with Xcalibur 3.0.63 software) using a data-dependent Top 15 method. Each cycle included one full MS scan (resolution: 60,000) in the Orbitrap at 10^6 AGC target, followed by up to 20 tandem mass spectra (MS/MS) for the most intense ions. Ions with a single or unassigned charge were not fragmented for MS/MS. For each full MS scan the maximum ion accumulation time was 1000 ms, and for each MS/MS scan the maximum time was 50 ms.

MS/MS fragmentation precursors were checked for incorrect monoisotopic peak assignments while refining precursor ion mass measurements [295]. The SEQUEST algorithm (version 28) [296] was used to search all MS/MS spectra by matching against a database encompassing sequences of all proteins in the UniProt Bovine database (downloaded March 2014) and common contaminants. To estimate the false discovery rate (FDR) of peptide identifications, each protein sequence was listed in forward and reversed orientations. The following parameters were used for database searching: 20 ppm precursor mass tolerance, 1.0 Da product ion mass tolerance, Lys-C and Glu-C

digestion, up to 3 missed cleavage sites. The modifications included in the search were oxidation of methionine (+15.9949) and carbamidomethylation of cysteine (+57.0215). To further control the FDRs of peptide identification, the target-decoy method was employed [297, 298]. Linear discriminant analysis (LDA) was employed to distinguish correct and incorrect peptide identifications [295, 299]. Peptides containing less than six amino acids were discarded and peptide spectral matches were filtered to a less than 1% FDR based on the final number of decoy sequences in the dataset.

7.2.11 Statistical Analysis

All data are reported as mean ± standard error of the mean. *In vitro* experiments were run with a minimum of three replicates for each experimental group. For BMP-2 loading and release from nanofiber meshes, three samples were obtained from each mesh, and a total of 3-10 meshes were analyzed from each group. For *in vivo* bone defect experiments, longitudinal micro-CT was conducted on 8-9 femurs per group, and biomechanical testing was conducted on 7-8 femurs per group. Statistical significance was determined using one-way or two-way ANOVA as appropriate, followed by Bonferroni's post hoc analysis (Graphpad Prism, Version 5.0, La Jolla, CA). For data that did not satisfy the assumptions of equal variances and Gaussian distributions, the nonparametric Kruskal-Wallis test was used. $P < 0.05$ was considered statistically significant.

7.3 Results

7.3.1 Polycaprolactone Mesh Characterization

Safranin O/Fast Green staining of representative 5 μm thick cross-sections of PCL nanofiber meshes revealed two distinct layers of heparin microparticles (red) entrapped between PCL layers (gray) in both the 0.05 mg MP/cm^2 meshes (Figure 7.1C, F) and 0.10 mg MP/cm^2 meshes (Figure 7.1D, G). In contrast, meshes without heparin microparticles consisted of a single continuous PCL layer (Figure 7.1B, E). Some mesh delamination and microparticle loss was observed in the 0.10 mg MP/cm^2 meshes, demonstrated by separation of the mesh layers and presence of microparticles at the mesh surface (Figure 7.1D, G); this may have been caused by the intervening ethanol spray step in the fabrication technique or histology processing. Meshes that exhibited delamination during manipulation prior to *in vivo* implantation were excluded from the study; however, this did not eliminate the possibility of *in vivo* mesh delamination, which was qualitatively assessed through histology of representative femurs after 12 weeks.

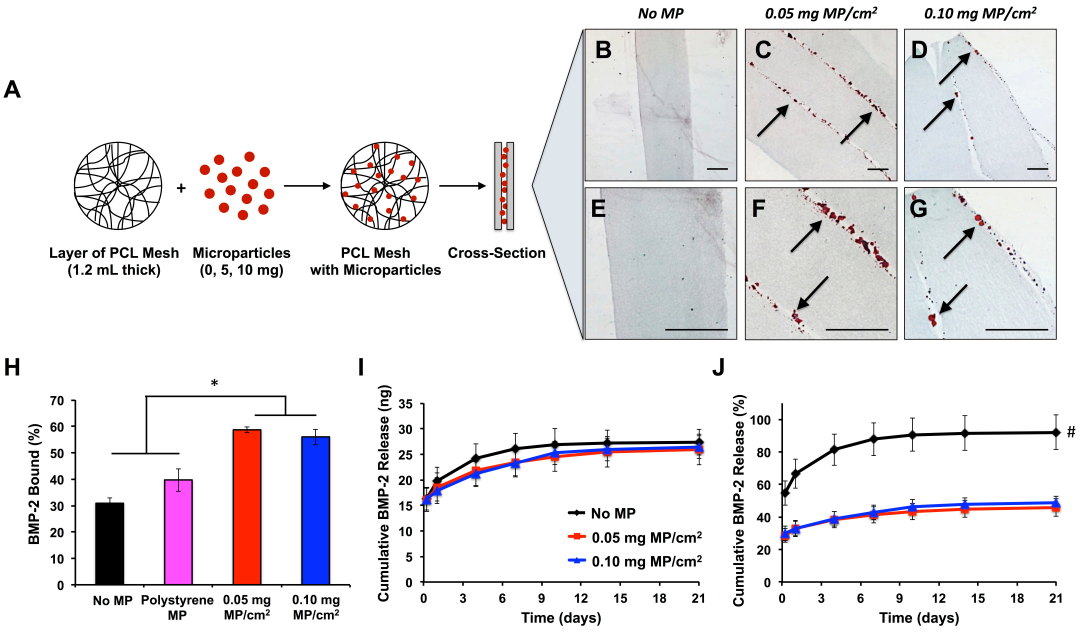

Figure 7.1. Fabrication and Characterization of Heparin Microparticle-Containing Polycaprolactone Nanofiber Meshes. A) Schematic of microparticle-containing mesh fabrication. B, C, D) Low magnification images of mesh cross-sections stained with Safranin O and Fast Green demonstrated microparticles distributed throughout two layers in microparticle-containing meshes. E, F, G) High magnification images of mesh cross-sections stained with Safranin O/Fast Green. All scale bars = 100 μm. H) 6-mm diameter meshes loaded with 100 ng of BMP-2 demonstrated higher BMP-2 loading in the presence of heparin microparticles compared to no microparticles and polystyrene microparticles. (* = $p < 0.05$ as indicated.) I) Cumulative mass of BMP-2 released over 21 days was similar between meshes without microparticles and with heparin microparticles. J) Cumulative BMP-2 release as a percentage of initial loading was higher for meshes without microparticles compared to meshes with microparticles. (# = $p < 0.05$ compared to 0.05 mg MP/cm^2 and 0.10 mg MP/cm^2 meshes at each time point.)

7.3.2 BMP-2 Loading and Release from Meshes

PCL nanofiber meshes containing 0.05 and 0.10 mg/cm^2 of heparin microparticles depleted more BMP-2 from solution (58.7% ± 1.1%, 56.0% ± 3.0%, respectively) than meshes without heparin microparticles or with 0.05 mg/cm^2 of uncharged 4 μm polystyrene microparticles that lacked similar electrostatic affinity for BMP-2 (30.9% ± 2.0%, 39.7% ± 4.3%, respectively; n=4-10, $p<0.05$) when loaded with 100 ng of BMP-2 (Figure 7.1H). Meshes with and without heparin microparticles exhibited similar BMP-2

release profiles in 0.1% BSA in PBS at 37°C, releasing 25-27 ng of BMP-2 after 21 days *in vitro* (Figure 7.1I). However, when BMP-2 release was evaluated as a percentage of initial BMP-2 loading, meshes without microparticles released almost all of the bound BMP-2 (88.6% ± 10.3%), compared to meshes with 0.05 and 0.10 mg/cm^2 of heparin microparticles, which released less than half of the bound BMP-2 over 21 days (44.1% ± 5.1% and 47.2% ± 4.0%, respectively; n=3, $p<0.001$) (Figure 7.1J).

7.3.3 In Vivo Faxitron and Micro-Computed Tomography

Longitudinal radiographs revealed progressive mineralization in and around the bone defect area in all groups over time (Figure 7.2A), resulting in robust bony bridging in almost all samples after 12 weeks (9/9 of No MP, 8/9 of 0.05 mg MP/cm^2, 8/8 of 0.10 mg MP/cm^2, 8/8 of Perforated No MP, 8/9 of Perforated 0.10 mg MP/cm^2). Heterotopic ossification outside of the defect was observed in all groups at 2 weeks post-surgery and persisted through 12 weeks. Overall, no qualitative reduction in heterotopic ossification was observed with the inclusion of heparin microparticles in meshes (Figure 7.2A).

Micro-CT reconstructions confirmed radiographic observations, revealing heterotopic ossification in all treatment groups with no reduction associated with microparticle-containing meshes (Figure 7.2B). Quantitative micro-CT analysis of bone regeneration within the defect site revealed increased mineralization over time, with no differences in total bone volume between groups at each time point. Furthermore, when the thigh region was divided (axially) into defect bone volume (corresponding to the 5 mm diameter of the nanofiber mesh tube) and heterotopic bone volume (outside of the

diameter of the mesh tube) as pictured in Figure 6.4, bone volume between groups remained comparable (Figure 7.3A). The spatial distribution of newly formed bone from the central axis of the femur was also quantified by calculating the polar moment of inertia for each sample from micro-CT reconstructions, and did not exhibit differences between the groups with time (Figure 7.3B). Similarly, no notable morphological differences in the regenerated bone could be detected between groups by micro-CT analysis (Figure 7.4).

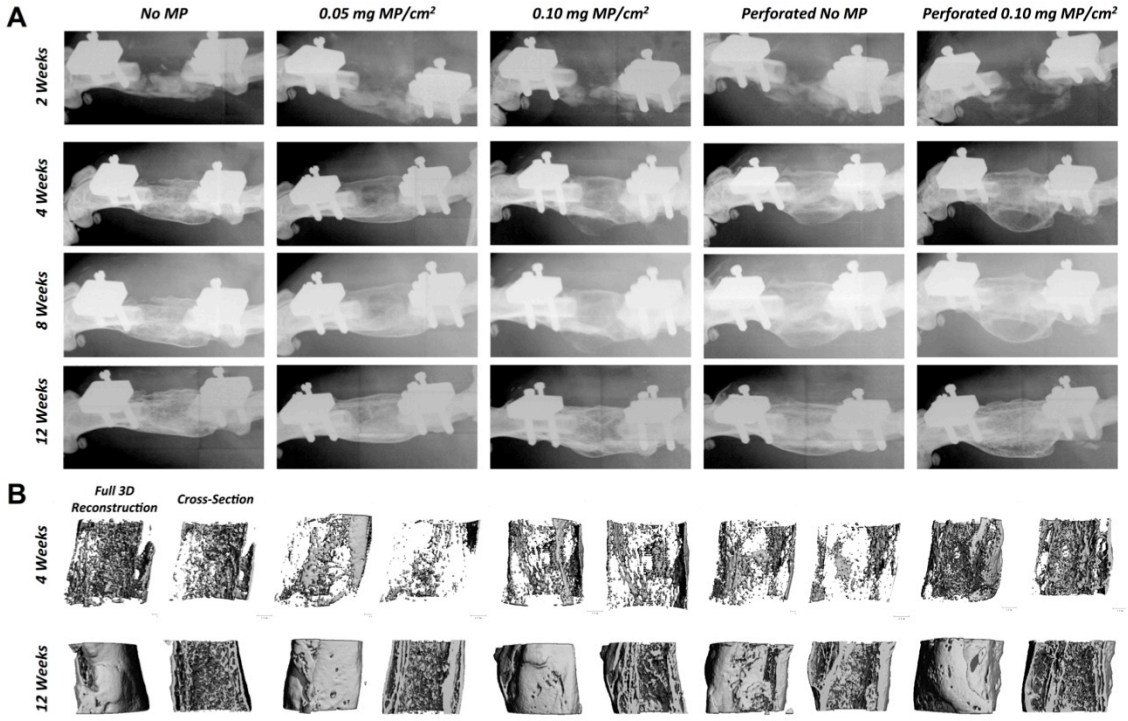

Figure 7.2. Representative Radiographs and Three-dimensional Micro-CT Reconstructions of Femoral Bone Defects. A) Radiographs and B) micro-CT reconstructions (full reconstructions and cross-sections) of defects treated with No MP, 0.05 mg MP/cm^2, and 0.10 mg MP/cm^2, No MP (Perforated), and 0.10 mg MP/cm^2 (Perforated) meshes. Bridging was achieved in 9/9 of No MP, 8/9 of 0.05 mg MP/cm^2, 8/8 of 0.10 mg MP/cm^2, 8/8 of No MP (Perforated), 8/9 of 0.10 mg MP/cm^2 (Perforated) mesh treated defects.

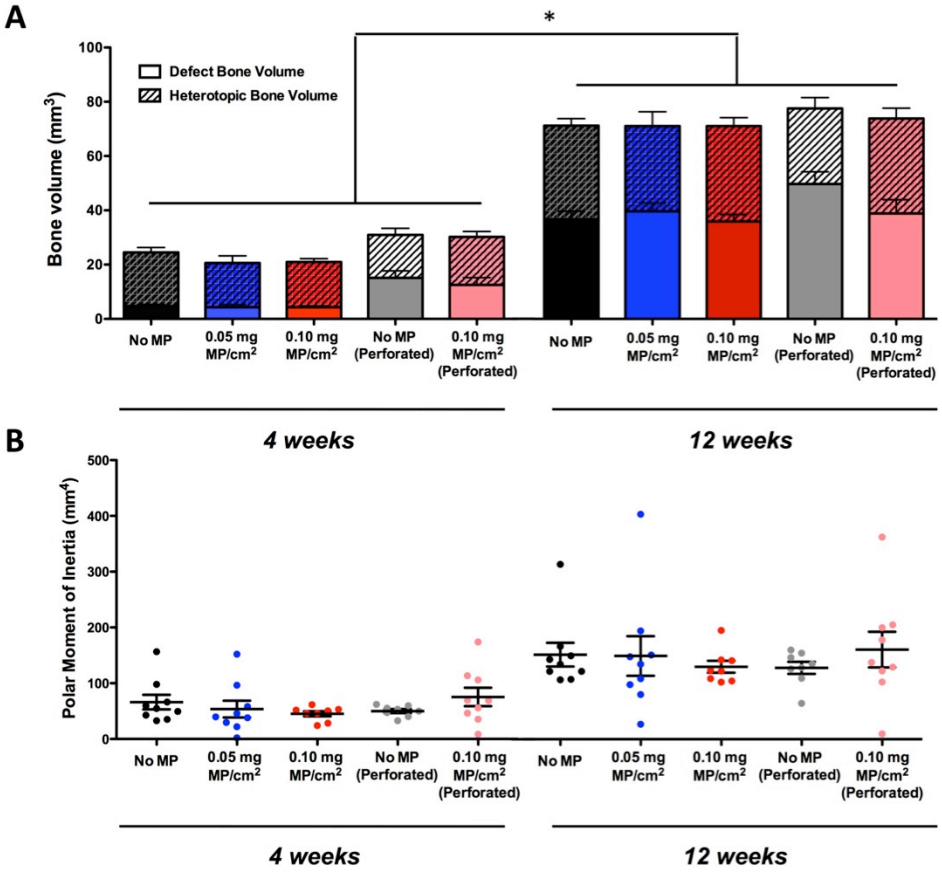

Figure 7.3. Quantitative Micro-CT Analysis of Bone Defects After 4 and 12 Weeks. A) Defect bone volume (solid bars), heterotopic bone volume (diagonal line bars), and total bone volume (combined bars) were not different between treatment groups. Bone volume in each group increased over time (* = $p < 0.05$ as indicated). B) Polar moment of inertia was calculated to determine distribution of newly formed bone from the central axis of the femur and was also not different between groups.

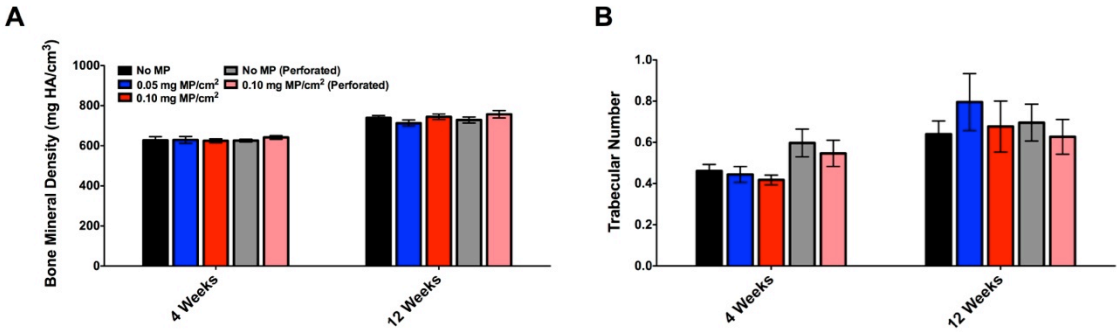

Figure 7.4. Micro-CT Analysis of Bone Morphology Parameters. Micro-CT analysis on regenerated bone at 4 and 12 week post-surgery demonstrated no differences in A) bone mineral density and B) trabecular number between groups.

7.3.4 Biomechanical Properties of Regenerated Femurs

Torsion testing was used to determine the strength of the regenerated bone after 12 weeks post-surgery. Maximum torque (Figure 7.5A) and torsional stiffness (Figure 7.5B) were comparable between all groups and did not differ from the properties of age-matched intact femurs.

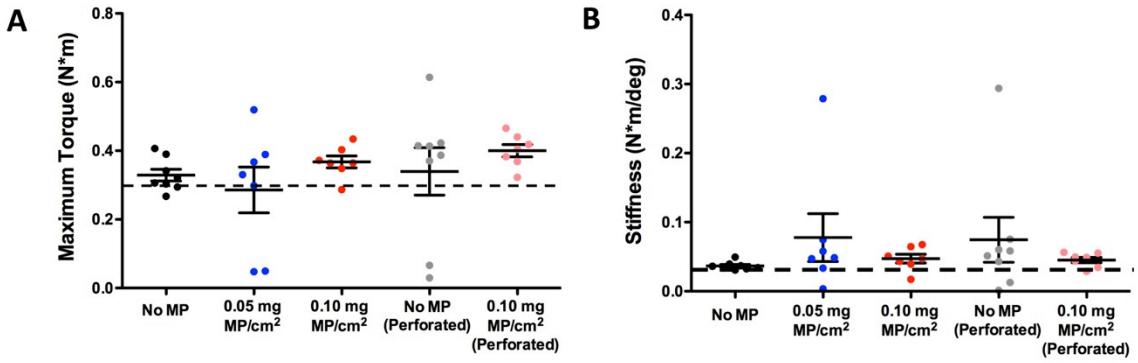

Figure 7.5. Maximum Torque and Torsional Stiffness of Regenerated Bone at 12 Weeks. Regenerated femurs underwent torsion testing to failure after 12 weeks post-surgery. Both maximum torque and torsional stiffness were not different between groups or compared to that of intact femurs of age-matched rats. Dashed line represents properties of intact femurs.

7.3.5 Histological Analysis of Femurs

Sections from representative femurs stained with Safranin O and Fast Green revealed that heparin microparticles remained entrapped within the mesh after 12 weeks *in vivo* (Figure 7.6; indicated by red arrows). Mesh integrity was better maintained in the 0.05 mg MP/cm^2 meshes, which exhibited two distinct layers of heparin microparticles and were comparable in appearance to intact meshes prior to implantation (Figure 7.6B, E). However, some areas of mesh disintegration were observed and were

indistinguishable from processing artifacts. The 0.10 mg MP/cm^2 meshes displayed greater mesh delamination, as illustrated by large gaps within the meshes and an overall expansion of mesh area. Some heparin microparticles were located in close proximity to the 0.10 mg MP/cm^2 meshes (indicated by red arrow, Figure 7.6C) or entrapped within them (Figure 7.6F), but overall fewer microparticles were retained in the 0.10 mg MP/cm^2 meshes compared to 0.05 mg MP/cm^2 meshes. Notably, heparin microparticles were not observed outside of the nanofiber mesh boundary (indicated by black arrows), in the defect region, or surrounding muscle. Overall, the regenerated bone in each of the groups demonstrated a trabecular structure (indicated by red arrowheads) interspersed with areas of loose fibrous tissue, as has been previously demonstrated with collagen sponge-mediated delivery of BMP-2 in this model [300].

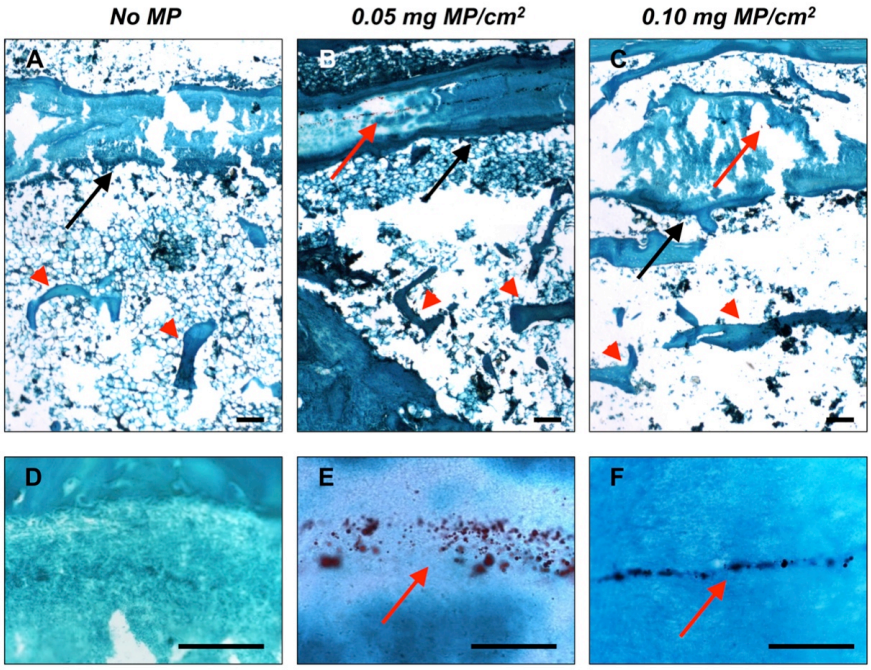

Figure 7.6. Safranin O and Fast Green Staining of Bone Defects at 12 weeks. Safranin O and Fast Green staining was performed on defects treated with A, D) No MP meshes, B, E) 0.05 mg MP/cm^2 meshes, and C, F) 0.10 mg MP/cm^2 meshes. Black arrows denote the mesh boundary, and red arrowheads denote areas of new bone. Heparin microparticles, which are denoted by red arrows, were found entrapped within 0.05 mg MP/cm^2 and 0.10 mg MP/cm^2 meshes; however, 0.10 mg MP/cm^2 meshes demonstrated greater delamination. All scale bars = 100 μm.

7.3.6 Effect of Incubation Time on BMP-2 Loading onto Microparticles

Since the presence of heparin microparticles in the nanofiber meshes did not appear to have an impact on bone regeneration *in vivo*, the minimal contact time required for BMP-2 loading onto heparin microparticles was evaluated *in vitro* by repeating BMP-2 depletion experiments with microparticle samples collected at time points between 0 and 16 hours. Analysis of BMP-2 remaining in solution following incubation with heparin microparticles and normalized to solutions containing BMP-2 alone revealed that 64.1 ± 6.5% of the BMP-2 was depleted by the microparticles immediately after contact, and increased to 83.3 ± 4.3% within the first hour (Figure 7.7A). BMP-2 loading continued to increase over the next 4 hours before reaching a plateau of ~90% BMP-2 loading, after which additional incubation time did not increase BMP-2 loading to microparticles.

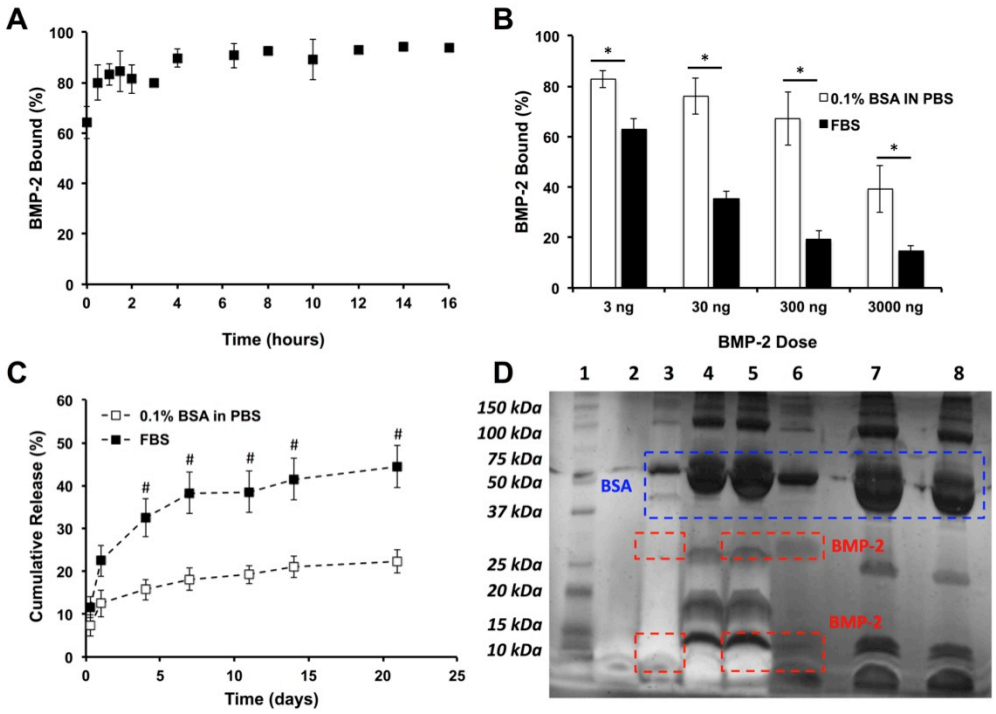

Figure 7.7. Effect of Contact Time and Presence of Serum on BMP-2 Loading and Release from Heparin Microparticles. A) 0.1 mg of microparticles loaded with BMP-2 over different periods of time exhibited >60% BMP-2 loading immediately upon contact and a maximum loading of ~90% after 4 hours. B) 10 µg of microparticles loaded with 3-3000 ng of BMP-2 over 16 hours at 37°C demonstrated reduced loading in the presence of FBS compared to 0.1% BSA in PBS. (* = $p < 0.01$ as indicated.) C) When 0.1 mg of heparin microparticles were loaded with 100 ng of BMP-2 and allowed to release BMP-2 into 0.1% BSA in PBS or FBS, cumulative release of BMP-2 was higher in FBS after 4 days. (# = $p < 0.05$ between 0.1% BSA in PBS and FBS at indicated time points.) D) Gel electrophoresis followed by silver staining was completed on the following samples: 1 – Ladder, 2 – Unloaded MPs, 3 – MPs loaded with 30 ng of BMP-2, 4 – MPs loaded with FBS, 5 – MPs loaded with FBS + 30 ng of BMP-2, 6 – 30 ng of soluble BMP-2, 7 – FBS diluted 1:25, 8 – FBS diluted 1:50. Blue dashed box indicates BSA bands, and red dashed boxes indicate BMP-2 monomer and dimer bands.

7.3.7 Competitive Binding of Serum Proteins to Microparticles

Because contact between BMP-2 and heparin microparticles embedded within nanofiber meshes *in vivo* occurred at 37°C in the presence of numerous blood borne soluble factors, *in vitro* BMP-2 loading and release experiments were performed in the presence of FBS, as a substitute for rat serum, and compared to results obtained in 0.1%

(w/v) BSA in PBS. Overall, heparin microparticles loaded less BMP-2 in the presence of FBS when incubated in BMP-2 concentrations between 3-3000 ng/mL (corresponding to 0.3-300 μg of BMP-2 per mg of microparticles) (Figure 7.7B). Heparin microparticles incubated with BMP-2 in 0.1% BSA in PBS depleted ~75% of the BMP-2 at lower doses, while loading was reduced to 39.3 ± 9.3% at the highest dose (300 μg BMP-2/mg MPs); the BMP-2 loading efficiencies obtained in 0.1% BSA in PBS at higher growth factor concentrations were similar to results documented in Chapter 3 [107]. In contrast, heparin microparticles incubated with BMP-2 in the presence of FBS depleted less BMP-2 at each dose, with the highest loading percentage at the lowest dose (63.0 ± 3.9% compared to 82.8 ± 3.3% in BSA/PBS; $p < 0.01$) and lowest loading percentage at the highest dose (14.7 ± 2.2% compared to 39.3 ± 9.3% in BSA in PBS, $p < 0.01$). Similarly, the presence of FBS during BMP-2 release from heparin microparticles increased the amount of BMP-2 released after 4 days of incubation (Figure 7.7C). Over 21 days *in vitro*, BMP-2-loaded microparticles incubated at 37°C in 0.1% BSA in PBS released 22.3 ± 4.6 % of the loaded BMP-2, whereas BMP-2-loaded microparticles incubated in FBS released double this amount (44.4 ± 8.4%; $p < 0.05$).

Gel electrophoresis and mass spectrometry were performed to identify the serum proteins interfering with BMP-2 loading and increasing BMP-2 release. Silver staining of SDS-PAGE gels revealed BMP-2 monomer and dimer bands (red boxes) in the soluble BMP-2 lane (#6) at ~13 kDa and ~26 kDa, respectively, as well as a BSA band (blue box) at ~63 kDa (Figure 7.7D). The BMP-2 monomer (red box) and BSA (blue box) bands were also visible in the BMP-2-loaded microparticle lane (#3), although no BMP-2 dimer band was observed and the bands were considerably less intense, indicating, as

expected, incomplete capture of BMP-2 by the microparticles. When the BSA bands in the FBS-loaded microparticle lanes (#4, #5) and the diluted FBS lanes (#7, #8) were compared, the BSA bands in the FBS-loaded microparticle lanes were found to be similar in size to that of the 1:50 diluted FBS lane (#8), demonstrating that only a fraction of the BSA in FBS was entrapped by heparin microparticles. Interestingly, several distinct bands emerged in the FBS-loaded microparticle lanes between 15-37 kDa, which were not present in the diluted FBS lanes, suggesting the concentration of multiple proteins within this molecular weight range. When heparin microparticles were loaded with BMP-2 in the presence of FBS (#5), similar protein bands were observed compared to FBS loading alone; however, the BMP-2 monomer band was faint in comparison, suggesting that serum proteins were preferentially captured by the microparticles in much higher abundance than BMP-2.

Mass spectrometry-based proteomics analysis was used to identify proteins on FBS-loaded heparin microparticles. All proteins detected on FBS-loaded microparticles are listed in Table 7.2. Proteins identified based on only two or fewer unique peptides were excluded from the analysis. Out of 33 total proteins identified, 20 were known heparin-binding proteins, including several apolipoproteins and thrombospondins. Selected peptides identified from these heparin-binding proteins are highlighted in Table 7.1. The extracellular matrix protein fibronectin, which has a known heparin binding site and specific affinity for heparin [301], was confidently identified based on 26 unique peptides. For example, one peptide from fibronectin, SLPLVGQQSTVSDVPRDLE, was very confidently identified with an XCorr of 4.2 and mass accuracy of 0.04 ppm. XCorr signifies the correlation between the experimental mass spectra and theoretical mass

spectra of the peptide; higher XCorr values indicate higher confidence in the peptide identification. Similarly, the mass accuracy of each peptide demonstrates how closely the theoretical mass of the peptide matches the experimentally measured mass. High mass accuracy (less than 3 ppm) is another good indication of confident peptide identifications. On microparticles loaded with both FBS and BMP-2, BMP-2 was only identified based on one unique peptide and thus was not included in the list of detected proteins. This further suggests that FBS borne proteins were entrapped by the microparticles in larger quantities than BMP-2 and corroborates the results obtained from gel electrophoresis.

Table 7.1. Selected Peptides from Known Heparin Binding Proteins Identified on FBS-Incubated Heparin Microparticles. Ppm indicates mass accuracy and XCorr indicates correlation between experimental and theoretical mass spectra for each peptide.

Protein	Peptide	ppm	XCorr
Apolipoprotein-A1	D.NWDTLASTLSK.V	1.03	3.3
	E.TLRQQLAPYSDD.L	0.63	2.9
	E.QLGPVTQE.F	0.27	2.6
Apolipoprotein-B	E.TSRSLPYAQNIQDQLSGLQE.L	1.30	5.9
	K.VSDSLIGVTQGYSVTVK.H	-0.28	4.5
	E.ITVPASQLTVSQFTLPK.S	0.77	4.1
Apolipoprotein-C2	K.TYLPAVDEK.I	0.55	2.4
	D.QVFSVLSGKD.-	0.71	2.0
	E.SLLGYWDTAK.A	0.83	2.9
Apolipoprotein-E	E.LQAAQARLGSDME.D	0.64	4.6
	D.YLRWVQTLSDQVQE.E	-0.06	4.3
	E.QGQSRAATLSTLAGQPLLE.R	0.73	3.8
Thrombospondin-1	K.DHSGQVFSVISNGK.A	-0.37	4.8
	K.FQDLVDAVRAE.K	0.45	3.6
	K.GPDPSSPAFRIE.D	0.83	3.1
Thombospondin-4	E.FQTQNFDRLD.K	-0.13	2.4
	K.SSATIFGLYSSADHSK.Y	0.70	2.3
	K.SSATIFGLYSSADHSK.Y	0.04	3.8
Fibronectin-1	K.LGVRPSQGGEAPRE.V	0.62	4.4
	E.SLPLVGQQSTVSDVPRDLE.V	0.04	4.2
	E.YVYTISVLRDGQE.R	-0.21	4.2

Table 7.2. Complete List of Proteins Identified on FBS-Incubated Heparin Microparticles. Known heparin binding proteins are italicized. Unique peptides represent the number of unique peptides identified from each protein, while total peptides indicates the total number of peptides identified for each protein. Average XCorr was calculated from all peptides.

Symbol	Protein	Unique Peptides	Total Peptides	Average XCorr
APOB	*Apolipoprotein B*	*62*	*66*	*2.9*
FN1	*Embryo-specific fibronectin 1*	*26*	*29*	*2.9*
TLN1	Talin 1	21	22	2.9
POSTN	*Periostin*	*16*	*19*	*2.9*
APOE	*Apolipoprotein E*	*14*	*14*	*3.1*
SERPINA1	*Alpha-1-antiproteinase*	*12*	*13*	*2.8*
ALB	Serum albumin	10	12	2.6
ITIH4	Inter-alpha-trypsin inhibitor heavy chain H4	10	10	2.8
THBS1	*Thrombospondin-1*	*9*	*9*	*2.8*
APOA1	*Apolipoprotein A-I*	*9*	*9*	*2.5*
HBA	Hemoglobin subunit alpha	8	10	2.7
AHSG	Alpha-2-HS-glycoprotein	8	9	3.0
FGA	*Fibrinogen alpha chain*	*8*	*9*	*2.9*
ITIH2	Inter-alpha-trypsin inhibitor heavy chain H2	7	8	2.7
AFP	Alpha-fetoprotein	7	8	2.4
FGG	*Fibrinogen gamma-B chain*	*6*	*8*	*3.2*
GAPDH	*Glyceraldehyde-3-phosphate dehydrogenase*	*6*	*6*	*2.8*
C3	*Complement C3*	*6*	*6*	*2.6*
A2M	Alpha-2-macroglobulin	5	6	3.0
FGB	*Fibrinogen beta chain*	*4*	*10*	*2.9*
KNG1	*Kininogen-1*	*4*	*5*	*3.3*
MYH9	Myosin heavy chain 9 (non-muscle)	4	4	2.9
VTN	*Vitronectin*	*4*	*4*	*2.3*
THBS4	*Thrombospondin-4*	*3*	*4*	*2.7*
COL18A1	*Collagen type XVII alpha 1*	*3*	*3*	*3.0*
SERPINA	*Serpin A3-2*	*3*	*3*	*2.8*
TF	*Serotransferrin*	*3*	*3*	*2.7*
FETUB	Fetuin-B	3	3	2.5
APOC2	*Apolipoprotein C-2*	*3*	*3*	*2.4*
LBP	*Lipopolysaccharide-binding protein*	*3*	*3*	*2.1*

7.4 Discussion

Poor BMP-2 localization and rapid release following delivery is a limiting factor in the widespread use of BMP-2 therapy for bone healing applications. Most delivery approaches have focused on controlled release of growth factors from scaffolds either through non-specific electrostatic binding, which may result in rapid growth factor dissociation, or covalent localization, which may reduce growth factor bioactivity [302, 303]. In this study, we designed a hybrid nanofiber mesh barrier system containing entrapped heparin microparticles with the goal of creating a growth factor sink to impede BMP-2 diffusion outside of the site of interest and subsequently reduce the incidence of heterotopic ossification *in vivo*. We incorporated heparin-based microparticles in order to increase the BMP-2 loading capacity of PCL nanofiber mesh tubes and localize the delivered growth factor within the bone defect. The novel airbrush technique that we employed to incorporate heparin microparticles resulted in uniform meshes with a reproducible distribution of microparticles. Furthermore, the addition of heparin microparticles into the nanofiber meshes resulted in increases in BMP-2 loading capacity and decreases in BMP-2 release from the meshes. Despite promising results achieved *in vitro*, the microparticle-containing meshes did not perform as hypothesized *in vivo*, since no impact was observed on heterotopic ossification, regenerated bone volume, or mechanical properties.

With its high affinity for BMPs, heparin has been previously incorporated into a number of biomaterial scaffolds to reversibly bind BMP-2 through electrostatic interactions and provide sustained delivery *in vivo* to induce mineralization in both

ectopic and orthotopic sites [101, 116, 178, 227, 304-306]. These include heparin-functionalized alginate microparticles [178], heparin-conjugated PLGA nanoparticles and bulk scaffolds [227, 307], and poly-ethylene glycol (PEG) hydrogels modified with heparin chains [172]. Unlike most heparin-containing biomaterials, which are typically used to deliver BMP-2 to bone defects, we employed heparin microparticles entrapped within PCL nanofiber meshes as a composite material to localize BMP-2 release from a primary biomaterial (collagen sponge) with a lower BMP-2 affinity. This biomimetic concept of using heparin as both a physical barrier to diffusion as well as a growth factor sink resembles the natural role played by other GAGs (heparan sulfate and chondroitin sulfate) during development, in which areas of high GAG content sequester cell-secreted growth factors, such as fibroblast growth factors (FGFs) and BMPs, in order to provide spatial localization of mitogenic and morphogenic cues [308]. While a few other studies have used empty heparin-based materials to sequester cell-secreted growth factors [309, 310], to our knowledge, this is the first study that demonstrates the use of an empty heparin-based biomaterial to locally sequester co-delivered BMP-2 *in vivo*.

The fact that the hybrid mesh system exhibited favorable BMP-2 loading and release kinetics *in vitro*, but could not spatially control bone distribution *in vivo*, could be due to a number of reasons. Inadequacies in the physical mesh barrier itself (irrespective of the presence of microparticles) may have contributed to the patterns of bone formation observed. Firstly, the mesh tubes did not fit tightly around the bone ends, such that there was a reduced barrier to diffusion at the bone ends, potentially allowing BMP-2 to exit the collagen sponge without contacting the embedded microparticles; secondly, the possible delamination of these meshes *in vivo* may have further disrupted the intended

barrier. Despite these scaffold limitations, radiographic images and micro-CT reconstructions demonstrated that heterotopic ossification was not limited to the bone ends alone (Figure 7.2), and was also evident in femurs treated with 0.05 mg MP/cm^2 meshes, which remained intact with localized heparin microparticles throughout the 12 week study (Figure 7.6). Furthermore, even with the loss of mesh integrity observed in the 0.10 mg MP/cm^2 meshes, microparticles were observed within the mesh region, accessible to diffusing BMP-2. Lastly, mesh perforations, which accelerated early mineralization at a lower BMP-2 dose (5 μg) in an alginate delivery vehicle [234], did not impact early bone formation in this study, potentially due to the increased BMP-2 dose and use of a collagen sponge delivery vehicle with low BMP-2 affinity.

To further explain the *in vivo* results, we also sought to investigate the conditions under which the heparin microparticles entrapped within the mesh tubes would contact and capture BMP-2 released from the collagen sponge and how this differed from our initial *in vitro* investigation. Insufficient contact time between BMP-2 and heparin microparticles *in vivo* and impaired BMP-2-microparticle interactions in the presence of competing biomolecules may have reduced the ability of entrapped heparin microparticles to impede BMP-2 diffusion. Contact time between heparin microparticles and BMP-2 did not appear to play an important role *in vitro*, as >60% of the BMP-2 in solution was captured by the microparticles immediately upon contact and only 4 hours of incubation were required for >90% loading. This further suggested that the hybrid mesh could readily capture BMP-2 diffusing from the collagen sponge following implantation *in vivo*. On the other hand, the presence of bovine serum decreased the BMP-2 loading capacity of the heparin microparticles and promoted BMP-2 release.

In our previous publication, heparin microparticles displayed a maximum loading capacity of ~300 μg BMP-2 per mg of microparticles in 0.1% BSA in PBS [107]. Based on this loading capacity, the density of microparticles embedded in the meshes (0.11-0.23 mg MPs per mesh) should have been sufficient to capture the entire mass of BMP-2 loaded into the collagen sponge (30 μg). However, given the reduced BMP-2 loading capacity of heparin microparticles in the presence of FBS *in vitro* (~120 μg BMP-2/mg MPs), it is possible that the loading capacity of the microparticles *in vivo* may have also been somewhat reduced in the presence of serum borne soluble factors in the bone defect environment. At the highest BMP-2 dose evaluated *in vitro* (300 μg BMP-2/mg MPs), the BMP-2 loading capacity of the microparticles was reduced by >60% in the presence of FBS. Moreover, BMP-2 release from the microparticles in the presence of serum was double that of BMP-2 release in 0.1% BSA in PBS over 21 days. Additionally, mass spectrometry analysis of the serum proteins bound to heparin microparticles incubated in FBS revealed a number of known heparin binding proteins that display affinity for native heparin, including fibronectin (K_D = 4 μM) [311], thrombospondins (K_D = 4-14 nM) [312], and apolipoproteins (K_D = 22-4000 nM) [313, 314]. Since the dissociation constant of heparin and BMP-2 is on a similar order of magnitude (K_D = 20 nM) [3] to fibronectin, thrombospondins, and apolipoproteins, it is possible that these serum proteins may competitively bind to heparin and may interfere with BMP-2 loading or increase its release *in vivo*. Others have also observed the binding of serum borne and endogenously added fibronectin to heparin-containing materials *in vitro* [127, 315]. Since fibronectin also contains heparin-like growth factor binding domains [316, 317], this ECM molecule may out-compete heparin for protein binding. Growth factor binding to fibronectin has

been demonstrated extensively using both native fibronectin and purified fibronectin fragments containing integrin and growth factor binding domains, which have demonstrated enhanced binding of BMP-2 and other growth factors both *in vitro* and *in vivo* [136, 318, 319].

Since incorporating more heparin microparticles into the nanofiber mesh appeared to increase the risk of mesh delamination, linear heparin chains could be alternatively incorporated into the meshes to provide a more dispersed network of BMP-2 binding sites. Several studies have investigated the addition of varying amounts of heparin into PCL scaffolds using electrospinning [320], covalent immobilization [321], or electrostatic assembly [322]. These methods could also be used to more evenly disperse heparin on the surfaces of the mesh tubes in order to facilitate more immediate contact between the immobilized heparin and diffusing BMP-2. Finally, since the promiscuity of heparin's binding sites may be responsible for the potential saturation of binding sites with serum components, the use of BMP-2-specific binding domains may help to circumvent some of the potential issues caused by serum adsorption and binding to microparticle-containing meshes. A more nuanced approach could include engineered protein-specific binding ligands [10] and derivatives of extracellular matrix molecules that possess a high affinity for specific proteins, such as fibronectin [318, 319]. Ultimately, the incorporation of specific affinity molecules into biomaterials may improve the efficacy of growth factor sink approaches *in vivo*.

7.5 Conclusions

While significant research has focused on developing materials for growth factor delivery, our approach to spatially control local BMP-2 diffusion presents a novel strategy to address clinical concerns of supraphysiological growth factor dose exposure. The mismatch between *in vitro* and *in vivo* results observed in this study also highlights an important caveat in developing biomaterials for *in vivo* applications. While growth factor loading and release performed *in vitro* provides valuable information about a biomaterial's ability to function as a delivery vehicle, it does not necessarily recapitulate the *in vivo* injury environment, and can lead to an overestimation of a material's growth factor loading capacity and underestimation of its growth factor release. Thus, the results of this study may provide insight into the development of other heparin-based protein delivery systems by demonstrating the importance of evaluating materials in serum-containing environments, to better mimic the complex *in vivo* environment and take competitive protein binding into account.

CHAPTER 8: SEQUESTRATION AND DELIVERY OF STEM CELL MORPHOGENS USING HEPARIN MICROPARTICLES

8.1 Introduction

Stem cells are functionally defined as cells that possess the ability to self-renewal and differentiate into a variety of mature cell types, making them a promising cell source for many regenerative medicine applications. Current tissue engineering research has expanded beyond the initial premise of using stem cells as a means of directly replacing diseased and damaged cell populations, resulting in a broadened interest in their utility. The unique properties of stem cells have led to their more widespread use for other applications, such as *in vitro* screening platforms for pharmaceutical testing and models of predictive toxicology [323, 324]. Furthermore, recent research has also revealed that complex mixtures of stem cell-secreted soluble factors can exert beneficial paracrine effects on other cell populations, thereby enabling transplanted stem cells to serve as reservoirs of secreted factors *in vivo* that can influence endogenous cell populations to repair and regenerate damaged tissues through a variety of mechanisms [79]. This is contrary to the traditional notion that transplanted stem cells directly contributed to tissue repair through stable engraftment and differentiation and represents a paradigm shift in the way researchers consider applying stem cells for regenerative medicine, placing emphasis on both the viability of the cells themselves and duration, amount, and efficacy of soluble factors they secrete.

Pluripotent stem cells (PSCs), such as embryonic stem cells (ESCs) and induced

pluripotent stem cells (iPSCs), which were described in more detail in Chapter 2, are particularly promising candidates for exploiting paracrine factor secretion, since concerns of tumorigenicity and low cell engraftment often impede their *in vivo* transplantation [325]. Moreover, ESCs are known to secrete a number of growth factors and other biomolecules that play key roles in development [50, 79, 235], and subsequently may also be harnessed for tissue regeneration.

Previous studies have used mass spectrometry and antibody-based approaches to identify a myriad of soluble factors that make up the ESC secretome, including a number of fibroblast growth factors (FGFs), transforming growth factors (TGF-βs), insulin-like growth factors (IGFs), Wnts, insulin-like growth factor binding proteins (IGFBPs), bone morphogenetic proteins (BMPs), vascular endothelial growth factors (VEGFs), and growth differentiation factors (GDFs), as well as stromal cell-derived factor-1 (SDF-1) and stem cell factor (SCF) [48-51]. Many of these growth factors have been implicated in tissue development and regeneration, and several studies have attributed positive outcomes observed *in vivo* following ESC transplantation to various stem cell-secreted factors. For example, transplantation of ESCs following myocardial infarction resulted in improvements in heart function, potentially due to ESC-secreted VEGF, IGF-1, and IL-10 [80], while injection of ESCs into an embryonic mouse model of cardiac defects, rescued a normal cardiac phenotype through increased Wnt5a and IGF-1 secretion and

without cell engraftment [326]. Similar results have also been demonstrated *in vitro*, in studies wherein ESC-conditioned media elicited proliferation and migration of progenitor cells and terminally differentiated cells, including muscle satellite cells, neural progenitor cells, fibroblasts, endothelial cells, and hematopoietic progenitor cells [7, 8, 51, 52].

Despite the promising results that have been attributed to ESC paracrine effects thus far, few researchers have attempted to deliver stem cell secreted factors without transplanting the cells themselves [8, 82]. The short half-life and high diffusivity of soluble factors *in vivo* coupled with the dilute nature of these molecules in ESC-conditioned media present significant technical challenges to developing paracrine-based tissue regeneration strategies. Consequently, we aimed to develop a robust biomaterial approach for concentrating ESC-derived morphogens and providing their enhanced delivery both *in vitro* and *in vivo*.

We have previously developed heparin-based microparticles that demonstrate a high capacity for BMP-2 (>1000 times greater than other heparin-based materials), as well as a number of other heparin binding proteins [107]. These microparticles can be used to locally concentrate large amounts of growth factor, while maintaining growth factor bioactivity and ability to induce functional cellular responses. Heparin-based biomaterials have been used extensively for the sequestration and delivery of various growth factors, including BMP-2, VEGF, and FGF-2 [112, 173, 327-329], due to

heparin's natural ability to strongly and reversibly bind positively charged proteins with its negatively charged sulfate groups [91]. However, heparin biomaterials have not previously been used to sequester and concentrate multiple proteins of interest from a complex mixture of biomolecules such as conditioned media.

In this first proof-of-concept study, we aimed to harness the promiscuous growth factor binding ability of heparin to selectively enrich a number of potent stem cell-derived morphogens from ESC-conditioned media, while excluding cellular wastes and metabolites. Conditioned media was collected from ESC aggregates undergoing differentiation and analyzed via proteomics analysis such as SDS-PAGE and mass spectrometry to demonstrate that multiple proteins from conditioned media could be sequestered by heparin microparticles. Morphogen-laden microparticles were then delivered to multiple cell types *in vitro* to assess their ability to induce functional cellular responses, such as cell proliferation and differentiation. Finally, since stem cell paracrine-based strategies may eventually be used in conjunction with existing growth factor delivery therapies, the ability to co-deliver the potent osteogenic protein BMP-2 with ESC-derived morphogens from conditioned media was also investigated *in vitro* to inform future *in vivo* bone regeneration applications.

8.2 Materials and Methods

8.2.1 Embryonic Stem Cell Culture

Undifferentiated murine embryonic stem cells (mESCs, D3 cell line; ATCC) were maintained and expanded on tissue culture polystyrene plates (Corning) coated with 0.1% gelatin (Millipore), in high glucose Dulbecco's Modified Eagle Medium (DMEM; Corning Mediatech) containing 16% fetal bovine serum (FBS; Thermo Scientific – Hyclone), 1X Minimal Essential Media (MEM) non-essential amino acid solution (Corning Mediatech), 2 mM of L-glutamine (Corning Mediatech), 100 units/mL of penicillin (Corning Mediatech), 100 μg/mL of streptomycin (Corning Mediatech), 0.25 μg/mL of amphotericin (Corning Mediatech), 0.1 mM of β-mercaptoethanol (Sigma Aldrich), and 100 units/mL of leukemia inhibitory factor (LIF; Millipore), as previously described [330]. Media was completely exchanged every two days, and cells were passaged after reaching ~80% confluence.

8.2.2 Embryoid Body Formation, Culture, and Conditioned Media Collection

Embryoid bodies (EBs) were formed from undifferentiated mESCs using a forced aggregation technique, as previously described [330-332]. mESCs were trypsinized using 0.05% trypsin-EDTA (Thermo Fisher Scientific) and plated at a density of 1.2 million cells/well in 24-well 3% agarose inserts containing ~1200 individual 400 μm x 400 μm pyramidal microwells, in order to create ~1200 uniform embryoid bodies containing

~1000 cells each. 500 μL of 16% FBS in DMEM were added to the microwell inserts, which were centrifuged at 3000 rcf for 5 minutes to remove air bubbles; 500 μL of mESCs at a density of 2.4 million cells/mL were then added to the microwells, allowed to settle for 5 minutes, and centrifuged at 200 rcf for 3 minutes. Embryoid bodies were maintained in microwell inserts in serum-containing media without LIF for approximately 20 hours to promote aggregation and then removed from the microwells and suspended in non-adherent, bacteriological grade polystyrene Petri dishes at a density of ~1200 EBs per 10 mL of media.

Embryoid bodies (EBs) were cultured on a rotary orbital shaker set to 45 rpm in serum free media, consisting of 1X N2 and B27 supplements (Thermo Fisher Scientific), 1X MEM non-essential amino acid solution, 2 mM of L-glutamine, 100 units/mL of penicillin, 100 μg/mL of streptomycin, 0.25 μg/mL of amphotericin, and 0.1 mM of β-mercaptoethanol in KnockOut^{TM} DMEM (Thermo Fisher Scientific). Media was completely exchanged and collected after 4, 7, 9, 10, 11, 12, 13, and 14 days of culture; the frequency of media exchanges increased over time as the total number of cells in culture increased, and media became exhausted more quickly. Collected conditioned media was centrifuged at 3000 rcf for 10 minutes to remove any cellular debris and stored at -20°C until use. Unconditioned media was generated by incubating serum free media without cells in Petri dishes at 37°C on rotary culture for 48 hours prior to use, in order to permit protein adsorption and degradation similar to that which would occur in conditioned media samples.

8.2.3 Embryoid Body Characterization

Phase images were taken of EBs before and after initial formation in microwells and at Day 4, 7, 10, 12 and 14 of differentiation in Petri dishes. EBs were also collected at each of these time points for histological analysis as previously described [330]. EBs were sampled from Petri dishes, washed once in PBS, and fixed in 10% neutral buffered formalin at 4ºC for 30 minutes, before being washed in 1% polysorbate 20 and 1% BSA in PBS. Fixed EBs were then embedded in 2% (w/v) agarose in PBS at 4ºC overnight, dehydrated through submersion in a series of alcohol and xylene solutions, and embedded in paraffin wax at 60°C. 5 μm sections were obtained and stained with Safranin O/Fast Green and Hematoxylin/Eosin (H&E).

8.2.4 Analysis of Conditioned Media Protein Content

Total protein content of EB conditioned media samples was determined using a bicinchoninic acid (BCA) protein assay (Thermo Fisher Scientific) according to manufacturer's instructions and normalized to the protein content of unconditioned media samples. Specific growth factors of interest in conditioned media samples were evaluated using enzyme linked immunosorbent assay (ELISA) kits for BMP-2, BMP-4, VEGF, and IGF-2 (R&D Systems).

8.2.5 Loading Heparin Microparticles with EB Conditioned Media

Heparin microparticles were loaded with EB conditioned media similar to loading with a single growth factor solution [107]. 0.2 mg of microparticles were incubated with either 1 mL or 5 mL of conditioned media collected from each aforementioned time point and rotated at 4ºC for 16 hours. The microparticles were then centrifuged at 3000 rcf for 5 minutes, washed once in PBS to remove any loosely bound media components, and used for SDS-PAGE analysis, mass spectrometry, or functional cellular assays. Day 1-4 EB conditioned media depleted of microparticle-binding components were also assayed for remaining BMP-4 and VEGF using ELISA.

For loading with both conditioned media and BMP-2, microparticles were either (1) incubated in 30 ng of BMP-2 in 1 mL of 0.1% BSA in PBS for 16 hours first, followed for 16 hours of incubation in conditioned media, (2) incubated in conditioned media first, followed by incubation in BMP-2, or (3) BMP-2 was added directly to the conditioned media and microparticles were incubated in both simultaneously. BMP-2 loading efficiency from conditioned media was evaluated using ELISA.

8.2.6 Removal of Proteins from Heparin Microparticles

It was necessary to elute proteins bound to heparin microparticles for SDS-PAGE and mass spectrometry analysis, and these methods are described in the respective sections below. Removal of proteins was confirmed using a fluorescamine binding assay [333], since fluorescamine fluoresces in the presence of free amines and can be used to

determine the amount of protein remaining on a sample of heparin microparticles. 0.01% (w/v) fluorescamine (Sigma Aldrich) in acetone was added to 0.1 mg of heparin microparticles in a 1:3 fluorescamine to sample volume ratio, and the solution was read on a microplate reader (Biotek) at an excitation of 390 nm and emission of 475 nm. The fluorescent signal intensity was compared to that of a glycine standard curve (0.05-8 μg/mL). 0.1 mg of heparin microparticles were loaded with PBS (no protein control), 1 mg of BSA in PBS, 150 ng of BMP-2 in PBS, and 1-5 mL of Day 1-4 EB conditioned media. Microparticles were washed once with PBS, treated for SDS-PAGE analysis, or treated for mass spectrometry analysis (trypsin treatment) to determine the efficacy of each of these protein removal methods; results were compared to that of untreated, protein-loaded microparticles and unloaded microparticles.

8.2.7 Gel Electrophoresis and Silver Staining

In order to characterize the proteins in EB conditioned media samples that bound to heparin microparticles, eluted proteins from microparticles were analyzed via sodium dodecyl sulfate polyacrylamide gel electrophoresis (SDS-PAGE) followed by silver staining for all proteins bands [334], as well as protein mass spectrometry. For SDS-PAGE analysis, 0.2 mg of heparin microparticles were incubated in solutions as indicated in Table 8.1 and Table 8.2 at 4°C, prepared as mentioned above, and resuspended in SDS-PAGE loading buffer, containing a mixture of SDS, Tris-HCl, glycerol, bromophenol blue, and β-mercaptoethanol. Soluble BMP-2 was also suspended in SDS-PAGE loading buffer and run on the gel as an additional control. All solutions were

heated to 95°C for 10 minutes prior to loading onto a 12% Mini-PROTEAN TGX gel (Bio-Rad Laboratories, Hercules, CA). Gel electrophoresis was performed in SDS/PAGE running buffer under reducing and denaturing conditions using a Mini-PROTEAN Tetra Cell system (Bio-Rad) set at a constant voltage (200 V) for 30 minutes. A 10-250 kDa protein ladder (Precision Plus Kaleidoscope, Bio-Rad) was used as a molecular weight reference. Silver staining of SDS/PAGE gels was performed using a Silver Staining Plus Kit (Bio-Rad) as per the manufacturer's instructions, rinsed, and imaged using a CanoScan LiDE 220 Flatbed Scanner (Canon USA, Melville, NY).

Table 8.1. Protein Samples Analyzed Using SDS-PAGE Following By Silver Stain (Gel #1)

Lane	Description
1	10-250 kDa Protein Ladder
2	Unloaded Microparticles (MPs)
3	5 mL Unconditioned Media Loaded onto MPs
4	5 mL Undifferentiated ESC Conditioned Media Loaded onto MPs
5	5 mL Day 1-4 EB Conditioned Media Loaded onto MPs
6	5 mL Day 4-7 EB Conditioned Media Loaded onto MPs
7	5 mL Day 9-10 EB Conditioned Media Loaded onto MPs
8	5 mL Day 11-12 EB Conditioned Media Loaded onto MPs
9	5 mL Day 13-14 EB Conditioned Media Loaded onto MPs

Table 8.2. Protein Samples Analyzed Using SDS-PAGE Following By Silver Stain (Gel #2)

Lane	Description
1	10-250 kDa Protein Ladder
2	30 ng Soluble BMP-2
3	0.1% BSA in PBS Loaded onto Microparticles (MPs)
4	30 ng BMP-2 Loaded onto MPs
5	1 mL Unconditioned Media Loaded onto MPs
6	1 mL Conditioned Media (Day 1-4 EBs) Loaded onto MPs
7	1 mL Unconditioned Media + 30 ng BMP-2 Loaded onto MPs
8	1 mL Conditioned Media (Day 1-4 EBs) + 30 ng BMP-2 Loaded onto MPs
9	5 mL Unconditioned Media
10	5 mL Conditioned Media (Day 1-4 EBs)

8.2.8 Mass Spectrometry

Mass spectrometry was also used to further characterize a) proteins in Day 1-4 EB conditioned media samples and b) proteins bound to heparin microparticles from Day 1-4 EB conditioned media. For conditioned media samples, 100 μL of each sample were digested with 2 units of Glu-C (16 hours) and 10 units of Lys-C (3.5 hours) in 50 mM HEPES (pH=7.9). For protein-loaded microparticle samples, 0.2 mg of microparticles were incubated in 5 mL of conditioned media overnight, then centrifuged, washed once with PBS, and digested with 2 units of Glu-C (16 hours) and 10 units of Lys-C (3.5 hours) in 50 mM HEPES (pH=7.9). Peptides from all samples were then purified, dried, and resuspended in 5% acetonitrile and 4% formic acid for liquid chromatography-tandem mass spectrometry (LC-MS/MS) analysis. Detailed mass spectrometry methods can be found in Chapter 7 and in the listed references [294, 296, 335].

8.2.9 C2C12 Alkaline Phosphatase Activity and DNA Assays

Mouse skeletal myoblasts (C2C12; ATCC) were cultured in growth media consisting of DMEM (Corning) supplemented with 16% FBS and maintained at 37ºC in a 5% CO_2 humidified incubator. Alkaline phosphatase (ALP) and DNA content assays were performed as previously described [107]. C2C12 cells were seeded in 96-well plates at an initial density of 20,000 cells per well and allowed to attach for 6 hours under growth conditions (16% FBS in DMEM). Cells were then switched to low serum media (1% FBS in DMEM), and the following treatments were added: 0.1 mg of unloaded heparin microparticles, EB conditioned media, 0.1 mg of microparticles loaded with 0.5 mL of EB conditioned media (1x MPs), 0.1 mg of microparticles loaded with 2.5 mL of EB conditioned media (5x MPs), and EB conditioned media depleted of microparticle-binding components. Conditioned media collected after 4, 7, 10, 12, and 14 days of EB differentiation were tested. Low serum (1% FBS) and high serum (16% FBS) media were used as controls. After 72 hours of treatment, cells were washed with PBS and lysed using 100 µL of CelLytic M (Sigma Aldrich). Cell lysate was stored at -80ºC prior to analysis.

ALP activity of C2C12 cultures was measured by incubating 50 µL of cell lysate with 50 µL of CelLytic M and 100 µL of a substrate solution consisting of 3.33 mM $MgCl_2$ (VWR), 500 mM 2-amino-2-methyl-1-propanol (Sigma Aldrich), and 6.67 mM p-nitrophenyl phosphate (pNPP; Sigma Aldrich). The reaction was terminated with 0.2 M NaOH after one hour, and absorbance measured at 405 nm on a microplate reader. A

standard curve for total ALP activity was generated using graded concentrations of the ALP product, 4-nitrophenol (0-1 nmol/μL; Sigma Aldrich).

DNA content of C2C12 cultures was measured using the QuantiFluor dsDNA kit (Promega). Briefly, 20 μL of cell lysate was incubated with 80 μL of the assay buffer and 100 μL of the fluorescent DNA-binding dye for five minutes, protected from light. Fluorescence was measured on a microplate reader, using an excitation wavelength of 504 nm and emission wavelength of 519 nm. Total DNA content was correlated to fluorescence by comparison to a lambda DNA standard curve (48.5 kb). Fold-change in DNA was determined by dividing the final DNA content after 72 hours of culture by DNA content after 6 hours of initial cell attachment (Day 0).

8.2.10 NIH/3T3 DNA and Cell Proliferation Assays

Mouse embryonic fibroblasts (NIH/3T3; ATCC) were cultured in growth media consisting of DMEM (Corning) supplemented with 16% FBS and maintained at 37ºC in a 5% CO_2 humidified incubator. DNA content assays were performed as previously published [107] and were described for C2C12 cells in the preceding section. NIH/3T3 cells (20,000 cells/well) were treated with the following for 72 hours: 0.1 mg of unloaded heparin microparticles, EB conditioned media, 0.1 mg of microparticles loaded with 0.5 mL of EB conditioned media (1x MPs), 0.1 mg of microparticles loaded with 2.5 mL of EB conditioned media (5x MPs), and EB conditioned media depleted of microparticle-binding components. Conditioned media collected after 4, 7, 10, 12, and 14 days of EB differentiation were tested. Low serum and high serum media were used as controls.

EdU (5-ethynyl-2'-deoxyuridine) incorporation was used to evaluate active DNA synthesis as an indication of cell proliferation [336]. Since Day 1-4 EB conditioned media had a greatest effect on NIH/3T3 DNA content, treatment with 0.2 mg of microparticles loaded with 1 mL of Day 1-4 EB conditioned media was compared to treatment with 0.2 mg of unloaded microparticles, low serum medium, and high serum medium. The Click-iT® Edu Alexa Fluor 488 Imaging Kit (Thermo Fisher Scientific) was used according to manufacturer's instructions and previously established protocols [336]. 10,000 cells were plated in a 25 mm x 75 mm well of a glass chamber slide (Nunc™ Lab-Tek™ II Chamber Slide™ System, Thermo Fisher Scientific) and allowed to attach in 16% FBS in DMEM overnight. Media was then removed and replaced with low serum (1% FBS) media for the next 8 hours to slow cell proliferation. Following this, cells were subjected with the aforementioned treatments for a total of 24 hours, in which 10 μM of EdU was added to the cultures for the last 6 hours. EdU was allowed to incorporate into cellular DNA over this period of time, after which cells were fixed in 3.7% paraformaldehyde in PBS for 30 minutes, permeabilized with 0.5% Triton-X in PBS for 20 minutes, and stained with Hoechst 33342 (1:2000 dilution) for cell nuclei and Alexa Fluor 488 hydrazide for EdU detection via a copper-catalyzed click reaction.

8.2.11 Analysis of C2C12 and NIH/3T3 Cell Morphology

Morphological differences in C2C12 cultures caused by treatment with Day 1-4 EB conditioned media-loaded microparticles were analyzed using rhodamine-conjugated phalloidin staining for visualizing filamentous actin (Thermo Fisher Scientific). 10,000

cells were plated in a 25 mm x 75 mm well of a glass chamber slide, allowed to attach in 16% FBS in DMEM overnight, and treatments were added. After 24 hours of treatment, cells were fixed in 3.7% paraformaldehyde in PBS, permeabilized with 0.5% Triton-X in PBS, and stained with rhodamine-conjugated phalloidin (165 nM) and Hoechst 33342 (1:2000 dilution).

8.2.12 Statistical Analysis

All data are reported as mean ± standard error of the mean. Experiments were run with a minimum of four replicates for each experimental group. Statistical significance was determined using one-way or two-way ANOVA as appropriate, followed by Bonferroni's post hoc analysis (Graphpad Prism, Version 5.0, La Jolla, CA). $P < 0.05$ was considered statistically significant.

8.3 Results

8.3.1 Embryoid Body Characterization

Embryonic stem cells were aggregated into 1000-cell embryoid bodies in agarose microwells over 20 hours and cultured on a rotary orbital shaker at a density of 1200 EBs per 10 mL of serum-free media for 14 days (Figure 8.1). Phase images before and after initial formation (Figure 8.1) and at 4, 7, 10, 12, and 14 of rotary suspension culture (Figure 8.2A-E) depict EBs increasing in size from ~200 μm in diameter initially to >750

μm in diameter at Day 14. Images of EBs stained with Hematoxylin/Eosin (Figure 8.2F-J) and Safranin O/Fast Green (Figure 8.2K-O) demonstrate that this increase in EB area is due mainly to an increase in cell number, as indicated by the number of hematoxylin-stained cell nuclei. Histology images also demonstrate areas of extracellular matrix deposition at later time points (indicated by arrows), as well as tightly packed, epithelial-like and sparse, mesenchymal-like morphologies (indicated by yellow and black arrowheads, respectively).

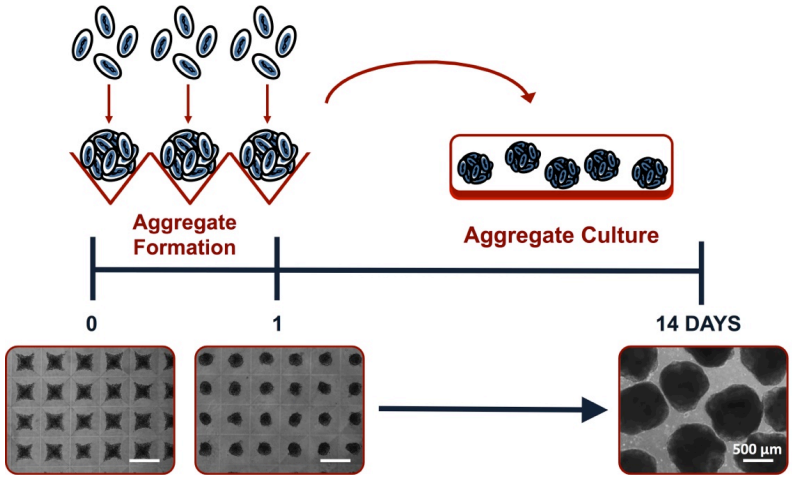

Figure 8.1. Schematic of Embryoid Body Culture. Undifferentiated embryonic stem cells were formed into embryoid bodies in agarose microwells overnight using a forced aggregation technique and then cultured in suspension for 14 days on a rotary orbital shaker. Images depict cells in microwells following centrifugation, after ~20 hours of formation, and in rotary suspension culture at Day 14.

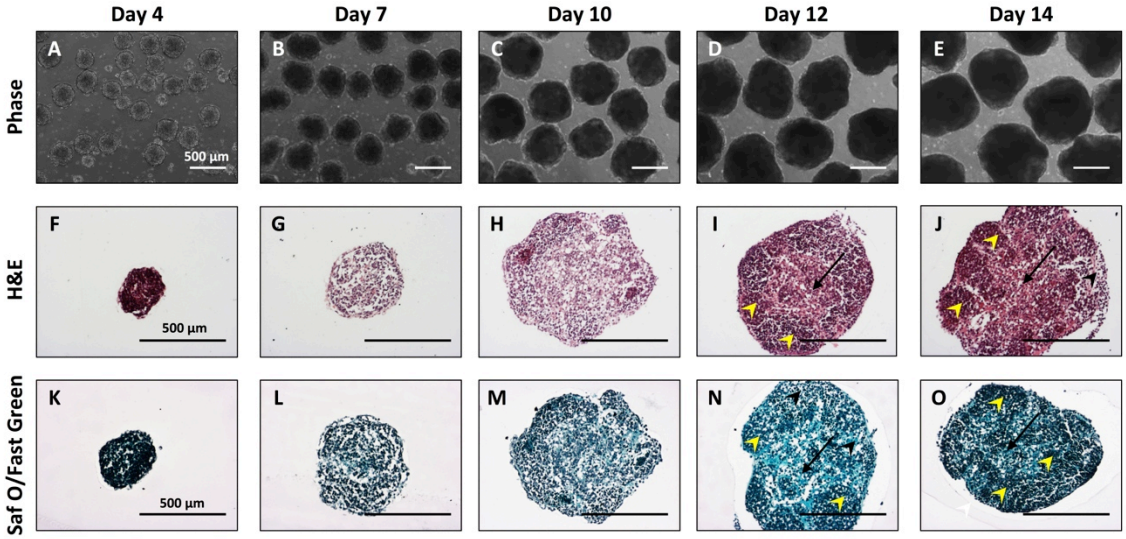

Figure 8.2. Size and Morphology of Differentiating Embryoid Bodies. A-E) Phase images of EBs in rotary suspension culture at Day 4, 7, 10, 12, and 14 of differentiation depict EBs increasing in size over time. EBs were also fixed, embedded in paraffin, and sectioned for histological analysis at the aforementioned time points. F-J) Images of EBs stained with Hematoxylin/Eosin and K-O) Safranin O/Fast Green depict aggregates that increased in size and cell number over time and contained areas of extracellular matrix (black arrows) at later time points. ESCs within EBs demonstrated both epithelial-like and mesenchymal-like morphologies (yellow arrowheads and black arrowheads, respectively). All scale bars = 500 µm.

8.3.2 Conditioned Media Characterization

A BCA protein assay was used to determine the protein content of media conditioned by EBs during Day 1-4, Day 4-7, Day 9-10, and Day 11-12, and Day 13-14 of differentiation, and normalized to the protein content of unconditioned media. EB conditioned media was found to contain between 200-500 µg/mL of secreted protein with higher protein content in Day 1-4 EB conditioned media compared to media from later time points (Day 9-10, Day 13-14) (Figure 8.3A). Individual ELISAs for proteins in Day 4-7, Day 7-10, and Day 10-12 EB conditioned media revealed variable levels of BMP-4 and VEGF, consistent levels of IGF-2, and no detectable BMP-2 (Figure 8.3B).

8.3.3 Characterization of Microparticle-Bound Conditioned Media Proteins

The abundance of proteins in cell conditioned media makes analysis of individual protein types difficult. We have previously demonstrated that heparin microparticles can be used to sequester specific heparin-binding proteins from both fetal bovine serum (Chapter 7) and conditioned media [337], resulting in a reduction in bovine serum albumin content, which can mask other less abundant proteins, and an enrichment in smaller, 15-37 kDa proteins, enabling easier protein detection. Consequently, ESC and EB conditioned media samples from multiple time points of differentiation were incubated with heparin microparticles, and the loaded proteins were eluted and qualitatively assessed via SDS-PAGE following by silver staining (Figure 8.3C).

SDS-PAGE revealed a prominent BSA band in the unconditioned media lane (red box) followed by minimal staining for additional proteins. On the other hand, lanes containing EB conditioned media proteins exhibit both a reduced presence of BSA (red box) and increased staining for a number of protein bands within the 10-20 kDa and 25-37 kDa molecular weight ranges (blue boxes). Furthermore, the protein content in these samples appeared to be dependent on the stage of EB differentiation from which the conditioned media was taken, as multiple dark bands were evident at earlier time points of differentiation (Day 1-4, Day 4-7, and Day 9-10 EB conditioned media). Microparticles loaded with conditioned media from undifferentiated ESCs demonstrated fewer protein bands with less intense staining than that of EB conditioned media.

Select ELISAs were also performed on Day 1-4 EB conditioned media and depleted conditioned media following overnight incubation with heparin microparticles.

Based on the amount of growth factor remaining in solution, heparin microparticles bound 47.6 ± 7.5% of VEGF and 88.6 ± 2.8% of BMP-4 contained in EB conditioned media (Figure 8.4A), demonstrating that sequestration of specific heparin-binding proteins still occurred in a complex solution containing numerous other soluble factors.

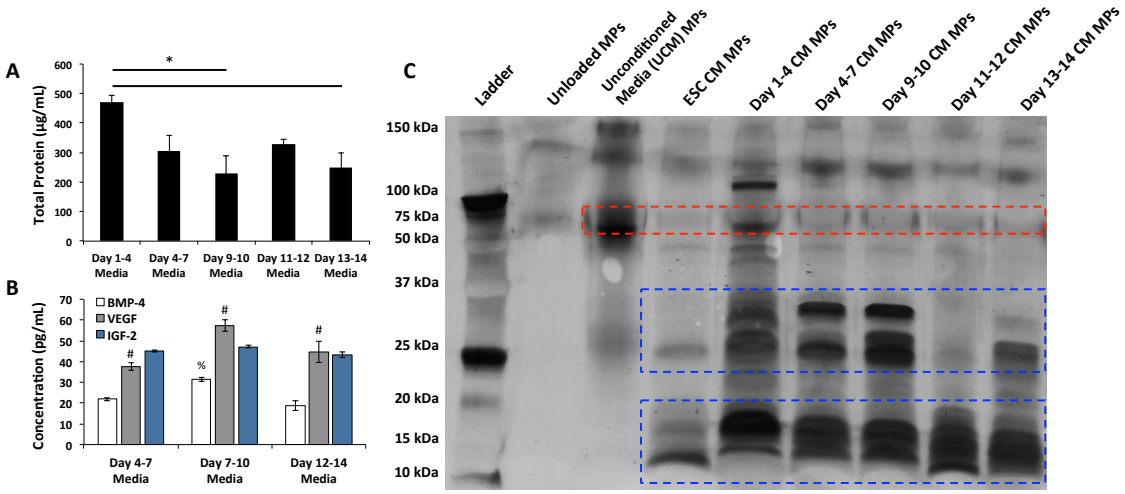

Figure 8.3. Characterization of Protein Content of EB Conditioned Media and Conditioned Media Loaded Microparticles. A) A BCA protein assay was used to determine total protein content of EB conditioned media. Media contained ~200-500 µg/mL of additional secreted protein, when normalized to unconditioned media protein content. Day 1-4 EB conditioned media contained more secreted protein than conditioned media collected from Day 9-10 and Day 13-14. (* = $p < 0.05$ as indicated) B) ELISAs for BMP-4, VEGF, and IGF-2 content in Day 4-7, Day 7-10, and Day 12-14 EB conditioned media revealed that EB conditioned media collected from different time points contained varying amounts of BMP-4 and VEGF, and consistent amounts of IGF-2. BMP-2 was not detected. (% = $p < 0.05$ compared to BMP-4 content at other time points, # = $p < 0.05$ compared to VEGF content at other time points.) C) SDS-PAGE gel stained with silver stain to non-specifically detect all proteins eluted from heparin microparticles. 0.2 mg of microparticles were loaded overnight with 5 mL of unconditioned media, undifferentiated ESC conditioned media, and conditioned media from Day 1-4, Day 4-7, Day 9-10, Day 11-12, and Day 13-14 of EB differentiation. Proteins were eluted from microparticles in SDS-PAGE loading buffer after being heated for 10 minutes at 95ºC. Red dashed box represents BSA band, and blue dashed boxes represent proteins within the 10-20 kDa and 25-37 kDa ranges that were detected in EB conditioned media.

8.3.4 Depletion of Conditioned Media Components by Heparin Microparticles with or without Exogenous BMP-2 Addition

Future *in vivo* applications of heparin microparticles as delivery vehicles for EB conditioned media may require the addition of other potent proteins to help stimulate initial cellular responses. Since BMP-2 was not detected in conditioned media, additional recombinant BMP-2 would likely be necessary to develop this tissue engineering strategy for bone regeneration. Thus, the ability of heparin microparticles to deplete both conditioned media and exogenously added BMP-2 from solution was evaluated.

Heparin microparticles depleted ~90% of BMP-2 from solution when added prior to conditioned media incubation, following conditioned media incubation, or together with conditioned media (Figure 8.4B). This depletion of BMP-2 from solution was similar to what has been observed previously in a single growth factor solution containing BMP-2 alone [107] and multiple growth factor solution containing BMP-2 and VEGF (Figure 3.6), indicating minimal interference of conditioned media components on BMP-2-heparin microparticle interactions. BMP-2 loading onto heparin microparticles in the presence of 0.1% BSA in PBS, unconditioned media, and Day 1-4 EB conditioned media was confirmed via SDS-PAGE followed by silver staining and compared to protein staining in the soluble BMP-2 lane (Figure 8.4C); blue dashed boxes indicate BMP-2 bands. Similar to Figure 8.3C, the BSA bands in most microparticle-eluted samples were reduced compared to the BSA band in the soluble BMP-2 lane (red dashed boxes). Furthermore, when microparticles loaded with five times the volume of media (0.2 mg microparticles in 5 mL media vs. 1 mL media) were treated and run on the

gel, the densities of the protein bands increased, indicating that the total amount of protein bound to the microparticles also increased. This increase in the intensity of other protein bands was accompanied by a similar increase in the intensity of the BSA band.

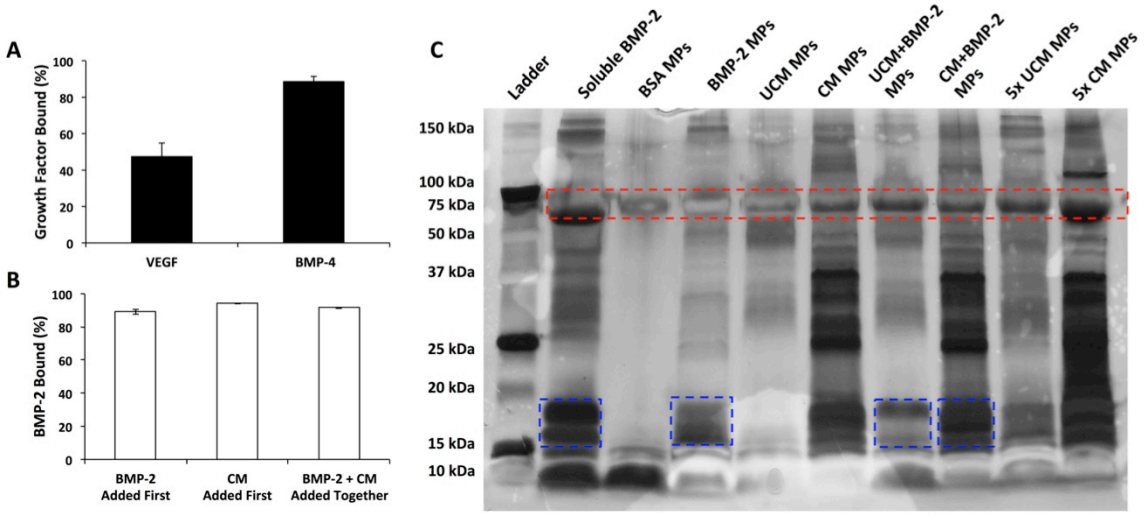

Figure 8.4. Analysis of Microparticle-Mediated Protein Depletion from Conditioned Media With or Without Exogenous BMP-2 Addition. A) Heparin microparticles incubated with Day 1-4 EB conditioned media overnight at 4ºC depleted 47.6 ± 7.5% of VEGF and 88.6 ± 2.8% of BMP-4 from solution. B) Microparticles bound ~90% of BMP-2 from solution when 30 ng of BMP-2 was added prior to conditioned media incubation, following conditioned media incubation, or when BMP-2 and conditioned media were added to microparticles simultaneously. C) SDS-PAGE gel stained with silver stain to detect all proteins eluted from microparticles. 0.2 mg of microparticles were loaded overnight with the solutions described in Table 8.2. Before running SDS-PAGE, proteins were eluted from microparticles in SDS-PAGE loading buffer. 30 ng of soluble BMP-2 were also heated in loading buffer and run on the gel as an additional control. Red dashed box indicates BSA band, and blue dashed boxes indicate BMP-2 bands.

8.3.5 *Dissociation of Proteins from Heparin Microparticles*

Dissociation of proteins from heparin microparticles was required for both SDS-PAGE and mass spectrometry analysis. A fluorescamine assay was conducted on protein-loaded microparticles treated for SDS-PAGE (10 min at 95ºC in SDS-PAGE loading buffer) and mass spectrometry (overnight trypsin digestion) and compared to protein-loaded microparticles that were washed once in PBS without any additional treatment.

Analysis of untreated microparticles revealed that 1296 ± 8 ng of BSA/mg microparticles bound from a 1 mg/mL BSA solution (~0.01%), 1349 ± 60 ng of BMP-2/mg microparticles bound from a 150 ng/mL BMP-2 solution (~90%), 461 ± 35 ng of protein/mg microparticles bound from 1 mL of conditioned media, and 631 ± 49 ng of protein/mg microparticles bound from 5 mL of conditioned media (Figure 8.5). The high efficiency of BMP-2 loading further corroborated a strong affinity between heparin microparticles and BMP-2 compared to the weak interactions between heparin microparticles and BSA. Additionally, loading heparin microparticles with increased amounts of conditioned media (5 mL vs. 1 mL) resulted in higher protein loading. Despite the different amounts and types of proteins captured by heparin microparticles, both SDS treatment and trypsin treatment resulted in removal of proteins from microparticles loaded with BSA, BMP-2, and conditioned media. There were no differences in efficacy between the two protein removal methods, and residual protein content was similar to that of unloaded microparticles.

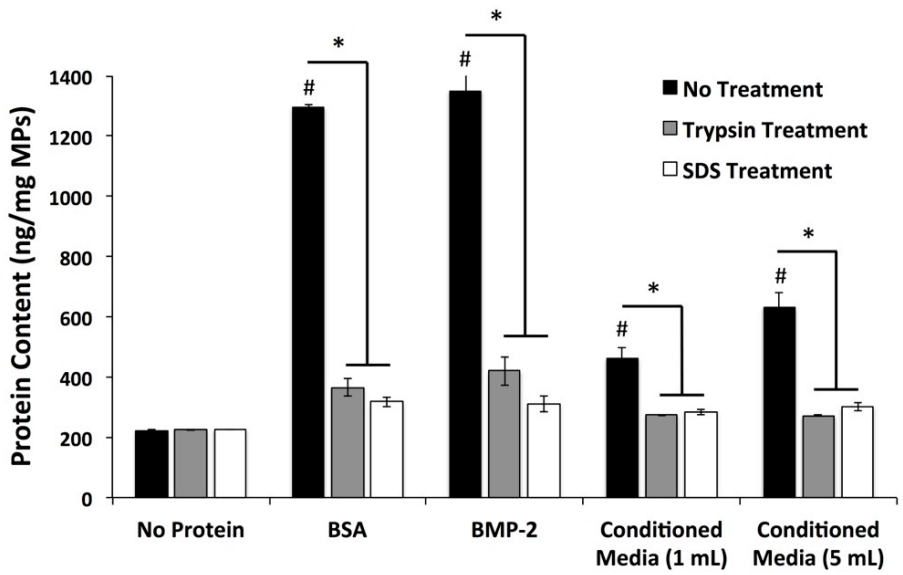

Figure 8.5. Protein Loading and Removal from Heparin Microparticles Based on Fluorescamine Assay. Microparticles were loaded with 1 mg of BSA in 1 mL of PBS, 150 ng of BMP-2 in 1 mL of PBS, or 1-5 mL of Day 1-4 EB conditioned media. Microparticles were then washed once with PBS (No Treatment), washed with PBS and digested with trypsin overnight (Trypsin Treatment), or washed once in PBS and heated for 10 minutes at 95ºC in SDS-PAGE loading buffer (SDS Treatment). Microparticles incubated in 1 mL of PBS overnight served as a "No Protein" control. Fluorescamine was used to evaluate the protein content of microparticles based on fluorescence microplate readings and compared to a glycine standard curve (0.05-8 μg/mL). (# = $p < 0.05$ compared to microparticles with no protein, * = $p < 0.01$ as indicated)

8.3.6 Mass Spectrometry Analysis of EB Conditioned Media and Microparticles Loaded with EB Conditioned Media

Mass spectrometry proteomic analysis was used as an unbiased approach to identify proteins in EB conditioned media and proteins bound to heparin microparticles after incubation in EB conditioned media. Prior to investigating this approach with conditioned media, heparin microparticles were loaded with single growth factor solutions of BMP-2 and TGF-β1 for mass spectrometry analysis; positive identification of these proteins confirmed that this method could identify microparticle-bound proteins.

Day 1-4 EB conditioned media was analyzed, due to the variety of protein bands displayed when Day 1-4 EB conditioned media was loaded onto heparin microparticles and run on SDS-PAGE (Figure 8.3). Proteins from conditioned media and loaded heparin microparticles were digested overnight using trypsin, which effectively removed proteins bound to microparticles (Figure 8.5). All proteins detected in EB conditioned media and media-loaded microparticles are listed in Table B.1 and Table B.2 in Appendix B. Human contaminants, such as keratins, and proteins identified based on two or fewer unique peptides were removed from the dataset.

Overall, mass spectrometry analysis identified 35 proteins in EB conditioned media and 169 proteins on conditioned media-loaded microparticles. Clustering of microparticle-bound proteins according to cellular compartment (Table 8.3) and biological process (Table 8.4) revealed that most proteins identified were intracellular and involved in metabolic processes and cellular component assembly. Heat shock proteins, as well as histones and ribosomal proteins, which were more frequently identified on microparticles, contributed largely to the clustering results. Some notable secreted proteins that were identified included left-right determination factor-2 (LEFTY-2), fibronectin, and osteopontin, as well as several thrombospondins, secreted frizzled related proteins (SFRPs), and apolipoproteins. Both thrombospondins and apolipoproteins are known heparin binding proteins [93]. The molecular weights of these proteins ranged from 10-400 kDa, with many in the 10-37 kDa range of interest identified via SDS-PAGE gels.

Table 8.3. Cellular Compartment Clustering of Peptides Identified via Mass Spectrometry from Heparin Microparticles Loaded with Day 1-4 EB Conditioned Media

Cellular Compartment	Number of Identified Peptides	Percentage of Total Peptides (%)	P Value
Intracellular	163	96.6	1.52E-10
Cytoplasm	138	81.4	1.24E-10
Membrane-bounded organelle part	109	64.4	2.79E-03
Macromolecular complex	97	57.6	6.93E-13
Nucleus	90	47.5	8.93E-04
Non-membrane-bounded organelle part	72	42.4	1.17E-08
Ribonucleoprotein complex	54	32.2	1.80E-14
Ribosome	46	27.1	1.39E-16
Nuclear part	26	15.3	7.47E-02
Vesicles	20	11.9	1.06E-02
Protein-DNA complex	8	5.08	2.98E-02

Table 8.4. Biological Process Clustering of Peptides Identified via Mass Spectrometry from Heparin Microparticles Loaded with Day 1-4 EB Conditioned Media

Biological Process	Number of Identified Peptides	Percentage of Total Peptides (%)	P Value
Cellular metabolic process	126	74.6	4.53E-07
Protein metabolic process	86	50.8	1.66E-08
Gene expression	83	49.2	5.38E-08
Translation	54	32.2	1.21E-16
RNA processing	28	16.9	4.73E-05
Cellular component biogenesis	28	16.9	6.35E-04
Organelle organization	26	15.3	5.91E-02
Cellular component assembly	20	11.9	1.58E-02
Macromolecular complex assembly	17	10.2	1.04E-02
Protein-DNA complex assembly	11	6.78	3.32E-03
Ribosome biogenesis	11	6.78	9.74E-03
Protein folding	8	5.08	8.93E-02

8.3.7 Response of C2C12 Cells to EB Conditioned Media Delivery

In order to determine whether cell-secreted factors in EB conditioned media were capable of inducing functional cellular responses, C2C12 myoblasts were cultured in (1) conditioned media delivered solubly, (2) low serum with conditioned media-loaded microparticles, or (3) microparticle-depleted conditioned media for 72 hours. C2C12 DNA content, ALP activity, and morphology were evaluated in response to conditioned media exposure. As expected, cells cultured in high serum (16% FBS) media exhibited a higher fold increase in DNA content over 72 hours compared to cells cultured in low serum (1% FBS) media (11.4 ± 0.1 vs. 3.0 ± 0.1; Figure 8.6A). The addition of unloaded heparin microparticles to low serum media decreased the fold change in DNA slightly, but not significantly (2.0 ± 0.2), similar to previously observed results [107].

C2C12 cells cultured in unconditioned serum-free media exhibited a similar fold increase in DNA to cells cultured in high serum media, demonstrating that the nutrients available in media formulated for ESCs was also sufficient for myoblast growth. However, while both unconditioned media-loaded microparticles and depleted unconditioned media also resulted in increased growth compared to low serum media, this increase was attenuated in comparison to soluble unconditioned media, suggesting that only some beneficial factors from unconditioned media were loaded onto heparin microparticles and removed from depleted media.

Conversely, soluble addition of conditioned media from all time points of EB differentiation (Day 1-4, Day 4-7, Day 9-10; Day 11-12, Day 13-14 not shown) resulted in poor cell growth, with fold increases in DNA lower than that of low serum culture.

This was likely due to the decrease in nutrients and increase in cellular metabolites associated with cell-conditioned media. Furthermore, microparticle-depleted conditioned media also resulted in poor cell growth, with DNA fold changes somewhat lower than that of conditioned media treatment, potentially indicating a removal of beneficial soluble factors by microparticle depletion. Lastly, C2C12 culture in low serum media with the addition of conditioned media-loaded microparticles had variable outcomes depending on the stage of EB differentiation from which the media was collected. Conditioned media-loaded microparticles from the earliest stage of EB differentiation (Day 1-4) induced increases in DNA content over that of low serum media alone. In fact, when the same amount of microparticles (0.1 mg) were loaded with five times the volume of conditioned media and added to C2C12 cells, the fold change in DNA content almost doubled (from 6.6 ± 0.6 to 12.2 ± 1.2), such that it was comparable to the culturing cells in high serum media (i.e. typical myoblast growth media). This suggests that heparin microparticles may be used to concentrate soluble factors from large volumes of conditioned media for *in vitro* delivery.

Despite positive effects observed using Day 1-4 EB conditioned media, conditioned media from other time points did not result in DNA content increases, even when conditioned media was loaded onto heparin microparticles. Although the use of microparticles to concentrate conditioned media biomolecules resulted in small increases in cell growth, these increases were not different from that soluble conditioned media treatment or low serum culture. EB conditioned media from Day 11-12 and Day 13-14 EBs yielded similar results to Day 4-7 EB conditioned media, but these results were excluded for simplicity.

ALP activity of C2C12 cultures was also investigated under these same conditions (Figure 8.7). It has been previously documented that C2C12 cells begin to express ALP and other osteogenic markers the presence of BMPs, such as BMP-2 and BMP-4, as early as 24 hours after exposure [101]; thus, ALP activity served as a means of identifying the osteogenic potential of C2C12 cells in the presence of EB conditioned media as well as a means of detecting active BMPs in solution. C2C12 cells incubated in low serum, high serum, unconditioned, and conditioned media did not exhibit any detectable ALP activity (data not shown). Additionally, cells treated with unloaded microparticles did not express ALP, despite previous results that demonstrated an increase in ALP activity with unloaded microparticle treatment [107].

On the other hand, when unconditioned and conditioned media were loaded onto heparin microparticles and delivered, C2C12 cells exhibited a positive ALP activity response (Figure 8.7A). More specifically, while microparticles loaded with unconditioned media and Day 11-12 EB conditioned media induced low levels of detectable ALP activity, microparticles loaded with Day 1-4, Day 4-7, Day 9-10, and Day 13-14 EB conditioned media induced higher ALP activity in comparison. Interestingly, a concentration effect similar to that observed with DNA content was observed with ALP activity, in which loading larger volumes of Day 1-4 and Day 13-14 EB conditioned media onto heparin microparticles (5x MPs) also induced higher ALP activity. Furthermore, phalloidin staining for F-actin in C2C12 cultures revealed a reduction in multi-nucleated, myoblast-like cells (white arrows) following treatment with Day 1-4 conditioned media-loaded microparticles (Figure 8.7C, E) compared to low serum media alone (Figure 8.7B, D). Taken together, these data suggest that the concentration of

soluble factors from EB conditioned media may enhance C2C12 osteogenesis and inhibit myogenesis.

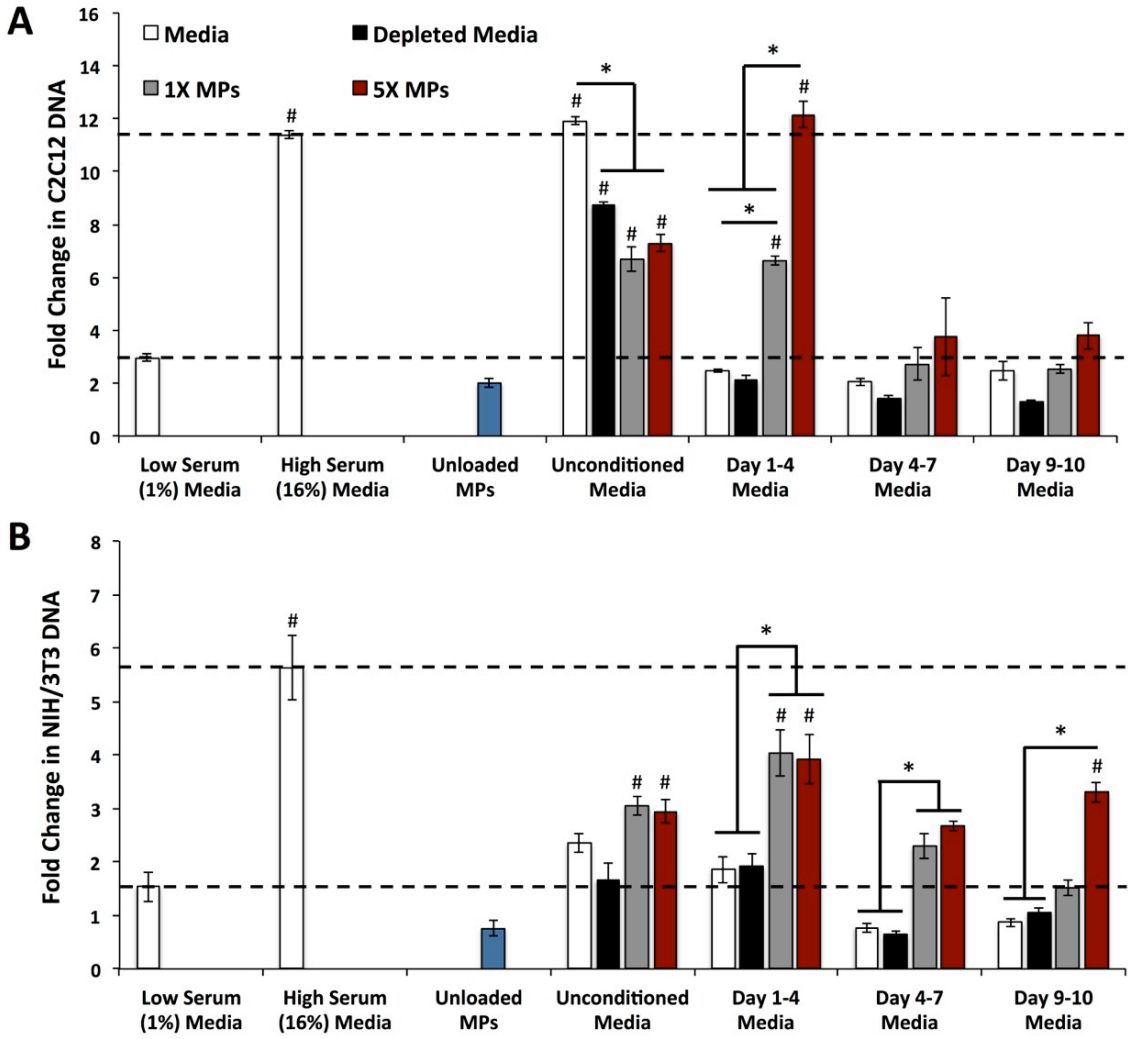

Figure 8.6. Effect of EB Conditioned Media on C2C12 and NIH/3T3 DNA Content. C2C12 myoblasts and NIH/3T3 fibroblasts were plated at an initial density of 20,000 cells/well in a 96-well plate for 72 hours in low serum media, high serum media, EB conditioned media, and microparticle-depleted EB conditioned media, as well as low serum media supplemented with 0.1 mg of unloaded microparticles and 0.1 mg of microparticles loaded with 0.5 mL or 2.5 mL of EB conditioned media overnight. A) Fold change in DNA content of C2C12 cultures after 72 hours of treatment. B) Fold change in DNA content of NIH/3T3 cultures after 72 hours of treatment. DNA content was normalized to initial Day 0 DNA content. Dashed lines indicate fold change in DNA content of cell cultures treated with low serum media and high serum media. (* = $p < 0.05$ as indicated, # = $p < 0.05$ compared to low serum media treatment)

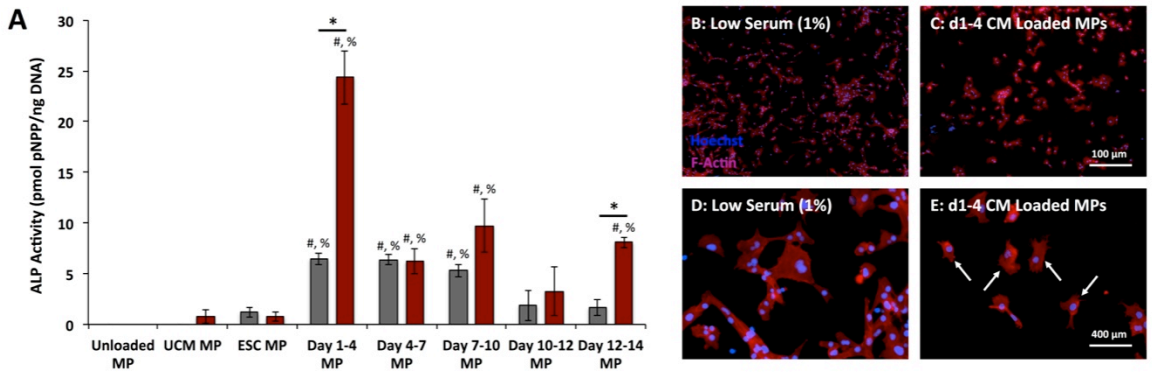

Figure 8.7. Effect of EB Conditioned Media on C2C12 ALP Activity and Morphology. A) For analysis of ALP activity, C2C12 cells were plated at 20,000 cells/well in a 96-well plate for 72 hours in low serum media, high serum media, EB conditioned media, and microparticle-depleted EB conditioned media, as well as low serum media supplemented with 0.1 mg of unloaded microparticles and 0.1 mg of microparticles loaded with 0.5 mL or 2.5 mL of EB conditioned media overnight. Treatment with EB conditioned media and microparticle depleted conditioned media did not induce detectable ALP activity, while treatment with conditioned media-loaded microparticles induced varying levels of ALP activity. (* = $p < 0.05$ as indicated, # = $p < 0.05$ compared to unloaded microparticles, % = $p < 0.05$ compared to microparticles loaded with unconditioned media) For F-actin staining, C2C12 cells were plated at an 10,000 cells/well in a chamber slide and treated for 24 hours in A, D) low serum media or C, D) low serum media supplemented with 0.2 mg of Day 1-4 conditioned media-loaded microparticles. Cells were then fixed and stained with rhodamine-conjugated phalloidin and Hoechst.

8.3.8 Response of NIH/3T3 Cells to EB Conditioned Media Delivery

Growth of NIH/3T3 fibroblasts in response to EB conditioned media was also evaluated, since fibroblasts are often employed to investigate cell proliferation and have been used previously to assess the mitogenic potential of EB conditioned media [7]. Similar to C2C12 experiments described above, NIH/3T3 fibroblasts were cultured in (1) conditioned media, (2) low serum with conditioned media-loaded heparin microparticles, or (3) microparticle-depleted conditioned media for 72 hours. NIH/3T3 cells cultured in high serum media also displayed increased DNA content at the end of the culture period compared to cells cultured in low serum media (5.6 ± 0.1 fold change vs. 1.5 ± 0.6 fold

change; Figure 8.6B); moreover, exposure of NIH/3T3 cells to unconditioned serum-free media similarly increased cell growth, although this increase was only significant when unconditioned media were loaded on heparin microparticles.

NIH/3T3 cells exposed to EB conditioned media responded comparably to C2C12 myoblasts, exhibiting poor cell growth regardless of time point of conditioned media collection, especially in the case of the later stages of EB differentiation (Day 4-7, Day 9-10; Day 11-12, Day 13-14 not shown). However, when EB conditioned media were loaded onto heparin microparticles, increases in DNA content were observed in response to media from all stages of EB differentiation (Day 11-12, Day 13-14 not shown for simplicity). Although delivering microparticles loaded with five times the volume of Day 1-4 EB conditioned media resulted in a dramatic concentration effect in C2C12 cultures, this was not observed in NIH/3T3 cultures; instead, this concentration effect was more evident at later conditioned media time points of Day 9-10 and onwards, in which 5x MPs induced greater cell growth than 1x MPs.

EdU staining, demonstrating cell proliferation, further supported the increases in DNA content observed in NIH/3T3 cultures. As expected, treatment with low serum media resulted in few proliferating cells (Figure 8.8A), while treatment with high serum media induced higher cell proliferation (Figure 8.8D). In the case of cultures treated with unloaded microparticles, images of cells adhered to the glass slide surface (Figure 8.8B) and the microparticles themselves (Figure 8.8E), revealed a low proportion of proliferating cells; however, when cultures were treated with Day 1-4 EB conditioned media-loaded microparticles, more cells stained positively with EdU on both the glass slide surface (Figure 8.8C) and attached to the microparticles (Figure 8.8F). Interestingly,

more proliferating cells were found on the microparticles than adhered to the glass slide, potentially due to the presence of conditioned media proteins and other ECM molecules on the microparticles, promoting cell attachment and subsequent growth.

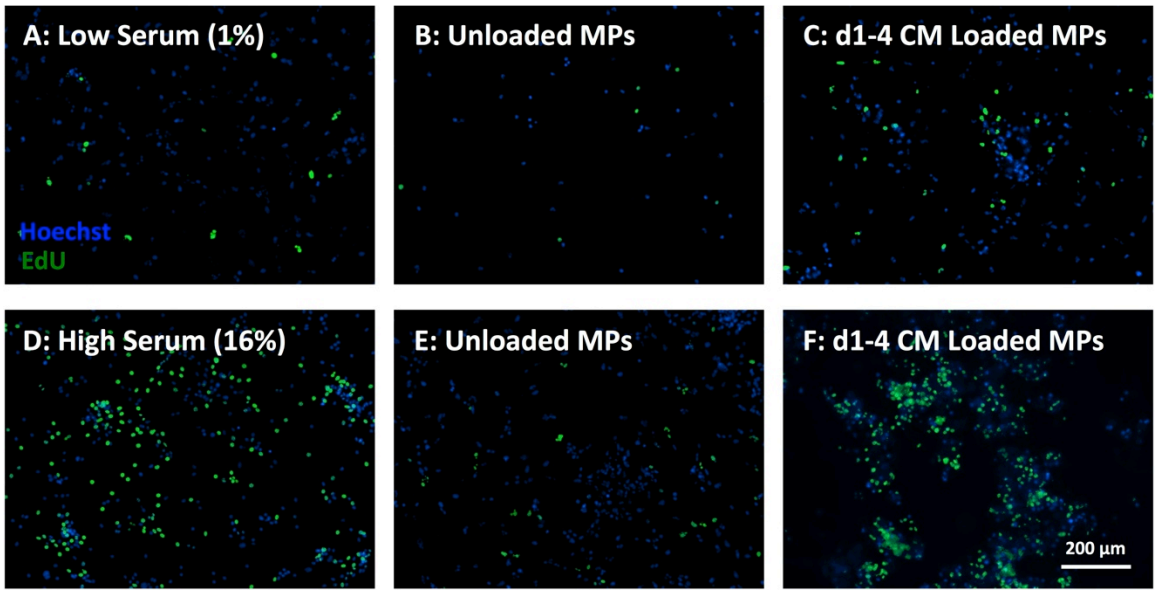

Figure 8.8. Effect of Conditioned Media-Loaded Microparticles on NIH/3T3 Proliferation. NIH/3T3 cells were plated in chamber slides at an initial density of 10,000 cells/well, serum starved for 8 hours, and treated for 24 hours with A) low serum media, D) high serum media, or B, E) low serum media supplemented with 0.2 mg of unloaded heparin microparticles or C, F) 0.2 mg of Day 1-4 EB conditioned media-loaded microparticles. Cells were pulsed with EdU for 6 hours before being fixed and stained. Since cells adhered to the microparticles during culture, images were taken of both cells adhered to glass slide surfaces (B, C) and cells adhered to unloaded and loaded heparin microparticles (E, F).

8.4 Discussion

In this study, we demonstrated that heparin microparticles could be used to sequester and deliver a variety of soluble biomolecules from EB conditioned media. Microparticles loaded with conditioned media from different stages of EB differentiation were analyzed for protein content using a wide variety of proteomic methods, including

BCA and fluorescamine assays, ELISA, SDS-PAGE, and mass spectrometry. When morphogen-laden microparticles were delivered to *in vitro* cultures of NIH/3T3 fibroblasts and C2C12 myoblasts, increases in cell proliferation and alkaline phosphatase activity were observed that were absent in cultures treated with conditioned media alone, indicating the ability of concentrated ESC-secreted factors to induce functional cellular responses. While several studies have previously examined the effects of ESC conditioned media on cell phenotype, this study investigates a unique approach to conditioned media delivery in which ESC-derived proteins are concentrated and delivered in a localized manner via a biomaterial platform.

One major hurdle in using cell-secreted products for tissue engineering applications is the difficulty of characterizing the complex mixture of biomolecules present in conditioned media. In this study, we used SDS-PAGE and silver staining to visualize the profile of proteins concentrated by heparin microparticles during different stages of EB differentiation. We demonstrated that proteins of various molecular weights could be concentrated to detectable levels using the protein depletion capacity of heparin, while simultaneously reducing the signal of BSA, which does not specifically bind heparin but is abundant in cell culture media. Many of the proteins observed were also in the expected molecular weight range of a number of heparin binding proteins [93, 94]. This method provides a significant advantage in visualizing conditioned media proteins on SDS-PAGE gels, as our previous work has demonstrated that when soluble conditioned media is run on a gel, the BSA protein band typically floods the gel, obscuring other proteins, while more dilute species cannot be detected [337]. Most importantly, this technique allowed visualization of clear differences in the heparin-

bound fraction of proteins secreted by differentiating EBs over time, corroborating results which indicate that the ESC secretome changes during differentiation [50, 338].

Previous analysis of ESC and EB conditioned media using mass spectrometry techniques has also revealed a variety of proteins, including a number of secreted growth factors and intracellular components [48-50]; thus, we sought to use mass spectrometry to further analyze the heparin-bound fraction of the differentiating ESC secretome. Based on clustering analysis of 169 proteins found on loaded microparticles, the majority of the proteins identified were intracellular and involved in general metabolic processes. Farina, et al. previously reported similar results from clustering of ESC proteomic data, as well as the presence of a number of comparable proteins, including heat shock proteins (i.e. endoplasmin) and ribosomal subunits [50]. Furthermore, Farina, et al. highlighted the secretion of isoforms of thrombospondin and Lefty – both of which were also identified in our dataset. Several of the proteins we identified in our analysis are also known heparin binding proteins, such as thrombospondin-1, thrombospondin-3, apolipoprotein B, and apolipoprotein E [93].

The abundance of intracellular components identified in EB conditioned media was likely due to cell lysis following cell death. However, ELISA analysis of conditioned media revealed that growth factors such as BMP-4, VEGF, and IGF-2 were also present in relatively dilute concentrations on the order of 10-60 pg/mL. Although we expected heparin microparticles to concentrate these growth factors from conditioned media over the limit of detection of several proteomics analyses, none of these growth factors were identified in mass spectrometry analysis, suggesting that they were present in much lower quantities than the intracellular components identified. In future studies, additional

upstream processing techniques, such as fractionation, or downstream analysis methods, such as iterative elusion of identified proteins, may be employed to improve the sensitivity of mass spectrometry for dilute protein species. We have previously separated protein fractions using SDS-PAGE followed by in-gel digestion prior to mass spectrometry analysis and have obtained similar results to direct digestion of proteins from microparticles. Iterative elusion of abundantly identified proteins has been successfully used by others to characterize ESC and embryonic fibroblast conditioned media samples, resulting in the identification of a number of morphogenic proteins [48]. Thus, more sophisticated analysis tools may be required in the future to improve mass spectrometry-based approaches to identifying proteins bound to heparin microparticles.

In addition to characterizing EB conditioned media and its heparin binding fraction, the effects of soluble conditioned media and protein-laden microparticles on cell phenotype were investigated using two different cell lines. Morphogen-laden microparticles induced increases in cell number in cultures of NIH/3T3 fibroblasts and C2C12 myoblasts, as well as increases the ALP activity and osteogenic differentiation of C2C12 myoblasts. Interestingly, the effects observed were dictated by both the cell type and stage of EB differentiation during conditioned media collection. Microparticles loaded with conditioned media from the earliest time points of EB differentiation elicited the greatest cell proliferation responses, presumably due to the presence of mitogenic biomolecules in the media, secreted by EBs that were growing rapidly between Day 4-10. Although growth effects were only observed on C2C12 cells with microparticles loaded with media collected from Day 1-4 of EB differentiation, growth effects were observed on NIH/3T3 cells with microparticles loaded with media collected from all time points,

suggesting different interactions with heparin-presented biomolecules. Similarly, modest increases in muscle progenitor cell proliferation have been achieved using the heparin binding fraction of human ESC conditioned media, although no biomaterial delivery platform was employed [8]. While FGFs and PDGFs both stimulate C2C12 and NIH/3T3 proliferation [339-341], C2C12 growth is also largely regulated by myostatin and IGF-1 [342-344]. However, since none of these proteins were detected in our proteomic analyses, more information is required to explain the proliferation responses observed.

One advantage of evaluating conditioned media effects on C2C12 myoblasts is that it enables simultaneous investigation of proliferation and differentiation towards osteogenic and myogenic lineages. In this study, we found that, although soluble delivery of conditioned media did not induce any detectable ALP in cell lysates, conditioned media delivery using heparin microparticles resulted in robust ALP induction. More specifically, ALP activity was dependent on stage of EB differentiation, and was observed following treatment with microparticles loaded with Day 1-4 4-7, 9-10, and 12-14 EB conditioned media, with Day 1-4 EB conditioned media eliciting the greatest response. These data suggest that the heparin binding fraction of conditioned media may push C2C12 cells towards a more osteogenic phenotype – a conclusion that was also supported by the lack of multinucleated, myogenic-like cells observed in these cultures. Although no BMP-2 was detected in conditioned media, appreciable levels of BMP-4 were detected via ELISA. BMP-4 has been previously shown to induce C2C12 ALP activity [104], and thus heparin microparticles may be enriching and presenting BMP-4 to the cells in a similar manner to BMP-2 delivery [107].

It is important to note that the effects on cell proliferation and ALP activity that were observed following treatment of cell cultures with morphogen-laden microparticles were not observed with soluble delivery of conditioned media alone. Moreover, in several cases, incubating microparticles in an increased volume of conditioned media stimulated greater cell responses, suggesting that this approach to conditioned media delivery may enrich growth factors responsible for cell proliferation and osteogenic differentiation and/or remove cellular wastes and biomolecules that inhibit these processes.

Ultimately, this study provides initial proof of concept that heparin-based microparticles can be used to sequester and subsequently deliver ESC-derived morphogens from cell conditioned media. Few other studies have attempted to use biomaterial-based platforms for conditioned media delivery, with the most notable of these being self-assembling peptide nanofibers that can be soaked in conditioned media to form a hydrogel [345, 346] and heparin-containing hyaluronic acid hydrogels that can enhance the effects of morphogens secreted by encapsulated cells [125, 126]. Despite some positive effects, challenges still exist in identifying the proteins that were sequestered by these materials and contributed to the results observed. Herein, we used several methods of proteomic analysis to further investigate the components of the ESC secretome captured by heparin microparticles, revealing differences in the profiles of proteins secreted at various stages of EB differentiation; however, additional studies are required to identify the biomolecules that were responsible for the proliferation and differentiation effects.

These experiments were completed using a non-degradable form of heparin microparticles that allows for long-term entrapment of proteins for analysis and delivery

and has previously exhibited enhanced growth factor (BMP-2) presentation when cultured *in vitro* in direct contact with cells [107]. Future studies may be conducted using degradable heparin-PEG microparticles [120], which may be better suited to morphogen delivery for *in vivo* studies. Degradable heparin microparticles would allow for the delivery of highly concentrated molecular cargo while also providing enhanced release of bioactive proteins, such that these proteins can influence more cells throughout the tissue of interest. Furthermore, as this platform for conditioned media delivery is developed, the sequestration of proteins from other cell conditioned media can be considered. For example, similar mass spectrometry analysis of microparticles loaded with media conditioned by adherent human mesenchymal stem cells (MSCs) revealed fewer intracellular proteins than EB conditioned media (47% clustered as extracellular space) and a number of heparin binding proteins, including fibronectin, collagen, apolipoproteins, and thrombospondins, and IGFBPs (Tables B.3 and B.4 in Appendix B). Thus, MSC-conditioned media may also be investigated in the future as a source of potent morphogens.

Finally, in the context of this thesis work, we demonstrated that the potent osteogenic morphogen BMP-2 could be co-sequestered with EB conditioned media using heparin microparticles. Since the bone healing cascade involves a series of events characterized by a wide variety of morphogens and cell phenotypes [1], the co-delivery of a complex mixture of cell secreted morphogens, including VEGF, BMP-4, and IGF-2 identified in EB conditioned media, may target multiple stages of the bone healing cascade and enhance typical BMP-2-induced bone healing. Future work in this area will

involve developing this biomaterial platform for *in vivo* conditioned media delivery and eventual investigation in a critically sized bone defect model.

8.5 Conclusions

In this study, we demonstrated a novel method to sequester and deliver ESC-secreted morphogens using a heparin-based biomaterial. This approach enables the concentration of desired proteins, without collecting cellular metabolites that may have detrimental effects on target cell populations. By exploiting the growth factor binding properties of heparin in a biomaterial platform, these concentrated growth factors can be delivered to cell cultures and tissue injury sites in a more localized manner than a bolus injection of soluble conditioned media. Future work in this area will involve further characterization of the key heparin-bound proteins responsible for the positive effects observed *in vitro* and development of this biomaterial platform for *in vivo* morphogen delivery.

CHAPTER 9: CONCLUSIONS AND FUTURE DIRECTIONS

9.1 Contributions to the Field

This innovative two-fold approach aimed to improve current growth factor delivery strategies by both creating a heparin-based affinity biomaterial for clinically approved BMP-2 delivery and investigating heparin-bound PSC morphogens as a source of growth factors for the treatment of bone injuries. Thus, this work presents significant contributions to bone tissue engineering, affinity-based biomaterial design, and the translation of stem cell-based therapeutics, as outlined below.

9.1.1 Fabrication of a Novel Affinity-Based Biomaterial

Heparin-based materials have thus far demonstrated an inconsistent ability to improve osteogenesis and bone regeneration within critically sized bone defects [101, 105, 106, 116]. This work resulted in the creation of a novel microparticle-based delivery vehicle, which consists purely of heparin, and thus can incorporate and retain large amounts of growth factor. The spatial concentration of molecular cargo that can be achieved using heparin microparticles enabled highly localized delivery of BMP-2 doses needed to stimulate endogenous repair mechanisms, while minimizing rapid growth factor diffusion and spatially limiting bone formation. As a result, heparin microparticles may provide more effective delivery of clinically relevant doses of BMP-2 than the clinical collagen sponge delivery system in humans, thereby improving outcomes and

reducing adverse events. Furthermore, given that heparin exhibits promiscuous binding for a number of different growth factors, this biomaterial presents a versatile delivery system that may be used for other protein delivery applications in the future.

9.1.2 Development of a Computational Model Describing In Vivo BMP-2 Diffusion

Since heparin microparticles can be dose-dependently incorporated into tissue engineering constructs, they enable truly tunable growth factor delivery systems. Computational modeling of affinity-based biomaterials provides a significant advantage for developing these systems with the appropriate features to attain desired protein release profiles. The computational model of BMP-2 release developed within this work predicted BMP-2 release kinetics for different BMP-2 and microparticle doses, as well as different microparticle loading regimes, following *in vivo* implantation in the bone defect site; this information drastically reduced the number of conditions that required *in vivo* testing and highlighted potential reasons for the differences in *in vivo* outcomes observed with microparticle-mediated delivery. While several other computational models of affinity-based growth factor delivery have been reported [248, 257, 258, 260], this model is one of the few that attempts to describe BMP-2 release *in vivo* within the implantation site of interest. The COMSOL-based framework of this model also enables easy adjustment of diffusion coefficients of the biomaterial and surrounding tissue, or the interactions between the protein and affinity ligand, such that this model can be widely applied to a number of affinity-based growth factor delivery systems.

9.1.3 Ability to Enrich and Deliver Cell-Secreted Morphogens as a Cell-Free Therapy

Heparin microparticles can also be used to selectively enrich growth factors from a complex mixture of biomolecules found in cell-conditioned media, thereby enabling concentration of desired proteins, without collecting cellular metabolites that may have detrimental effects on target cell populations. By exploiting the growth factor binding properties of heparin in a biomaterial platform, we demonstrated that concentrated growth factors could be delivered to multiple mature cell types *in vitro*, resulting in higher potency than the delivery of dilute conditioned media components alone. In the future, heparin microparticles could serve as a platform to sequester, concentrate, and deliver complex mixtures of morphogens to tissue injury sites in a more localized manner than a bolus injection of conditioned media itself. The long term goal of this approach is to one day eliminate the need for stem cell transplantation by harnessing the regenerative potential of PSCs through their secreted proteins.

9.2 Future Directions

The work completed within the scope of thesis has broadened the current understanding of affinity-based delivery systems for bone tissue engineering and stem cell paracrine factor delivery. The promising results achieved within this work motivate further development of this growth factor delivery platform and present new opportunities to investigate the effects of growth factor delivery on *in vitro* cell fate and *in vivo* tissue regeneration.

9.2.1 Tunable Affinity-based Delivery Systems

Perhaps the most recognizable new avenue of research stemming from this work is the investigation of degradable heparin-based delivery systems. The pure heparin microparticles developed and evaluated within this thesis were fabricated from methacrylamide-modified, covalently cross-linked heparin [128], which did not facilitate hydrolytic degradation and reduced susceptibility to heparinase-mediated degradation. Heparin microparticles delivered to *in vitro* cell cultures remained visibly intact throughout the entire culture period [107], while heparin microparticles delivered *in vivo* to the femoral bone defect were likely taken up by phagocytic cells or swept into the bloodstream, although a portion of these microparticles were also found in the defect site after 12 weeks post-surgery (Chapter 4). Despite being non-degradable and releasing <20% of bound BMP-2, BMP-2-loaded heparin microparticles still induced BMP-2 signaling events in skeletal myoblasts, which were enhanced when microparticles and cells were cultured in direct contact [107]. BMP-2-loaded microparticles also stimulated considerable mineralization in the femoral defect site using both low and high doses of BMP-2, further confirming the maintenance of microparticle-bound BMP-2 bioactivity. These findings corroborated previous results that demonstrated the enhancement of BMP-2 bioactivity in the presence of soluble GAGs [101, 104] and supported the theory that growth factor presentation enabled by ECM molecules may be as influential as growth factor release.

More recently, efforts have been led to fabricate degradable heparin-based microparticles, which offer greater tunability in heparin content and subsequent growth

factor release kinetics. Temenoff and colleagues reported the fabrication of heparin-functionalized PEG microparticles and bulk hydrogels, in which heparin content could be varied from 1-10% of the total dry hydrogel weight [120, 347, 348], and degradable or non-degradable cross-linkers could be employed via Michael Type addition [120, 348]. Degradable heparin microparticles may increase the bioavailability of delivered growth factors by facilitating greater release. These materials also offer the additional advantage of incorporating both native and selectively desulfated heparin, allowing further manipulation of growth factor affinity and reducing heparin's anticoagulant effects [144, 349]. Other groups have also fabricated similar degradable heparin-containing materials, including heparin-functionalized alginate and PEG hydrogels [187, 350].

While we successfully modulated the properties of our bulk alginate/PCL constructs by changing the total number of 100% heparin microparticles incorporated into the system, the use of 1-10% heparin-functionalized microparticles and selectively desulfated heparin species may provide alternative methods of easily changing the heparin content (and subsequent affinity ligand density) of the system. The use of heparin-functionalized alginate could also be used to more directly alter the heparin content of the system without drastically changing the cross-linking density of the bulk alginate hydrogel. These approaches represent more advanced engineering strategies for modulating the growth factor sequestration properties of heparin-based materials and warrant further investigation in the future.

On the other hand, given that heparin is a naturally occurring affinity molecule, the ability to manipulate its growth factor binding properties is limited. While timed material degradation and modification of electrostatic binding affinity provide tunability

for heparin-based systems, "bottom-up," modular creation of synthetic affinity-based delivery systems may offer an alternative method of controlling growth factor release. Several groups have developed ligands with high affinity for specific therapeutic proteins of interest using naturally occurring biomolecules as templates. Hubbell and colleagues demonstrated that the fused growth factor and integrin binding domains of fibronectin (FN III9-10/12-14) exhibited increased affinity for a number of heparin-binding growth factors [134, 135], while Murphy, et al. developed specific protein-binding ligands for VEGF by isolating its receptor (VEGFR2) [272, 334]. Conversely, proteins with heightened affinity for specific ligands have also been engineered. These include modular peptides with bioactive BMP-2 domains fused to mineral binding domains, which enable binding to calcium phosphate coatings [351], and growth factors containing Src homology 3 (SH3) domains, which can be differentially captured by low and high affinity SH3 binding ligands [260, 352].

Synthetic ligands with specific protein affinity have the additional advantage of circumventing issues caused by non-specific protein binding, which may reduce the overall loading capacity of a material for the protein of interest and accelerate its release. In Chapter 7, we demonstrated that competitive binding of serum components, such as fibronectin, apolipoproteins, and thrombospondins, for heparin could interfere with BMP-2 binding and release from heparin microparticles; we expect that a similar phenomenon may also occur following *in vivo* implantation of heparin-based materials into protein-rich injury environments, and may result in off-target effects. Conversely, when materials containing specific protein binding ligands, such as VEGF receptor ligands, were investigated in the presence of serum, VEGF binding was not reduced in the presence of

whole serum, serum-borne heparin, or exogenously added heparin, indicating strong and specific affinity for VEGF [334]; interestingly, VEGF release from VEGFR-containing microparticles was increased in the presence of serum due to competitive binding of proteins to VEGF and not the affinity ligand [256]. These studies highlight both the utility of specific affinity ligands and the challenges of creating ligands with the characteristics needed for sustained release in different environments.

The ability to create synthetic affinity ligands for proteins of interest using a variety of methods has dramatically increased the potential of affinity-based protein delivery vehicles. A number of technologies have emerged that can be used to better design affinity ligands for particular applications [10], such as screening affinity ligands using cell-surface display methods, selecting high affinity ligands using competitive binding and directed evolution of peptides, and designing desired protein-ligand interactions computationally. These methods may enable the selection of ligands with well-defined dissociation constants and highly specific binding affinities for a single protein. In the context of protein delivery for tissue regeneration, these technologies could generate of a range of affinity ligands that provide precise, customizable protein release, allowing for more systematic investigation into the effect of protein release on tissue healing and creation of delivery vehicles with more optimal release kinetics.

9.2.2 Multiple Growth Factor Delivery

Despite the drawbacks of the promiscuous binding nature of heparin for effective single growth factor delivery, it is important to note that this characteristic can also be

harnessed for other applications. There are several instances in this work in which we utilize the non-specific protein sequestration abilities of heparin-based microparticles for the entrapment and delivery of multiple growth factors. In Chapter 3, we demonstrated that heparin microparticles could be used for the sequential delivery of BMP-2 and VEGF, while in Chapter 8, we used heparin microparticles to capture multiple stem cell-derived factors from embryonic stem cell conditioned media.

The use of heparin-based materials for the delivery of numerous other biomolecules has been reported in literature [163-165, 348]; additionally, we have recently published on the use of these same heparin methacrylamide microparticles for the sustained delivery of interferon gamma (IFN-γ) to modulate the behavior of mesenchymal stem cell aggregates [353]. Thus, it should be unsurprising that the high protein loading capacity of heparin can be harnessed to deliver multiple growth factors simultaneously from heparin-containing materials. A number of previous studies have co-delivered BMP-2 and VEGF using other biomaterials in an attempt to improve revascularization of large bone defects in concert with remineralization [194, 195, 354]. It has been hypothesized that preceding remineralization with a revascularization phase, similar to the natural bone healing cascade, may accelerate healing by increasing local exposure to circulating biomolecules and cells [193]. However, previous dual delivery approaches have required the fabrication of complex delivery systems with multiple materials to provide sequential growth factor release. We have demonstrated the fortuitous sequential release of VEGF followed by BMP-2 using heparin microparticles as a single delivery vehicle, likely due to natural differences in affinity to heparin. Future work may focus on investigating the dual delivery of VEGF and BMP-2 from heparin

microparticles *in vivo*, as a strategy to target both vascular and mineral deficits in large bone defects. Previously, in our femoral defect model, we have demonstrated that multiple growth factor delivery (BMP-2, TGF-β3, VEGF) results in modest gains in mineral volume [239, 355]; thus, this approach may be better suited to tissue defect models with compromised vasculature, such as composite models of muscle and bone injuries, which have also been developed in our laboratory [356].

The delivery of multiple recombinant growth factors represents a "bottom up" modular approach to tissue regeneration, which limits the investigation to 2-3 recombinant growth factors at a time. Conversely, the use of ESC morphogens presents a "top down" biomimetic approach to tissue regeneration, in which the effects of a complex mixture of growth factors from cells with high regenerative capacity can be explored. This initial work examining the sequestration and delivery of ESC-derived morphogens using heparin microparticles was the first step in developing a platform to harness the paracrine effects of pluripotent stem cells to enhance tissue regeneration. Our initial goal was to develop ESC morphogen-laden microparticles as an alternative strategy for bone repair; however, while morphogen-laden microparticles induced ALP activity in C2C12 myoblasts, this was the only indicator of osteogenic potential observed throughout these studies, and no osteogenic proteins were detected in mass spectrometry analyses. In the future, directed osteogenic differentiation of embryoid bodies may be employed to increase the secretion of osteogenic growth factors [357]. *In vivo* studies may be conducted in the rat femoral defect model to evaluate stem cell morphogen-laden microparticles as a method to supplement BMP-2 delivery, thereby decreasing supraphysiological BMP-2 doses in favor of the mitogenic effects of stem cell

morphogens demonstrated in this work. Additionally, stem cell morphogen-based therapies are currently being applied to other tissue regeneration applications in our laboratory, including dermal wound healing and hindlimb ischemia. Taken together, these approaches may eventually provide new insight into the synergistic, regenerative effects of stem cell morphogens on mature mammalian tissues.

We expect that the work completed on complex protein delivery using heparin microparticles will also open doors to other sequestration-based approaches to tissue regeneration. The ability to capture and concentrate numerous cell-secreted and serum-borne morphogens using biomaterials may provide novel, facile means of analyzing cell-secreted products and potentiating cell growth and differentiation through dynamic feedback between cells and biomolecules. Because many morphogens are heparin binding growth factors, GAG-based biomaterials are prime candidates for sequestering cell-secreted proteins. In a recent study by Yousef, et al., heparin-coated Sepharose beads were used to concentrate stem cell-derived, heparin binding growth factors for *in vivo* delivery [8]. However, thus far, no study has attempted to deliver soluble stem cell-derived factors via heparin materials.

Heparin-based morphogen sequestration is not limited to the collection of morphogens from cell conditioned media alone. In the future, heparin materials may also be used for the *in vivo* sequestration of circulating biomolecules to enhance their effect within a site of interest. This concept has been recently explored in a study by Liu, et al., in which empty chitosan hydrogels delivered following myocardial infarction increased both local SDF-1 concentrations and c-kit^{+} cell recruitment [358]. This mechanism of action may have also been responsible for some of the recent results reported by Healy

and colleagues, in which heparin-containing hyaluronic acid hydrogels containing cardiac progenitor cells (CPCs) and TGF-β1 sequestered CPC-secreted soluble factors *in vitro* and induced a neovascular response *in vivo* [125, 126]. As a long term goal, *in vivo* morphogen capture could be combined with the material-based mass spectrometry techniques we have developed within this work, such that heparin microparticles could be explanted and purified following implantation in the femoral defect site to provide valuable information about the proteins sequestered *in vivo*.

As a final future avenue of research stemming from complex protein sequestration, heparin microparticles could also be developed as a platform to concentrate and capture dilute biomolecules from complex solutions for proteomic analysis. We have begun to demonstrate this concept in the proteomic analysis reported in Chapter 8; however, additional work is required to ensure that proteins of interest are concentrated beyond their levels of detection. A similar platform has been recently reported using the thermosensitive polymer, poly-nisopropylacrylamide (pNIPAm), which can easily absorbing proteins from *in vitro* cell cultures and protein-rich body fluids [359, 360]. pNIPAm hydrogels are highly porous, charged materials with tunable mesh sizes, which allow them to act as molecular sieves to capture biomolecules of specific sizes while excluding others. Consequently, pNIPAm microparticles have been successfully used as molecular sieves to separate and concentrate dilute proteins of interest such as insulin, SDF-1, and myoglobin from complex protein mixtures, while excluding more abundant proteins such as albumin and immunoglobins on the basis of size [361]. pNIPAm has also been used to isolate proteins biomarkers for diseases from body fluids. The most notable of these is PDGF, which can be captured and concentrated 10-fold from a large volume

of human serum into a small volume of pNIPAm microparticles and subsequently shielded from proteolytic degradation prior to analysis [361]. Given that heparin binds and similarly protects proteins on the basis of electrostatic interactions, heparin microparticles engineered with different mesh sizes could be used to concentrate positively charged, heparin binding proteins of specific molecular weights. Using SDS-PAGE analysis, we have demonstrated in this work that heparin microparticles can concentrate less abundant proteins from both serum and cell conditioned media, while reducing BSA capture. This characteristic of heparin microparticles lends itself to further development for somewhat selective protein capture. Furthermore, since both SDF-1 and PDGF are known heparin binding growth factors [347, 362], heparin microparticles could be used to concentrate these biomarkers in a manner similar to pNIPAm microparticles. Although the promiscuous binding nature of heparin may reduce its ability to very precisely capture single proteins from solution, heparin microparticles could still be used to drastically reduce the complex nature of protein rich solutions.

9.2.3 Clinical Application

The eventual goal of designing a novel growth factor delivery system for tissue regeneration is clinical application. Since BMP-2 has already been approved for clinical use via a absorbable collagen sponge [4], improving current BMP-2 delivery strategies ideally involves the creation of readily translatable delivery vehicles with low adoption barriers for orthopedic surgeons. The alginate/PCL construct described throughout this work consists of clinically approved biomaterials [363, 364] with BMP-2 or BMP-2-

containing heparin microparticles pre-loaded into the injectable hydrogel phase. Despite its ease of use, the method for implantation of this tissue engineering construct differs considerably from current methods for collagen sponge implantation, in which the sponge is typically soaked in BMP-2 solution and press-fit into the bone defect [6, 365]. In Chapter 7, we incorporated empty heparin microparticles into a PCL nanofiber mesh tube to serve as a barrier to BMP-2 diffusion from the collagen sponge; this approach was designed for use with standard clinical procedures to facilitate easy adoption in the future. However, the lack of success demonstrated *in vivo* with this system encourages the development of other methods of incorporating heparin microparticles into BMP-2 delivery vehicles.

Perhaps the most clinically relevant method of delivering heparin microparticles that has not yet been investigated in this work is the incorporation of microparticles into the absorbable collagen sponge. Several groups have fabricated porous collagen sponges and collagen sponge composites by physically entangling or chemically cross-linking collagen fibers into hydrogels and lyophilizing them to create sponges [116, 261, 366-369]. Furthermore, soluble GAG chains [116, 367] and alginate, chitosan, and glass microparticles [370-372] have been successfully integrated into collagen sponges using these methods. We have conducted some preliminary studies to attempt to incorporate heparin microparticles into collagen hydrogels at a density of 1 mg of microparticles per 150 μL of collagen gel, which was the highest microparticle density used in alginate hydrogels used throughout this work. Since heparin microparticles can be lyophilized for long term storage, much like the collagen sponge, the heparin microparticle/collagen hydrogel composite material can similarly be lyophilized until use. Moreover, in Chapter

3, we demonstrated that BMP-2-loaded microparticles could be lyophilized, while maintaining BMP-2 bioactivity. This gives us the choice of two BMP-2 loading regimes, in which composite sponges could come pre-loaded with a fixed concentration of BMP-2, simply requiring re-hydration upon implantation, or unloaded composite sponges could be soaked in BMP-2 solution immediately prior to delivery. It is expected that the presence of high affinity heparin microparticles would greatly increase the BMP-2 loading capacity of the low affinity collagen sponge and significantly attenuate the detrimental burst release of BMP-2 from this material. Future studies in this area could investigate incorporation of heparin microparticles into both collagen hydrogels and collagen sponges at various densities, following by *in vivo* comparison to the clinically used collagen sponge in the rat femoral defect model. Overall, we expect that the development of multiple biomaterial platforms in which heparin microparticles can be easily integrated will continue to demonstrate the vast versatility of this system.

APPENDIX A: MATLAB CODE FOR PROTEIN DIFFUSION

MAIN CODE

```
% Specify the bounds for the diffusion coefficient in cm^2/s
lowbound = 10e-15;
upbound = 10e-4;

% Set options for running the fmincon
% Enable plotting of the results
options = optimset('PlotFcns',{@optimplotfval,@optimplotstepsize});
pmin = 10e-6;
[pminf,Smin,exitflag,output]=fmincon(@MarianData_ToMinimize,...
    pmin,[],[],[],[],lowbound,upbound,[],options);
```

FUNCTION TO MINIMIZE

```
function S = MarianData_ToMinimize(p)

load('fluorescence_1')

% Parameter to solve for: diffusion of protein
D_eff = p; % cm^2/s

% Time in seconds for each image
t = 60*time; % s

% Convert distance to centimeters

x = 10^-4*(Data_X); %cm

% Calculate the value to plug into our erfc, defined in Clauss, et al. 1990

% First, create empty vectors
y = zeros(length(t),length(x)); % Value to plug into the equation
C = zeros(length(t),length(x)); % Calculated concentration, as fcn of time and position

% Step through each time point to calculate the input variable, y
% And the resulting concentration, C
for i = 1:length(t)
    y(i,:) = x./(2*sqrt(D_eff.*t(i)));
    C(i,:) = erfc(y(i,:));
end
```

```
% Create plots

plot(x*10000,Data_M,'LineWidth',2)
subplot(2,1,1)
xlabel('Distance, µm')
ylabel('Normalized Fluorescence')
ax = gca;
ax.LineWidth = 1;
ax.FontSize = 14;


plot(x*10000,C,'LineWidth',2)
subplot(2,1,2)
xlabel('Distance, µm')
ylabel('Normalized Fluorescence')
ax = gca;
ax.LineWidth = 1;
ax.FontSize = 14;

% Error Function
S = 0;
for i = 1:length(x)

    S = S + sum(((C(:,i) - Data_M(:,i))./Data_M(:,i)).^2);

end


end
```

APPENDIX B: MASS SPECTROMETRY RESULTS

Table B.1. Mass Spectrometry Results for Day 1-4 EB Conditioned Media

Symbol	Protein	Molecular Weight (kDa)	Unique Peptides	Total Peptides	Average XCorr
Hsp90aa1	90 kDa Heat shock protein α	84.73	15	12	3.3937
Hspa8	71 kDa Heat shock protein	70.83	12	11	3.371
Ncl	Nucleolin	76.68	12	8	2.8017
Hsp90ab1	90 kDa Heat shock protein β (Endoplasmin)	83.23	11	8	3.4602
Actb	Actin, cytoplasmic 1	41.71	10	9	3.2182
Eno1	α-enolase	47.11	10	8	3.6471
Serpinc1	Antithrombin-III	51.97	8	6	2.8124
Aldoa	Fructose-bisphosphate aldolase A	39.33	7	4	4.2843
Prdx1	Peroxiredoxin-1	22.16	7	3	2.9617
Eef1a1	Elongation factor 1-α 1	50.08	6	6	2.841
Pkm	Pyruvate kinase	57.81	6	5	3.4992
Eef2	Elongation factor 2	95.25	5	5	2.9917
Pfn1	Profilin-1	14.95	5	5	2.8193
Hist1h4a	Histone H4	11.36	5	4	2.7632
Ppia	Peptidyl-prolyl cis-trans isomerase A	17.96	4	4	2.5761
Ywhaz	14-3-3 protein ζ/δ	27.75	4	3	4.4702
Ybx1	Nuclease-sensitive element-binding protein 1	35.71	4	3	2.9704
Hspa4	70 kDa Heat shock protein 4	94.07	4	3	2.9065
Tubb4b	Tubulin β-4B chain	49.8	4	3	2.8342
Hpx	Hemopexin	51.29	4	2	2.3923
Cat	Catalase	59.76	3	3	4.0551
Hspd1	60 kDa Heat shock protein	60.92	3	3	4.0264
Tkt	Transketolase	67.59	3	3	3.8275
Fkbp4	Peptidyl-prolyl cis-trans isomerase	51.54	3	3	3.0905
Ldha	L-lactate dehydrogenase A chain	36.48	3	3	2.7714
Hnrnpa2 b1	Heterogeneous nuclear ribonucleoproteins A2/B1	37.38	3	3	2.6214
Fn1	Fibronectin	272.37	3	3	2.3814
Kpnb1	Importin subunit β-1	97.12	3	3	2.1949

Table B.1. Mass Spectrometry Results for Day 1-4 EB Conditioned Media (Contd)

Symbol	Protein	Molecular Weight (kDa)	Unique Peptides	Total Peptides	Average XCorr
Hnrnpab	Heterogeneous nuclear ribonucleoprotein A/B	30.81	3	2	3.626
Gapdh	Glyceraldehyde-3-phosphate dehydrogenase	35.79	3	2	2.9579
Rps18	40S ribosomal protein S18	17.71	3	2	2.414
Spp1	Osteopontin	32.44	3	2	4.129
Hspg2	Basement membrane-specific heparan sulfate proteoglycan core protein	398.04	3	2	3.4984
Eef1d	Elongation factor 1-δ	31.27	3	2	3.2875

Table B.2. Mass Spectrometry Results for Day 1-4 EB Conditioned Media-Loaded Microparticles

Symbol	Protein	Molecular Weight (kDa)	Unique Peptides	Total Peptides	Average XCorr
Iqgap1	Ras GTPase-activating-like protein IQGAP1	188.62	32	34	3.6
Hsp90aa	90 kDa Heat shock protein α	84.73	22	24	3.2
Ncl	Nucleolin	76.68	20	23	2.9
Mybbp1	Myb-binding protein 1A	151.94	17	19	3.5
Apoe	Apolipoprotein E	35.84	15	17	3.6
Hsp90ab	90 kDa Heat shock protein β (Endoplasmin)	83.23	14	17	3.1
Eef1a1	Elongation factor 1-α 1	50.08	13	18	3.4
Eif2a	Eukaryotic translation initiation factor 2A	64.36	12	14	3.4
Rpl5	60S ribosomal protein L5	34.38	12	14	2.8
Ipo5	Importin-5	123.51	12	13	3.5
Kpnb1	Importin subunit β-1	97.12	12	13	3.5
Ssb	Lupus La protein homolog	47.73	12	13	3.0
Rps3	40S ribosomal protein S3	26.66	12	12	3.3
Npm1	Nucleophosmin	32.54	11	14	3.8
Actb	Actin, cytoplasmic 1	41.71	11	14	2.9
Sf3b1	Splicing factor 3B subunit 1	145.72	11	12	3.9
Rpl7	60S ribosomal protein L7	31.4	11	12	2.5
Rps3a	40S ribosomal protein S3a	29.87	10	14	2.8
Serbp1	Plasminogen activator inhibitor 1 RNA-binding protein	44.69	10	12	3.3
Fn1	Fibronectin	272.37	10	12	3.0
Tuba1b	Tubulin α-1B chain	50.12	9	11	3.6
Eno1	α-enolase	47.11	9	10	3.3
Rpl6	60S ribosomal protein L6	33.49	9	10	3.1
Rps2	40S ribosomal protein S2	31.21	9	10	2.8
Pxdn	Peroxidasin homolog	165	9	9	3.4
Rpl13a	60S ribosomal protein L13a	23.45	9	9	2.0
Tubb4b	Tubulin β-4B chain	49.8	8	8	3.5
Rps4x	40S ribosomal protein S4	29.58	8	8	2.9
Rps19	40S ribosomal protein S19	16.08	8	8	2.8
Serpine2	Glia-derived nexin	44.18	8	8	2.8
Rpl13	60S ribosomal protein L13	24.29	8	8	2.6

Table B.2. Mass Spectrometry Results for Day 1-4 EB Conditioned Media-Loaded Microparticles (Contd)

Symbol	Protein	Molecular Weight (kDa)	Unique Peptides	Total Peptides	Average XCorr
Rpl23a	60S ribosomal protein L23a	17.68	8	8	2.4
Rps10	40S ribosomal protein S10	18.9	7	10	2.4
Hist1h2b	Histone H2B type 1-F/J/L	13.93	7	9	2.9
Top2a	DNA topoisomerase 2-α	172.68	7	8	3.7
Rps6	40S ribosomal protein S6	28.66	7	8	3.0
Pkm	Pyruvate kinase PKM	57.81	7	7	3.8
Cct4	T-complex protein 1 subunit δ	58.03	7	7	3.3
Dhx9	ATP-dependent RNA helicase A	149.38	7	7	3.1
Rps18	40S ribosomal protein S18	17.71	7	7	2.9
Rps9	40S ribosomal protein S9	22.58	7	7	2.6
Rpl4	60S ribosomal protein L4	47.12	7	7	2.6
Hist1h4a	Histone H4	11.36	6	11	3.2
Ybx1	Nuclease-sensitive element-binding protein 1	35.71	6	9	3.9
Lamb1	Laminin subunit β-1	196.96	6	8	4.4
Rpl10a	60S ribosomal protein L10a	24.9	6	8	2.8
Rpl27	60S ribosomal protein L27	15.79	6	8	2.7
Vcp	Transitional endoplasmic reticulum ATPase	89.27	6	7	3.6
Rpl35a	60S ribosomal protein L35a	12.55	6	7	2.0
Eif3a	Eukaryotic translation initiation factor 3 subunit A	161.84	6	6	3.6
Lama1	Laminin subunit α-1	337.95	6	6	3.3
Eef2	Elongation factor 2	95.25	6	6	3.2
Hnrnpk	Heterogeneous nuclear ribonucleoprotein K	50.94	6	6	3.1
Rsu1	Ras suppressor protein 1	31.53	6	6	3.1
Rpl7a	60S ribosomal protein L7a	29.96	6	6	2.7
Fus	RNA-binding protein FUS	52.64	5	7	2.9
Acly	ATP-citrate synthase	119.65	5	6	4.0
Rps15	40S ribosomal protein S15	17.03	5	6	3.9
Set	Protein SET	33.36	5	6	3.8
Naca	Nascent polypeptide-associated complex subunit α, muscle-specific	220.36	5	6	3.7
Ldha	L-lactate dehydrogenase A chain	36.48	5	6	3.3

Table B.2. Mass Spectrometry Results for Day 1-4 EB Conditioned Media-Loaded Microparticles (Contd)

Symbol	Protein	Molecular Weight (kDa)	Unique Peptides	Total Peptides	Average XCorr
Rpl12	60S ribosomal protein L12	17.79	5	6	2.9
Psmd3	26S proteasome non-ATPase regulatory subunit 3	60.68	5	5	3.8
Tubb5	Tubulin β-5 chain	49.64	5	5	3.7
Api5	Apoptosis inhibitor 5	56.75	5	5	3.6
Rplp0	60S acidic ribosomal protein P0	34.19	5	5	3.6
Eif3l	Eukaryotic translation initiation factor 3 subunit L	66.57	5	5	3.6
Rps7	40S ribosomal protein S7	22.11	5	5	3.5
Rpl18	60S ribosomal protein L18	21.63	5	5	3.5
Tcp1	T-complex protein 1 subunit α	60.41	5	5	3.4
Trim28	Transcription intermediary factor 1-β	88.79	5	5	3.2
D1Pas1	Putative ATP-dependent RNA helicase Pl10	73.1	5	5	3.1
Rbmxl1	RNA binding motif protein	42.14	5	5	3.1
Hmgb1	High mobility group protein B1	24.88	5	5	3.1
Map4	Microtubule-associated protein	117.36	5	5	2.8
Pabpc1	Polyadenylate-binding protein	70.63	5	5	2.2
Btf3	Transcription factor BTF3	22.02	4	6	4.5
Rps17	40S ribosomal protein S17	15.51	4	6	4.3
Kpna2	Importin subunit α-1	57.89	4	5	4.0
Rpl3	60S ribosomal protein L3	46.08	4	5	3.1
Rpl31	60S ribosomal protein L31	14.45	4	5	2.6
Hnrnpab	Heterogeneous nuclear ribonucleoprotein A/B	30.81	4	4	4.1
Snrpa1	U2 small nuclear ribonucleoprotein	28.34	4	4	3.9
G3bp1	Ras GTPase-activating protein-binding protein 1	51.8	4	4	3.8
Rps14	40S ribosomal protein S14	16.26	4	4	3.8
Eif4a2	Eukaryotic initiation factor 4A-2	46.37	4	4	3.6
Ilf2	Interleukin enhancer-binding factor	43.04	4	4	3.3
Rps8	40S ribosomal protein S8	24.19	4	4	3.3
Aldh2	Aldehyde dehydrogenase, mitochondrial	56.5	4	4	3.2
Rpl24	60S ribosomal protein L24	17.77	4	4	3.1
Rif1	Telomere-associated protein RIF1	266.06	4	4	3.1

Table B.2. Mass Spectrometry Results for Day 1-4 EB Conditioned Media-Loaded Microparticles (Contd)

Symbol	Protein	Molecular Weight (kDa)	Unique Peptides	Total Peptides	Average XCorr
Cct7	T-complex protein 1 subunit	59.61	4	4	3.1
Eef1d	Elongation factor 1-δ	31.27	4	4	3.0
Cand1	Cullin-associated NEDD8-dissociated protein 1	136.24	4	4	3.0
Glud1	Glutamate dehydrogenase 1, mitochondrial	61.3	4	4	3.0
Rpl26	60S ribosomal protein L26	17.25	4	4	3.0
Ran	GTP-binding nuclear protein Ran	24.41	4	4	2.9
Pygl	Glycogen phosphorylase, liver form	97.4	4	4	2.9
Rps23	40S ribosomal protein S23	15.8	4	4	2.7
Rpl15	60S ribosomal protein L15	24.13	4	4	2.7
Kars	Lysine - tRNA ligase	67.8	4	4	2.7
Hnrnpa3	Heterogeneous nuclear ribonucleoprotein A3	39.63	4	4	2.6
Sfrp2	Secreted frizzled-related protein 2	33.45	4	4	2.6
Snrpb2	U2 small nuclear ribonucleoprotein	25.31	4	4	2.6
Rps15a	40S ribosomal protein S15a	14.83	4	4	2.5
Rrbp1	Ribosome-binding protein 1	172.78	4	4	2.5
Snrnp70	U1 small nuclear ribonucleoprotein 70 kDa	51.96	4	4	2.5
Sf3b2	Protein Sf3b2	98.14	4	4	2.4
Ddx5	Probable ATP-dependent RNA helicase DDX5	69.25	4	4	2.4
Rpl30	60S ribosomal protein L30	12.78	4	4	2.3
H3f3c	Histone H3.3C	15.31	4	4	2.2
Rplp2	60S acidic ribosomal protein P2	11.64	3	5	3.8
Sf3b3	Splicing factor 3B subunit 3	135.46	3	4	4.3
Eif3f	Eukaryotic translation initiation factor 3 subunit F	37.96	3	4	4.0
Fasn	Fatty acid synthase	272.26	3	4	3.8
Nap1l1	Nucleosome assembly protein 1-like	45.32	3	4	3.7
Rpl9	60S ribosomal protein L9	21.87	3	4	3.7
Rps24	40S ribosomal protein S24	15.41	3	4	3.6
Sub1	Activated RNA polymerase II transcriptional coactivator p15	14.42	3	4	3.0
Sfrp1	Secreted frizzled-related protein 1	35.39	3	4	2.8

Table B.2. Mass Spectrometry Results for Day 1-4 EB Conditioned Media-Loaded Microparticles (Contd)

Symbol	Protein	Molecular Weight (kDa)	Unique Peptides	Total Peptides	Average XCorr
Rps13	40S ribosomal protein S13	17.21	3	4	2.5
Hspd1	60 kDa heat shock protein, mitochondrial	60.92	3	3	4.6
Rpsa	40S ribosomal protein SA	32.82	3	3	4.5
Lamc1	Laminin subunit γ-1	177.18	3	3	4.2
St13	Hsc70-interacting protein	41.63	3	3	4.1
Thumpd1	THUMP domain-containing protein	38.86	3	3	3.9
Thbs3	Thrombospondin-3	104.05	3	3	3.8
Cct2	T-complex protein 1 subunit β	57.44	3	3	3.8
Psme3	Proteasome activator complex subunit 3	29.49	3	3	3.7
Prpf4b	Serine/threonine-protein kinase PRP4 homolog	116.9	3	3	3.6
Cltc	Clathrin heavy chain 1	191.43	3	3	3.6
Xpo1	Exportin-1	123.01	3	3	3.6
Dek	Protein DEK	43.13	3	3	3.6
Hspa8	Heat shock cognate 71 kDa protein	70.83	3	3	3.5
Psmd2	26S proteasome non-ATPase regulatory subunit 2	100.14	3	3	3.5
Eif3b	Eukaryotic translation initiation factor 3 subunit B	91.31	3	3	3.5
Cul1	Cullin-1	89.63	3	3	3.5
Hspa1l	Heat shock 70 kDa protein 1-like	70.59	3	3	3.5
Pltp	Phospholipid transfer protein	54.42	3	3	3.4
Aldoa	Fructose-bisphosphate aldolase	39.33	3	3	3.3
Snrpd2	Small nuclear ribonucleoprotein Sm D2	13.52	3	3	3.3
Vars	Valine-tRNA ligase	140.13	3	3	3.3
Parp1	Poly ADP-ribose polymerase 1	113.03	3	3	3.2
Hnrnpc	Heterogeneous nuclear ribonucleoproteins C1/C2	34.36	3	3	3.2
Sfpq	Splicing factor, proline- and glutamine-rich	75.39	3	3	3.1
Cul4b	Cullin-4B	110.63	3	3	3.1
Rpf2	Ribosome production factor 2	35.34	3	3	3.1
Hnrnpa1	Heterogeneous nuclear ribonucleoprotein A1	34.18	3	3	3.0
Rps25	40S ribosomal protein S25	13.73	3	3	2.9

Table B.2. Mass Spectrometry Results for Day 1-4 EB Conditioned Media-Loaded Microparticles (Contd)

Symbol	Protein	Molecular Weight (kDa)	Unique Peptides	Total Peptides	Average XCorr
H2afz	Histone H2A.Z	13.54	3	3	2.8
Hmgb2	High mobility group protein B2	24.15	3	3	2.8
Hist1h1c	Histone H1.2	21.25	3	3	2.7
Tubb1	Tubulin β-1 chain	50.41	3	3	2.7
Hsd17b4	Peroxisomal multifunctional enzyme type 2	79.43	3	3	2.7
Uba1	Ubiquitin-like modifier-activating enzyme 1	117.73	3	3	2.7
Gapdh	Glyceraldehyde-3-phosphate dehydrogenase	35.79	3	3	2.7
Rpl17	60S ribosomal protein L17	21.41	3	3	2.7
Tnpo1	Transportin-1	102.29	3	3	2.6
Lyar	Cell growth-regulating nucleolar protein	43.71	3	3	2.6
Hist1h1b	Histone H1.5	22.56	3	3	2.6
Hnrnpa2b1	Heterogeneous nuclear ribonucleoproteins A2/B1	37.38	3	3	2.5
Rps16	40S ribosomal protein S16	16.44	3	3	2.4
Rpl36	60S ribosomal protein L36	12.21	3	3	2.3
Lefty2	Left-right determination factor	41.15	2	2	3.0
Rpl22	60S ribosomal protein L22 (Heparin-binding protein HBp15)	14.75	2	2	2.8

Table B.3. Cellular Compartment Clustering of MSC Conditioned Media-Loaded Microparticles

Cellular Compartment	Number of Identified Peptides	Percentage of Total Peptides (%)	P Value
Intracellular	28	82.4	3.91E-02
Organelle part	18	52.9	1.36E-03
Extracellular space	16	47.1	9.66E-11
Protein complex	13	38.2	3.18E-03
Non-membrane-bounded organelle	12	35.3	1.01E-02
Extracellular matrix	7	20.6	5.77E-05
Vesicle	7	20.6	1.99E-03
Insulin-like growth factor binding protein complex	2	5.88	8.08E-03
Fibrinogen complex	2	5.88	1.41E-02

Table B.4. Mass Spectrometry Results for MSC Conditioned Media-Loaded Microparticles

Symbol	Protein	Molecular Weight (kDa)	Unique Peptides	Total Peptides	Average XCorr
THBS1	Thrombospondin-1	129.3	25	27	3.2045
RRBP1	Ribosome-binding protein 1	152.38	14	16	2.7645
COL1A1	Collagen α-1 chain	138.86	11	12	2.6359
FN1	Fibronectin	262.46	10	11	3.0034
F5	Coagulation factor V	251.55	9	9	2.8696
ITIH2	Inter-α-trypsin inhibitor heavy chain H2	106.4	7	7	2.6648
GSN	Gelsolin	85.64	6	8	2.8178
ACTB	Actin, cytoplasmic 1	41.71	5	6	2.9129
EEF1A1	Elongation factor 1-α 1	50.11	5	6	2.7799
HBA1	Hemoglobin subunit α	15.25	5	8	3.1793
APOE	Apolipoprotein E	36.13	4	5	3.284
COL1A2	Collagen α-2 chain	129.24	4	5	2.8195
EDF1	Endothelial differentiation-related factor 1	16.36	3	4	2.8132
C4A	Complement C4-A	192.66	3	3	2.5517
HMGB2	High mobility group protein B2	24.02	3	4	2.8803
IQGAP1	Ras GTPase-activating-like protein IQGAP1	189.13	3	3	2.4108
HMGB1P1	Putative high mobility group protein B1-like 1	24.22	2	2	2.9811
LECT2	Leukocyte cell-derived chemotaxin-2	16.38	2	3	2.224
CHAD	Chondroadherin	40.45	2	2	4.7743
F13A1	Coagulation factor XIII A chain	83.21	2	2	2.8772
HBD	Hemoglobin subunit δ	16.05	2	2	2.7413
AFP	α-fetoprotein	68.63	2	2	2.9331
APOB	Apolipoprotein B-100	515.28	2	2	2.9615
HMGN1	Non-histone chromosomal protein HMG-14	10.65	2	2	2.6728
ANXA2	Annexin A2	38.58	2	3	3.752
HMGB1	High mobility group protein B1	24.88	2	2	3.7922
HIST1H1E	Histone H1.4	21.85	2	2	2.795
PKM	Pyruvate kinase PKM	57.9	2	4	2.411
IGFBP3	Insulin-like growth factor-binding protein 3	31.65	2	2	2.404

Table B.4. Mass Spectrometry Results for MSC Conditioned Media-Loaded Microparticles (Contd)

Symbol	Protein	Molecular Weight (kDa)	Unique Peptides	Total Peptides	Average XCorr
FLNA	Filamin-A	280.56	2	3	2.8689
IGFBP5	Insulin-like growth factor-binding protein 5	30.55	2	2	3.1013
KIF5B	Kinesin-1 heavy chain	109.62	2	3	2.6433
RNASE4	Ribonuclease 4	16.83	2	3	3.2315
THBS4	Thrombospondin-4	105.8	2	2	2.133
SERBP1	Plasminogen activator inhibitor 1 RNA-binding protein	44.94	2	2	3.7359
LRRC59	Leucine-rich repeat-containing protein 59	34.91	2	3	1.9339

REFERENCES

1. Mehta, M., et al., *Biomaterial delivery of morphogens to mimic the natural healing cascade in bone.* Advanced Drug Delivery Reviews, 2012. **64**(12): p. 1257-1276.
2. Laurencin, C., Y. Khan, and S.F. El-Amin, *Bone graft substitutes.* 2006.
3. Ruppert, R., E. Hoffmann, and W. Sebald, *Human bone morphogenetic protein 2 contains a heparin‐binding site which modifies its biological activity.* Eur J Biochem, 1996. **237**(1): p. 295-302.
4. Einhorn, T.A., *Clinical Applications of Recombinant Human BMPs: Early Experience and Future Development.* The Journal of Bone & Joint Surgery, 2003. **85**(suppl_3): p. 82-88.
5. Bridwell, K.H., et al., *What's New in Spine Surgery.* J Bone Joint Surg Am, 2013. **95**(12): p. 1144-1150.
6. McKay, W.F., S.M. Peckham, and J.M. Badura, *A comprehensive clinical review of recombinant human bone morphogenetic protein-2 (INFUSE® Bone Graft).* International orthopaedics, 2007. **31**(6): p. 729-734.
7. Ngangan, A.V., et al., *Soluble factors secreted by differentiating embryonic stem cells stimulate exogenous cell proliferation and migration.* Stem Cell Res. Ther., 2014. **5**: p. 26.
8. Yousef, H., et al., *hESC-secreted proteins can be enriched for multiple regenerative therapies by heparin-binding.* Aging, 2013. **5**(5): p. 357.
9. Shields, L.B., et al., *Adverse effects associated with high-dose recombinant human bone morphogenetic protein-2 use in anterior cervical spine fusion.* Spine, 2006. **31**(5): p. 542-547.
10. Pakulska, M.M., S. Miersch, and M.S. Shoichet, *Designer protein delivery: From natural to engineered affinity-controlled release systems.* Science, 2016. **351**(6279): p. aac4750.
11. Hettiaratchi, M., R. Guldberg, and T. McDevitt, *Biomaterial strategies for controlling stem cell fate via morphogen sequestration.* Journal of Materials Chemistry B, 2016. **4**: p. 3464-3481.
12. Bilezikian, J.P., L.G. Raisz, and T.J. Martin, *Principles of Bone Biology: Two-Volume Set*. 2008: Academic Press.
13. Kay, M.I., R. Young, and A. Posner, *Crystal structure of hydroxyapatite.* 1964.
14. Young, M.F., *Bone matrix proteins: their function, regulation, and relationship to osteoporosis.* Osteoporosis international, 2003. **14**(3): p. 35-42.
15. Kalfas, I.H., *Principles of bone healing.* Neurosurgical Focus, 2001. **10**(4): p. 1-4.
16. Zysset, P.K., et al., *Elastic modulus and hardness of cortical and trabecular bone lamellae measured by nanoindentation in the human femur.* Journal of biomechanics, 1999. **32**(10): p. 1005-1012.
17. Bayraktar, H.H., et al., *Comparison of the elastic and yield properties of human femoral trabecular and cortical bone tissue.* Journal of Biomechanics, 2004. **37**(1): p. 27-35.

18. Ornitz, D.M. and P.J. Marie, *FGF signaling pathways in endochondral and intramembranous bone development and human genetic disease.* Genes & development, 2002. **16**(12): p. 1446-1465.
19. Gilbert, S.F., *Osteogenesis: the development of bones.* 2000.
20. Ash, P., J. Loutit, and K. Townsend, *Osteoclasts derived from haematopoietic stem cells.* Nature, 1980. **283**(5748): p. 669-670.
21. Kolar, P., et al., *The early fracture hematoma and its potential role in fracture healing.* Tissue Engineering Part B: Reviews, 2010. **16**(4): p. 427-434.
22. Wang, Y., et al., *The hypoxia-inducible factor α pathway couples angiogenesis to osteogenesis during skeletal development.* Journal of Clinical Investigation, 2007. **117**(6): p. 1616-1626.
23. Mountziaris, P.M. and A.G. Mikos, *Modulation of the inflammatory response for enhanced bone tissue regeneration.* Tissue Engineering Part B: Reviews, 2008. **14**(2): p. 179-186.
24. Mountziaris, P.M., et al., *Harnessing and modulating inflammation in strategies for bone regeneration.* Tissue Engineering Part B: Reviews, 2011. **17**(6): p. 393-402.
25. Cho, T.J., L.C. Gerstenfeld, and T.A. Einhorn, *Differential temporal expression of members of the transforming growth factor β superfamily during murine fracture healing.* Journal of Bone and Mineral Research, 2002. **17**(3): p. 513-520.
26. Kempen, D.H., et al., *Growth factor interactions in bone regeneration.* Tissue Engineering Part B: Reviews, 2010. **16**(6): p. 551-566.
27. Deschaseaux, F., L. Sensébé, and D. Heymann, *Mechanisms of bone repair and regeneration.* Trends in molecular medicine, 2009. **15**(9): p. 417-429.
28. Nanes, M.S., *Tumor necrosis factor-α: molecular and cellular mechanisms in skeletal pathology.* Gene, 2003. **321**: p. 1-15.
29. Devescovi, V., et al., *Growth factors in bone repair.* La Chirurgia degli organi di movimento, 2008. **92**(3): p. 161-168.
30. Blank, E., et al., *Early analysis of the United States Army's telemedicine orthopaedic consultation program.* Journal of surgical orthopaedic advances, 2011. **20**(1): p. 50.
31. Sampath, T., N. Muthukumaran, and A. Reddi, *Isolation of osteogenin, an extracellular matrix-associated, bone-inductive protein, by heparin affinity chromatography.* Proceedings of the National Academy of Sciences, 1987. **84**(20): p. 7109-7113.
32. Urist, M.R., A. Mikulski, and A. Lietze, *Solubilized and insolubilized bone morphogenetic protein.* Proceedings of the National Academy of Sciences, 1979. **76**(4): p. 1828-1832.
33. Wozney, J.M., et al., *Novel Regulators of Bone Formation: Molecular Clones and Activities.* Science, 1988. **242**(4885): p. 1528-1534.
34. Burkus, J.K., et al., *Anterior lumbar interbody fusion using rhBMP-2 with tapered interbody cages.* Journal of spinal disorders & techniques, 2002. **15**(5): p. 337-349.
35. Burkus, J.K., et al., *Is INFUSE Bone Graft Superior to Autograft Bone? An Integrated Analysis of Clinical Trials Using the LT-CAGE Lumbar Tapered*

Fusion Device. Journal of Spinal Disorders & Techniques, 2003. **16**(2): p. 113-122.
36. Boden, S.D., et al., *Use of Recombinant Human Bone Morphogenetic Protein-2 to Achieve Posterolateral Lumbar Spine Fusion in Humans: A Prospective, Randomized Clinical Pilot Trial 2002 Volvo Award in Clinical Studies.* Spine, 2002. **27**(23): p. 2662-2673.
37. Govender, S., et al., *Recombinant human bone morphogenetic protein-2 for treatment of open tibial fractures a prospective, controlled, randomized study of four hundred and fifty patients.* The Journal of Bone & Joint Surgery, 2002. **84**(12): p. 2123-2134.
38. Boyne, P.J., et al., *De novo bone induction by recombinant human bone morphogenetic protein-2 (rhBMP-2) in maxillary sinus floor augmentation.* Journal of Oral and Maxillofacial Surgery, 2005. **63**(12): p. 1693-1707.
39. Friess, W., et al., *Characterization of absorbable collagen sponges as rhBMP-2 carriers.* International Journal of Pharmaceutics, 1999. **187**(1): p. 91-99.
40. Geiger, M., R.H. Li, and W. Friess, *Collagen sponges for bone regeneration with rhBMP-2.* Advanced Drug Delivery Reviews, 2003. **55**(12): p. 1613-1629.
41. Uludag, H., et al., *rhBMP-Collagen Sponges as Osteoinductive Devices: Effects of in Vitro Sponge Characteristics and Protein pI on in Vivo rhBMP Pharmacokinetics.* Annals of the New York Academy of Sciences, 1999. **875**(1): p. 369-378.
42. Uludag, H., et al., *Implantation of recombinant human bone morphogenetic proteins with biomaterial carriers: a correlation between protein pharmacokinetics and osteoinduction in the rat ectopic model.* J Biomed Mater Res, 2000. **50**(2): p. 227-238.
43. Wong, D.A., et al., *Neurologic impairment from ectopic bone in the lumbar canal: a potential complication of off-label PLIF/TLIF use of bone morphogenetic protein-2 (BMP-2).* The Spine Journal, 2008. **8**(6): p. 1011-1018.
44. Smucker, J.D., et al., *Increased swelling complications associated with off-label usage of rhBMP-2 in the anterior cervical spine.* Spine (Phila Pa 1976), 2006. **31**(24): p. 2813-9.
45. Chen, N.F., et al., *Symptomatic ectopic bone formation after off-label use of recombinant human bone morphogenetic protein-2 in transforaminal lumbar interbody fusion.* J Neurosurg Spine, 2010. **12**(1): p. 40-6.
46. Thomson, J.A., et al., *Embryonic stem cell lines derived from human blastocysts.* Science, 1998. **282**(5391): p. 1145-1147.
47. Evans, M.J. and M.H. Kaufman, *Establishment in culture of pluripotential cells from mouse embryos.* Nature, 1981. **292**(5819): p. 154-156.
48. Bendall, S.C., et al., *An enhanced mass spectrometry approach reveals human embryonic stem cell growth factors in culture.* Mol. Cell. Proteomics, 2009. **8**(3): p. 421-432.
49. Sarkar, P., et al., *Targeted proteomics of the secretory pathway reveals the secretome of mouse embryonic fibroblasts and human embryonic stem cells.* Mol. Cell. Proteomics, 2012. **11**(12): p. 1829-1839.

50. Farina, A., et al., *Temporal proteomic profiling of embryonic stem cell secretome during cardiac and neural differentiation.* Proteomics, 2011. **11**(20): p. 3972-3982.
51. Guo, Y., B. Graham‐Evans, and H.E. Broxmeyer, *Murine Embryonic Stem Cells Secrete Cytokines/Growth Modulators That Enhance Cell Survival/Anti‐Apoptosis and Stimulate Colony Formation of Murine Hematopoietic Progenitor Cells.* Stem Cells, 2006. **24**(4): p. 850-856.
52. Guo, Y., et al., *SDF-1/CXCL12 Enhances Survival and Chemotaxis of Murine Embryonic Stem Cells and Production of Primitive and Definitive Hematopoietic Progenitor Cells.* Stem Cells, 2005. **23**(9): p. 1324-1332.
53. Gadue, P., et al., *Wnt and TGF-β signaling are required for the induction of an in vitro model of primitive streak formation using embryonic stem cells.* Proceedings of the National Academy of Sciences, 2006. **103**(45): p. 16806-16811.
54. Nostro, M.C., et al., *Wnt, Activin, and BMP Signaling Regulate Distinct Stages in the Developmental Pathway from Embryonic Stem Cells to Blood.* Cell Stem Cell, 2008. **2**(1): p. 60-71.
55. Kinney, M.A., R. Saeed, and T.C. McDevitt, *Mesenchymal morphogenesis of embryonic stem cells dynamically modulates the biophysical microtissue niche.* Scientific Reports, 2014. **4**: p. 4290.
56. Xu, R.-H., et al., *Basic FGF and suppression of BMP signaling sustain undifferentiated proliferation of human ES cells.* Nature Methods, 2005. **2**(3): p. 185-190.
57. Levenstein, M.E., et al., *Basic fibroblast growth factor support of human embryonic stem cell self‐renewal.* Stem Cells, 2006. **24**(3): p. 568-574.
58. Kattman, S.J., et al., *Stage-Specific Optimization of Activin/Nodal and BMP Signaling Promotes Cardiac Differentiation of Mouse and Human Pluripotent Stem Cell Lines.* Cell Stem Cell, 2011. **8**(2): p. 228-240.
59. Yuasa, S., et al., *Transient inhibition of BMP signaling by Noggin induces cardiomyocyte differentiation of mouse embryonic stem cells.* Nature Biotechnology, 2005. **23**(5): p. 607-611.
60. Laflamme, M.A., et al., *Cardiomyocytes derived from human embryonic stem cells in pro-survival factors enhance function of infarcted rat hearts.* Nature Biotechnology, 2007. **25**(9): p. 1015-1024.
61. Bendall, S.C., et al., *IGF and FGF cooperatively establish the regulatory stem cell niche of pluripotent human cells in vitro.* Nature, 2007. **448**(7157): p. 1015-1021.
62. Greber, B., et al., *Conserved and Divergent Roles of FGF Signaling in Mouse Epiblast Stem Cells and Human Embryonic Stem Cells.* Cell Stem Cell, 2010. **6**(3): p. 215-226.
63. Breier, G., et al., *Expression of vascular endothelial growth factor during embryonic angiogenesis and endothelial cell differentiation.* Development, 1992. **114**(2): p. 521-532.
64. Vasiliauskas, D. and C.D. Stern, *Patterning the Embryonic Axis: FGF Signaling and How Vertebrate Embryos Measure Time.* Cell, 2001. **106**(2): p. 133-136.
65. Takahashi, K., et al., *Induction of pluripotent stem cells from adult human fibroblasts by defined factors.* Cell, 2007. **131**(5): p. 861-872.

66. Takahashi, K. and S. Yamanaka, *Induction of pluripotent stem cells from mouse embryonic and adult fibroblast cultures by defined factors.* Cell, 2006. **126**(4): p. 663-676.
67. Zhang, Y., et al., *Potent Paracrine Effects of human induced Pluripotent Stem Cell-derived Mesenchymal Stem Cells Attenuate Doxorubicin-induced Cardiomyopathy.* Scientific Reports, 2015. **5**: p. 11235.
68. Gazdhar, A., et al., *The secretome of induced pluripotent stem cells reduces lung fibrosis in part by hepatocyte growth factor.* Stem Cell Res. Ther., 2014. **5**(6): p. 123.
69. Baraniak, P.R. and T.C. McDevitt, *Stem cell paracrine actions and tissue regeneration.* Regener. Med., 2010. **5**(1): p. 121-143.
70. Chen, L., et al., *Paracrine factors of mesenchymal stem cells recruit macrophages and endothelial lineage cells and enhance wound healing.* PLoS One, 2008. **3**(4): p. e1886.
71. Montes, R., et al., *Feeder-free maintenance of hESCs in mesenchymal stem cell-conditioned media: distinct requirements for TGF-β and IGF-II.* Cell Res., 2009. **19**(6): p. 698-709.
72. Majumdar, M.K., et al., *Human Marrow-Derived Mesenchymal Stem Cells (MSCs) Express Hematopoietic Cytokines and Support Long-Term Hematopoiesis When Differentiated Toward Stromal and Osteogenic Lineages.* J. Hematother. Stem Cell Res., 2000. **9**(6): p. 841-848.
73. Jing, D., et al., *Hematopoietic stem cells in co-culture with mesenchymal stromal cells-modeling the niche compartments in vitro.* Haematologica, 2010. **95**(4): p. 542-550.
74. Walenda, T., et al., *Co-culture with mesenchymal stromal cells increases proliferation and maintenance of haematopoietic progenitor cells.* J. Cell. Mol. Med., 2010. **14**(1-2): p. 337-350.
75. Murry, C.E. and G. Keller, *Differentiation of Embryonic Stem Cells to Clinically Relevant Populations: Lessons from Embryonic Development.* Cell, 2008. **132**(4): p. 661-680.
76. Lee, J.-P., et al., *Stem cells act through multiple mechanisms to benefit mice with neurodegenerative metabolic disease.* Nature Medicine, 2007. **13**(4): p. 439-447.
77. Dupont, K.M., et al., *Human stem cell delivery for treatment of large segmental bone defects.* Proceedings of the National Academy of Sciences, 2010. **107**(8): p. 3305-10.
78. Ben-Hur, T., et al., *Transplantation of Human Embryonic Stem Cell–Derived Neural Progenitors Improves Behavioral Deficit in Parkinsonian Rats.* Stem Cells, 2004. **22**(7): p. 1246-1255.
79. Ratajczak, M., et al., *Pivotal role of paracrine effects in stem cell therapies in regenerative medicine: can we translate stem cell-secreted paracrine factors and microvesicles into better therapeutic strategies&quest.* Leukemia, 2012. **26**(6): p. 1166-1173.
80. Crisostomo, P.R., et al., *Embryonic stem cells attenuate myocardial dysfunction and inflammation after surgical global ischemia via paracrine actions.* American Journal of Physiology-Heart and Circulatory Physiology, 2008. **295**(4): p. H1726-H1735.

81. Lu, P., et al., *Neural stem cells constitutively secrete neurotrophic factors and promote extensive host axonal growth after spinal cord injury.* Experimental neurology, 2003. **181**(2): p. 115-129.
82. Osugi, M., et al., *Conditioned media from mesenchymal stem cells enhanced bone regeneration in rat calvarial bone defects.* Tissue Engineering Part A, 2012. **18**(13-14): p. 1479-89.
83. Kuhn, L.T., et al., *Developmental-Like Bone Regeneration by Human Embryonic Stem Cell-Derived Mesenchymal Cells.* Tissue Engineering Part A, 2013. **20**(1-2): p. 365-377.
84. Bielby, R.C., et al., *In vitro differentiation and in vivo mineralization of osteogenic cells derived from human embryonic stem cells.* Tissue engineering, 2004. **10**(9-10): p. 1518-1525.
85. Gnecchi, M., et al., *Paracrine mechanisms in adult stem cell signaling and therapy.* Circulation Research, 2008. **103**(11): p. 1204-1219.
86. Nguyen, B.-K., et al., *Improved Function and Myocardial Repair of Infarcted Heart by Intracoronary Injection of Mesenchymal Stem Cell-Derived Growth Factors.* J. Cardiovasc. Transl. Res., 2010. **3**(5): p. 547-558.
87. Sadat, S., et al., *The cardioprotective effect of mesenchymal stem cells is mediated by IGF-I and VEGF.* Biochem. Biophys. Res. Commun., 2007. **363**(3): p. 674-679.
88. Ranganath, S.H., et al., *Harnessing the mesenchymal stem cell secretome for the treatment of cardiovascular disease.* Cell Stem Cell, 2012. **10**(3): p. 244-258.
89. Tang, J.-M., et al., *VEGF/SDF-1 promotes cardiac stem cell mobilization and myocardial repair in the infarcted heart.* Cardiovasc. Res., 2011. **91**(3): p. 402-411.
90. Hynes, R.O., *The extracellular matrix: not just pretty fibrils.* Science, 2009. **326**(5957): p. 1216-1219.
91. Miller, T., et al., *Molecular engineering of glycosaminoglycan chemistry for biomolecule delivery.* Acta Biomater., 2014. **10**(4): p. 1705-1719.
92. Lindahl, U. and M. Hook, *Glycosaminoglycans and their binding to biological macromolecules.* Annu Rev Biochem, 1978. **47**: p. 385-417.
93. Cool, S.M. and V. Nurcombe, *Heparan sulfate regulation of progenitor cell fate.* Journal of cellular biochemistry, 2006. **99**(4): p. 1040-1051.
94. Seyrek, E. and P. Dubin, *Glycosaminoglycans as polyelectrolytes.* Advanced Colloid Interface Science, 2010. **158**(1): p. 119-129.
95. Hricovíni, M., et al., *Active conformations of glycosaminoglycans. NMR determination of the conformation of heparin sequences complexed with antithrombin and fibroblast growth factors in solution.* Semin. Thromb. Hemostasis, 2002. **28**(4): p. 325-334.
96. Guimond, S., et al., *Activating and inhibitory heparin sequences for FGF-2 (basic FGF). Distinct requirements for FGF-1, FGF-2, and FGF-4.* J. Biol. Chem., 1993. **268**(32): p. 23906-23914.
97. Baird, A., et al., *Receptor-and heparin-binding domains of basic fibroblast growth factor.* Proceedings of the National Academy of Sciences, 1988. **85**(7): p. 2324-2328.

98. Arai, T., W. Busby Jr, and D.R. Clemmons, *Binding of insulin-like growth factor (IGF) I or II to IGF-binding protein-2 enables it to bind to heparin and extracellular matrix.* Endocrinology, 1996. **137**(11): p. 4571-4575.
99. McCaffrey, T.A., D.J. Falcone, and B. Du, *Transforming growth factor‐β1 is a heparin‐binding protein: Identification of putative heparin‐binding regions and isolation of heparins with varying affinity for TGF‐β1.* Journal of Controlled Release, 1992. **152**(2): p. 430-440.
100. Ling, L., et al., *Synergism between Wnt3a and heparin enhances osteogenesis via a phosphoinositide 3-kinase/Akt/RUNX2 pathway.* J. Biol. Chem., 2010. **285**(34): p. 26233-26244.
101. Zhao, B., et al., *Heparin potentiates the in vivo ectopic bone formation induced by bone morphogenetic protein-2.* J Biol Chem, 2006. **281**(32): p. 23246-23253.
102. Saksela, O., et al., *Endothelial cell-derived heparan sulfate binds basic fibroblast growth factor and protects it from proteolytic degradation.* J. Cell Biol., 1988. **107**(2): p. 743-751.
103. Seto, S.P., T. Miller, and J.S. Temenoff, *Effect of Selective Heparin Desulfation on Preservation of Bone Morphogenetic Protein-2 Bioactivity after Thermal Stress.* Bioconjugate Chem., 2015. **26**(2): p. 286-293.
104. Takada, T., et al., *Sulfated polysaccharides enhance the biological activities of bone morphogenetic proteins.* J Biol Chem, 2003. **278**(44): p. 43229-43235.
105. Kanzaki, S., et al., *Heparin inhibits BMP-2 osteogenic bioactivity by binding to both BMP-2 and BMP receptor.* J Cell Physiol, 2008. **216**(3): p. 844-850.
106. Kanzaki, S., et al., *Dual effects of heparin on BMP-2-induced osteogenic activity in MC3T3-E1 cells.* Pharmacol Rep, 2011. **63**(5): p. 1222-1230.
107. Hettiaratchi, M.H., et al., *Heparin microparticle effects on presentation and bioactivity of bone morphogenetic protein-2.* Biomaterials, 2014. **35**(25): p. 7228-7238.
108. Koch, S., et al., *Enhancing angiogenesis in collagen matrices by covalent incorporation of VEGF.* Journal of Materials Science: Materials in Medicine, 2006. **17**(8): p. 735-741.
109. Bentz, H., J. Schroeder, and T. Estridge, *Improved local delivery of TGF‐β2 by binding to injectable fibrillar collagen via difunctional polyethylene glycol.* J. Biomed. Mater. Res., 1998. **39**(4): p. 539-548.
110. Bosnakovski, D., et al., *Chondrogenic differentiation of bovine bone marrow mesenchymal stem cells (MSCs) in different hydrogels: influence of collagen type II extracellular matrix on MSC chondrogenesis.* Biotechnol. Bioeng., 2006. **93**: p. 1152-1163.
111. Bertolo, A., et al., *Growth factors cross-linked to collagen microcarriers promote expansion and chondrogenic differentiation of human mesenchymal stem cells.* Tissue Engineering Part A, 2015. **21**(19-20): p. 2618-2628.
112. Bratt-Leal, A.M., et al., *A microparticle approach to morphogen delivery within pluripotent stem cell aggregates.* Biomaterials, 2013. **34**(30): p. 7227-7235.
113. Purpura, K.A., et al., *Systematic engineering of 3D pluripotent stem cell niches to guide blood development.* Biomaterials, 2012. **33**(5): p. 1271-1280.
114. Nguyen, A.H., et al., *Gelatin methacrylate microspheres for controlled growth factor release.* Acta Biomaterialia, 2015. **13**: p. 101-110.

115. Ratanavaraporn, J. and Y. Tabata, *Enhanced osteogenic activity of bone morphogenetic protein-2 by 2-O-desulfated heparin.* Acta Biomaterialia, 2012. **8**(1): p. 173-182.
116. Johnson, M.R., et al., *Functional restoration of critically sized segmental defects with bone morphogenetic protein-2 and heparin treatment.* Clin Orthop Relat Res, 2011. **469**(11): p. 3111-3117.
117. Wissink, M.J.B., et al., *Endothelial cell seeding of (heparinized) collagen matrices: effects of bFGF pre-loading on proliferation (after low density seeding) and pro-coagulant factors.* Journal of Controlled Release, 2000. **67**(2–3): p. 141-155.
118. Knaack, S., et al., *Heparin modification of a biomimetic bone matrix for controlled release of VEGF.* J. Biomed. Mater. Res., Part A, 2014. **102**(10): p. 3500-3511.
119. Park, Y.J., et al., *Controlled release of platelet-derived growth factor-BB from chondroitin sulfate–chitosan sponge for guided bone regeneration.* Journal of Controlled Release, 2000. **67**(2): p. 385-394.
120. Tellier, L.E., et al., *Hydrolysis and sulfation pattern effects on release of bioactive bone morphogenetic protein-2 from heparin-based microparticles.* Journal of Materials Chemistry B, 2015. **3**(40): p. 8001-8009.
121. Park, J.S., et al., *The promotion of chondrogenesis, osteogenesis, and adipogenesis of human mesenchymal stem cells by multiple growth factors incorporated into nanosphere-coated microspheres.* Biomaterials, 2011. **32**(1): p. 28-38.
122. Yang, H.S., et al., *Heparin-conjugated fibrin as an injectable system for sustained delivery of bone morphogenetic protein-2.* Tissue Engineering Part A, 2010. **16**(4): p. 1225-1233.
123. Benoit, D.S., S.D. Collins, and K.S. Anseth, *Multifunctional hydrogels that promote osteogenic human mesenchymal stem cell differentiation through stimulation and sequestering of bone morphogenic protein 2.* Advanced Functional Materials, 2007. **17**(13): p. 2085-2093.
124. Benoit, D.S. and K.S. Anseth, *Heparin functionalized PEG gels that modulate protein adsorption for hMSC adhesion and differentiation.* Acta Biomaterialia, 2005. **1**(4): p. 461-470.
125. Jha, A.K., et al., *Molecular weight and concentration of heparin in hyaluronic acid-based matrices modulates growth factor retention kinetics and stem cell fate.* Journal of Controlled Release, 2015. **209**: p. 308-316.
126. Jha, A.K., et al., *Enhanced survival and engraftment of transplanted stem cells using growth factor sequestering hydrogels.* Biomaterials, 2015. **47**: p. 1-12.
127. Benoit, D.S., A.R. Durney, and K.S. Anseth, *The effect of heparin-functionalized PEG hydrogels on three-dimensional human mesenchymal stem cell osteogenic differentiation.* Biomaterials, 2007. **28**(1): p. 66-77.
128. Seto, S.P., M.E. Casas, and J.S. Temenoff, *Differentiation of mesenchymal stem cells in heparin-containing hydrogels via coculture with osteoblasts.* Cell Tissue Res, 2012. **347**(3): p. 589-601.
129. Sangaj, N., et al., *Heparin mimicking polymer promotes myogenic differentiation of muscle progenitor cells.* Biomacromolecules, 2010. **11**(12): p. 3294-3300.

130. Mammadov, R., et al., *Growth factor binding on heparin mimetic peptide nanofibers.* Biomacromolecules, 2012. **13**(10): p. 3311-3319.
131. Mammadov, R., et al., *Heparin mimetic peptide nanofibers promote angiogenesis.* Biomacromolecules, 2011. **12**(10): p. 3508-3519.
132. Frescaline, G., et al., *Glycosaminoglycan mimetic associated to human mesenchymal stem cell-based scaffolds inhibit ectopic bone formation, but induce angiogenesis in vivo.* Tissue Engineering Part A, 2013. **19**(13-14): p. 1641-1653.
133. Chang, C.-W., et al., *Engineering cell–material interfaces for long-term expansion of human pluripotent stem cells.* Biomaterials, 2013. **34**(4): p. 912-921.
134. Martino, M.M. and J.A. Hubbell, *The 12th–14th type III repeats of fibronectin function as a highly promiscuous growth factor-binding domain.* FASEB J., 2010. **24**(12): p. 4711-4721.
135. Martino, M.M., et al., *Engineering the growth factor microenvironment with fibronectin domains to promote wound and bone tissue healing.* Science Translational Medicine, 2011. **3**(100): p. 100ra89-100ra89.
136. Llopis-Hernández, V., et al., *Material-driven fibronectin assembly for high-efficiency presentation of growth factors.* Science Advances, 2016. **2**(8): p. e1600188.
137. Ding, K., et al., *6-O-Sulfated Chitosan Promoting the Neural Differentiation of Mouse Embryonic Stem Cells.* ACS Appl. Mater. Interfaces, 2014. **6**(22): p. 20043-20050.
138. Hudalla, G.A., et al., *Harnessing endogenous growth factor activity modulates stem cell behavior.* Integr Biol (Camb), 2011. **3**(8): p. 832-842.
139. Lin, C.-C. and K.S. Anseth, *Controlling Affinity Binding with Peptide-Functionalized Poly(ethylene glycol) Hydrogels.* Advanced Functional Materials, 2009. **19**(14): p. 2325-2331.
140. Gomez, N., et al., *Immobilized nerve growth factor and microtopography have distinct effects on polarization versus axon elongation in hippocampal cells in culture.* Biomaterials, 2007. **28**(2): p. 271-284.
141. De Paoli Lacerda, S.H., B. Ingber, and N. Rosenzweig, *Structure–release rate correlation in collagen gels containing fluorescent drug analog.* Biomaterials, 2005. **26**(34): p. 7164-7172.
142. Brown, K.E., et al., *Gelatin/chondroitin 6‐sulfate microspheres for the delivery of therapeutic proteins to the joint.* Arthritis Rheum., 1998. **41**(12): p. 2185-2195.
143. Coburn, J.M., et al., *Bioinspired nanofibers support chondrogenesis for articular cartilage repair.* Proceedings of the National Academy of Sciences, 2012. **109**(25): p. 10012-10017.
144. Bramono, D.S., et al., *Bone marrow-derived heparan sulfate potentiates the osteogenic activity of bone morphogenetic protein-2 (BMP-2).* Bone, 2012. **50**(4): p. 954-964.
145. Lim, J.J., et al., *Development of nano-and microscale chondroitin sulfate particles for controlled growth factor delivery.* Acta Biomater, 2011. **7**(3): p. 986-995.
146. Nakamura, S., et al., *Controlled release of FGF‐2 using fragmin/protamine microparticles and effect on neovascularization.* J. Biomed. Mater. Res., Part A, 2009. **91**(3): p. 814-823.

147. Hudalla, G.A., J.T. Koepsel, and W.L. Murphy, *Surfaces That Sequester Serum-Borne Heparin Amplify Growth Factor Activity.* Advanced Materials, 2011. **23**(45): p. 5415-5418.
148. Vaibhav, B., et al., *Bone morphogenic protein and its application in trauma cases: a current concept update.* Injury, 2007. **38**(11): p. 1227-1235.
149. Cahill, K.S., et al., *Prevalence, complications, and hospital charges associated with use of bone-morphogenetic proteins in spinal fusion procedures.* JAMA, 2009. **302**(1): p. 58-66.
150. Gautschi, O.P., S.P. Frey, and R. Zellweger, *Bone morphogenetic proteins in clinical applications.* ANZ J Surg, 2007. **77**(8): p. 626-631.
151. Ennett, A.B., D. Kaigler, and D.J. Mooney, *Temporally regulated delivery of VEGF in vitro and in vivo.* J Biomed Mater Res A, 2006. **79**(1): p. 176-184.
152. van de Wetering, P., et al., *Poly(ethylene glycol) hydrogels formed by conjugate addition with controllable swelling, degradation, and release of pharmaceutically active proteins.* J Control Release, 2005. **102**(3): p. 619-627.
153. Uludag, H., et al., *Characterization of rhBMP-2 pharmacokinetics implanted with biomaterial carriers in the rat ectopic model.* J Biomed Mater Res, 1999. **46**(2): p. 193-202.
154. Tao, L., et al., *Synthesis and bioactivity of poly(HPMA)-lysozyme conjugates: the use of novel thiazolidine-2-thione coupling chemistry.* Org Biomol Chem, 2009. **7**(17): p. 3481-3485.
155. Al-Azzam, W., et al., *Effect of the covalent modification of horseradish peroxidase with poly (ethylene glycol) on the activity and stability upon encapsulation in polyester microspheres.* J Pharm Sci, 2005. **94**(8): p. 1808-1819.
156. Capila, I. and R.J. Linhardt, *Heparin–protein interactions.* Angew Chem Int Ed Engl, 2002. **41**(3): p. 390-412.
157. Schönherr, E. and H.-J. Hausser, *Extracellular matrix and cytokines: a functional unit.* Dev Immunol, 2000. **7**(2-4): p. 89-101.
158. Deepa, S.S., et al., *Specific molecular interactions of oversulfated chondroitin sulfate E with various heparin-binding growth factors: Implications as a physiological binding partner in the brain and other tissues.* J Biol Chem, 2002. **277**(46): p. 43707-43716.
159. Guimond, S.E. and J.E. Turnbull, *Fibroblast growth factor receptor signalling is dictated by specific heparan sulphate saccharides.* Curr Biol, 1999. **9**(22): p. 1343-1346.
160. Gandhi, N.S. and R.L. Mancera, *Prediction of heparin binding sites in bone morphogenetic proteins (BMPs).* Biochim Biophys Acta, 2012. **1842**(12): p. 1374-1381.
161. Slack, J., et al., *Mesoderm induction in early Xenopus embryos by heparin-binding growth factors.* Nature, 1987. **326**(6109): p. 197-200.
162. Damon, D.H., et al., *Heparin potentiates the action of acidic fibroblast growth factor by prolonging its biological half-life.* J Cell Physiol, 1989. **138**(2): p. 221-226.
163. Ye, L., et al., *Heparin-conjugated PCL scaffolds fabricated by electrospinning and loaded with fibroblast growth factor 2.* J Biomater Sci Polym Ed, 2011. **22**(1-3): p. 389-406.

164. Liu, L.S., et al., *Hyaluronate-heparin conjugate gels for the delivery of basic fibroblast growth factor (FGF-2).* J Biomed Mater Res, 2002. **62**(1): p. 128-135.
165. Pike, D.B., et al., *Heparin-regulated release of growth factors in vitro and angiogenic response in vivo to implanted hyaluronan hydrogels containing VEGF and bFGF.* Biomaterials, 2006. **27**(30): p. 5242-5251.
166. Schroeder-Tefft, J., H. Bentz, and T. Estridge, *Collagen and heparin matrices for growth factor delivery.* J Control Release, 1997. **49**(2-3): p. 291-298.
167. Zhao, J., et al., *Preparation, structure and BMP-2 controlled release of heparin-conjugated hyaluronan microgels.* Carbohyd Polym, 2011. **86**(2): p. 806-811.
168. Xu, X., et al., *Heparin-decorated, hyaluronic acid-based hydrogel particles for the controlled release of bone morphogenetic protein 2.* Acta Biomaterialia, 2011. **7**(8): p. 3050-3059.
169. Hausser, H.J. and R.E. Brenner, *Low doses and high doses of heparin have different effects on osteoblast-like Saos-2 cells in vitro.* J Cell Biochem, 2004. **91**(5): p. 1062-1073.
170. Yang, L., et al., *The effect of heparin on osteoblast differentiation and activity in primary cultures of bovine aortic smooth muscle cells.* Atherosclerosis, 2005. **179**(1): p. 79-86.
171. Jiao, X., et al., *Heparan sulfate proteoglycans (HSPGs) modulate BMP2 osteogenic bioactivity in C2C12 cells.* J Biol Chem, 2007. **282**(2): p. 1080-1086.
172. Bhakta, G., et al., *Hyaluronic acid-based hydrogels functionalized with heparin that support controlled release of bioactive BMP-2.* Biomaterials, 2012. **33**(26): p. 6113-6122.
173. Jeon, O., et al., *Enhancement of ectopic bone formation by bone morphogenetic protein-2 released from a heparin-conjugated poly (l-lactic-< i> co</i>-glycolic acid) scaffold.* Biomaterials, 2007. **28**(17): p. 2763-2771.
174. Kang, S.-W., et al., *Bone morphogenetic protein-2 enhances bone regeneration mediated by transplantation of osteogenically undifferentiated bone marrow-derived mesenchymal stem cells.* Biotechnol Lett, 2008. **30**(7): p. 1163-1168.
175. Teixeira, S., et al., *Heparinized hydroxyapatite/collagen three-dimensional scaffolds for tissue engineering.* J Mater Sci Mater Med, 2010. **21**(8): p. 2385-2392.
176. Bae, M.S., et al., *Development of novel photopolymerizable hyaluronic acid/heparin-based hydrogel scaffolds with a controlled release of growth factors for enhanced bone regeneration.* Macromolecular Research, 2016: p. 1-9.
177. Cui, C. and S.P. Schwendeman, *One-step surface modification of poly (lactide-co-glycolide) microparticles with heparin.* Pharm Res, 2007. **24**(12): p. 2381-2393.
178. Abbah, S.A., et al., *Enhanced control of in vivo bone formation with surface functionalized alginate microbeads incorporating heparin and human bone morphogenetic protein-2.* Tissue Engineering Part A, 2012. **19**(3-4): p. 350-359.
179. Hannink, G., et al., *Evaluation of collagen/heparin coated TCP/HA granules for long-term delivery of BMP-2.* J Mater Sci Mater Med, 2013. **24**(2): p. 325-332.
180. Denizli, A., *Heparin-immobilized poly(2-hydroxyethylmethacrylate)-based microspheres.* J Appl Polym Sci, 1999. **74**(3): p. 655-662.

181. Park, Y.D., N. Tirelli, and J.A. Hubbell, *Photopolymerized hyaluronic acid-based hydrogels and interpenetrating networks.* Biomaterials, 2003. **24**(6): p. 893-900.
182. Lamprecht, M.R., D.M. Sabatini, and A.E. Carpenter, *CellProfiler: free, versatile software for automated biological image analysis.* Biotechniques, 2007. **42**(1): p. 71-75.
183. Ferrara, N., et al., *The vascular endothelial growth factor family of polypeptides.* J Cell Biochem, 1991. **47**(3): p. 211-218.
184. Gospodarowicz, D., et al., *Structural characterization and biological functions of fibroblast growth factor.* Endocr Rev, 1987. **8**(2): p. 95-114.
185. Aggarwal, B.B., et al., *Human tumor necrosis factor. Production, purification, and characterization.* J Biol Chem, 1985. **260**(4): p. 2345-2354.
186. Katagiri, T., et al., *Bone morphogenetic protein-2 converts the differentiation pathway of C2C12 myoblasts into the osteoblast lineage.* J Cell Biol, 1994. **127**(6 Pt 1): p. 1755-1766.
187. Jeon, O., et al., *Affinity-based growth factor delivery using biodegradable, photocrosslinked heparin-alginate hydrogels.* J Control Release, 2011. **154**(3): p. 258-266.
188. Jha, A.K., et al., *Perlecan domain I-conjugated, hyaluronic acid-based hydrogel particles for enhanced chondrogenic differentiation via BMP-2 release.* Biomaterials, 2009. **30**(36): p. 6964-6975.
189. La, W.G., et al., *The effect of the delivery carrier on the quality of bone formed via bone morphogenetic protein‐2.* Artif Organs, 2012. **36**(7): p. 642-647.
190. Yamamoto, M., Y. Ikada, and Y. Tabata, *Controlled release of growth factors based on biodegradation of gelatin hydrogel.* J Biomater Sci Polym Ed, 2001. **12**(1): p. 77-88.
191. Kawai, K., et al., *Accelerated tissue regeneration through incorporation of basic fibroblast growth factor-impregnated gelatin microspheres into artificial dermis.* Biomaterials, 2000. **21**(5): p. 489-499.
192. Zhao, Y., et al., *Preparation of gelatin microspheres encapsulated with bFGF for therapeutic angiogenesis in a canine ischemic hind limb.* J Biomater Sci Polym Ed, 2011. **22**(4-6): p. 665-682.
193. Krishnan, L., N.J. Willett, and R.E. Guldberg, *Vascularization strategies for bone regeneration.* Annals of Biomedical Engineering, 2014. **42**(2): p. 432-444.
194. Kempen, D.H., et al., *Effect of local sequential VEGF and BMP-2 delivery on ectopic and orthotopic bone regeneration.* Biomaterials, 2009. **30**(14): p. 2816-2825.
195. Young, S., et al., *Dose effect of dual delivery of vascular endothelial growth factor and bone morphogenetic protein-2 on bone regeneration in a rat critical-size defect model.* Tissue Engineering Part A, 2009. **15**(9): p. 2347-2362.
196. Vonau, R.L., et al., *Combination of growth factors inhibits bone ingrowth in the bone harvest chamber.* Clinical orthopaedics and related research, 2001. **386**: p. 243-251.
197. Strayhorn, C.L., et al., *Growth factors regulate expression of osteoblast-associated genes.* Journal of periodontology, 1999. **70**(11): p. 1345-1354.

198. Kuo, W.-J., M.A. Digman, and A.D. Lander, *Heparan sulfate acts as a bone morphogenetic protein coreceptor by facilitating ligand-induced receptor hetero-oligomerization.* Mol Biol Cell, 2010. **21**(22): p. 4028-4041.
199. Terada, K., et al., *Interaction of Wnt signaling with BMP/Smad signaling during the transition from cell proliferation to myogenic differentiation in mouse myoblast-derived cells.* Int J Cell Biol, 2013. **2013**: p. 616294.
200. Ito, Y., L. Shu Qin, and Y. Imanishi, *Enhancement of cell growth on growth factor-immobilized polymer film.* Biomaterials, 1991. **12**(5): p. 449-453.
201. Mann, B.K., R.H. Schmedlen, and J.L. West, *Tethered-TGF-β increases extracellular matrix production of vascular smooth muscle cells.* Biomaterials, 2001. **22**(5): p. 439-444.
202. Schultz, G.S. and A. Wysocki, *Interactions between extracellular matrix and growth factors in wound healing.* Wound Repair Regen, 2009. **17**(2): p. 153-162.
203. Dombrowski, C., et al., *Heparan sulfate mediates the proliferation and differentiation of rat mesenchymal stem cells.* Stem Cells and Development, 2009. **18**(4): p. 661-670.
204. Furue, M.K., et al., *Heparin promotes the growth of human embryonic stem cells in a defined serum-free medium.* Proceedings of the National Academy of Sciences, 2008. **105**(36): p. 13409-13414.
205. Boergermann, J.H., et al., *Dorsomorphin and LDN-193189 inhibit BMP-mediated Smad, p38 and Akt signalling in C2C12 cells.* Int J Biochem Cell Biol, 2010. **42**(11): p. 1802-1807.
206. Gallea, S., et al., *Activation of mitogen-activated protein kinase cascades is involved in regulation of bone morphogenetic protein-2-induced osteoblast differentiation in pluripotent C2C12 cells.* Bone, 2001. **28**(5): p. 491-498.
207. Einhorn, T.A., *Clinically applied models of bone regeneration in tissue engineering research.* Clinical orthopaedics and related research, 1999. **367**: p. S59-S67.
208. Hollinger, J.O. and J.C. Kleinschmidt, *The critical size defect as an experimental model to test bone repair materials.* Journal of Craniofacial Surgery, 1990. **1**(1): p. 60-68.
209. Schmitz, J.P. and J.O. Hollinger, *The critical size defect as an experimental model for craniomandibulofacial nonunions.* Clinical orthopaedics and related research, 1986. **205**: p. 299-308.
210. Reichert, J.C., et al., *The challenge of establishing preclinical models for segmental bone defect research.* Biomaterials, 2009. **30**(12): p. 2149-2163.
211. Scott, M.A., et al., *Brief review of models of ectopic bone formation.* Stem Cells and Development, 2011. **21**(5): p. 655-667.
212. Allen, A.B., et al., *In vivo bioluminescent tracking of mesenchymal stem cells within large hydrogel constructs.* Tissue Engineering Part C: Methods, 2014. **20**(10): p. 806-816.
213. Dosier, C.R., et al., *Effect of cell origin and timing of delivery for stem cell-based bone tissue engineering using biologically functionalized hydrogels.* Tissue Engineering Part A, 2014. **21**(1-2): p. 156-165.

214. Freeman, F.E., et al., *Effects of in vitro endochondral priming and pre-vascularisation of human MSC cellular aggregates in vivo.* Stem Cell Research & Therapy, 2015. **6**(1): p. 1.
215. Agrawal, V. and M. Sinha, *A review on carrier systems for bone morphogenetic protein-2.* Journal of Biomedical Materials Research Part B: Applied Biomaterials, 2016: p. n/a-n/a.
216. Wang, H., et al., *Osteogenic effect of controlled released rhBMP-2 in 3D printed porous hydroxyapatite scaffold.* Colloids and Surfaces B: Biointerfaces, 2016. **141**: p. 491-498.
217. Yuan, H., et al., *Cross-species comparison of ectopic bone formation in biphasic calcium phosphate (BCP) and hydroxyapatite (HA) scaffolds.* Tissue engineering, 2006. **12**(6): p. 1607-1615.
218. Takaoka, K., et al., *Ectopic bone induction on and in porous hydroxyapatite combined with collagen and bone morphogenetic protein.* Clinical orthopaedics and related research, 1988. **234**: p. 250-254.
219. Le Nihouannen, D., et al., *Ectopic bone formation by microporous calcium phosphate ceramic particles in sheep muscles.* Bone, 2005. **36**(6): p. 1086-1093.
220. Hulsart-Billström, G., et al., *Calcium phosphates compounds in conjunction with hydrogel as carrier for BMP-2: A study on ectopic bone formation in rats.* Acta Biomaterialia, 2011. **7**(8): p. 3042-3049.
221. Hulsart-Billström, G., et al., *Morphological differences in BMP-2-induced ectopic bone between solid and crushed hyaluronan hydrogel templates.* Journal of Materials Science: Materials in Medicine, 2013. **24**(5): p. 1201-1209.
222. Kang, S.-W., et al., *Surface modification with fibrin/hyaluronic acid hydrogel on solid-free form-based scaffolds followed by BMP-2 loading to enhance bone regeneration.* Bone, 2011. **48**(2): p. 298-306.
223. Park, K.-H., et al., *Bone morphogenic protein-2 (BMP-2) loaded nanoparticles mixed with human mesenchymal stem cell in fibrin hydrogel for bone tissue engineering.* Journal of Bioscience and Bioengineering, 2009. **108**(6): p. 530-537.
224. Park, D.-J., et al., *Injectable bone using chitosan-alginate gel/mesenchymal stem cells/BMP-2 composites.* Journal of Cranio-Maxillofacial Surgery, 2005. **33**(1): p. 50-54.
225. Saito, N., et al., *Local bone formation by injection of recombinant human bone morphogenetic protein-2 contained in polymer carriers.* Bone, 2003. **32**(4): p. 381-386.
226. Kato, M., et al., *Optimized use of a biodegradable polymer as a carrier material for the local delivery of recombinant human bone morphogenetic protein-2 (rhBMP-2).* Biomaterials, 2006. **27**(9): p. 2035-2041.
227. Jeon, O., et al., *Enhancement of ectopic bone formation by bone morphogenetic protein-2 released from a heparin-conjugated poly (L-lactic-co-glycolic acid) scaffold.* Biomaterials, 2007. **28**(17): p. 2763-2771.
228. Jeon, O., et al., *Long-term delivery enhances in vivo osteogenic efficacy of bone morphogenetic protein-2 compared to short-term delivery.* Biochemical and Biophysical Research Communications, 2008. **369**(2): p. 774-780.
229. Hu, Y., et al., *Development of a porous poly(L-lactic acid)/hydroxyapatite/collagen scaffold as a BMP delivery system and its use in*

healing canine segmental bone defect. Journal of Biomedical Materials Research Part A, 2003. **67A**(2): p. 591-598.
230. Yamamoto, M., Y. Takahashi, and Y. Tabata, *Enhanced bone regeneration at a segmental bone defect by controlled release of bone morphogenetic protein-2 from a biodegradable hydrogel.* Tissue engineering, 2006. **12**(5): p. 1305-1311.
231. Chu, T.-M.G., et al., *Segmental bone regeneration using a load-bearing biodegradable carrier of bone morphogenetic protein-2.* Biomaterials, 2007. **28**(3): p. 459-467.
232. Liu, Y., et al., *Segmental bone regeneration using an rhBMP-2-loaded gelatin/nanohydroxyapatite/fibrin scaffold in a rabbit model.* Biomaterials, 2009. **30**(31): p. 6276-6285.
233. Boerckel, J.D., et al., *Effects of protein dose and delivery system on BMP-mediated bone regeneration.* Biomaterials, 2011. **32**(22): p. 5241-5251.
234. Kolambkar, Y.M., et al., *An alginate-based hybrid system for growth factor delivery in the functional repair of large bone defects.* Biomaterials, 2011. **32**(1): p. 65-74.
235. Hettiaratchi, M., R. Guldberg, and T. McDevitt, *Biomaterial strategies for controlling stem cell fate via morphogen sequestration.* Journal of Materials Chemistry B, 2016.
236. Kim, S.E., et al., *The effect of immobilization of heparin and bone morphogenic protein-2 (BMP-2) to titanium surfaces on inflammation and osteoblast function.* Biomaterials, 2011. **32**(2): p. 366-373.
237. Hannink, G., et al., *Evaluation of collagen/heparin coated TCP/HA granules for long-term delivery of BMP-2.* Journal of Materials Science: Materials in Medicine, 2013. **24**(2): p. 325-332.
238. He, T., et al., *Photo-crosslinking hyaluronan-heparin hybrid hydrogels for BMP-2 sustained delivery.* Journal of Polymer Engineering, 2016.
239. Oest, M.E., et al., *Quantitative assessment of scaffold and growth factor‐mediated repair of critically sized bone defects.* Journal of orthopaedic research, 2007. **25**(7): p. 941-950.
240. Pakulska, M.M., et al., *Encapsulation-free controlled release: Electrostatic adsorption eliminates the need for protein encapsulation in PLGA nanoparticles.* Science Advances, 2016. **2**(5): p. e1600519.
241. Shah, N.J., et al., *Adaptive growth factor delivery from a polyelectrolyte coating promotes synergistic bone tissue repair and reconstruction.* Proceedings of the National Academy of Sciences, 2014. **111**(35): p. 12847-12852.
242. Kohane, D.S., *Microparticles and nanoparticles for drug delivery.* Biotechnology and bioengineering, 2007. **96**(2): p. 203-209.
243. Yin Win, K. and S.-S. Feng, *Effects of particle size and surface coating on cellular uptake of polymeric nanoparticles for oral delivery of anticancer drugs.* Biomaterials, 2005. **26**(15): p. 2713-2722.
244. Lind, M., E. Eriksen, and C. Bünger, *Bone morphogenetic protein-2 but not bone morphogenetic protein-4 and-6 stimulates chemotactic migration of human osteoblasts, human marrow osteoblasts, and U2-OS cells.* Bone, 1996. **18**(1): p. 53-57.

245. Majack, R.A., L.V. Goodman, and V.M. Dixit, *Cell surface thrombospondin is functionally essential for vascular smooth muscle cell proliferation.* The Journal of cell biology, 1988. **106**(2): p. 415-422.
246. García, A.J., M.a.D. Vega, and D. Boettiger, *Modulation of cell proliferation and differentiation through substrate-dependent changes in fibronectin conformation.* Molecular biology of the cell, 1999. **10**(3): p. 785-798.
247. Swertfeger, D.K. and D.Y. Hui, *Apolipoprotein E Receptor Binding VersusHeparan Sulfate Proteoglycan Binding in Its Regulation of Smooth Muscle Cell Migration and Proliferation.* Journal of Biological Chemistry, 2001. **276**(27): p. 25043-25048.
248. Wood, M.D. and S.E. Sakiyama-Elbert, *Release rate controls biological activity of nerve growth factor released from fibrin matrices containing affinity-based delivery systems.* Journal of Biomedical Materials Research Part A, 2008. **84A**(2): p. 300-312.
249. Veldhuis, J.D., et al., *Influence of the high-affinity growth hormone (GH)-binding protein on plasma profiles of free and bound GH and on the apparent half-life of GH. Modeling analysis and clinical applications.* Journal of Clinical Investigation, 1993. **91**(2): p. 629.
250. Pardridge, W.M. and E.M. Landaw, *Tracer kinetic model of blood-brain barrier transport of plasma protein-bound ligands. Empiric testing of the free hormone hypothesis.* Journal of Clinical Investigation, 1984. **74**(3): p. 745.
251. Miller, T., et al., *Molecular engineering of glycosaminoglycan chemistry for biomolecule delivery.* Acta Biomaterialia, 2014. **10**(4): p. 1705-1719.
252. Sakiyama-Elbert, S.E., *Incorporation of heparin into biomaterials.* Acta Biomaterialia, 2014. **10**(4): p. 1581-1587.
253. Lin, C.-C. and A.T. Metters, *Metal-chelating affinity hydrogels for sustained protein release.* Journal of Biomedical Materials Research Part A, 2007. **83A**(4): p. 954-964.
254. Fan, T.-H., et al., *An aptamer-functionalized hydrogel for controlled protein release: A modeling study.* Soft Matter, 2011. **7**(19): p. 9326-9334.
255. Koehler, K.C., K.S. Anseth, and C.N. Bowman, *Diels–Alder mediated controlled release from a poly (ethylene glycol) based hydrogel.* Biomacromolecules, 2013. **14**(2): p. 538-547.
256. Belair, D.G., et al., *Serum-dependence of affinity-mediated VEGF release from biomimetic microspheres.* Biomacromolecules, 2014. **15**(6): p. 2038-2048.
257. Sakiyama-Elbert, S.E. and J.A. Hubbell, *Development of fibrin derivatives for controlled release of heparin-binding growth factors.* Journal of Controlled Release, 2000. **65**(3): p. 389-402.
258. Maxwell, D.J., et al., *Development of rationally designed affinity-based drug delivery systems.* Acta Biomaterialia, 2005. **1**(1): p. 101-113.
259. Ehrbar, M., et al., *Endothelial cell proliferation and progenitor maturation by fibrin-bound VEGF variants with differential susceptibilities to local cellular activity.* Journal of Controlled Release, 2005. **101**(1–3): p. 93-109.
260. Vulic, K., et al., *Mathematical model accurately predicts protein release from an affinity-based delivery system.* Journal of Controlled Release, 2015. **197**: p. 69-77.

261. Quinlan, E., et al., *Long-term controlled delivery of rhBMP-2 from collagen–hydroxyapatite scaffolds for superior bone tissue regeneration.* Journal of Controlled Release, 2015. **207**: p. 112-119.
262. García, J.R., A.Y. Clark, and A.J. García, *Integrin-specific hydrogels functionalized with VEGF for vascularization and bone regeneration of critical-size bone defects.* Journal of Biomedical Materials Research Part A, 2015.
263. Shekaran, A., et al., *Bone Regeneration using an Alpha 2 Beta 1 Integrin-Specific Hydrogel as a BMP-2 Delivery Vehicle.* Biomaterials, 2014. **35**(21): p. 5453-5461.
264. Wong, C., et al., *Multistage nanoparticle delivery system for deep penetration into tumor tissue.* Proceedings of the National Academy of Sciences, 2011. **108**(6): p. 2426-2431.
265. Clauss, M.A. and R.K. Jain, *Interstitial transport of rabbit and sheep antibodies in normal and neoplastic tissues.* Cancer Research, 1990. **50**(12): p. 3487-3492.
266. Crank, J., *The mathematics of diffusion*. 1979: Oxford university press.
267. Leach, J.B. and C.E. Schmidt, *Characterization of protein release from photocrosslinkable hyaluronic acid-polyethylene glycol hydrogel tissue engineering scaffolds.* Biomaterials, 2005. **26**(2): p. 125-135.
268. Amsden, B., *Solute diffusion within hydrogels. Mechanisms and models.* Macromolecules, 1998. **31**(23): p. 8382-8395.
269. Johnson, E.M., et al., *Hindered diffusion in agarose gels: test of effective medium model.* Biophysical journal, 1996. **70**(2): p. 1017-1023.
270. Paradee, N., et al., *Effects of crosslinking ratio, model drugs, and electric field strength on electrically controlled release for alginate-based hydrogel.* Journal of Materials Science: Materials in Medicine, 2012. **23**(4): p. 999-1010.
271. Chary, S.R. and R.K. Jain, *Direct measurement of interstitial convection and diffusion of albumin in normal and neoplastic tissues by fluorescence photobleaching.* Proceedings of the National Academy of Sciences, 1989. **86**(14): p. 5385-5389.
272. Impellitteri, N.A., et al., *Specific VEGF sequestering and release using peptide-functionalized hydrogel microspheres.* Biomaterials, 2012. **33**(12): p. 3475-3484.
273. Lee, J.S., J.S. Lee, and W.L. Murphy, *Modular Peptides Promote Human Mesenchymal Stem Cell Differentiation on Biomaterial Surfaces.* Acta biomaterialia, 2010. **6**(1): p. 21-28.
274. Priddy, L.B., et al., *Oxidized alginate hydrogels for bone morphogenetic protein-2 delivery in long bone defects.* Acta Biomaterialia, 2014. **10**(10): p. 4390-4399.
275. Boontheekul, T., H.-J. Kong, and D.J. Mooney, *Controlling alginate gel degradation utilizing partial oxidation and bimodal molecular weight distribution.* Biomaterials, 2005. **26**(15): p. 2455-2465.
276. Rowley, J.A., G. Madlambayan, and D.J. Mooney, *Alginate hydrogels as synthetic extracellular matrix materials.* Biomaterials, 1999. **20**(1): p. 45-53.
277. Zhang, X., L. Li, and C. Luo, *Gel integration for microfluidic applications.* Lab on a Chip, 2016. **16**(10): p. 1757-1776.
278. Swaminathan, R., C.P. Hoang, and A. Verkman, *Photobleaching recovery and anisotropy decay of green fluorescent protein GFP-S65T in solution and cells:*

cytoplasmic viscosity probed by green fluorescent protein translational and rotational diffusion. Biophysical journal, 1997. **72**(4): p. 1900.
279. Fu, R., et al., *Effectiveness and harms of recombinant human bone morphogenetic protein-2 in spine fusion: a systematic review and meta-analysis.* Annals of internal medicine, 2013. **158**(12): p. 890-902.
280. Ratko, T., et al., *Bone Morphogenetic Protein: The State of the Evidence of On-Label and Off-Label Use.*, in *Blue Cross and Blue Shield EPC*. 2010.
281. Nunamaker, D., *Experimental models of fracture repair.* Clinical orthopaedics and related research, 1998. **355**: p. S56-S65.
282. Taher, F., et al., *Contralateral psoas seroma after transpsoas lumbar interbody fusion with bone morphogenetic protein-2 implantation.* The Spine Journal, 2013. **13**(2): p. e1-e5.
283. Tannoury, C.A. and H.S. An, *Complications with the use of bone morphogenetic protein 2 (BMP-2) in spine surgery.* The Spine Journal, 2014. **14**(3): p. 552-559.
284. Zara, J.N., et al., *High Doses of Bone Morphogenetic Protein 2 Induce Structurally Abnormal Bone and Inflammation In Vivo.* Tissue Engineering. Part A, 2011. **17**(9-10): p. 1389-1399.
285. Sciadini, M.F. and K.D. Johnson, *Evaluation of recombinant human bone morphogenetic protein‐2 as a bone‐graft substitute in a canine segmental defect model.* Journal of Orthopaedic Research, 2000. **18**(2): p. 289-302.
286. Boland, E.D., et al., *Tailoring tissue engineering scaffolds using electrostatic processing techniques: a study of poly (glycolic acid) electrospinning.* Journal of Macromolecular Science, Part A, 2001. **38**(12): p. 1231-1243.
287. Sandhu, H.S., et al., *Effective doses of recombinant human bone morphogenetic protein‐2 in experimental spinal fusion.* Spine, 1996. **21**(18): p. 2115-2122.
288. Shoichet, M.S., et al., *Stability of hydrogels used in cell encapsulation: An in vitro comparison of alginate and agarose.* Biotechnology and bioengineering, 1996. **50**(4): p. 374-381.
289. Boerckel, J.D., et al., *Effects of in vivo mechanical loading on large bone defect regeneration.* Journal of Orthopaedic Research, 2012. **30**(7): p. 1067-1075.
290. Sciadini, M.F. and K.D. Johnson, *Evaluation of recombinant human bone morphogenetic protein‐2 as a bone‐graft substitute in a canine segmental defect model.* J Orthop Res, 2000. **18**(2): p. 289-302.
291. Zara, J.N., et al., *High doses of bone morphogenetic protein 2 induce structurally abnormal bone and inflammation in vivo.* Tissue Eng Part A, 2011. **17**(9-10): p. 1389-1399.
292. Boland, E.D., et al., *Tailoring tissue engineering scaffolds using electrostatic processing techniques: a study of poly (glycolic acid) electrospinning.* J Macromol Sci Part A, 2001. **38**(12): p. 1231-1243.
293. Oest, M.E., et al., *Quantitative assessment of scaffold and growth factor‐mediated repair of critically sized bone defects.* J Orthop Res, 2007. **25**(7): p. 941-950.
294. Rappsilber, J., M. Mann, and Y. Ishihama, *Protocol for micro-purification, enrichment, pre-fractionation and storage of peptides for proteomics using StageTips.* Nature Protocols, 2007. **2**(8): p. 1896-1906.
295. Huttlin, E.L., et al., *A tissue-specific atlas of mouse protein phosphorylation and expression.* Cell, 2010. **143**(7): p. 1174-1189.

296. Eng, J.K., A.L. McCormack, and J.R. Yates, *An approach to correlate tandem mass spectral data of peptides with amino acid sequences in a protein database.* Journal of the American Society for Mass Spectrometry, 1994. **5**(11): p. 976-989.
297. Peng, J.M., et al., *Evaluation of multidimensional chromatography coupled with tandem mass spectrometry (LC/LC-MS/MS) for large-scale protein analysis: The yeast proteome.* Journal of Proteome Research, 2003. **2**(1): p. 43-50.
298. Elias, J.E. and S.P. Gygi, *Target-decoy search strategy for increased confidence in large-scale protein identifications by mass spectrometry.* Nature Methods, 2007. **4**(3): p. 207-214.
299. Kall, L., et al., *Semi-supervised learning for peptide identification from shotgun proteomics datasets.* Nature Methods, 2007. **4**(11): p. 923-925.
300. Kolambkar, Y.M., et al., *Spatiotemporal delivery of bone morphogenetic protein enhances functional repair of segmental bone defects.* Bone, 2011. **49**(3): p. 485-492.
301. Hayashi, M. and K. Yamada, *Divalent cation modulation of fibronectin binding to heparin and to DNA.* J Biol Chem, 1982. **257**(9): p. 5263-5267.
302. Allen, A.B., et al., *Functional augmentation of naturally-derived materials for tissue regeneration.* Ann Biomed Eng, 2015. **43**(3): p. 555-567.
303. Hettiaratchi, M., R. Guldberg, and T. McDevitt, *Biomaterial strategies for controlling stem cell fate via morphogen sequestration.* J Mater Chem B, 2016. **4**: p. 3464-3481.
304. Kisiel, M., et al., *Complexation and sequestration of BMP-2 from an ECM mimetic hyaluronan gel for improved bone formation.* PLOS ONE, 2013. **8**(10).
305. Hu, T., et al., *Novel Protamine-Based Polyelectrolyte Carrier Enhances Low-Dose rhBMP-2 in Posterolateral Spinal Fusion.* Spine, 2015. **40**(9): p. 613-621.
306. Yang, D.H., et al., *Surface modification of titanium with hydroxyapatite–heparin–BMP‐2 enhances the efficacy of bone formation and osseointegration in vitro and in vivo.* J Tissue Eng Regen Med, 2015. **9**(9): p. 1067-1077.
307. Chung, Y.-I., et al., *Enhanced bone regeneration with BMP-2 loaded functional nanoparticle–hydrogel complex.* J Control Release, 2007. **121**(1–2): p. 91-99.
308. Lin, X., *Functions of heparan sulfate proteoglycans in cell signaling during development.* Development, 2004. **131**(24): p. 6009-6021.
309. Benoit, D.S., S.D. Collins, and K.S. Anseth, *Multifunctional hydrogels that promote osteogenic human mesenchymal stem cell differentiation through stimulation and sequestering of bone morphogenic protein 2.* Adv Funct Mater, 2007. **17**(13): p. 2085-2093.
310. Hudalla, G.A., et al., *Harnessing endogenous growth factor activity modulates stem cell behavior.* Integr Biol, 2011. **3**(8): p. 832-842.
311. Ingham, K.C., S. Brew, and D.H. Atha, *Interaction of heparin with fibronectin and isolated fibronectin domains.* Biochem J, 1990. **272**(3): p. 605-611.
312. Gupta, K., et al., *Binding and displacement of vascular endothelial growth factor (VEGF) by thrombospondin: effect on human microvascular endothelial cell proliferation and angiogenesis.* Angiogenesis, 1999. **3**(2): p. 147-158.
313. Futamura, M., et al., *Two-step mechanism of binding of apolipoprotein E to heparin: Implications for the kinetics of apolipoprotein E-heparan sulfate*

proteoglycan complex formation on cell surfaces. J Biol Chem, 2005. **280**(7): p. 5414-5422.
314. Gigli, M., et al., *Heparin binding to human plasma low-density lipoproteins: dependence on heparin sulfation degree and chain length.* Biochemistry, 1992. **31**(26): p. 5996-6003.
315. Benoit, D.S. and K.S. Anseth, *Heparin functionalized PEG gels that modulate protein adsorption for hMSC adhesion and differentiation.* Acta BIomater, 2005. **1**(4): p. 461-470.
316. Wijelath, E.S., et al., *Heparin-II domain of fibronectin is a vascular endothelial growth factor-binding domain: Enhancement of VEGF biological activity by a singular growth factor/matrix protein synergism.* Circ Res, 2006. **99**(8): p. 853-860.
317. Rahman, S., et al., *Novel hepatocyte growth factor (HGF) binding domains on fibronectin and vitronectin coordinate a distinct and amplified Met-integrin induced signalling pathway in endothelial cells.* BMC Cell Biol, 2005. **6**(1): p. 8.
318. Martino, M.M., et al., *Engineering the growth factor microenvironment with fibronectin domains to promote wound and bone tissue healing.* Sci Transl Med, 2011. **3**(100): p. 100ra89.
319. Martino, M.M., et al., *Extracellular matrix-inspired growth factor delivery systems for bone regeneration.* Adv Drug Deliv Rev, 2015. **94**: p. 41-52.
320. Luong-Van, E., et al., *Controlled release of heparin from poly(ε-caprolactone) electrospun fibers.* Biomaterials, 2006. **27**(9): p. 2042-2050.
321. Singh, S., B.M. Wu, and J.C.Y. Dunn, *The enhancement of VEGF-mediated angiogenesis by polycaprolactone scaffolds with surface cross-linked heparin.* Biomaterials, 2011. **32**(8): p. 2059-2069.
322. Liu, L., et al., *Surface modification of polycaprolactone membrane via layer-by-layer deposition for promoting blood compatibility.* J Biomed Mater Res B Appl Biomater, 2008. **87B**(1): p. 244-250.
323. Lee, M.-Y., et al., *Three-dimensional cellular microarray for high-throughput toxicology assays.* Proceedings of the National Academy of Sciences, 2008. **105**(1): p. 59-63.
324. Jensen, J., J. Hyllner, and P. Björquist, *Human embryonic stem cell technologies and drug discovery.* Journal of cellular physiology, 2009. **219**(3): p. 513-519.
325. Goldring, Chris E.P., et al., *Assessing the Safety of Stem Cell Therapeutics.* Cell Stem Cell, 2011. **8**(6): p. 618-628.
326. Fraidenraich, D., et al., *Rescue of cardiac defects in id knockout embryos by injection of embryonic stem cells.* Science, 2004. **306**(5694): p. 247-252.
327. Chung, Y.-I., et al., *Enhanced bone regeneration with BMP-2 loaded functional nanoparticle–hydrogel complex.* Journal of Controlled Release, 2007. **121**(1–2): p. 91-99.
328. Jeon, O., et al., *Long-term and zero-order release of basic fibroblast growth factor from heparin-conjugated poly (L-lactide-co-glycolide) nanospheres and fibrin gel.* Biomaterials, 2006. **27**(8): p. 1598-1607.
329. Nillesen, S.T., et al., *Increased angiogenesis and blood vessel maturation in acellular collagen–heparin scaffolds containing both FGF2 and VEGF.* Biomaterials, 2007. **28**(6): p. 1123-1131.

330. Kinney, M.A., R. Saeed, and T.C. McDevitt, *Systematic analysis of embryonic stem cell differentiation in hydrodynamic environments with controlled embryoid body size.* Integrative Biology, 2012. **4**(6): p. 641-650.
331. Ungrin, M.D., et al., *Reproducible, Ultra High-Throughput Formation of Multicellular Organization from Single Cell Suspension-Derived Human Embryonic Stem Cell Aggregates.* PLoS ONE, 2008. **3**(2): p. e1565.
332. Hookway, T.A., et al., *Aggregate formation and suspension culture of human pluripotent stem cells and differentiated progeny.* Methods, 2016. **101**: p. 11-20.
333. Böhlen, P., et al., *Fluorometric assay of proteins in the nanogram range.* Archives of Biochemistry and Biophysics, 1973. **155**(1): p. 213-220.
334. Belair, D.G. and W.L. Murphy, *Specific VEGF sequestering to biomaterials: Influence of serum stability.* Acta Biomaterialia, 2013. **9**(11): p. 8823-8831.
335. Peng, J., et al., *Evaluation of multidimensional chromatography coupled with tandem mass spectrometry (LC/LC-MS/MS) for large-scale protein analysis: the yeast proteome.* Journal of proteome research, 2003. **2**(1): p. 43-50.
336. Salic, A. and T.J. Mitchison, *A chemical method for fast and sensitive detection of DNA synthesis in vivo.* Proceedings of the National Academy of Sciences, 2008. **105**(7): p. 2415-2420.
337. Sullivan, D.D., *Incorporation of Bio-inspired Microparticles within Embryonnic Stem Cell Aggregates for Directed Differentiation.* 2015.
338. Makridakis, M., M.G. Roubelakis, and A. Vlahou, *Stem cells: Insights into the secretome.* Biochimica et Biophysica Acta (BBA) - Proteins and Proteomics, 2013. **1834**(11): p. 2380-2384.
339. Cirri, P., et al., *Insulin Inhibits Platelet-derived Growth Factor-induced Cell Proliferation.* Molecular Biology of the Cell, 2005. **16**(1): p. 73-83.
340. Milasincic, D.J., et al., *Stimulation of C2C12 myoblast growth by basic fibroblast growth factor and insulin-like growth factor 1 can occur via mitogen-activated protein kinase-dependent and-independent pathways.* Molecular and cellular biology, 1996. **16**(11): p. 5964-5973.
341. Boilly, B., et al., *FGF signals for cell proliferation and migration through different pathways.* Cytokine & growth factor reviews, 2000. **11**(4): p. 295-302.
342. Taylor, W.E., et al., *Myostatin inhibits cell proliferation and protein synthesis in C2C12 muscle cells.* American Journal of Physiology-Endocrinology And Metabolism, 2001. **280**(2): p. E221-E228.
343. Rodgers, B.D., et al., *Myostatin stimulates, not inihibits, C2C12 myoblast proliferation.* Endocrinology, 2014. **155**(3): p. 670-675.
344. Joulia, D., et al., *Mechanisms involved in the inhibition of myoblast proliferation and differentiation by myostatin.* Experimental cell research, 2003. **286**(2): p. 263-275.
345. Webber, M.J., et al., *Capturing the stem cell paracrine effect using heparin-presenting nanofibres to treat cardiovascular diseases.* Journal of tissue engineering and regenerative medicine, 2010. **4**(8): p. 600-610.
346. Bakota, E.L., et al., *Injectable multidomain peptide nanofiber hydrogel as a delivery agent for stem cell secretome.* Biomacromolecules, 2011. **12**(5): p. 1651-1657.

347. Krieger, J.R., et al., *Spatially localized recruitment of anti-inflammatory monocytes by SDF-1α-releasing hydrogels enhances microvascular network remodeling.* Biomaterials, 2016. **77**: p. 280-290.
348. Peng, Y., L.E. Tellier, and J.S. Temenoff, *Heparin-based hydrogels with tunable sulfation & degradation for anti-inflammatory small molecule delivery.* Biomaterials Science, 2016. **4**(9): p. 1371-1380.
349. Roy, S., et al., *Bioactivity screening of partially desulfated low-molecular-weight heparins: a structure/activity relationship study.* Glycobiology, 2011. **21**(9): p. 1194-1205.
350. Kim, M., et al., *Heparin-based hydrogel as a matrix for encapsulation and cultivation of primary hepatocytes.* Biomaterials, 2010. **31**(13): p. 3596-3603.
351. Suárez-González, D., et al., *Controlled multiple growth factor delivery from bone tissue engineering scaffolds via designed affinity.* Tissue Engineering Part A, 2013. **20**(15-16): p. 2077-2087.
352. Pakulska, M.M., et al., *Hybrid crosslinked methylcellulose hydrogel: A predictable and tunable platform for local drug delivery.* Advanced Materials, 2015. **27**(34): p. 5002-5008.
353. Zimmermann, J.A., M.H. Hettiaratchi, and T.C. McDevitt, *Enhanced Immunosuppression of T Cells by Sustained Presentation of Bioactive Interferon-γ Within Three-Dimensional Mesenchymal Stem Cell Constructs.* Stem Cells Translational Medicine, 2016: p. sctm. 2016-0044.
354. Patel, Z.S., et al., *Dual delivery of an angiogenic and an osteogenic growth factor for bone regeneration in a critical size defect model.* Bone, 2008. **43**(5): p. 931-940.
355. Oest, M.E., *Dual osteogenic and angiogenic growth factor delivery as a treatment for segmental bone defects.* 2007.
356. Willett, N.J., et al., *Attenuated Human Bone Morphogenetic Protein-2–Mediated Bone Regeneration in a Rat Model of Composite Bone and Muscle Injury.* Tissue Engineering Part C: Methods, 2012. **19**(4): p. 316-325.
357. Sutha, K., et al., *Osteogenic Embryoid Body-Derived Material Induces Bone Formation In Vivo.* Scientific Reports, 2015. **5**: p. 9960.
358. Liu, Z., et al., *The influence of chitosan hydrogel on stem cell engraftment, survival and homing in the ischemic myocardial microenvironment.* Biomaterials, 2012. **33**(11): p. 3093-3106.
359. Saxena, S., C.E. Hansen, and L.A. Lyon, *Microgel Mechanics in Biomaterial Design.* Acc. Chem. Res., 2014. **47**(8): p. 2426-2434.
360. Luchini, A., et al., *Smart hydrogel particles: biomarker harvesting: one-step affinity purification, size exclusion, and protection against degradation.* Nano Lett., 2008. **8**(1): p. 350-361.
361. Luchini, A., et al., *Nanoparticle Technology: Addressing the fundamental roadblocks to protein biomarker discovery.* Curr. Mol. Med., 2010. **10**(2): p. 133-141.
362. Sun, B., et al., *Crosslinking heparin to collagen scaffolds for the delivery of human platelet-derived growth factor.* Journal of Biomedical Materials Research Part B: Applied Biomaterials, 2009. **91B**(1): p. 366-372.

363. Christensen, B., *Alginates as biomaterials in tissue engineering.* Carbohydrate Chemistry: Chemical and Biological Approaches, 2011. **37**: p. 227-258.
364. Hutmacher, D.W., et al., *Mechanical properties and cell cultural response of polycaprolactone scaffolds designed and fabricated via fused deposition modeling.* Journal of biomedical materials research, 2001. **55**(2): p. 203-216.
365. Bessa, P.C., M. Casal, and R. Reis, *Bone morphogenetic proteins in tissue engineering: the road from laboratory to clinic, part II (BMP delivery).* Journal of tissue engineering and regenerative medicine, 2008. **2**(2‐3): p. 81-96.
366. O'brien, F.J., J.P. Gleeson, and N. Plunkett, *Collagen/hydroxyapatite composite scaffold, and process for the production thereof*. 2013, Google Patents.
367. Hortensius, R.A. and B.A. Harley, *The use of bioinspired alterations in the glycosaminoglycan content of collagen–GAG scaffolds to regulate cell activity.* Biomaterials, 2013. **34**(31): p. 7645-7652.
368. Goissis, G., et al., *Biocompatibility studies of anionic collagen membranes with different degree of glutaraldehyde cross-linking.* Biomaterials, 1999. **20**(1): p. 27-34.
369. Yamamoto, M., Y. Takahashi, and Y. Tabata, *Controlled release by biodegradable hydrogels enhances the ectopic bone formation of bone morphogenetic protein.* Biomaterials, 2003. **24**(24): p. 4375-4383.
370. Quinlan, E., et al., *Controlled release of vascular endothelial growth factor from spray‐dried alginate microparticles in collagen–hydroxyapatite scaffolds for promoting vascularization and bone repair.* Journal of tissue engineering and regenerative medicine, 2015.
371. Hou, J., et al., *Segmental bone regeneration using rhBMP-2-loaded collagen/chitosan microspheres composite scaffold in a rabbit model.* Biomedical Materials, 2012. **7**(3): p. 035002.
372. Bergeron, E., et al., *Differentiation of preosteoblasts using a delivery system with BMPs and bioactive glass microspheres.* Journal of Materials Science: Materials in Medicine, 2007. **18**(2): p. 255-263.